DOCTOR OF PHILOSOPHY

Degradation and outdoor performance monitoring of next generation solar cells for building integrated appliscation

Stoichkov, Vasil

Award date:
2018

Awarding institution:
Bangor University

DEGRADATION AND OUTDOOR PERFORMANCE MONITORING OF NEXT GENERATION SOLAR CELLS FOR BUILDING INTEGRATED APPLICATIONS

Vasil Stoichkov

School of Electronic Engineering

Bangor University

A thesis submitted in partial fulfilment for the degree of

Doctor of Philosophy

January 2018

Abstract

This thesis focuses on the manufacturing, indoor characterisation and outdoor monitoring of Perovskite solar cells (PSCs) and Organic photovoltaics (OPVs). In order for emerging PV technologies to become commercially viable it is important that their performance under these conditions is defined.

In this thesis, the outdoor performance parameters of PSCs and OPVs monitored over the course of several campaigns are reported and benchmarked against polycrystalline silicon (poly-Si) solar cells. The data has been analysed in detail against solar irradiance dose, climatic conditions and stability. It was discovered that in common with poly-Si PVs, PSCs also exhibits a distinctive negative temperature coefficient across all performance parameters (V_{OC}, I_{SC}, FF and PCE) which decreases with increasing irradiation dose. In all outdoor campaigns the main causes for early-life degradation were noted to be sealant failure leading to oxygen and water ingress, although longer-term degradation has been observed and assigned to photo-oxidation which in some cases was effectively suppressed by the utilisation of UV filtering.

The stability of PSCs and active layers was improved by the use of luminescent down-shifting coatings which were applied as a substitute to conventional UV filters.

This thesis also demonstrates the benefit of multidirectional orientation of OPVs laminated onto an industrial building prototype for building-integrated applications. It is shown that positioning OPVs to more directions than South improves the overall diurnal yield and can potentially double the energy produced per year, in particular for peak generation hours in the UK.

The benefit of unreacted lead iodide as partial filter to the highly damaging UV component of sunlight is shown. The importance of a thin residue lead iodide layer in PSCs shows an improvement in the stability of fabricated devices.

One of the most significant findings in this thesis is the first report on the stability of perovskite absorber layers and solar cells conducted with irradiance levels at 1sun or 100sun concentrated natural sunlight. By accelerating the aging process, this method provides invaluable information about the long-term performance of absorber layers and devices which is an immense contribution to the PV community in improving the compositions and structure of PSCs.

The stability of 3rd generation PV remains a critical issue preventing the appearance of these new and exciting, flexible and highly efficient PVs on the market. The last part of this thesis shows the second important finding in this thesis which focuses on an in-depth study of the stability of OPVs subjected to a multi-stress accelerated lifetime testing (ALT). This study is conducted indoors which facilitates the most destructive elements to the life of an OPV exposed outdoors to be clearly determined by exposing the modules to well-defined exposure conditions.

Acknowledgements

First and foremost, I would like to thank my supervisor Dr Jeff Kettle for giving me the opportunity to work on such exciting material as perovskite, and more importantly for his support and guidance during this entire PhD.

I would like to thank the Sêr Cymru National Research Network for their financial support during this research.

I would like to thank Dr Tracy Sweet of Cardiff University for her support and the use of equipment at Cardiff. I would also like to thank Prof. Graham Smith for being so helpful and supportive throughout the past three years.

I would like to thank Dr Beatriz Fernandez from the University of Oviedo for her support and interest in analysing the properties of the perovskite layers fabricated during this work using Depth Profiling by GD-MS.

I would like to thank Dr Trystan Watson and the entire team at SPECIFIC for their collaboration throughout this entire PhD and the modules which they supplied for the outdoor lifetime studies.

I would like to thank Assistant Prof. Iris Visoly-Fisher and Prof. Eugene Katz for their kindness and support during the time I worked with them at Ben Gurion University of the Negev, Israel.

I also would like to thank all my colleagues at Bangor University for sharing this journey with me: Noel, Huw, Dinesh, Priyanka, Tudur, Luke, James, Jake, Ding, Eifion, Colin, Helder, Ricardo, Dr Paul Sayers, Iwan, Wendy, David, Yvonne, Julie, Siân and Gaynor.

Without my family I would have never accomplished so much. I would like to thank them for their never-ending love, encouragement and support which have always been the foundation for my success.

Finally, I thank Polina for being there for me when I needed her the most. You are my everything.

Publications

V. Stoichkov, P. Tyagi, J. Troughton, K. Hooper, F. De Rossi, T. M. Watson, J. Kettle. Outdoor monitoring of single and triple cation perovskite mini-modules. (being prepared for submission)

V. Stoichkov, D. Kumar, P. Tyagi, J. Kettle. Multi stress testing of OPV modules for accurate predictive ageing and reliability predictions. (recently submitted to IEEE Journal of Photovoltaics)

V. Stoichkov, N. Bristow, T. Sweet, J. Kettle. Studying the outdoor performance of Organic Building-Integrated Photovoltaics laminated to the cladding of a building prototype. (recently submitted to Applied Energy)

A. Melvin, **V. Stoichkov**, J. Kettle, D. Mogilyansky, E. Katz, I. V.-F. Lead iodide as a buffer layer in UV-induced degradation of $CH_3NH_3PbI_3$ films. Sol. Energy 159, 794–799 (2018).

D. Kumar, **V. Stoichkov**, S. Ghosh, G. Smith, J. K. Mixed-dimension silver nanowires for solution-processed, flexible, transparent and conducting electrodes with improved optical and physical properties. Flex. Print. Electron. 2, 15005 (2017).

M. Rolley, T. Sweet, **V. Stoichkov**, N. Bristow, J. Kettle, G. M. Triple-Junction Concentrator Photovoltaic- Thermoelectric Hybrid Receivers : Robustness , Validation and Preliminary Reliability Studies. no. April, 2017.

R. Fernandes, N. Bristow, **V. Stoichkov**, H. Anizelli, J. Duarte, E. Laureto, J. K. Development of multidye UV filters for OPVs using luminescent materials. J. Phys. D. Appl. Phys. 50, (2017).

S. Ghosh, **V. Stoichkov**, L. Haponow, J. Kettle, A. L. Martínez, D. Gómez, P. S. Accelerated weathering test for evaluating ‘ transparent encapsulants on steel substrate ’ and prediction of lifetime improvement of solar cell. no. July, pp. 10–14, 2017.

H. Anizelli, **V. Stoichkov**, R. Fernandes, J. Duarte, E. Laureto, J. Kettle, I. Visoly-Fisher, E. K. Application of luminescence downshifting materials for enhanced stability of $CH_3NH_3PbI_{3(1-x)}Cl_{3x}$ perovskite photovoltaic devices. Org. Electron. 49, 129–134 (2017).

J. Kettle, **V. Stoichkov**, D. Kumar, M. Corazza, S. Gevorgyan, F. K. Using ISOS consensus test protocols for development of quantitative life test models in ageing of organic solar cells. Sol. Energy Mater. Sol. Cells 167, 53–59 (2017).

Z. Ding, **V. Stoichkov**, M. Horie, E. Brousseau, J. K. Spray coated silver nanowires as transparent electrodes in OPVs for Building Integrated Photovoltaics applications. Sol. Energy Mater. Sol. Cells 157, 305–311 (2016).

Table of Contents

Chapter 1. Introduction

The world's total energy consumption has risen dramatically in the past 40 years. The average energy consumption per year increases by 1.8% [1]. In 40 years the global energy consumption has more than doubled reaching 110 terawatt-hours (TWh) per year in 2014 [2]. It is anticipated that in the coming years and until 2040 the energy demand will grow by 28% [3]. The main energy generation is produced by oil, coal and natural gas burning, providing a total of 85% of the energy demand, figure 1.1.

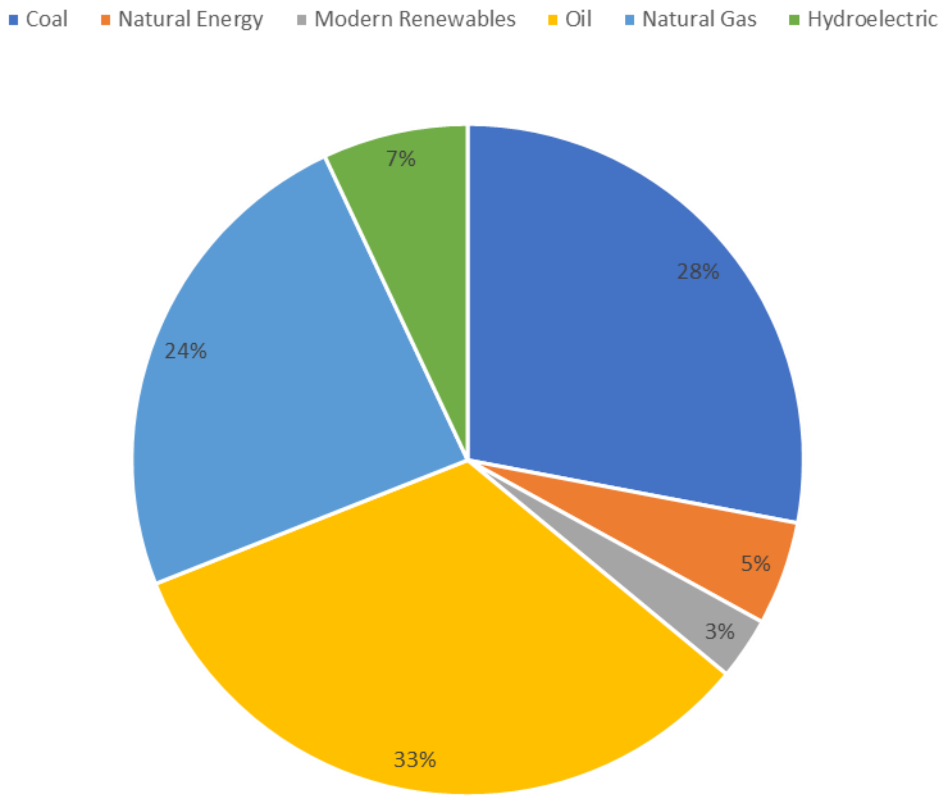

Figure 1.1 *– Global energy consumption chart showing the primary energy consumption by source* [3].

The exponential increase of carbon dioxide (CO_2) and other greenhouse gases are the main cause for global warming. An expected increase in temperature of over 2^{O}C and worst case up to 4.8^{O}C is predicted to occur by the end of this century [4]. The United States produce the most CO_2 emissions followed by China, Russia, Japan, India, Germany, United Kingdom, Canada, Italy and Mexico [5]. According to a recent report the United Kingdom is pinned as the 7th biggest CO_2 producer globally. The prognosis predicts a decrease of fossil fuels burning from approximately 65GW by the end of 2016 to below 20GW by the end of 2040, figure 1.2, allowing other sources of energy to develop.

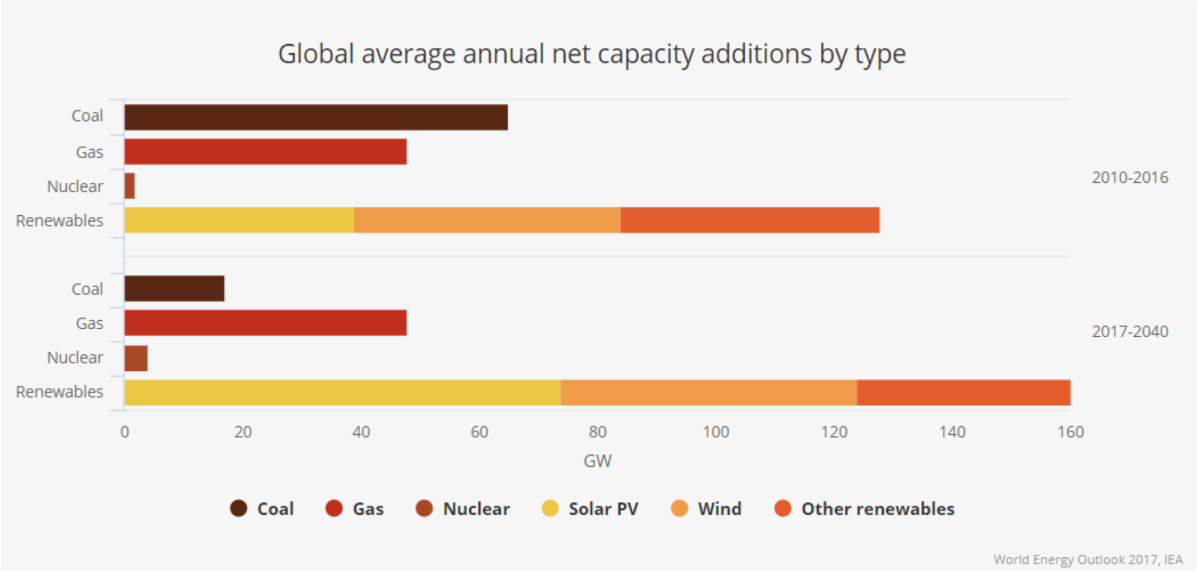

Figure 1.2 – *Global average energy generation capacity showing increasing interest in low-carbon renewable energy sources, predicting total renewable power generation to reach 40% by 2040* [6].

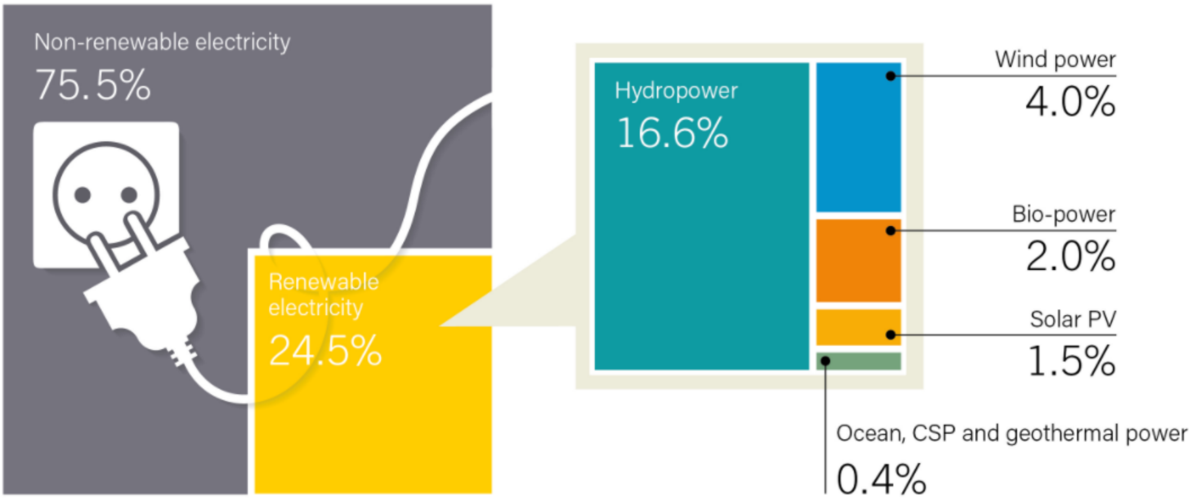

Figure 1.2 – *Renewable energy share of produced energy globally by the end of 2016* [7].

In order to reduce CO_2 emissions with the increasing energy demand, other means of energy generation must be stimulated to grow. In 2015 19.3% of the global energy generation came from renewable energy sources, which rose to 24.5% by 2017 with a total of 921GWp renewable power capacity globally [7]. Currently the main renewable energy sources are wind, biomass, hydro, geothermal, wave, tidal and solar. The electricity produced by hydropower generation holds the largest share of 16.6% of the total 24.5% renewable energy generated globally.

Perez *et al.* [8] demonstrate the potential for energy which can be generated by solar harvesting to be equal to 23,000TW/year which can provide enough energy to supply the whole world and still be in excess of just below 2,000TW [9], as shown in figure 1.3. The Earth will be supplied with enough power by covering only 0.4% of its surface with efficient (20% efficiency) photovoltaics (PVs).

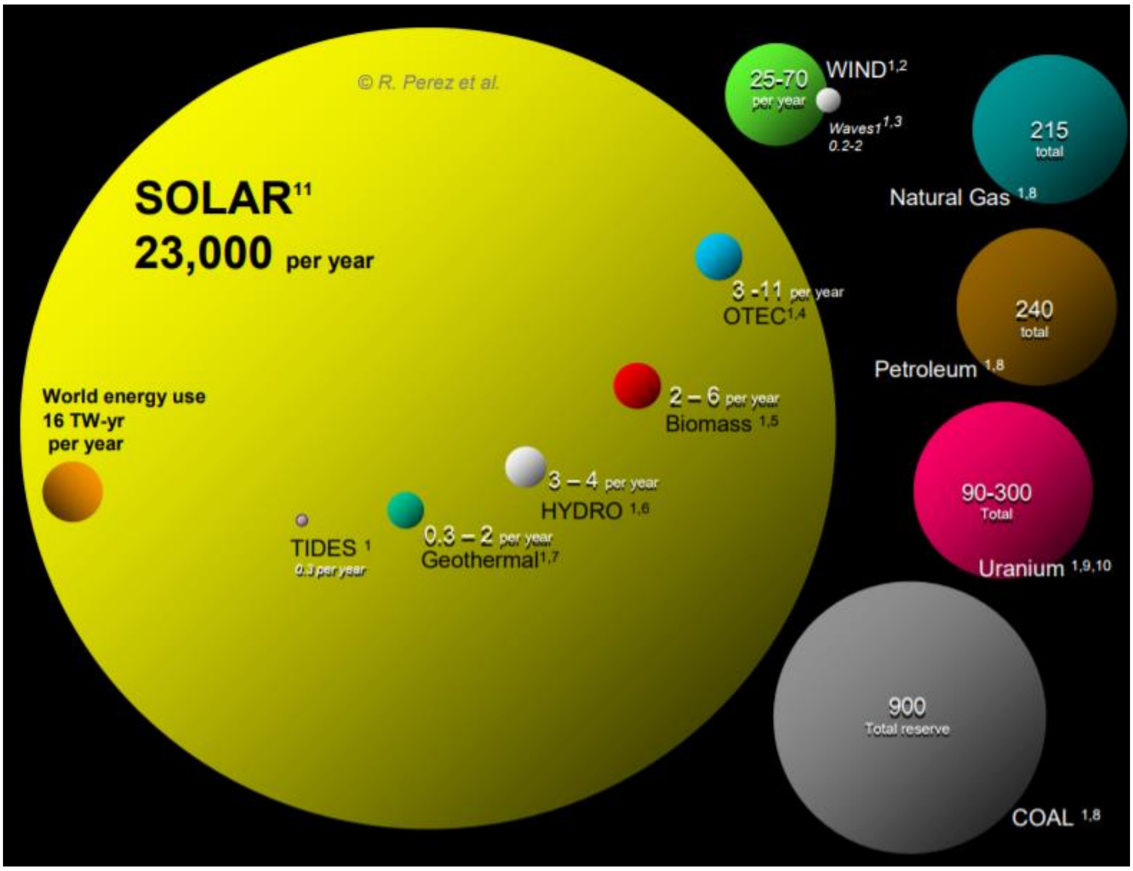

***Figure 1.3** – Comparison of renewable and finite energy sources in terawatt per year and the total amount of energy in terawatt remaining from the finite sources respectively* [8].

Solar and wind harvesting are the two fastest developing techniques for electricity production which are now affordable with an almost 50% cost drop for a utility-scale PV between 2011 and 2017 [10]. According to a report by the international energy agency (IEA) the levelized cost of electricity (LCOE) for wind and solar power has reduced substantially which brings the energy production cost to near identical figure as the conventional power generators [11]. By the end of 2016 over 303 GWp of total installed capacity and a total global PV output of 75.4GW, was reached representing 50% growth year-on-year [12].

With never ceasing efficiency record breaking competition, the PV industry may soon be able to meet the 20% efficiency requirement which Perez *et al.* suggested in 2009. Nevertheless, efficiencies over the 20% requirement have already been reported. In fact the Shockley-Queisser limit states that the maximum power conversion efficiency (PCE) obtainable for a single junction semiconductor device is 33% [13] where the record efficiency on single junction Gallium Arsenide (GaAs) already surpassed 29% and single crystal silicon has reached 25.8% [14].

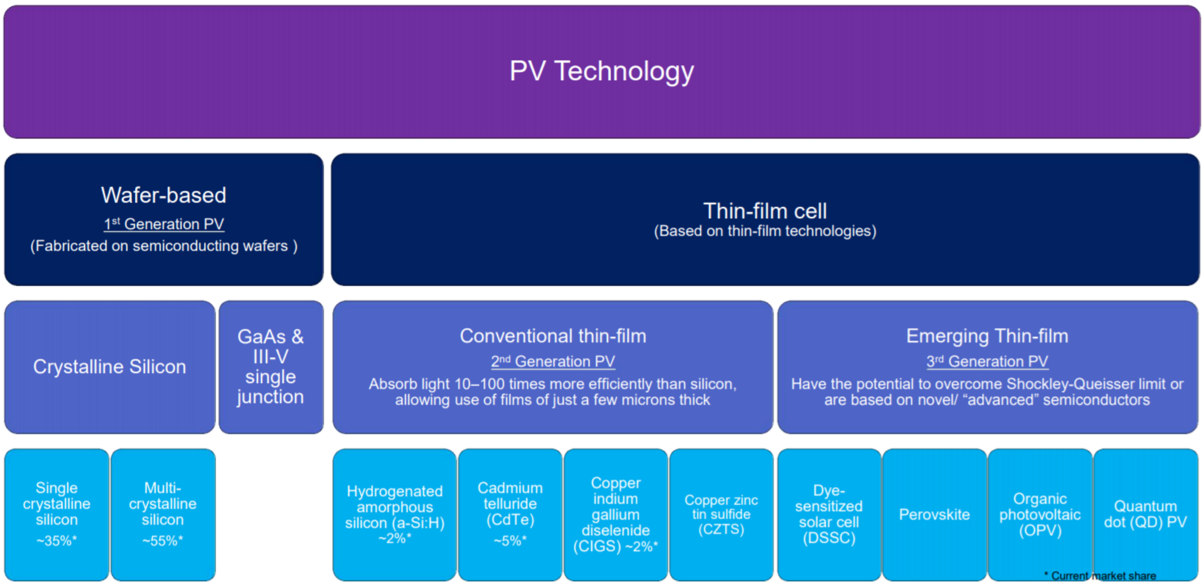

***Figure 1.4** – Photovoltaic technology chart including of emerging technologies* [15]

In accord with figure 1.4 the PV technology can be divided into three streams, 1st generation (Gen 1) wafer-based PVs and thin-film solar cells. Gen 1 consists of crystalline silicon (c-Si) which is sub-divided into monocrystalline (mono-Si) and polycrystalline (poly-Si). Worldwide until 2016 crystalline silicon occupied 94% of the solar harvesting market [16] with average commercial c-Si efficiency of 17%. Nevertheless, c-Si is an indirect band-gap semiconductor where the properties of GaAs make it a direct band-gap material which requires far less material to be classed as a light absorber. GaAs is the dominant of the wafer-based technologies due to its higher efficiency, however, it is very expensive due to its single-crystal nature and it is predominantly used with solar concentrators. Both c-Si and GaAs require very high process temperatures and chemical treatment which increases the overall price and is not environmentally friendly.

The thin-film solar cell stream is sub-divided into 2nd generation (Gen 2) and emerging PVs (Gen 3). Gen 2 which includes amorphous silicon (a-Si), Cadmium telluride (CdTe), copper indium gallium diselenide (CIGS) and copper zinc tin sulphide (CZTS) require less material in PV manufacturing and absorb between 10 to 100 times better than c-Si which make them very attractive for commercialisation due to the lower manufacturing costs. Currently Gen 2 holds 6% of the PV technology market globally [16]. Gen 3, are classed as technologies which are either novel or have the potential to overcome the Shockley-Queisser limit. The emerging PVs are aiming to compete with Gen 1 by being non-toxic and inexpensive to manufacture due to the abundance of renewable material resources. Gen 3 comprises of dye-sensitised solar cells (DSSCs), quantum dot (QD) PVs, organic photovoltaics (OPVs) and perovskite solar cells (PSCs) [15], [17], [18]. DSSCs, the first of many 3rd generation PVs were demonstrated in 1991 by O'Regan *et al.* [19] which yielded the unimaginable 7.9% PCE and in 2013 reached just under 12% [14]. The QD fabricated using cesium lead triiodide ($CsPbI_3$) reached the promising 13.4% in 2017 [20].

Regardless of the increasing performance of OPVs over the years, the flexible, solution processed devices still have not become completely commercially available. In 2012 UCLA-Sumitomo chem. reached 10.6% PCE with an organic tandem cell [21]. In the middle of 2015 Hong Kong University of Science and Technology (HKUST) reached 11.5% PCE [22] with their champion triple-junction OPV. In 2016 Heliatek after manufacturing a multi-junction device scored 13.2% efficiency record for OPVs [23].

Over the past seven years hybrid organic-inorganic PSCs have been attracting the attention of the PV community with an exponential rise in device efficiency. PSCs are mainly fabricated employing inexpensive, solution-processable materials which yield excellent devices with high efficiencies resulting in the fastest and most researched topic worldwide. PSCs have become the main contestant to resolve the global energy crisis. In just seven years the record efficiency for perovskite has reached the stunning 22.7% [14]. Regardless the sky rocketing efficiencies there are still many challenges associated with perovskite's inherent imperfections which must be addressed. Lead toxic effects and also the rigidity and lifetime of the devices remains an issue.

Some initial trials have been conducted. In December of 2013 Henry Snaith *et al.* reported a titanium dioxide-free (TiO_2)-free device with stable photocurrent under full spectrum for over 1000 hours of operation [24] and then quite recently in July 2015 Saparov *et al.* revealed a lead-free high quality thin-film perovskite with similar electronic configuration to the lead component [25]. Arianna Marchioro *et al.* [26] reported that charge recombination dictates the the lifetime of PSC which is supressed by adding porous TiO_2 electron transporting layer (ETL).

When it comes to lifetime and efficiency and cost (£/W_p), thin-film PV is not mature enough to compete with the c-Si. It is more likely that thin-film technologies will be used together with c-Si as a way of boosting device performance by using tandem stacking. In February 2017 Bush e*t al.* [27] published a report on tandem solar cells using mono-Si and perovskite where they were able to boost the device efficiency to 23.6% showing an impressive 1000 hours stability under extreme conditions of light and 85^{O}C-85% relative humidity (RH).

Building-integrated photovoltaics (BIPV) presents a possible application space for Gen 3 PVs as all of the family can be flexible and semi-transparent which is advantageous over silicon-based PV due to the aesthetic features of a building envelope being hidden by rigid and non-transparent silicon panels [28], [29].

1.1 Thesis outline

The structure of this thesis is as follows:

Chapter 2 discusses background of OPV and PSC, the current state of the two technologies and the outdoor monitoring progress achieved so far.

Chapter 3 details the experimental methods followed for manufacturing of PSCs. This chapter discusses the degradation setups built for indoor and outdoor aging of OPVs and PSCs and also the analytical techniques used to analyse the degradation of OPVs and PSCs.

Chapter 4 is the first of three results chapters which demonstrates the results PSC lifetime and performance optimisation. It details the analysis on light degradation and spectral filtration and also the effect of luminescent downshifters (LDS) on the performance of fabricated devices.

Chapter 5 presents the results from a number of outdoor monitoring campaigns conducted employing OPVs and PSCs. While the PSCs were exposed in plane with the incident solar radiation the OPV performance was studied at multiple orientations. This chapter also discusses an analytical method applied in defining the performance of OPVs installed at multiple geographical locations around the world.

Chapter 6 demonstrates an indoor characterisation method for defining the stability of OPVs and PSCs using accelerated lifetime testing (ALT) which assist in predicting the reliability of a photovoltaic device prior installing it outdoors.

Chapter 7 summarises the main findings from this thesis and also suggests possible future works which may be carried out.

The work in this thesis was completed using both PSCs and OPVs. In most cases OPVs were used as a replacement to PSCs due to the insufficient stability of PSC modules at the beginning of this thesis.

Chapter 2. Literature Review

This chapter details the current state and progress of following areas examined during this PhD: Perovskite Solar Cells (PSCs); Organic Photovoltaics (OPVs); ISOS stability test protocols; Lifetime improvement; Review of outdoor testing of BIPVs and Accelerated lifetime testing of OPVs/PSCs.

2.1 Perovskite solar cells

Over the past 10 years, most of the photovoltaic (PV) manufacturing companies in Europe have gone bankrupt, due to strong competition from Asia, which inevitably resulted in the massive reduction of manufacturing capabilities of renewable energy sources in the EU. The latest products in the PV industry are reaching a power conversion efficiency (PCE) of 25.3% with single-crystalline (non-concentrator) silicon. Perovskite Solar Cells (PSCs) are an emerging technology which over the last seven years has been a subject to an increasing interest due to its potential to be a source of clean electricity with low fabrication costs and high solution processed efficiencies. Due to the solution-processibility, it could be a strategy for Europe to regain manufacturing competitiveness as the energy costs/labour costs are not as high as a silicon plant, and could make a European company more competitive.

The perovskite solar cells are normally based on mesoporous structure or planar heterojunction organo-metal trihalide devices and are very attractive due to the abundance of materials and low temperature device fabrication configurations already available. Perovskite and its properties of transporting both holes and electrons over long distances makes the material ideal for thin-film architectures.

Mesoporous and Planar Heterojunction (PHJ) structures have already shown Power Conversion Efficiencies (PCEs) of up to 22.1% [30],[31]. This means it is already competitive with other thin film technologies, figure 2.1. Layer uniformity and pinhole free structures have been tirelessly investigated and observed to be considerably a difficult task to achieve when spin-coating a mixed halide methylammonium iodide ($CH_3NH_3PbX_X$). The resolution to was found to be the addition of an ‘antisolvent’ step during spin coating using commonly available solvents like ethyl acetate or toluene [32]. It was also found that pinhole-free perovskite films are also obtainable by introducing a 2-step spin coating process which has been proven to deliver leakage-free devices with up to 17% efficiency [33].

In contrast to the almost linear efficiency gradation of perovskite solar cells from 2013, since 2001 the organic photovoltaic technology has been on quite a gradual increase with the latest record efficiency claimed in 2015 by HKUST with their champion triple-junction 11.5% PCE cell, and 10.6% for organic tandem cells scored by UCLA-Sumitomo chem. in 2012 [21] [22], figure 2.2.

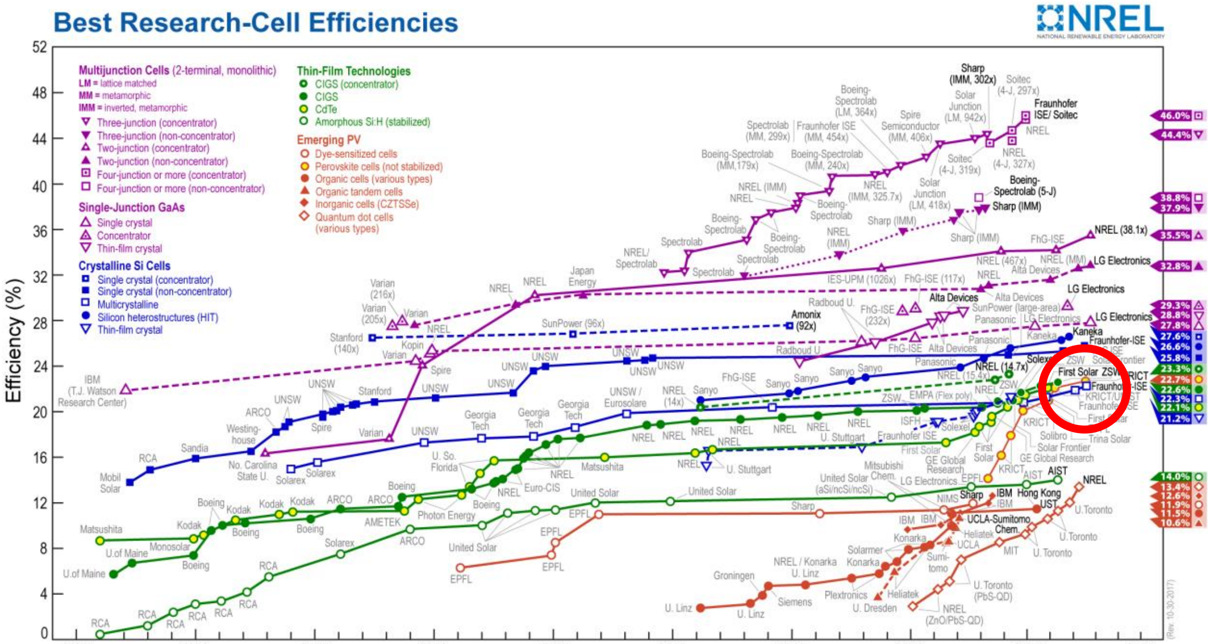

***Figure 2.1** – NREL photovoltaic progress chart made by various technologies. KRICT/UNIST leading the Perovskite efficiencies trend with 22.1%* [14]

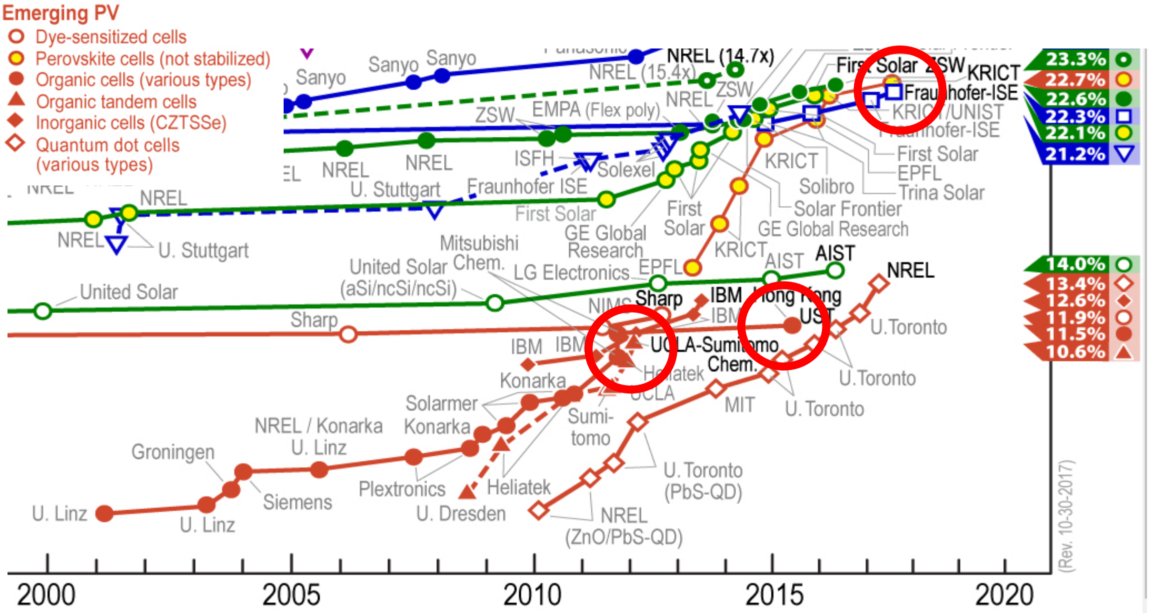

***Figure 2.2** – Progress and most recent record efficiencies reached by organic photovoltaics* [14].

2.1.1 Overview of perovskite solar cell technology

Traditionally the PV technology is divided into two general sections, 1st generation wafer-based PVs and thin-film solar cells. The wafer-based category includes of Gallium Arsenide (GaAs) devices of which the single-junction is the dominant performer after which the second position is reserved for the Crystalline Silicon (c-Si). The 2nd generation thin-film technology is constantly growing, perhaps due to the fact that it exhibits between 10 to 100 times better absorption compared to the conventional silicon cells, the leader of which, is the Cadmium Telluride (CdTe) which takes ~5% of the market share amongst Copper Indium Gallium Diselenide (CIGS), Copper Zinc Tin Sulfide (CZTS) and Hydrogenerated amorphous silicon (a-Si:H). A subsection of the thin-film PVs includes what is referred to as 3rd generation emerging thin-film devices, which are either novel technologies or technology having the potential to overcome the Shockley-Queisser limit.

Falling within this sub-category, the perovskite technology is considered currently immature for commercialisation due to poor stability, performance uncertainties, toxicity of lead and also the rigidity of the devices outdoors, which still have not been completely elucidated. In spite of this in December of 2013 Henry Snaith *et al.* reported a titanium dioxide-free (TiO_2)-free device with stable photocurrent under full spectrum for over 1000 hours of operation [24] and then quite recently in July 2015 Bayrammurad Saparov *et al.* revealed a lead-free high quality thin-film perovskite with a similar electronic configuration to the lead component [25]. Charge recombination is a key topic concerning the lifespan of the perovskite solar cells which was demonstrated by Arianna Marchioro *et al.* [34] to have a possibility of suppression by employing a porous TiO_2 film which the perovskite absorber penetrates. They also report that in fact the charge separation of the photoexcited PSC happens at both hole and electron junctions at an ultrafast rate assisting for the obtainability of extremely high efficiencies. The next section reviews the physics, architectures and failure mechanisms of PSCs.

2.1.2 Perovskite basics

The first perovskite material was a calcium titanium oxide ($CaTiO_3$) mineral discovered in Russia in 1839 and named after the Russian mineralogist Lev Perovski [35], [36]. Synthesised Perovskite material is of the form ABX_3, a crystal structure separated by thin sheets of intrusive material. **A** and **B** are cations where **A** is bigger than **B**. $\mathbf{BX_6}$ are corner-sharing octahedra where the **A** cations are positioned on the corners of the lattice [37], figure 2.3. In order to form a 3D structure the **A** cation can be realised by using most of the Alkali metals, such as Li+, Na+, Rb+, K+ and Cs+, in group 1. The most suitable divalent materials for photovoltaic applications to occupy the **B** cation are represented by carbon group 14 and are Sn^{2+}, Ge^{2+} and Pb^{2+}. Europium (Eu^{2+}) regardless not part of the carbon group has also been found a suitable match for occupying the **B** cation. **X** could be either of the materials in halogen group 17 such as F^-, Cr^-, Br^-, or I^-. Such a structure has been investigated to have a bandgap between 2.3eV and 1.57eV [38],[39] which is dependent on the halide mineral used. However, recent studies seek to minimise the bandgap which will essentially increase the device efficiency.

The perovskite structure used for absorber applications is most commonly synthesised using organic methylammonium/formamidinium lead trihalide with the chemical formula $CH_3NH_3/NH_2CHNH_2\ PbX_3$ [40], [41]. The generic crystal structure of an organo-metal trihalide Perovskite is of the shape of a cuboid formed of five atoms named α-phase [38], [42]. The central positively charged lead ion (cation) is surrounded by six negatively charged halogen ions (anions) and the positively charged ammonium ions (cations) are surrounded by eight negatively charged anions. In order the cuboid structure remain durable after excitement, the size of the ammonium ions must be greater than the lead ion. Nevertheless, this cuboid structure is hardly obtainable as a result to the obstacles formed by the specific sizes of the ions composing this crystal lattice. Yet the operational mechanisms of this vastly researched material has not been completely defined. It was shown in a report by Snaith *et al.* [43] that the formed perovskite exerts diffusion lengths of both electrons and holes of greater than 1µm by using mixed halide perovskite, property which makes it ideal for the thin-film PVs allowing it to transport positive and negative charges along its own structure over large areas.

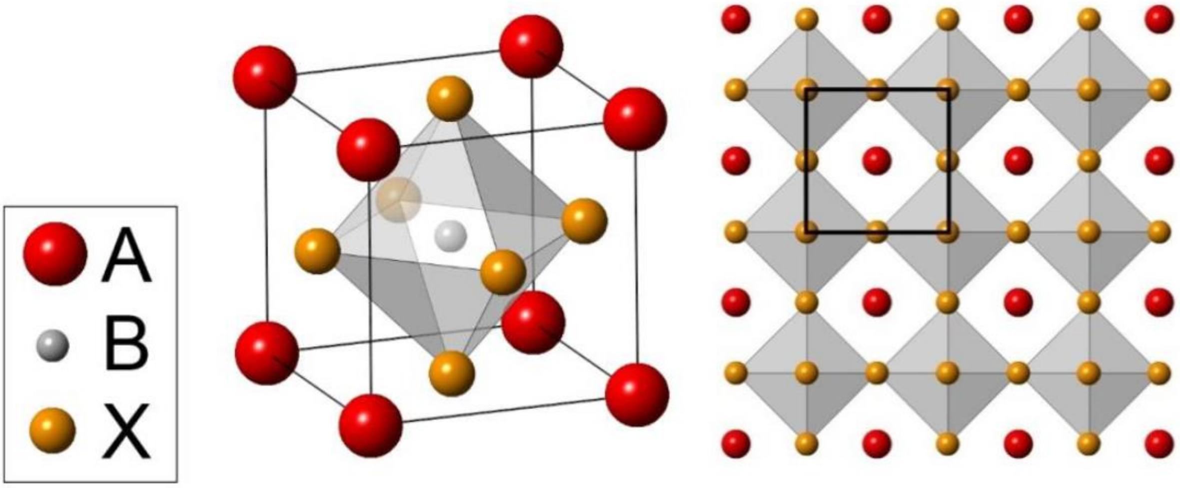

***Figure 2.3** – Perovskite atomic structure of α-phase cubic ABX_3 lattice (left); Broader view of unit cells outlined in black (right)* [44]. *A – Ammonium ion, B – Lead ion, X_3 – Halogen ion*

2.1.3 Device operation

PSCs convert absorbed photons into electrical energy by creating electrons (e) and holes (h) which are passed on to the respective electrodes as shown in figure 2.4. On one side the device consists of a transparent conductive oxide (TCO) patterned onto a glass plane through which the device is illuminated. In order to assist charge extraction charge-selective interfacial layers are applied. The planar architecture most often employs PEDOT:PSS as a hole transporting layer (HTL) where PCBM is preferred electron transporting layer (ETL). The non-inverted architectures are likely to be manufactured with TiO_2 as a ETL and Spiro-OMeTAD as HTL. Optimum performance depends not only on the active layer, it is a result of all components in the stack. The overall efficiency ($n_{efficiency}$), equation 2.1, is a product of optical reflection (n_{Opt}), photon absorption efficiency (n_{abs}), charge diffusion (n_{diff}), charge transport (n_{trans}) and charge collection (n_{col}).

$$\boldsymbol{n_{efficiency} = n_{Opt} \times n_{abs} \times n_{diff} \times n_{trans} \times n_{col}} \qquad \text{equation 2.1}$$

$\boldsymbol{n_{Opt}}$ – the irradiated solar photons must be absorbed by the active layer, however, due to reflection from the surface of the transparent conductive substrate the total number of possible absorbed photons reduces.

$\boldsymbol{n_{abs}}$ – In order an electron-hole pair to be excited the absorbed photons must have enough energy to excite an electron from the valence band to the conduction band. The absorber layer must have a relatively narrow band-gap, good absorption coefficient and optimal film thickness. As reported by Park *et al.* [45] at 700nm the absorption coefficient of perovskite is $0.5x10^4cm^{-1}$ which corresponds to a penetration depth of 2μm leading to the conclusion that most irradiated light can be absorbed by an absorber layer as thick as 2000nm.

$\boldsymbol{n_{diff}}$ – The efficiency of a perovskite device depends also on the lifetime and diffusion lengths of the electron-hole charge carriers. As reported be Chen *et al.* [46] perovskite can have diffusion lengths of up to 650μm and carrier lifetime of up to 3ms. Nevertheless, fabrication of perovskite absorbers involves high precision due to density of defects which are extremely likely to form where recombination can occur.

$\boldsymbol{n_{trans}}$ – The transport of electron-hole charge carriers depends on the electron and hole mobilities and the condition of the fabricated film. Nevertheless, the absorber layer must be at good contact with the interfacing transporting layers which must have matching work functions, if not the transporting layers form a barrier for the electrons and holes which require more energy to be overcome.

$\boldsymbol{n_{col}}$ – In order the generated electrons and holes to be efficiently collected by the end electrodes the Fermi levels of the electrodes should be very well aligned.

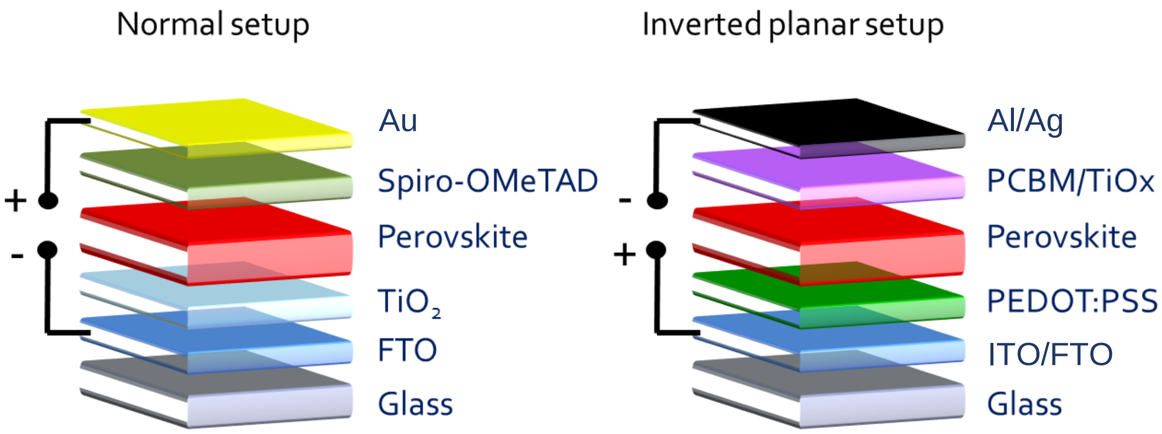

Figure 2.4 *– Example architectures (non-inverted, left and inverted, right) with possible transporting layers* [47]*. The photo-generated current is extracted via the TCO and back electrodes.*

2.1.4 Equivalent circuit model

The equivalent circuit model of a non-inverted PSC is presented in figure 2.5. Obtaining the maximum of generated photo-current I_{total} is possible with an infinitely high shunt resistance R_{SH} and very low series resistance R_S. I_{total} requires efficient n_{abs} and n_{diss} which are obtainable with a high-quality morphology of the active layer. Active layers with low-quality morphologies lead to bypassing of the rectification diode I_D, low R_{SH}, which results in poor n_{trans}. A large value R_S is usually the result of contact resistance between the transporting layer and the evaporated electrode which limits the effectiveness of n_{col} due to charge recombination losses.

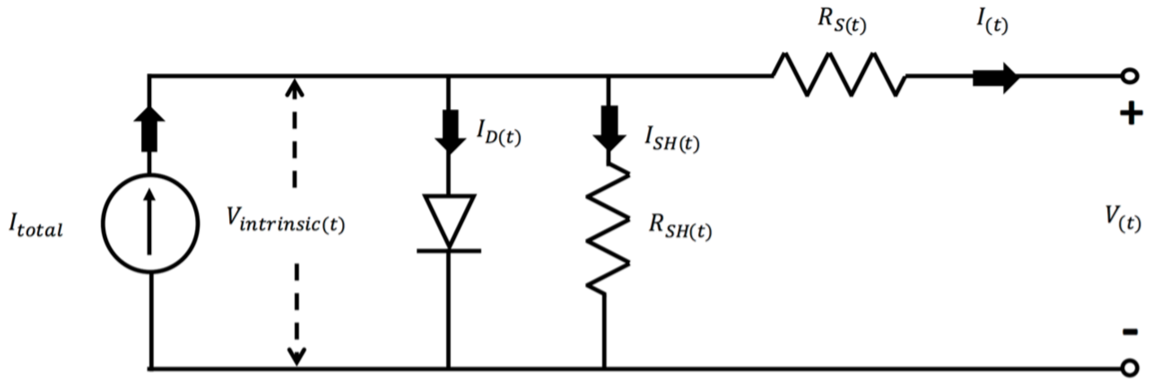

Figure 2.5 *– Equivalent circuit of non-inverted structure PSC device* [48]*. Ideally the device must have an infinitely high shunt resistance R_{SH} and very low series resistance R_S. Decreased R_{SH} and/or increased R_S lead to reduction in performance.*

2.1.5 Perovskite solar cell operation

The operation of PSCs can be described as a simple p-i-n junction, as shown in figure 2.6**,** with active layer having diffusion lengths of both electrons and holes of greater than 1µm. Methylammonium Lead Iodide ($MAPbI_3$) has a valance band (VB) energy of -5.4eV and conduction band (CB) energy of -3.9eV. The light absorbed by the active layer excites electrons in the CB and holes in the VB.

The low binding energy of the excitons cause the separation of the electrons and holes which consequently diffuse towards the interface and are extracted by the relative selective material, and passed on to the end electrodes.

In 2015 Yu *et al.* [49] presented a report on the progress of HTMs for PSCs where they show an overview of the charge-transfer processes in perovskite absorber as shown in figure 2.7. As it can be seen in the diagram, the absorbed light by the active layer excites electrons and holes (1). The free electrons are injected into the ETM (2) and the holes are transferred to the HTM (3). The process is finalised when the electrons and holes are collected by their respective electrodes. Nevertheless recombination of charge carriers is still an issue which can take place by several processes: radiative and non-radiative exciton recombination (4), back electron transfer at the ETM surface (5), charge recombination between ETM-HTM interfaces (6) and back charge transfer at the HTM surface (7) [26].

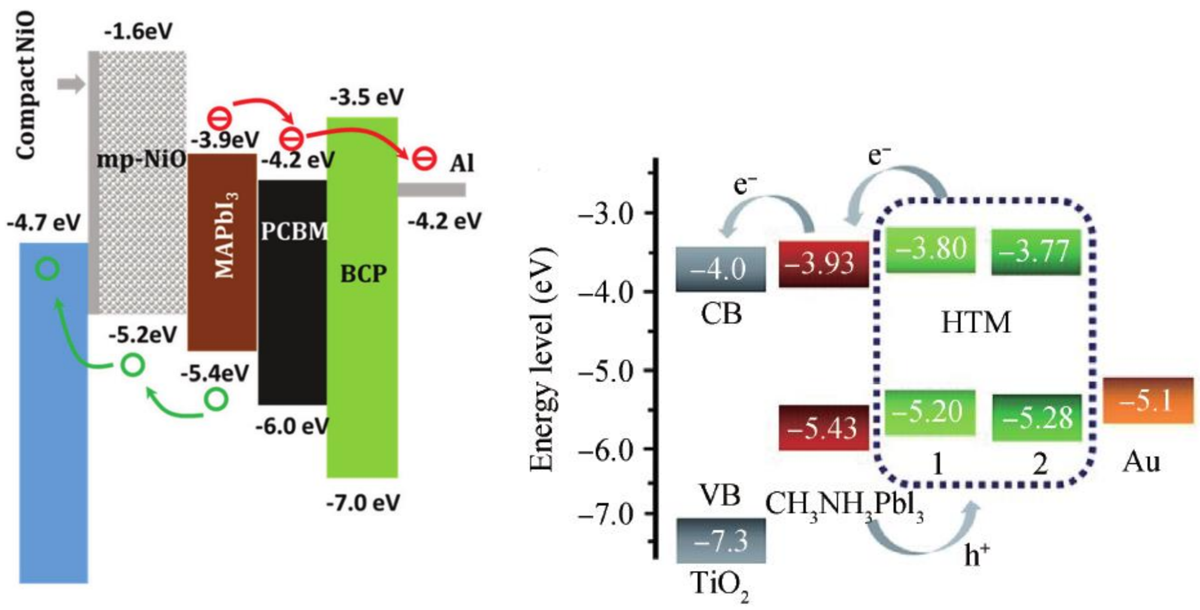

Figure 2.6 – *Operating mechanisms of inverted p-i-n PSC with compact and mesoporous NiOx instead of PEDOT:PSS* [50] and n-i-p PSC with TiO$_2$ and HTMs [51]

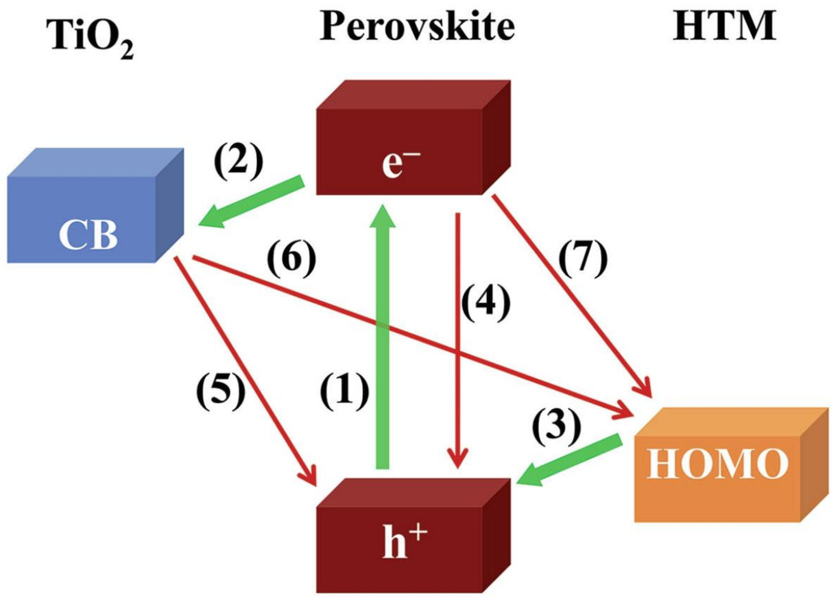

Figure 2.7 – *Charge-transfer diagram illustrating the dynamics of electron-hole generation, transfer to relative transporting materials and possible recombination patterns* [52]

2.1.6 Device characterisation

The performance parameters of a solar cell are obtained by subjecting the device to a current-voltage (I-V) measurement as shown in figure 2.8. In order to find the actual current generation, current density (J), by the device, the active area must be defined. Plotting the I-V measurement allows the open circuit voltage (V_{OC}) and short circuit current (I_{SC}) to be easily defined. The graph also allows the definition of current at maximum power point (I_{MPP}) and voltage at maximum power point (V_{MPP}). The fill factor can be defined using equation 2.2. The PCE is calculated using equation 2.3 where the irradiance level and device active area must be known.

$$\boldsymbol{FF = \frac{V_{MPP} \times I_{MPP}}{V_{OC} \times I_{SC}}}$$ equation 2.2

$$\boldsymbol{PCE = \frac{V_{OC} \times I_{SC} \times FF}{Irradiance \times Active\ area} = \frac{Power_{module}}{Power_{irradiance}}}$$ equation 2.3

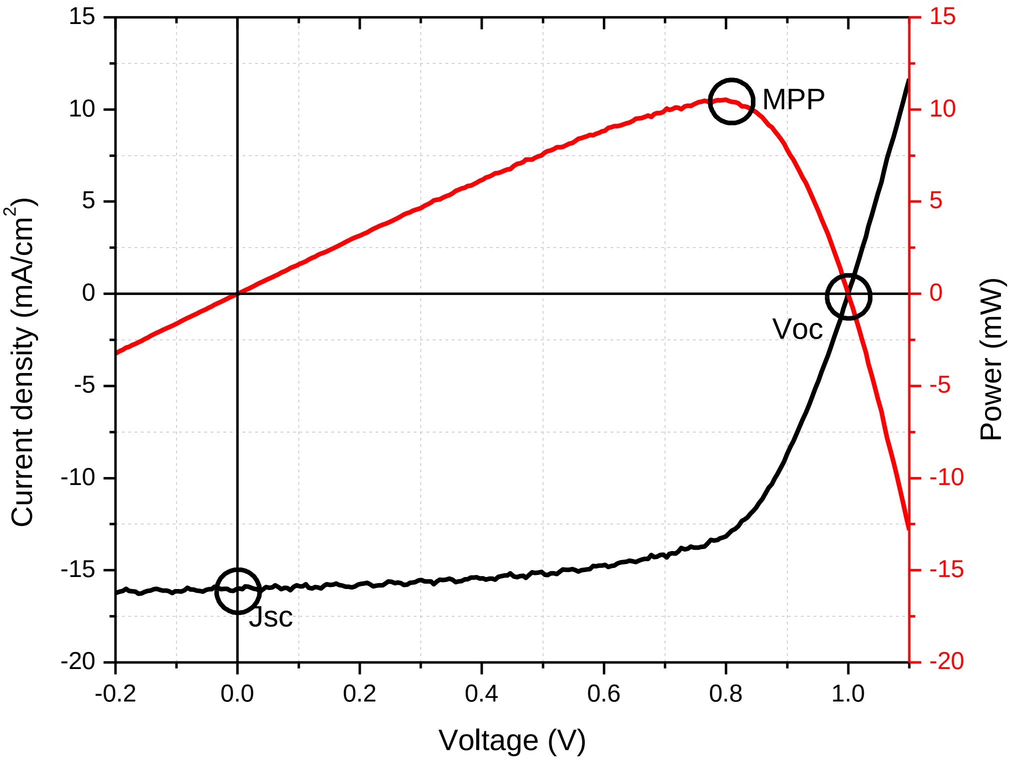

Figure 2.8 *– Current density-voltage (JV) and power output as a function of applied bias. The maximum power point (MPP) signifies the maximum power generated by the device during an I-V sweep.*

Device performance comparison is usually done under standard test conditions (STC) which are defined as: measured module temperature 25^{O}C and 1sun standard AM1.5G solar irradiation (1000W/m^2).

2.1.7 Architectures

The architecture of a device dictates its performance and long-lasting stability. Nevertheless, changing the architecture allows for selecting between a variety of transporting materials and their application to be feasible. Currently mesoporous and planar heterojunction are accepted to be the two main fabrication architectures where the planar architecture is also sub-divided into inverted and non-inverted constructions. In 2014, Gonzalez-Pedro *et al.* [53] defined that both architectures present virtually identical spectral characteristics with diffusion lengths of up to 1µm and that the carrier conductivity of both structures is also practically equal.

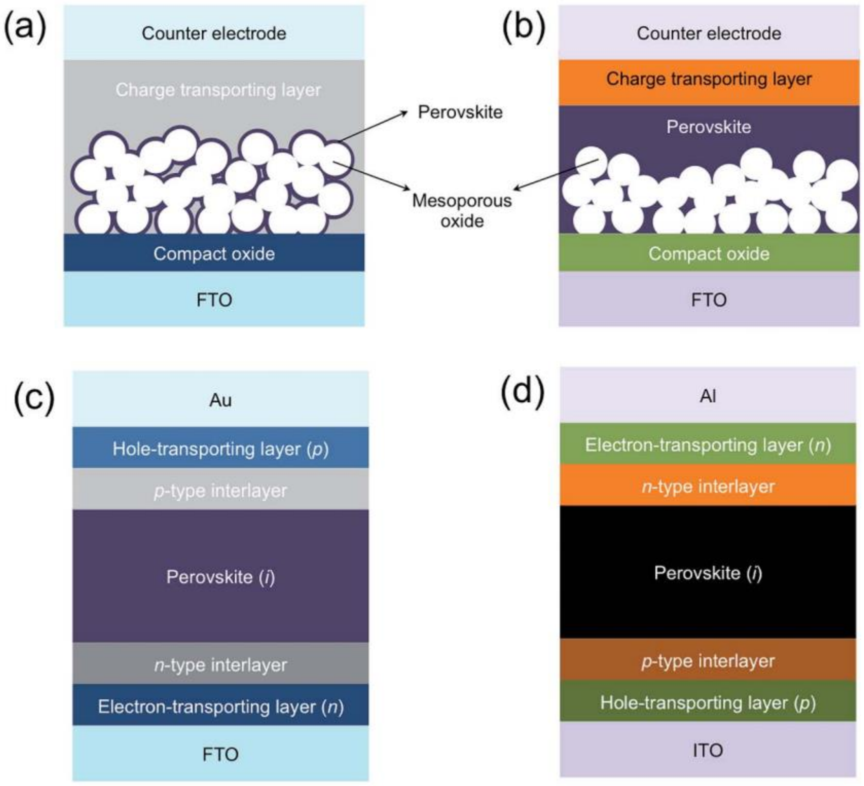

***Figure 2.9** – Illustrations of typical perovskite solar cell architectures* [54]. *a) structure with perovskite coating on mesoporous TiO_2/AlO_3, b) perovskite absorber infiltrated with mesoporous TiO_2/AlO_3, c) non-inverted planar n-i-p heterojunction, d) inverted planar p-i-n junction*

In the case of the mesoporous structures, figure 2.9 a-b), the perovskite material can be utilised as a coating on the oxide scaffold, the bulk being surrounded by a charge transporting layer or the perovskite can be introduced over the oxide scaffold completely infiltrating the oxide pores.

Manufacturing of planar architectures, figure 2.9 c-d), vary between the non-inverted and inverted configuration which is dictated by the selection of the transporting materials which control the direction of flow of electric current.

Planar architecture

The perovskite component in planar heterojunction solar cells acts as an ambipolar charge carrier [55]. After being exposed to a light source the perovskite layer produces holes and electrons which are then passed on to the corresponding transporting layers and their electrodes. The main benefit in manufacturing PSCs using planar heterojunction architectures is the substantial low-payback time realised through sub-100^{O}C device processing. The low annealing temperatures also allows for the employment of a variety of substrates which enables light harvesting with flexible PSCs [56], [57].

Planar heterojunction PSCs are manufactured in two streams, non-inverted “n-i-p” structure and inverted “p-i-n” structure. In the case of non-inverted the ETM is deposited on the TCO which is then covered by a layer of perovskite, HTM and back electrodes. When fabricating an inverted device, the deposition sequence of transporting materials must be inversed finished by an appropriate back electrode, preferably Aluminium (Al) or Silver (Ag).

The preferred n-type transporting materials found in many works are dense TiO_2, ZnO and PCBM layers. Conings *et al.* [58] used low-temperature (<150^{O}C) sol-gel TiO_2 nanoparticles to get an efficiency of 13.6%. They also reported a maximum annealing of no longer than 45 minutes after which the efficiency drops immensely. A. Yella *et al.* [59] reported using rutile TiO_2 to get a planar heterojunction device with V_{OC} of 1.11V and 13.7% efficiency which was achieved as a result of the better adhesion between the TiO_2 layer and the perovskite absorber. Likewise using ZnO as an n-type transporting material has been found to be very beneficial for the final performance of the fabricated PSCs. Liu *et al.* [60] demonstrated a low-temperature manufactured PSC incorporating ZnO to reach 15.7% efficiency which is due to the higher electron mobility of the oxide transporting layer. The n-type fullerene derivative PCBM has been used as the backbone of planar PSC research and development [50], [61]–[64] with remarkable state-of-the-art efficiencies of up to 18.3% [65]. Nevertheless, as reported by Guerrero *et al.* [66] PCBM is prone to degradation by the perovskite’s ion migration and also the diffusion of the evaporated back electrodes, making PCBM suitable for only short-term experiments and not preferred for lifetime prolonging.

In 2015 Tsai *et al.* [67] reported a planar inverted structure PSC with an efficiency of 11% which neglects a hole transporting layer. Their study still presents the need for a HTL which in comparison to the HTL-free device demonstrates higher Jsc and FF. Nevertheless, they show that $MAPbI_3$ perovskite reacts with ITO increasing its work function (0.3eV) which increases V_{OC} from 0.89V with HTL to 1.01V without. PEDOT:PSS is probably the most utilised HTM for inverted structures found in a number of works [62], [68]–[70]. Irrespectively its work function varies from ~4.9eV to 5.2eV depending on its ionomeric ratio and may not be perfect match for some of the perovskite blends. Also due to its heavily hydroscopic nature the long term stability of such PSCs is questionable. In 2014 Jeng *et al.* [71] successfully applied NiOx as a stable inorganic metal oxide substitute to PEDOT:PSS which was seen to be also be beneficial towards increasing V_{OC}. They showed that UV-ozone treatment modifies the work function of NiOx and also improves the wetting of the layer's surface resulting in 33% efficiency increase in agreement with Park *et al.* [72]. Recently in May 2017 Islam *et al.*[73] demonstrated over 1000 hours PSC stability using NiOx exposed to $85^{O}C$ ambient temperature. The thorough study demonstrates the importance of Ar pressure during sputter deposition as well as the final layer thickness resulting in over 15% device efficiency with no hysteresis.

Spiro-OMeTAD became the most commonly utilised HTM for mesoporous devices since its discovery in 2012 [74] where Kim *et al.* achieved a device efficiency of 9.7% with TiO_2 scaffold which PCE was vanquished just a few months later, 10.9% efficiency, by Michael *et al.* [75] where they substituted the mesoporous TiO_2 with insulating Al_2O_3 which has a wide band gap of 7eV to 9eV and instead of being an "active scaffold" it was purely functioning as a static scaffold over which perovskite active layer was coated. Nevertheless, as reported by Sanchez *et al.* [76] Spiro-OMeTAD is prone to photo-oxidation being it in its solid state or liquid phase. They discovered that the doping agents which are always used LiTFSI and tBP accelerate the photo-oxidation. Moreover the organic HTM not only oxidises in air but also degrades in performance in Argon.

In October 2015 You *et al.* [77] showed an all-metal oxide p-i-n device with p-type NiOx and n-type ZnO which demonstrated approximately 90 days of continuous light-soaking with no drop-off in performance. These results demonstrate that exclusion of organic materials might produce better stability. Organic transporting layers are still predominantly used due to the high initial device performance that they can produce [30]. Due to the simplicity of fabrication and versatility of deposition methods, planar heterojunction PSCs are used for researching novel transporting materials which can support increased the efficiency and lifetime of the PSC technology.

Many groups have also worked on flexible substrates. In 2015 M. Kaltenbrunner *et al.* presented a 12% efficiency ultrathin flexible planar heterojunction PSC with the capability of compressing up to 44%, figure 2.10, of its initial area.

Other developments include applications as tandem cells. In 2015 Fu *et al.* [78] successfully attained a semi-transparent bifacial low-temperature manufactured PSC with an excellent 14.2% efficiency which was then coupled with copper indium gallium diselenide (CIGS) to increase the final efficiency to 20.5% in a four-terminal tandem configuration.

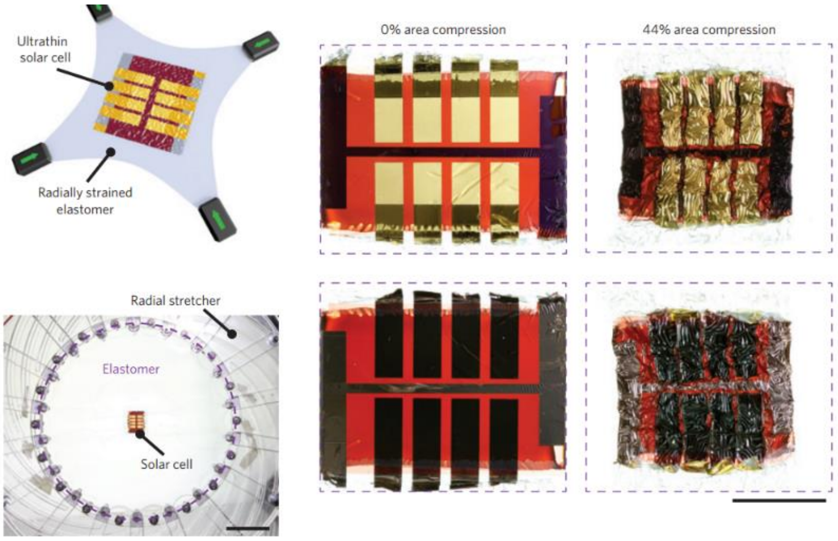

Figure 2.10 – *Flexible, stretchable perovskite solar cells manufactured on top of pre-stretched elastomer which compresses to 44% of initial area* [56]

Mesoporous architecture

In mesoporous structures the electrons are transferred to the TiO_2 scaffold and then passed on to a compact TiO_2 ETL and finally to the TCO. TiO_2 scaffold is also referred to as “active scaffold” which has a champion performance of 16.3% from a device with 2% Niobium doped TiO_2 layer [65]. Leijtens *et al.* [24] found that oxygen molecules can be absorbed by surface vacancies along the TiO_2 structure. It was proposed that due to UV light the trapped oxygen could be causing electron-hole recombination at the surface of TiO_2 resulting in instability of the PSC. The suggested solution was the replacement of TiO_2 with the insulating Al_2O_3 also referred to as “passive scaffold”. When using Al_2O_3 nanoparticles, the mesoporous structure can function as a scaffold to enhance film formation. As anticipated the stability of the devices increased immensely, up to 200 hours of light soaking and performance decrease of 50% which then stabilised at approximately 6% for more than 1000 hours. The main advantage of using Al_2O_3 instead of TiO_2 is the low temperature fabrication which was proven to be achievable. Ball *et al.* [79] demonstrated a solution deposition which involves only 150^{O}C during solution sintering and reached 12.3% PCE. Koushik *et al.*[80] presented remarkable performance and stability planar PSCs of using an atomic layer deposited (ALD) Al_2O_3 which dropped by only 40% in performance of its initial 18% PCE in 70 days continuous light soaking.

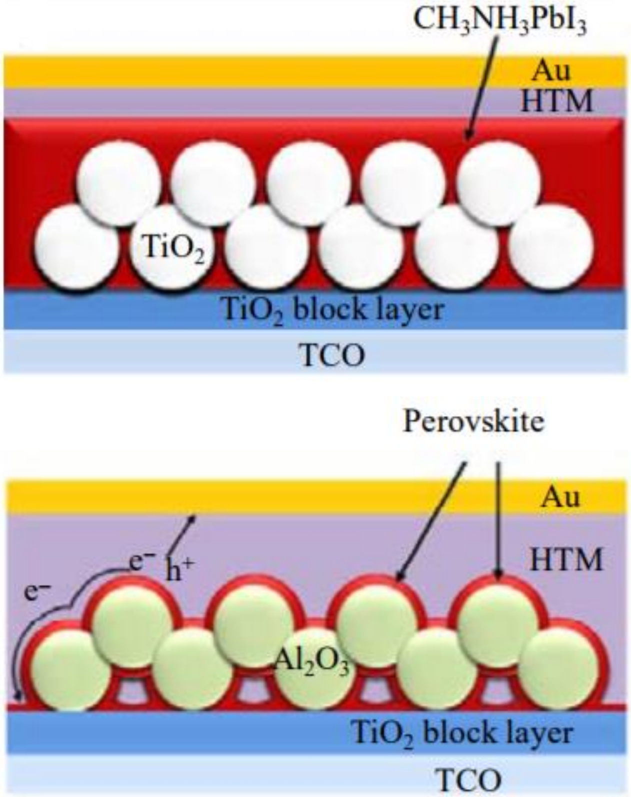

***Figure 2.11** – Mesoporous architecture with TiO_2 scaffold and Al_2O_3 where perovskite infiltrates the TiO_2 nanoparticles or is sensitized with Al_2O_3 nanoparticles and infiltrated with a HTM* [81]

2.1.8 State of the art in device performance

In 2009 Tsutomu Miyasaka *et al.* [82] reported the fabrication of the first methylammonium lead iodide based dye-sensitised solar cell (DSSC), which although impressive, resulted in the corrosion of the perovskite component due to the use of iodine redox and a low performance of 3.81%. The structure they applied was as follows: Pt-coated FTO/TiO_2/$CH_3NH_3PbI_3$/Liquid electrolyte

Then in 2012 after successfully synthesizing what is well-known now as Spiro-OMeTAD, a hole-transporting material and replacing the corrosive liquid electrolyte, iodine redox, a solar harvesting device with PCE of 9.7% was manufactured by a group of scientists which included Nam-Gyu Park and Michael Gratzel [74]. The device structure they manufactured had the architecture: FTO/mesoporous $TiO_2/CH_3NH_3PbI_3$/Spiro-MeOTAD/Au. These results created an avalanche of scientific research focusing on this novel material aiming at yet higher efficiencies and device structures. Followed by the accomplishment of 2012, 2013 was marked by simple planar heterojunction device employing vapour-deposited perovskite component with PCEs over 15% FTO/TiO_2/CH_3NH_3I (simultaneous vapour deposition) $PbCl_2$ (simultaneous vapour deposition)/Spiro-MeOTAD/Ag demonstrated by Henry Snaith *et al.* [83].

Later that year Julian Burschka together with Michael Gratzel demonstrated a novel technique for Perovskite layer fabrication through sequential deposition which generated efficiencies of approximately 15% [84] with FTO/TiO_2/ 2-step solution deposition $CH_3NH_3PbI_3$/Spiro-MeOTAD/Au

In 2014 Yang Yang *et al.* from the University of California reported their laboratory producing PCEs up to 19.3% [85] with a very unconventional structure ITO-PEIE/yttrium-doped TiO_2/ $CH_3NH_3PbICl_2$/Spiro-MeOTAD/Au where they used ITO instead of FTO and doped TiO_2 with yttrium.

In January of 2015 KRICT demonstrated a solar cell reaching 20.1% using, rather than the so favoured methylammonium iodide lead halide, the narrow bandgap formamidinium lead iodide ($FAPbI_3$) [86], FTO/mesoporous-$TiO_2/(FAPbI_3)1x(MAPbBr_3)x$/PTAA/Au.

In June 2017 KRICT together with UNIST improved the record from 2015 and reached 22.1% PCE, the highest certified efficiency for PSC device yet [30] with FTO (SnO_2 doped)/dense TiO_2/mesoporous-TiO_2/ $PbI_2(PbBr_2)$-DMSO/ PTAA is poly(triarylamine)/Au.

2.1.9 Perovskite solar cell degradation

One of the most significant drawbacks of PSC technology is stability. Despite the record efficiencies PSCs have reached [30],[31], hysteresis and rapid degradation are still the main topics under discussion. Light, high humidity and oxygen are seen to be highly abrasive to the integrity of solar cells. Water is a highly polar solvent which instantaneously dissolves the organic component in a $MAPbI_3$ structure.

It is accepted that perovskite degrades due to water ingress which damages the integrity of the film. It was proven that at 60% relative humidity (RH) and irradiation the perovskite peaks (530-800nm) decrease abruptly leaving behind only the halide component PbI_2 [87]. Wang *et al.* proposed the following degradation scheme:

$$CH_3NH_3PbI_3\,(s) \overset{H_2O}{\longleftrightarrow} CH_3NH_3I\,(aq) + PbI_2\,(s) \quad (1)$$

$$CH_3NH_3I\,(aq) \leftrightarrow CH_3NH_2\,(aq) + HI\,(aq) \quad (2)$$

$$4HI\,(aq) + O_2 \leftrightarrow 2I_2\,(s) + 2H_2O \quad (3)$$

$$2HI\,(aq) \overset{hv}{\leftrightarrow} H_2 \uparrow + I_2\,(s) \quad (4)$$

The scheme above represents a concept of the reaction of perovskite to the presence of water. Wang *et al.* propose that when exposed to humidity the complex $CH_3NH_3PbI_3$ separates into organic component (CH_3NH_3I) and halide (PbI_2) (1). The layer then consist of portions of the organic methylammonium iodide CH_3NH_3I together with methylamine (CH_3NH_2) and hydrogen iodide (HI) (2). Following separation, in presence of oxygen and water redox reaction occurs (3) or in the presence of light a photochemical reaction occurs where the hydrogen iodide separates into H_2 and I_2 (4).

As shown by Niu *et al.* [88] the degradation of a perovskite device in an atmosphere with increased humidity can be observed by the decreased absorption curve between 530-800nm. The analysis shows the evident discolouration of the device with contentious light exposure which a large number of groups neglect to describe.

Christians *et al.* [89] reported that water has an immense effect on the perovskite absorber as it does not only cause a crystal lattice decomposition but also when interacting with the material in dark conditions it bonds with it forming the product $CH_3NH_3PbI_6{\cdot}2H_2O$ which when illuminated decreases the device performance over the visible spectrum.

Snaith *et al.* [90] reported a complex encapsulation technique using single wall carbon nanotubes and P3HT below a layer of PMMA/poly(bisphenol A carbonate) for preventing water ingress in the perovskite solar cell devices, yet there is no established method for preventing the degradation of the hybrid material itself. Nevertheless, the presence of oxygen is proven to have the same degree of degradation as water which combined with light leads to photo-oxidation of the active layer [91]–[94]. It is believed that photon conversion in the presence of trapped oxygen accelerates the degradation due to oxygen diffusion. A purposed strategy for eliminating oxygen ingress is the use of efficient ETLs and oxygen blocking encapsulation.

It has been shown that compact and mesoporous TiO_2 are capable of boosting the PSC efficiency when used as ETLs in a non-inverted architecture. Nevertheless, in 2013

Snaith *et al.* [24] demonstrated that the presence of TiO_2 scaffold can be detrimental to the solar cell when exposed to UV light. They related the degradation under UV light to be due to the presence of oxygen vacancies which can absorb oxygen molecules and form the transfer complex ($O2^-$-Ti_4^+). When exposed to a light source an electron-hole pair is generated. The hole, located in the valance band was proven to recombine with the generated electron at the oxygen absorption site which leaves an unfilled, positively charged oxygen vacancy on the TiO_2 surface. The free electron is left in the conduction band which will recombine with the holes in the HTL. The device gradually decays in performance at the recombination of electrons and holes increases.

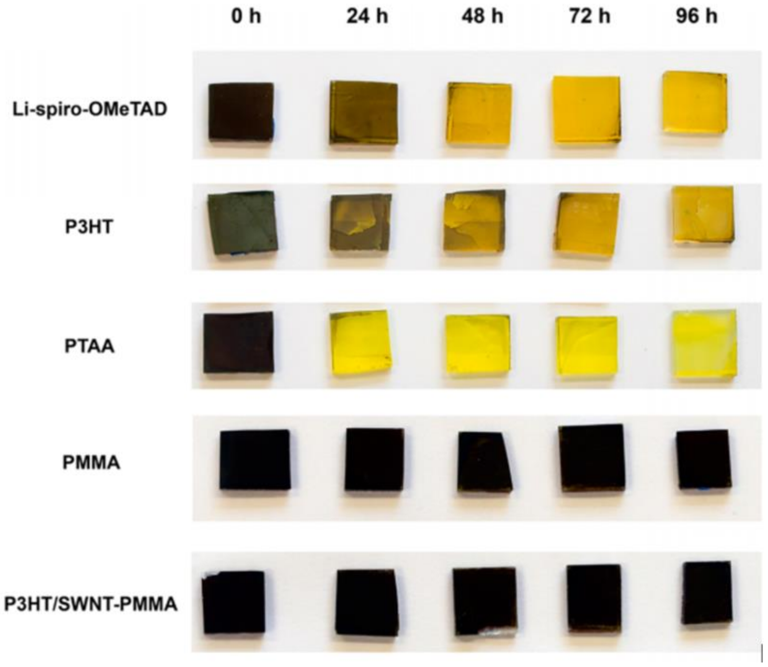

***Figure 2.12** – degradation pattern of a perovskite layer over a glass slide (with a number of capping layers),* [90]

In 2013 Julian Burschka *et al.* [84] reported one of the first highly stable performances observed by PSCs with metal oxide TiO_2 scaffolding which maintained over 80% of its initial efficiency for a period of 500 hours irradiated under white light emitting diodes (LEDs) excluding UV radiation. In December 2013, however, Snaith *et al.* [94] following on Burschka's finding considered fabricating mesoporous PSCs with TiO_2 nanoparticles which they saw as containing trapped oxygen which is believed to desorb under UV radiation (supressed by using a UV filter) and affect the stability of the PSCs under 1 sun AM1.5G. For this reason, they considered Al_2O_3 scaffolding. The TiO_2 infiltrated devices were seen to degrade to T_{80} (also called burn-in, section 2.2.2) in only 4.5 hours where the Al_2O_3 demonstrated a stable photocurrent for over 1000 hours of illumination under AM1.5G solar simulator.

Temperature degradation is a major degradation factor which also needs addressing. Katz *et al.* [95] showed that photoinduced decomposition is assisted by temperature increase which can be speculated to be as a result to the penetration of ambient species into the encapsulated perovskite layers. Leong *et al.* [96] reported that V_{OC} is linearly related to the increase in temperature in the temperature range -23^{O}C to 87^{O}C.

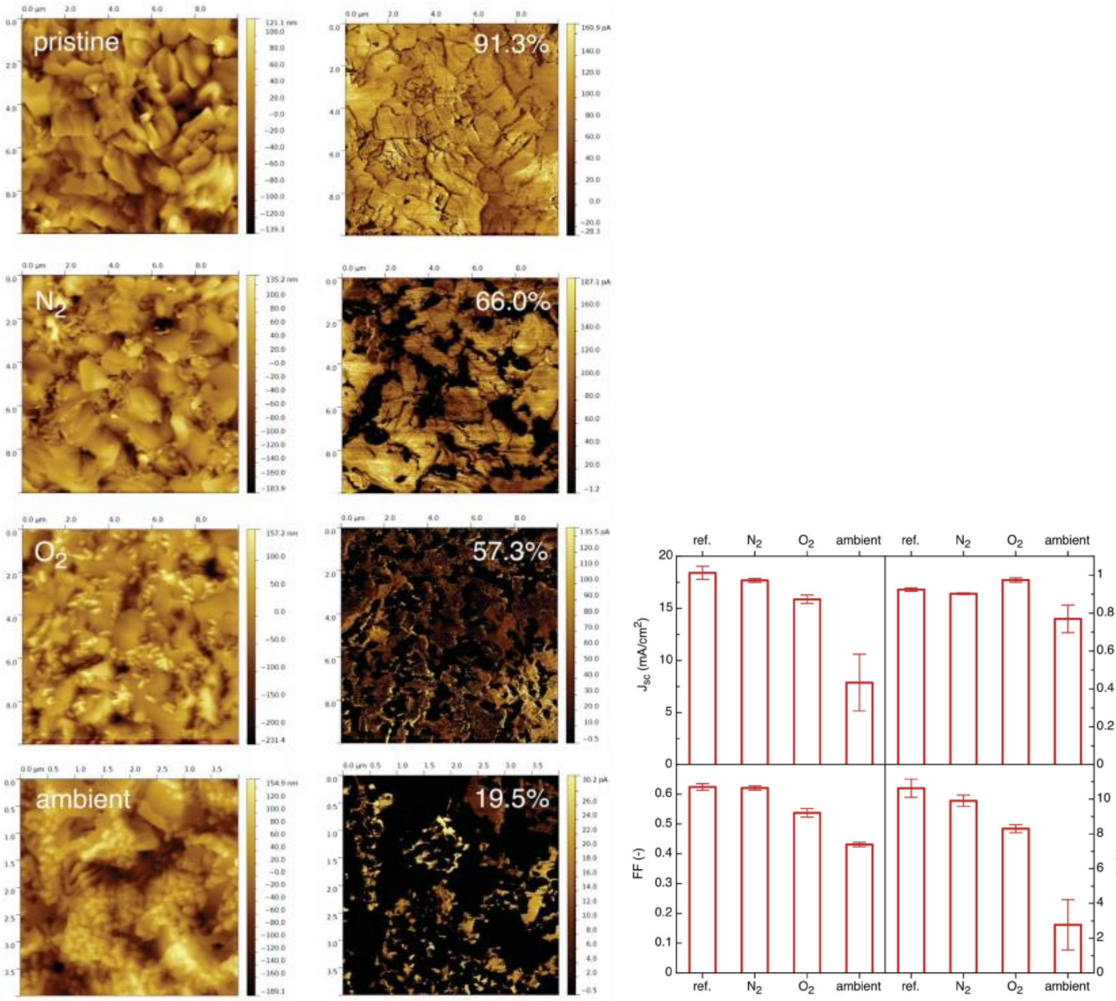

Figure 2.13 *– topographic AFM and conductive AFM images, with the conduction measured in percentage, of perovskite films exposed to 85^{O}C and three different atmospheres for 24 hours (left); Performance parameters of PSCs subjected to the three experiments (right).*

Cornings *et al.* [97] conducted a very comprehensive study on the thermal instability of perovskite in N_2, O_2 and air where they evaluated the electrical and chemical properties of the active layer fabricated on ITO and also the morphology and optical absorption changes. The measurements conducted in air with no light and 85^{O}C at 50% RH showed almost no change in the morphology, however, exposure to N_2 and O_2 led to notable changes, figure 2.13. Continuous heating causes breaking of the structure leaving PbI_2 crystal regions which reduces the electrical current generation. The results indicate that elevated temperature causes degradation, nevertheless, the degradation rate can be accelerated or decelerated as a result of the surrounding atmosphere.

2.1.10 Outdoor Monitoring of PSCs

Reports demonstrating the stability of perovskite devices show device indoor exposure mainly to soaking under LED light sources or shelf life with periodical light exposure during I-V measurement. Very few groups around the world have examined the performance of their products outdoors.

Misra *et al*. [98], [99] were one of the first groups to expose perovskite absorbers to direct sunlight and study the degradation giving invaluable insight to the community towards the stability of perovskite and its compositional performances. In 2015 Li *et al.* [100] demonstrated the first results from PSCs exposed outdoors with no UV filtration in Jeddah, Saudi Arabia following the ISOS O1 protocol, as shown in figure 2.14. The group also conducted an indoor accelerated lifetime testing (ALT) campaign on PSCs which were subjected to 80^{O}C-85^{O}C for 3 months following ISOS D2 protocol and measured under STC conditions.

In 2016 Reyna *et al.* [101] presented their work on mixed halide PSCs with over 1000 hours outdoor exposure mounted on a solar tracker, executed in Barcelona, Spain. They show a T_{80} occurring at the 846th hour after the beginning of the experiment which demonstrates superior stability of the mixed halide $FAPbI_{3(0.85)}MAPbBr_{3(0.15)}$ they have fabricated compared to the conventional $MAPbI_3$ perovskite devices. Nevertheless, even this composition of PSCs was found to be highly susceptible to UV light and quality of edge-sealant which were deemed to be the main causes for degradation in the first half of the experimental period.

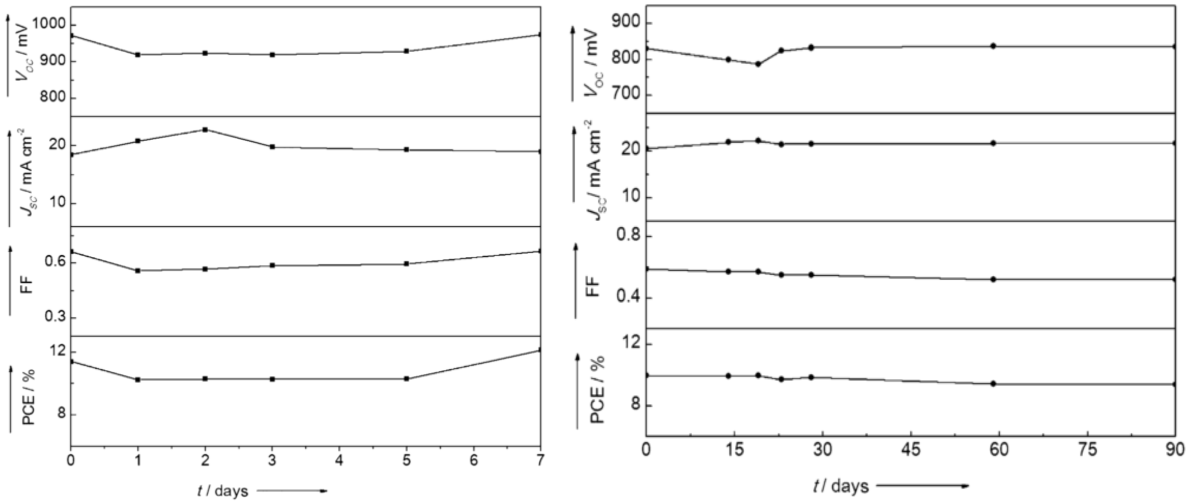

***Figure 2.14** – Performance parameters of encapsulated PSC exposed outdoors in Jeddah, Saudi Arabia (left) and performance parameters of encapsulated PSC subjected to indoor stress test at ambient air and 85^{O}C temperature (right)* [100].

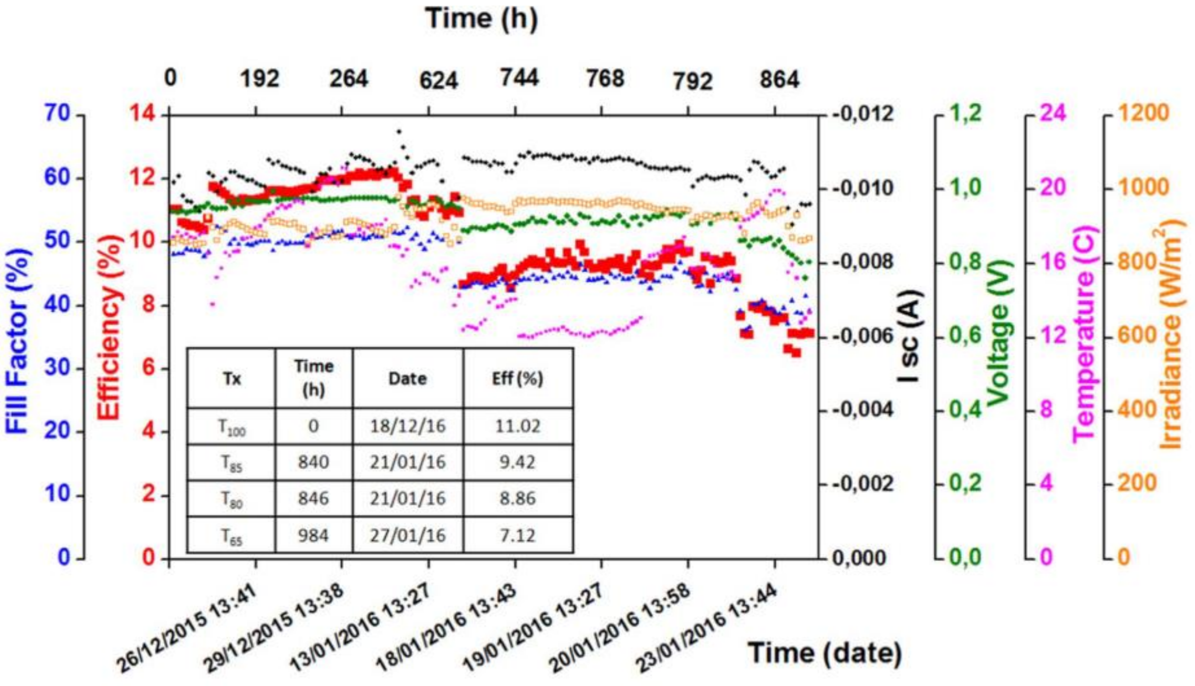

Tx	Time (h)	Date	Eff (%)
T_{100}	0	18/12/16	11.02
T_{85}	840	21/01/16	9.42
T_{80}	846	21/01/16	8.86
T_{65}	984	27/01/16	7.12

***Figure 2.15** – Performance parameters of the outdoors stability of PSCs following ISOS O2 test protocol* [101].

2.1.11 The Effect of Anti-Solvent treatment on the Performance PSCs

After its first use in a solar cell in 2009, the interest in perovskite rapidly increased and in 2012 reached a milestone in PCE of ~10%, [102]. This achievement was followed by many successive contributions and recently reached 22.1%, [30]. Over the past years perovskite manufacturing has been adopting various techniques, the most efficient of which aiming towards eliminating the pinhole defects formed along the surface of the absorber during crystallisation, [103]–[105]. The utilisation of solvents (anti-solvents) to accelerate the formation of perovskite during spin salts precipitation coating has been proven to be crucial point in the aim of producing pinhole-free uniform compact absorber layers, [106]. As reported by Jeon *et al.* including an anti-solvent presents a crucial step in obtaining hysteresis-free devices with over 16% efficiency [107]. Troughton *et al.* [32] show that by applying ethyl acetate as an anti-solvent during device fabrication yields up to 15% PCE which was obtained in elevated relative humidity of 75%.

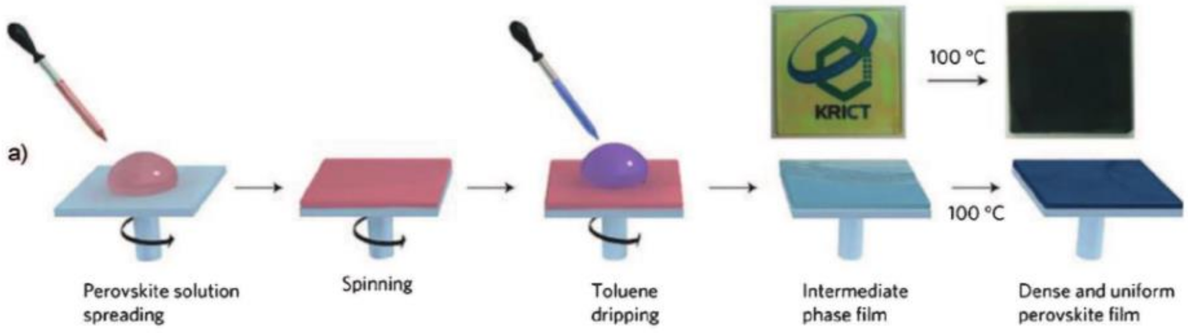

Figure 2.16 *– Step by step perovskite deposition technique utilising anti-solvent engineering*

2.2 Organic Photovoltaics (OPVs)

In the recent years the aim for upscaling small molecule and polymer 3rd generation OPV devices has been the ambition of many laboratories across the world. Flexible, lightweight and also semi-transparent [21], [108], [109], the OPV modules have the potential to be used for building envelope lamination in a building integrated photovoltaic (BIPV) application [28]. Upscaling OPVs leads to low-cost solar energy production with low-payback times due to the low-temperature inkjet and roll-to-roll options for manufacturing. Whilst the benefits of the technology are clear, studying their operation in the real world under a variety of atmospheric conditions is vital in order to evaluate the position of the technology on the market [110],[111]. Commercialized OPV modules have also been available in the market in both flexible and rigid applications, including green houses, iPad chargers, bus shelter roofs, and window applications [112],[28].

Most of the work related to outdoor monitoring of PV modules was completed employing OPV modules due to the lack of upscaled PSCs available during this project.

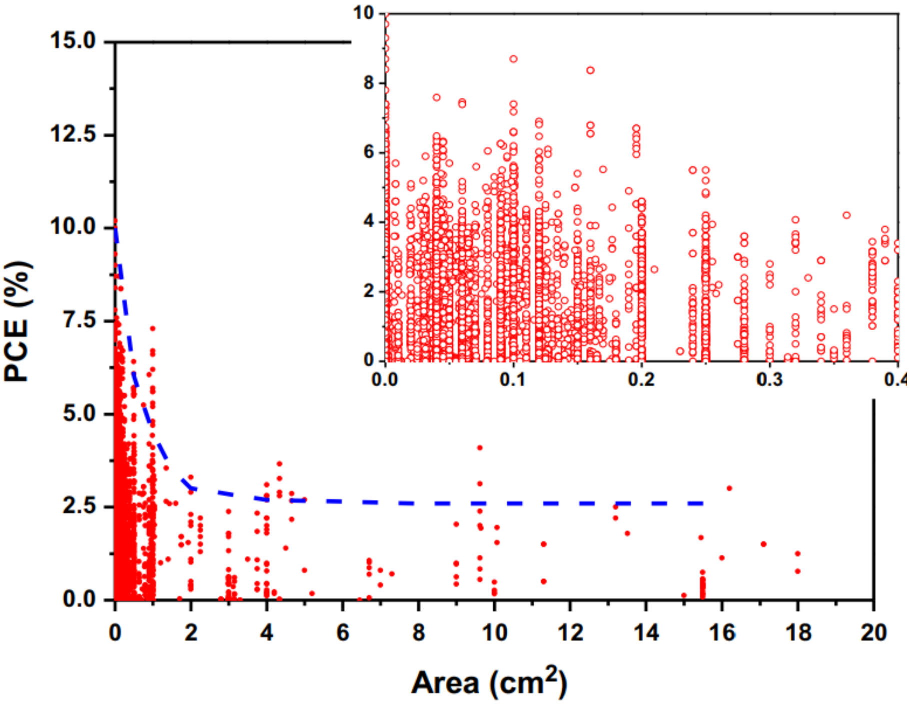

Figure 2.16 *– Device efficiency with increase in active area, inset showing the efficiency of devices below 0.4cm^2 active area* [113]*. The graph shows the main aim by the majority of laboratories being device efficiency and not large area research.*

2.2.1 State of the art

In the last two decades increasing OPV device efficiency has been the main aim for a number of research groups around the world [109], [114]. While laboratory grade small area OPVs already reached slightly over 13.2% efficiency with multi-junction cells [115], moving to large scale devices presents an obstacle in maintaining high efficiencies due to the increase in series resistance along the active area [116]–[119]. The increase in series resistance with light intensity causes a significant decrease in the measured fill factor. As reported by Jorgensen *et al.* [113], most of the manufactured OPV devices have an active area of less than 0.2cm^2 due to the higher sheet resistance of the transparent electrode at larger active area, figure 2.16. Nevertheless, at present Heliatek GmbH and infinityPV ApS offer roll-to-roll fabricated modules with up to 8.0% PCE [120], [121].

2.2.2 OPV degradation

Degradation of any type of photovoltaic module is normally measured by the time taken from the initial reading (accepted as 100% integrity) to its reduction to a set threshold value either 80% (T_{80}) or 50% (T_{50}), figure 2.17. The degradation can be plotted as the reduction of V_{OC}, I_{SC}, FF or PCE against time. In reality the degradation of a PV module is reported before and after the burn-in period and the value T_{s80} is often quoted. As discussed by Reese *et al.* omitting the burn-in period may lead to underestimation of the potential of the device [122].

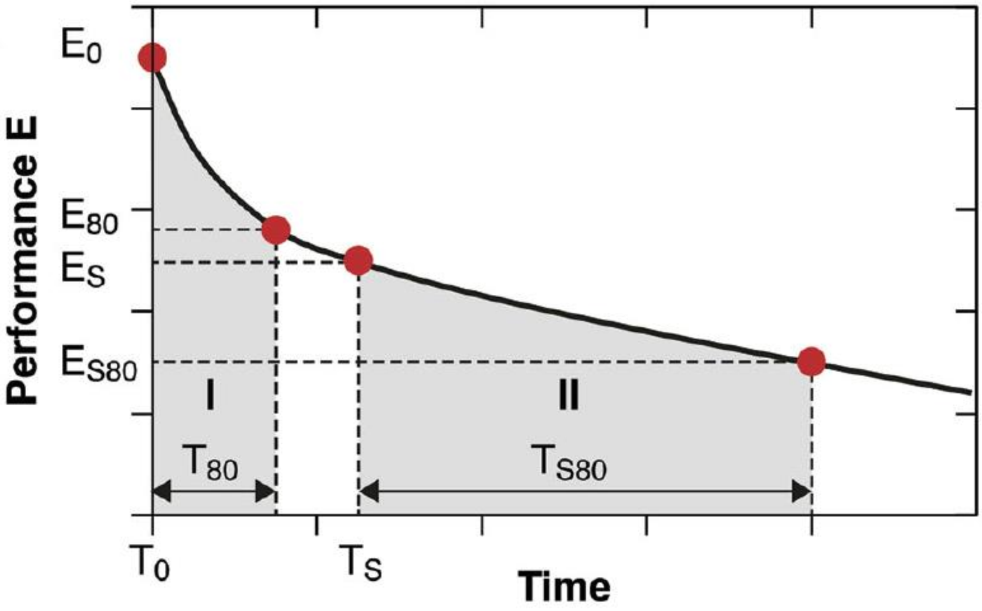

Figure 2.17 *– Monitoring of performance decay versus time* [123]*. In real life situations the decay of a solar cell is factored after the burn-in/stabilisation period* [122]*.*

2.2.3 Outdoor Monitoring of OPVs

As previously discussed most of the OPV devices available consist of under 0.2cm^2 of active area which makes outdoor stability testing a difficult task. Due to this reason only a few groups around the world have the complete facilities to carry out this crucial examination. One of the most successful centres for research and development of OPV modules is led by Professor Frederik Krebs at the Technical University of Denmark (DTU). Over the years the group at DTU have published a number of papers on OPV fabrication, upscaling and also performance, and stability [124]–[127].

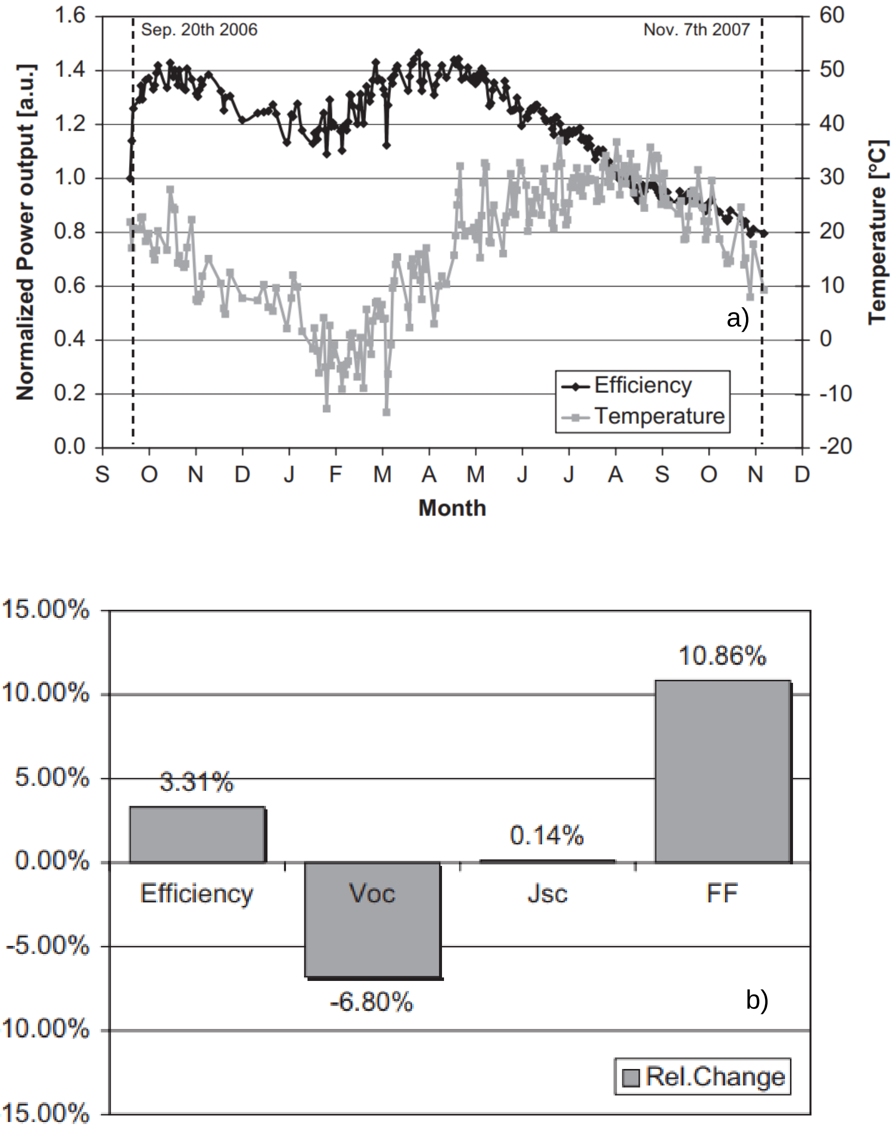

***Figure 2.18** – a) Evolution of performance over the course of one year on OPV modules tested at Konarka and b) Module performance evolution after 14 months of outdoor degradation* [128].

In 2008 a report by Hauch *et al.* [128] demonstrated a full one year study on eight flexible P3HT:PC$_{61}$BM based modules. Present in their report is the is the power density measured over the period of the investigation which decays by only 20%, figure 2.18 a). As shown after six months of exposure the modules start a linear degradation. Nevertheless, after 14 months the modules were retested under a solar simulator and demonstrated an increase on all parameters apart from V$_{OC}$, figure 2.18 b), which decayed due to inaccurate value fixed-load resistor which was not capable of adjusting the maximum power point (MPP) with the changes in weather and device performance. These results amplify the importance of sophisticated outdoor testing facilities without which the tested devices can be severely damaged.

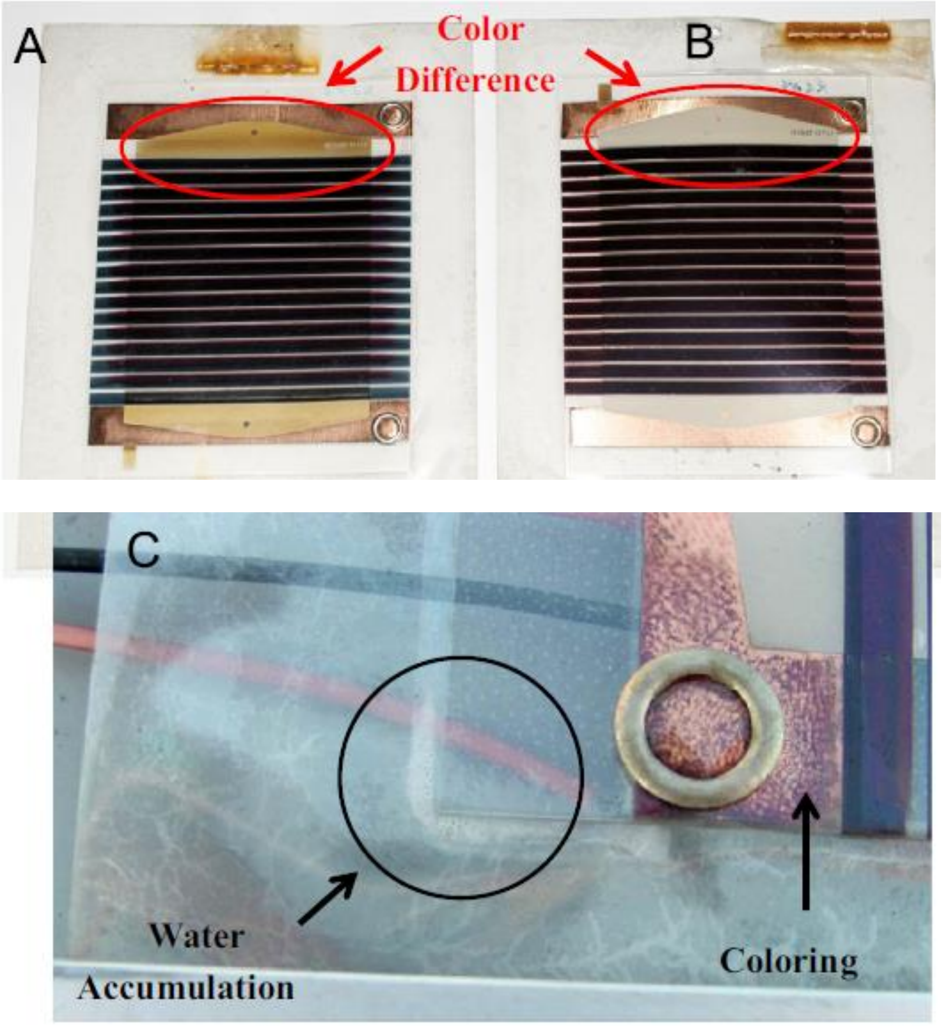

Figure 2.19 *– Rapid degradation of module exposed for 12 months at CSIRO Denmark. The photographs highlights the importance of appropriate testing methodology and monitoring of ambient conditions* [129]

It has been found that OPVs suffer from poor efficiency under low light levels. Bristow *et al.* [110] shows that under low light dose level the current-voltage curves suffer from inflection limiting the FF and V_{OC}. He also discusses the removal of this anomaly by photo-annealing of the modules as higher light dose occurring diurnally after sunrise. The report also shows that OPVs experience positive temperature coefficient which as shown improve the power conversion efficiency (PCE) by a gradual increase in the short-circuit current (I_{SC}) and FF.

In a report by Gevorgyan *et al.* [129] the influence of ambient weather conditions to the long-term performance of P3HT:$PC_{61}BM$ based OPVs aged at six geographic location is reported. The modules fabricated at DTU included UV filters and barrier encapsulation. The study shows how volatile the OPV performance can be depending on the test setup and also the exposure angle. The investigation also reveals that module performance is strongly affected by module encapsulation and positioning, figure 2.20. In a report by Sondergaard *et al.* [130], conducted in eight countries, seven in Europe and one in the Middle-East, show the immense influence of ambient conditions on the integrity and performance of OPV modules. The work demonstrates that OPV modules exposed at sea locations are prone to external corrosion followed by catastrophic performance failure, figure 2.20.

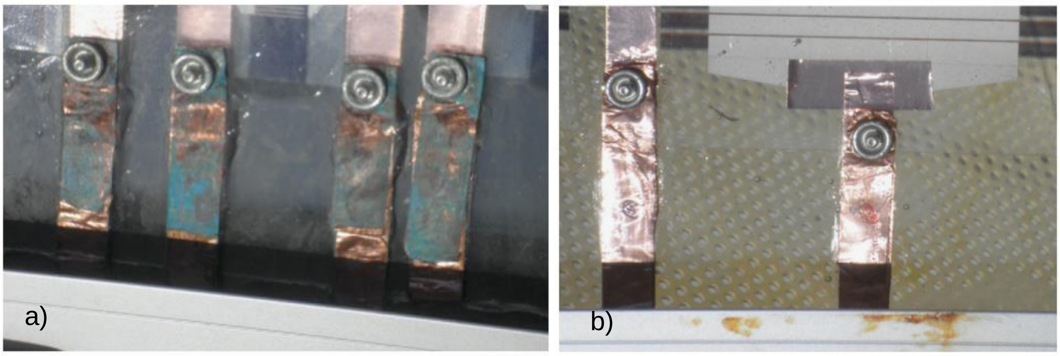

Figure 2.20 *– a) Degradation of the contacts of OPV modules installed in Petten – the Netherlands against, b) aged contacts of OPV modules installed in Clermont-Ferrand – France* [130].

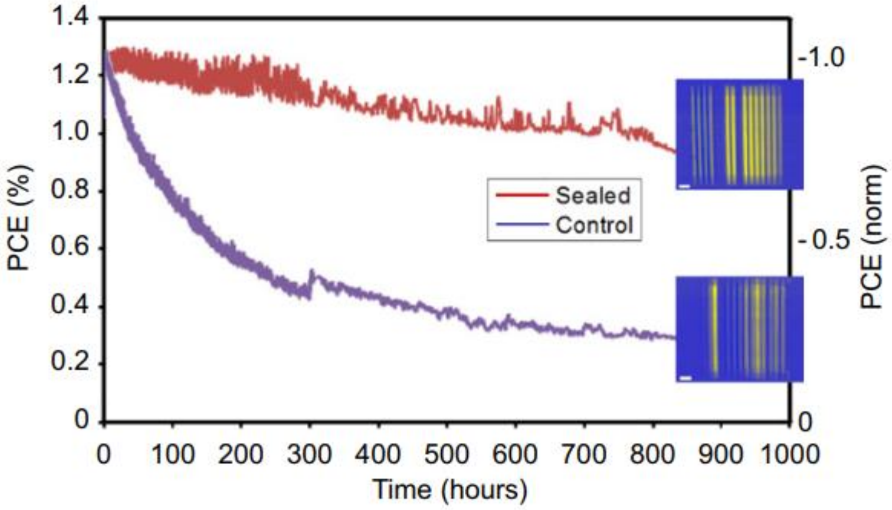

Figure 2.21 *– PCE decay of an encapsulated module versus module with exposed cut edges. Insets, Light Beam Induced Current (LBIC) images demonstrating the state of the cells after 1000 hours light soaking* [131].

In another study conducted by Tanenbaum *et al.* [131] at DTU it can be seen that even atmospheric ingress as a result of sealing failure will result in accelerated degradation and early device failure, figure 2.21.

Cloud lensing effect

Cloud lensing can substantially affect the performance of a solar module resulting in unusually high performance. Global radiation is comprised of direct normal irradiation (DNI), surface reflected radiation (albedo), [132], [133] and diffuse radiation. However, there are cases of patchy cloud coverage during days of high irradiation where a ray of sunlight can pass a gap in the clouds which causes a spike in the radiation due to cloud lensing effect, [134]. Cloud lensing can result in 20% increase in DNI which results in a sudden increase in the measured performance of solar receivers. This occurrence causes the highest spike in PCE on diffuse days when devices are normally colder.

2.3 ISOS stability test protocols

The International Summit on OPV Stability (ISOS) is the organisation who standardised test protocols for OPV devices including assessments of dark/shelf life, outdoor, laboratory weathering, thermal cycling and solar-thermal-humidity lifetime testing [122]. All of the categories comprise of three levels; level 1 – basic, level 2 – intermediate, level 3 – advanced. The total of fifteen test protocols allows laboratories to thoroughly examine the manufactured cell and receive a clear indication as to the lifetime expectancy of their products. Nevertheless, only a few laboratories around the world are certified to carry out level 3 protocols. Mainly the interest and capabilities of research laboratories reach as far as the intermediate level 2 category. Table A1 in the appendix illustrates all available protocols established by ISOS. For outdoor measurements the ISOS consensus recommends an accurate device measurement technique and thermopile pyranometer for irradiance measurements which has a flat spectral response from 300nm to 2800nm [135].

2.4 Lifetime improvement

It is clear that OPVs as with all emerging technologies there is a need to improve the lifetime and the efficiency in order for the technology to become cost effective. In a work by Mulligan *et al.* [136] they demonstrate a unique way of calculating cost effectiveness where they estimate that an OPV with 5% efficiency and 3-5 years lifetime would be a prominent competitor to coal-based electricity generation stations.

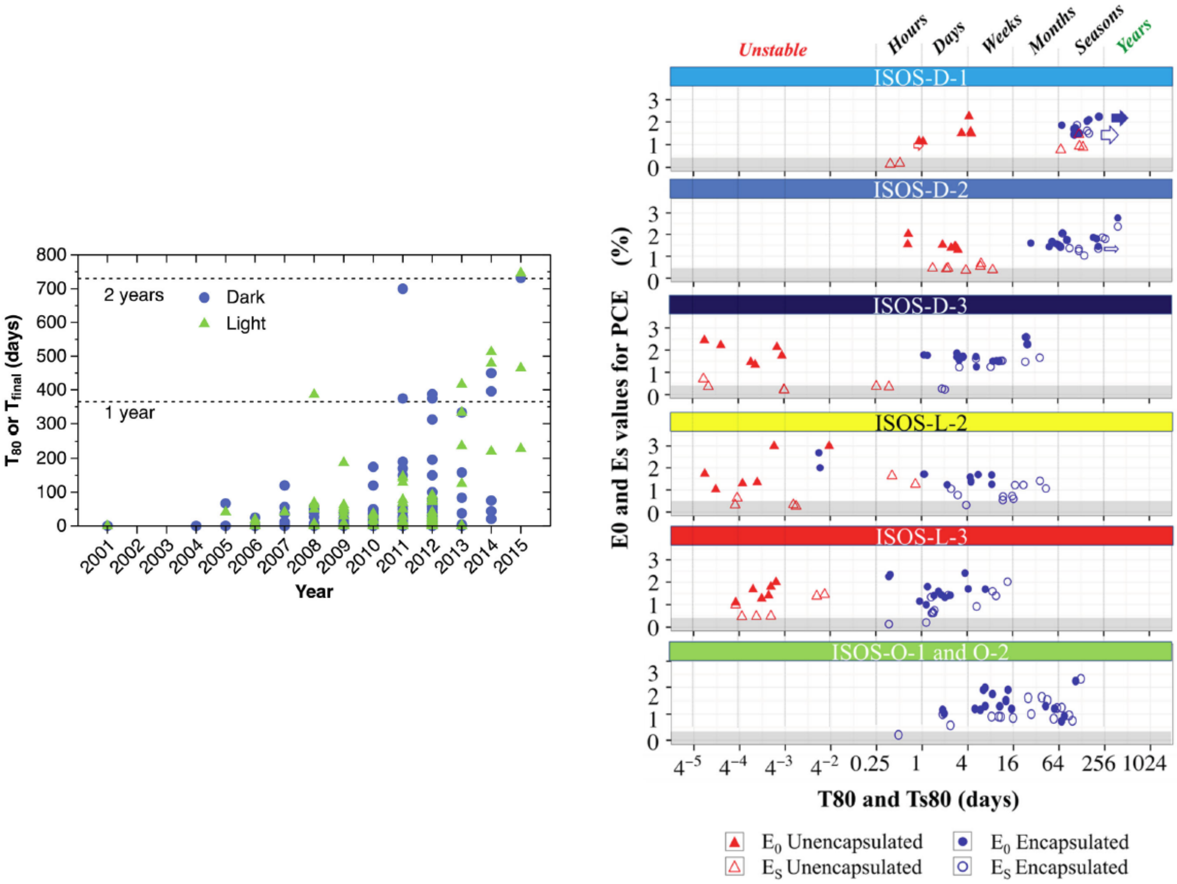

Figure 2.22 *– Comparison of lifetime versus exposure conditions of OPV modules examined at a range of ISOS conditions* [123]*.*

Gevorgyan *et al.* [123] presents a report on meta-analysis of the performance of large amount of OPV device data. It can be seen that apart from shelf-life testing the effect of encapsulation, light soaking and thermal exposure present the largest impact on the degradation of OPVs. Nonetheless, as reported outdoor aging of encapsulated modules has a lower detrimental effect on the lifetime compared to indoors at elevated temperatures, figure 2.22 a). The report also presents a summary of the progress of OPV lifetimes for the last 15 years, showing an impressive improvement of one year lifetime in 2013 to two years stability in 2015 both for modules tested in light and dark conditions, figure 2.22 b).

2.4.1 Spectral response and filtration

Enhancing the lifetime of OPVs under light soaking is a difficult task which many groups are still struggling to overcome. UV radiation plays an important role in the photo-oxidation of

b)

OPVs. Filtering the UV spectrum is the most common approach for limiting/preventing UV light propagation which suppresses the photo-oxidation of the active layers.

In 2010 Manceau *et al.* [137] published their work on the effect of UV-visible irradiation to the stability of P3HT and P3HT:PCBM in which they show the detrimental effect of irradiation on the polymer to T_{80} absorption in just over a year, and a substantial improvement when combined with a fullerene.

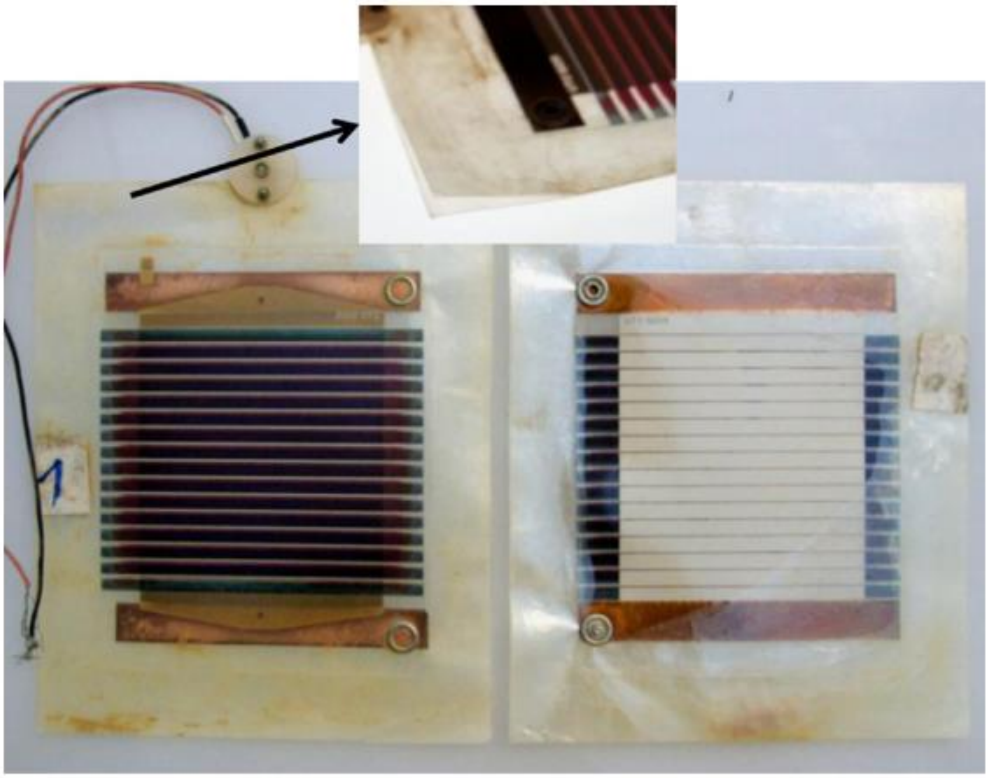

Figure 2.23 *– Degradation of module exposed for 17 months outdoors in the Negev desert in Israel. Bottom-right corner of module completely delaminated as a result of the harsh outdoor condition.*

Lira-Cantu *et al.* [138] conducted a study on hybrid solar cells (HSCs) with the structure ITO/ thin film oxide /MEH-PPV/Ag where they analysed three possible oxide layers, TiO_2; Nb_2O_5; ZnO. They exposed the whole range of electron transporting layer (ETL) HSCs to light soaking at AM1.5G solar simulator with and without UV filtration and determined that eliminating UV has a massive impact on the performance of the ETL.

In 2013 after an interlaboratory outdoor study conducted in a total of six counties Gevorgyan *et al.* [129] reported the results of 17 months of data collection from modules manufactured by DTU which all included a UV blocking layer. They demonstrated the impact of UV irradiation on modules installed in the Negev desert in Israel showing partial delamination of the barrier film resulting in a complete failure of the module in the region of delamination, figure 2.23.

2.4.2 Use of Luminescent Downshifting (LDS)

Despite the significant improvement in efficiency seen by both OPVs and PSCs photo-oxidation is one of the main reasons explaining why these two technologies are still not commercially available.

A well-studied approach to suppressing the photo-oxidation is the application of a LDS layer. Also in favour of the device performance LDS is well-known method of increasing the device efficiency achieved by absorption of light at short wavelengths and re-emission at long wavelengths. This technique is especially suitable for OPVs and PSCs which are known to be severely affected by UV radiation causing photo-oxidation of the active layer. This technique permits the energy to be transposed from the UV region to the more harmless visible region for example. Absorption and emission of the LDS is called the Stoke's shift [139] where when absorbed, the re-emitted light at a lower wavelength, loses some energy as a result of relaxation.

Nonetheless, LDS coatings have intrinsic flaws. As the application of LDS will alter the incident spectrum which is absorbed by the solar cell after losses and downshifting, the chosen material must match the least absorbing portion of the spectrum. The losses must be less than the overall increase of efficiency [140].

2.4.3 Review of Existing Studies of LDS with Different PV Technologies

LDS is rarely seen applied to OPVs and PSCs, however, there are some reports of its positive effects applied on conventional thin-film 2nd generation PVs and DSSCs.

Hovel *et al.* [140] reported the use of LDS in 1979, where he used Coumarin 540 and Rhodamine 6G on GaAlAs solar cell which increased the measured performance from 11.5% to 13.5%.

Kennedy *et al.* [140] applied Europium complexes on DSSCs in order to suppress the photo-oxidation due to UV irradiation. The predicted increase of energy production outdoors was to be between 3-5%. Furthering the investigation [141] they found that the high photoluminescence quantum yield (PLQY) obtained by dissolved dyes decreased by up to 50% when the dyes were mixed with PMMA or an epoxy carrier. Hosseini *et al.* [142] tried using a reflective LDS layer underneath a DSSC cell and compared it with the effect of an LDS in front of the cell. The LDS layer was made from Europium based phosphor. The results showed that the reflective LDS layer increased the light harvesting at the region 400-550nm which boosted to Jsc by 40-54%.

In 2013 Ma *et al.* [15] tried applying an AlQ_3 LDS onto P3HT:$PC_{61}BM$ based OPV. The results led to up to 15% enhancement in PCE compared to the reference device. Aiming to suppress UV photo-oxidation in PTB7:$PC_{71}BM$ based OPVs and boost the efficiency, Moudam et al. [143] applied an AgPOP complex which increased the current generation by 0.41mA/cm^2 leading to 3.5% increase in relative performance. A report by Fernandes et al. [144] showed the positive effects of multidye KB:AlQ_3 LDS the stability of P3HT:PCBM based OPVs where they observed up to 600% lifetime improvement. Kettle *et al.* [145] demonstrated a comparison between conventional UV filters and Europium in a variety of concentrations to increase the performance and also the stability of P3HT:PCBM based OPVs. They also showed the positive effects of LDS as printed top layer for 16-cell OPV modules achieving a relative enhancement in lifetime of 850% and 6.5% relative enhancement in current generation.

Possibly the first report on LDS used for enhancing the stability of PSCs against UV photo-oxidation was reported in June 2017 by Anizelli *et al.* [146]. The report demonstrates the influence of using LDS as compared to commercially available UV filter which reveals an even further increased stability performance in favour of LDS compared to the UV filter and also a lower efficiency drop due to re-emission.

2.4.4 Encapsulation

Robust encapsulation is essential for extending the lifetime performance of any photovoltaic module. Regardless of the quality of the barrier layers, the most common failure mechanism of the encapsulation is observed to appear around the edges of the packaging which in time becomes the main route for water and oxygen ingress.

Angom *et al.* [147] from DTU demonstrated ITO-free polymer OPVs with operational stability of over two years outdoors. The modules are fabricated on a roll-to-roll line under ambient conditions, figure 2.24. Over the period of the investigation it has been found that the encapsulation consists of some flaws leading to oxygen and water ingress which needs addressing. Overall, however, the technique applied here exceeds the performance, W/€, of conventional silicon modules due to the low-payback times originating from fabrication methodology which was developed.

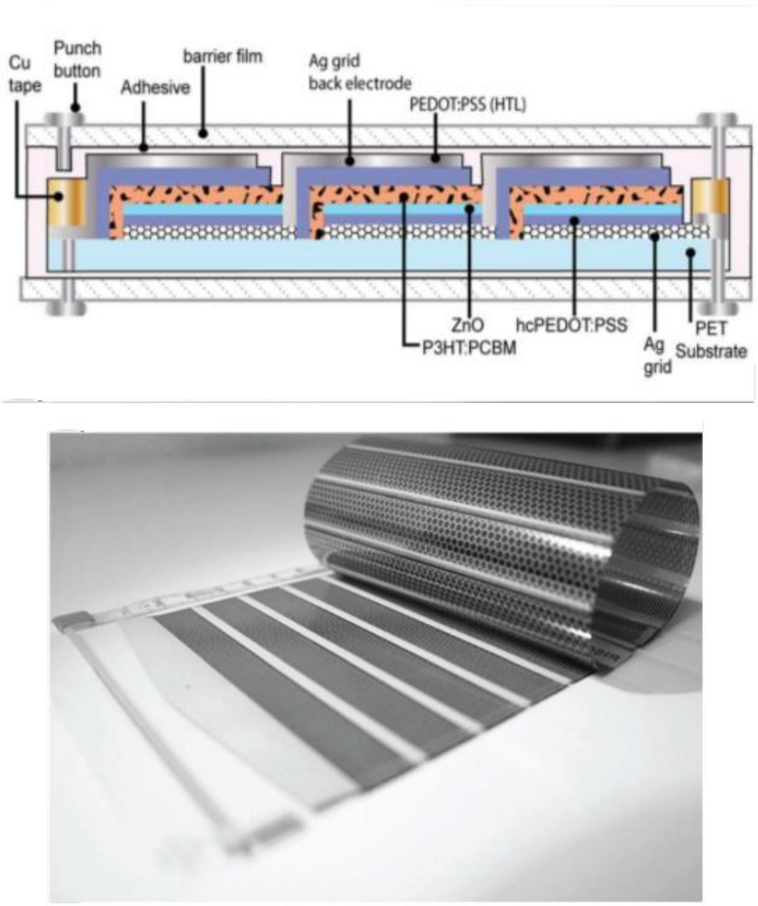

***Figure 2.24** – Cross-section of the module when full encapsulated (top) and the printed flexible module prior encapsulation (bottom)* [147].

In a report by Weerasinghe *et al.* [148] on flexible barrier layers and encapsulation techniques the importance of thorough sealing of OPV modules is presented by three levels of encapsulation. All encapsulation techniques utilise a front and back film supplied by 3M^{TM} Ultra Barrier Solar Film, figure 2.26. The barrier layers in method one and two were adhered to the module by adhesive transfer tape 3M^{TM} 467MP. The intention in the first method named 'partial', was the access to the electrodes from the back of the module where the barrier back film was intentionally narrower in order to expose the two opposite contacts. The second method, 'perforated', included a strip of copper (Cu) tape which was used for making the electrical connection to the electrodes and covering the entire module with oversized barrier film. The access to the Cu tape was made available by piercing the back barrier film just enough to establish a connection.

For the third method, 'complete', the Cu tape was longer so that it could be accessed externally to the encapsulation and also the adhesion of the barrier layers was established by using ethylene vinyl acetate (EVA) films supplied by 3M™ and the packaging was edge sealed using a moisture-barrier tape supplied by ADCO corp., HelioSeals PVS 101.

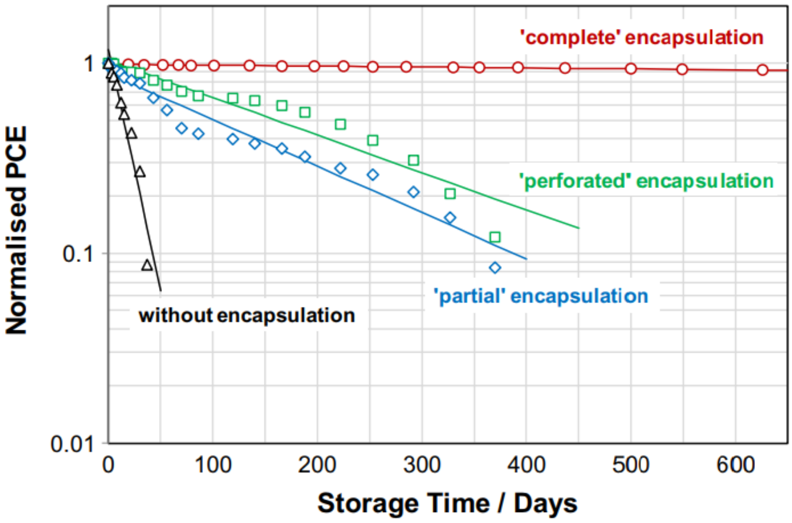

Figure 2.25 *– Normalised PCE of all encapsulation method versus a control non-encapsulated module. Proper encapsulation technique prolongs the lifetime of OPV modules preventing environmental degradation.*

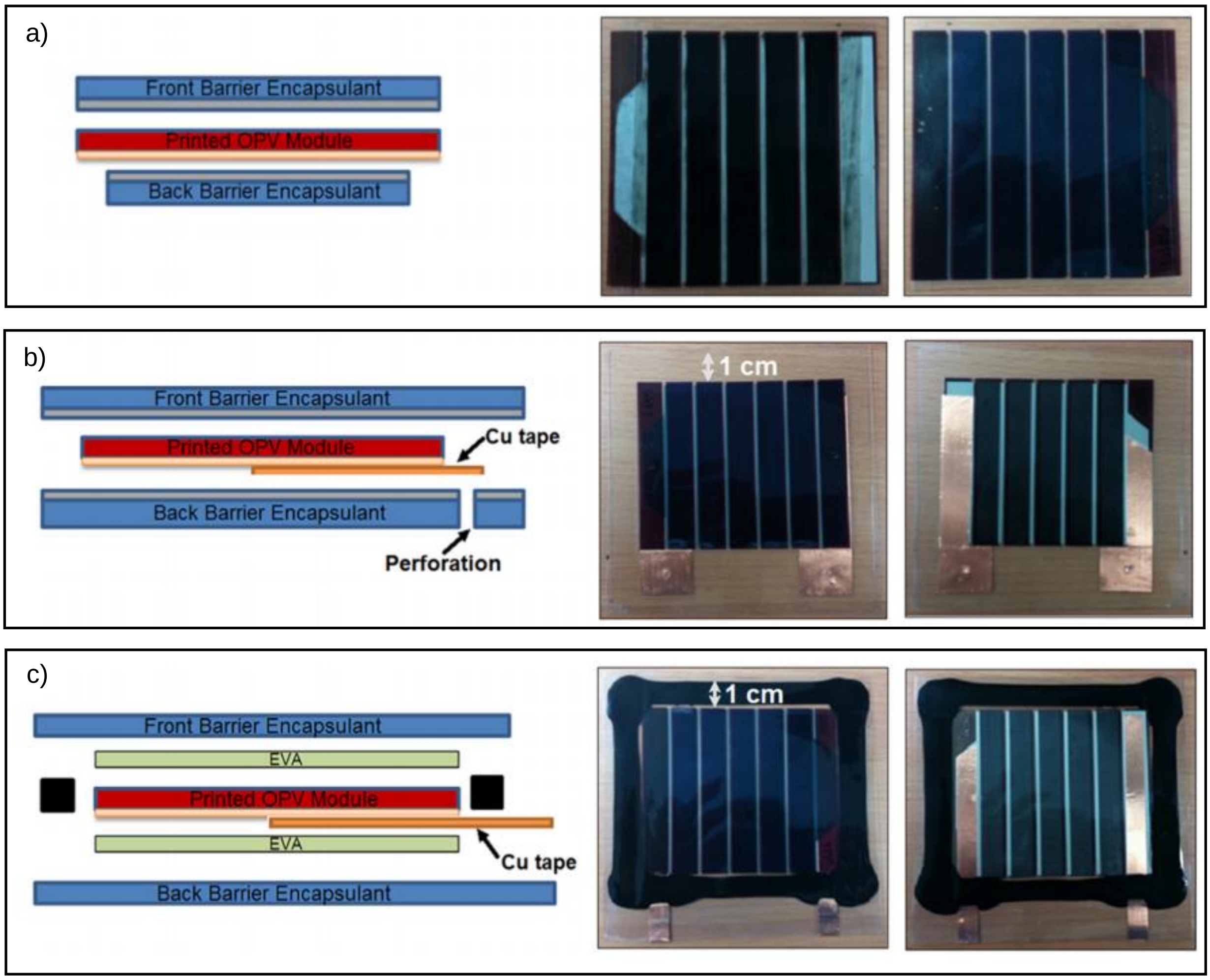

Figure 2.26 *– Cross-section and front/back photographs of encapsulated modules using method a) 'partial; b) 'perforated'; c) 'complete'.*

The modules encapsulated using the ‘partial’ and ‘perforated’ approach failed after near 400 days exposure reaching T_{80} lifetime after approximately 60 days, figure 2.25. All modules encapsulated using the ‘complete’ approach showed no evident degradation after 13 months continuous exposure and their anticipated T_{80} was to occur after at least 3 years.

2.5 Review of outdoor testing of BIPVs

Building integrated photovoltaics (BIPV) have been used over the past 20 years as a means to achieve new technical solutions to integrate PVs into conventional building materials such as for facades, roofing and skylights, amongst others. Through the application of BIPVs, parts of the building’s exterior can transform the building into being (at least partially) self-powering. In addition to cost constraints, many BIPV technologies only provide a comparatively small amount of output power as the mounting of the module is determined by the building architecture and not necessarily at the optimal incidence angle. Whilst technologies such as PSC or OPV have the potential to be used in BIPV due to their flexibility and greater aesthetic appeal,[112], [149], [150] there is insufficient information about how this affects the energy yield from BIPVs and how this changes as a function of diurnal and yearly solar position and climatic conditions. So far there have been very few reports related to outdoor performance monitoring and degradation due to natural climate conditions [110], [111], [128], [151], [152]. Gevorgyan *et al.* showed by carrying out a inter-laboratory study that flexible P3HT:PCBM on Polyethylene terephthalate (PET) modules can easily undergo 1000 hours of outdoor exposure and suffer an efficiency drop of as much as 40% [152]. Gevorgyan *et al.* also demonstrated the remarkable 10000 hours of outdoor stability on roll-to-roll P3HT:PCBM modules conducted in Denmark where OPV modules were fixed to a solar tracker [129]

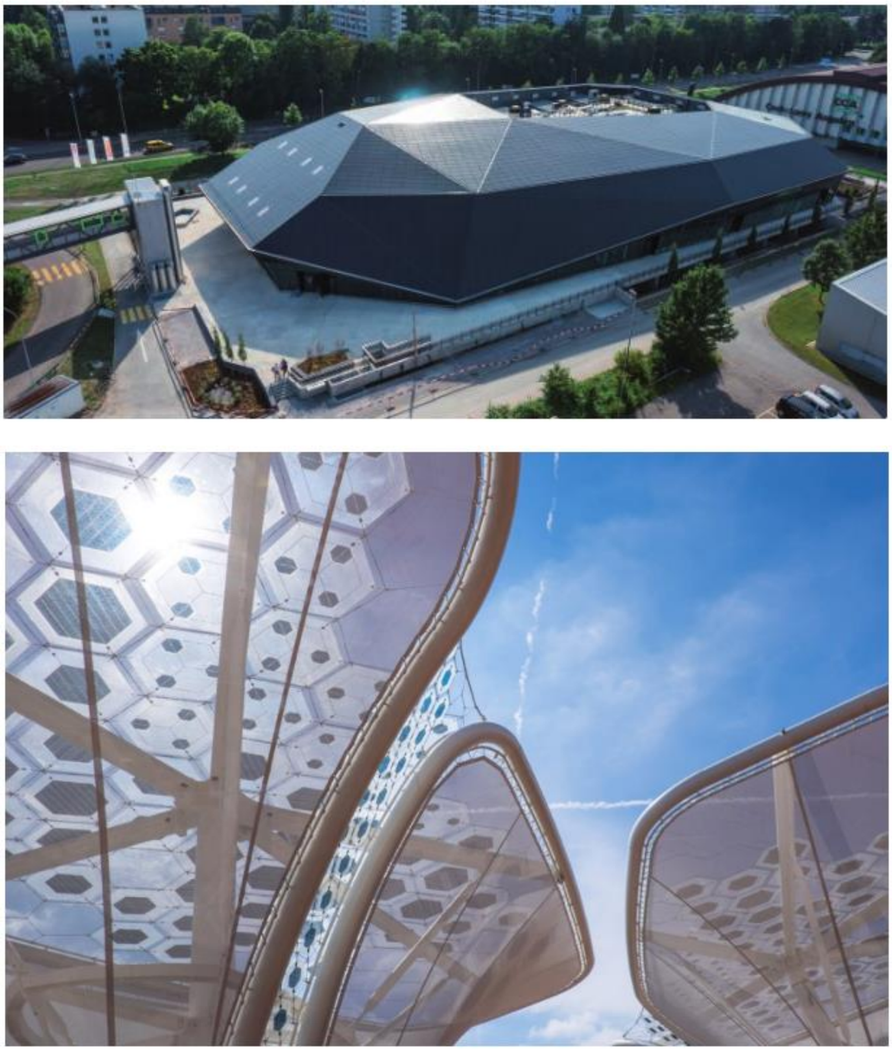

Figure 2.27 *– Umweltarena Spreitenbach, 750 kWp BIPV envelope consisting of c-Si panels with an anti-reflective coating* [28] *(Top) and tree shape structure with transparent hexagonal OPV solar modules demonstrated during expo Milano 2015* [150] *(Bottom).*

Furthermore Hauch et al., reported the use of PET as top barrier film in order to encapsulate P3HT:PCBM flexible modules which suffered only 20% drop in performance over 12 months of outdoor exposure [128]. Katz et al. published a comprehensive study related to the degradation of different active layer OPVs encapsulated with glass and aluminium. This study delivered a very exciting facts related to the degradation of OPVs showing short circuit density (Jsc) and fill factor (FF) decays corresponding to back contact degradation [151].

2.6 Accelerated lifetime testing of OPVs for lifetest models

Accelerated Lifetime Testing (ALT) is needed at various stage of a product development cycle, for example, when identifying optimal material sets [153], providing relative comparisons of module stability [154] and also information on the products failure mechanisms [145]. As OPV's are applied in more commercial applications there is a greater need in order to predict the expected life in outdoor operation. Longer term, companies trying to commercialise this technology would also need predictive ageing models in order to estimate warranty provisions. To date, the most commonly used strategies for relating outdoor degradation to indoor accelerated testing are the use of meta data analysis [113] and round robin experiments . An alternative technique is to use life test models based upon quantitative ALT to address lifetime and try to quantify the degradation through the application of a mathematical model. This has been explored by Halliant [9,10] for light induced degradation. Most ALT testing in the literature is based upon ISOS consensus standards, defined by Reese et al. [122].

Design of Experiments (DOE) is a very efficient strategy using multi-factorial analysis which allows for investigation of factors in the presence of other factors (known as an ‘interaction’) [155]. This is of high importance in OPV degradation analysis as very often interactions increase the degradation significantly; for example, when temperature and humidity are simultaneously applied, much greater degradation is observed as compared to a scenario where temperature or humidity is increased individually [156]. Hence, to fully characterise OPV degradation, investigation of the individual stress factors and their interactions should be undertaken. This will ensure the full range of weakness in OPV are resolved and provide an accelerated test that is more realistic to the outdoor conditions. Further benefits of multi-stress testing is that higher Acceleration Factors (AF) are possible, which will increase the speed of testing leading to faster acquisition of lifetime data [157].

2.6.1 Analysis of stress results

The first assumption when analysing results collected from a multi-stress ALT test is that all factors are individual and do not have an interaction. Yet, interactions between factors may have significant impact to the stability of a device and ignoring them may lead to erroneous conclusions, [158]–[161]. Eyring life-stress relationship, [162] is a technique which is often used when analysing a combination of non-thermal and thermal accelerated stresses which analyses precisely their interaction. The Eyring relationship evaluations the effect of change in one of the stress factors when keeping the other factor constant.

The results of the analysis are plotted in graphs using multiple probability density functions (pdfs) [163], where each pdf is located at a different stress level depending on the test values used in the experiment, [157]. The pdfs show the failure rate as a function of stress level where the variables (X) are fitted in the interval [a, b].

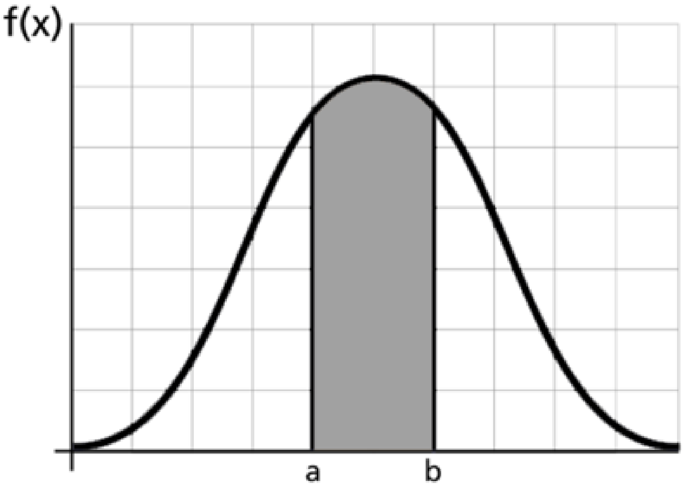

***Figure 2.28** – Example of a Probability Density Function with interval area between limits a-b,* [163]

$$P(a \leq X \leq b) = \int_a^b f(x)dx \qquad \text{equation 2.6}$$

When plotted [157], the pdfs show the range of data points for a given stress level which provides an understanding of the match between test samples exposed to identical stress conditions. The plot also provides an eta line. The eta line is an estimation of failure of 63% of the devices in a given group

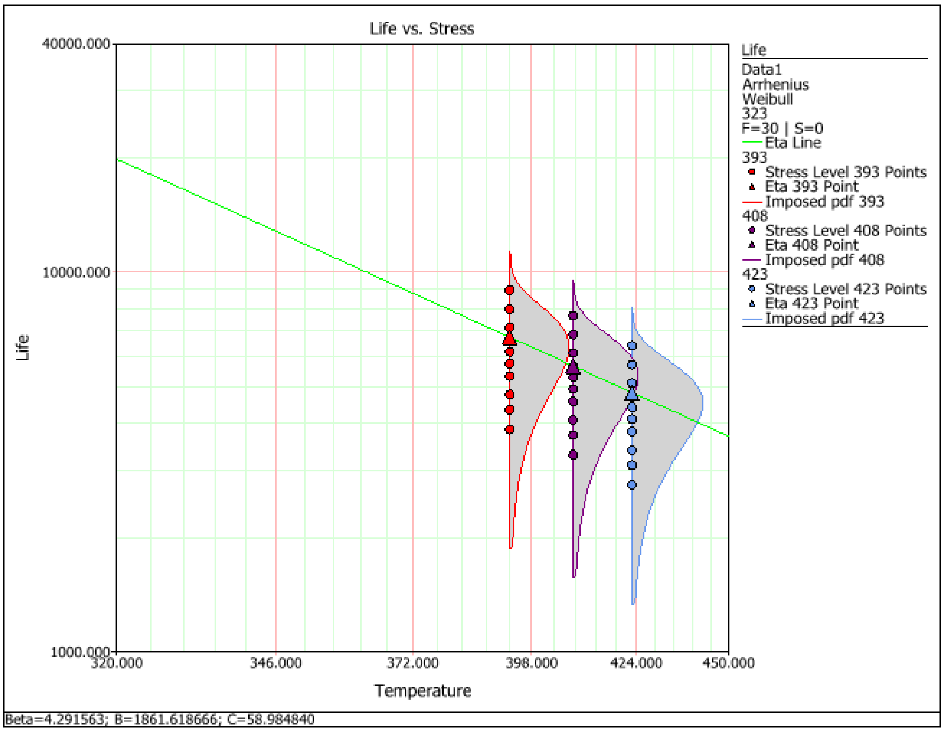

Figure 2.28 – Example Life vs. Stress plot showing a range of pdfs and data point along the base of each pdf demonstrating the spread of data collected for the same stress level, [164]

2.7 Absorption Degradation State method

The absorption degradation state is a method for more accurately express the degradation of an absorber layer by calculating the ratio of the number of absorbed photons ($\boldsymbol{N_{Tot}^{T}}$) by the layer when fresh to the number of photons after a period of aging [98], [165].

$$\boldsymbol{N_{Tot}^{T} = \sum_{\lambda 1}^{\lambda 2} N_0(\lambda)(1 - 10^{-At(\lambda)})} \qquad \text{equation 2.7}$$

In equation 2.7 $\boldsymbol{A}$ represents the absorbance measured at a specific wavelength ($\boldsymbol{\lambda}$) at time $\boldsymbol{t}$**.** $\boldsymbol{N_0(\lambda)}$ represents the incident photon flux. The standard AM1.5G photon flux was taken from the ASTM G-173, reference solar spectral irradiance, [166].

$\boldsymbol{N_{Tot}^{T}}$ is calculated as a function of exposure time. The percentage of absorbed photons in the range 400-800nm is then calculated and multiplied by the number of incident photons. To get $\boldsymbol{N_{Tot}^{T}}$ the product is then summed in the range 400-800nm.

2.8 Conclusion

The first part of this chapter presents a review of PSC basics, their operation and available device architectures. It also discusses the progress of the PSC technology demonstrating the state of the art devices and also the improvements in lifetime performance. Outdoor monitoring progress of PSCs is briefly examined as there are still very few groups which have analytical data to show on outdoor aging of perovskite. The second part of this chapter focuses on OPVs which were used as a replacement to PSCs during the course of this project. In this part state of the art OPVs, their reported degradation mechanisms and lifetime improvement are the main topics. The third part of the chapter looks at ISOS stability testing, spectral filtration, the use of LDS coating and impact of module encapsulation. The last part reviews reports on outdoor testing of BIPVs and accelerated lifetime testing of OPVs.

Chapter 3. Experimental details

3.1 Introduction

This chapter describes the experimental techniques undertaken during this PhD. Detailed explanations of solar cell manufacturing, indoor and outdoor measurements conducted and device characterisations are given, followed by details of the methods used to analyse the outdoor data. The technique to apply luminescent downshifting (LDS) layers to improve the performance and stability of Perovskite Solar Cells (PSCs) is also included.

Most of the solar cell manufacturing, device aging, and characterisation was performed in the School of Electronic Engineering at Bangor University (BU). Additional work was also conducted at Ben Gurion University where perovskite active layers were fabricated and aged using concentrated sunlight and SEM measurements were conducted. This was undertaken as part of a COST action funded by the EC.

3.2 Perovskite solar cell manufacturing

The material preparation and sample cleaning was undertaken in a Class 1000 cleanroom. The devices were then manufactured in a nitrogen filled glovebox with low oxygen and water content to as low as 0.5 ppm. All active layers were deposited from solution unless otherwise stated. All chemicals were used without further purification. The PSC devices were manufactured onto pre-patterned Indium Tin Oxide (ITO), and Florine Doped-Tin Oxide (FTO) with larger active area, glass substrates with sheet resistance of <15Ω/sq. The cell active area was defined by the overlap between top and bottom electrodes and it was 7 mm^2 for the ITO substrates and 50 mm^2 for the FTO substrates.

The following sections describes the preparation methodology for inverted perovskite architecture devices only. Non-inverted devices were also fabricated during the course of the PhD, however, due to time constraints and lower device performance, only the inverted architecture are reported in the results chapters.

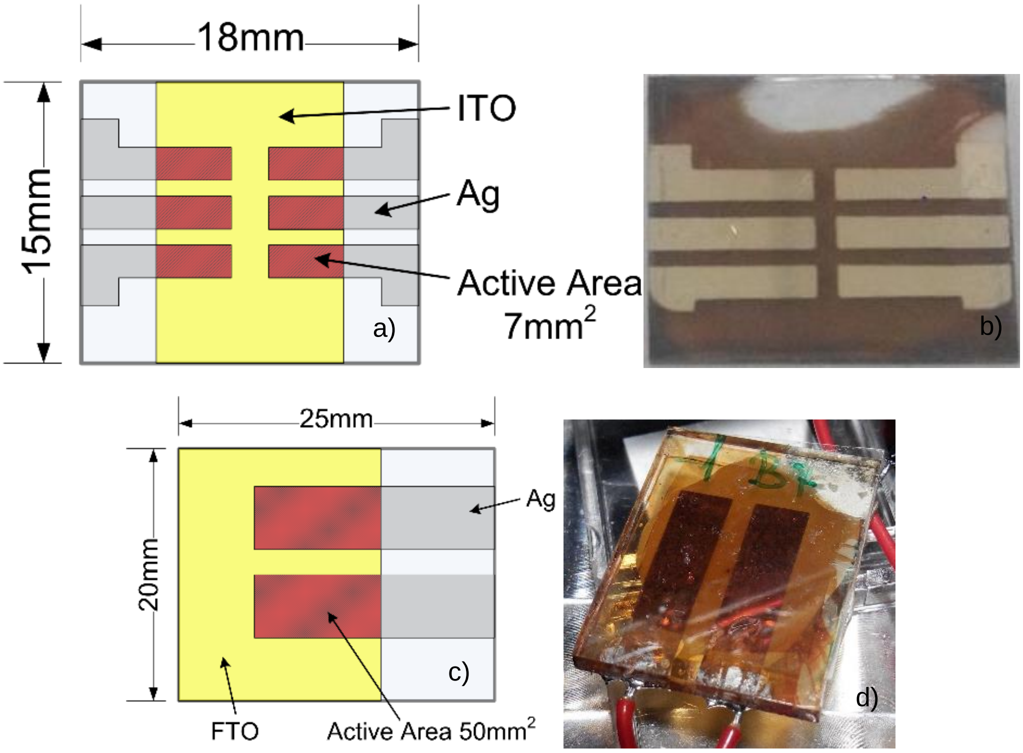

Figure 3.1 *– a) standard 6-cell device layout design, b) photograph of $CH_3NH_3IPbX_X$ device and 2-cell FTO device layout and c) photograph of manufactured $CH_3NH_3IPbX_X$ device.*

3.2.1 Process overview

An illustration representing the final device stack in a two step deposition PSC is shown in figure 3.2 a). A flow chart of the experimental procedure for device fabrication is shown in figure 3.2 b). This covers all the major steps for inverted device fabrication, for single and two step perovskite absorber layer fabrication.

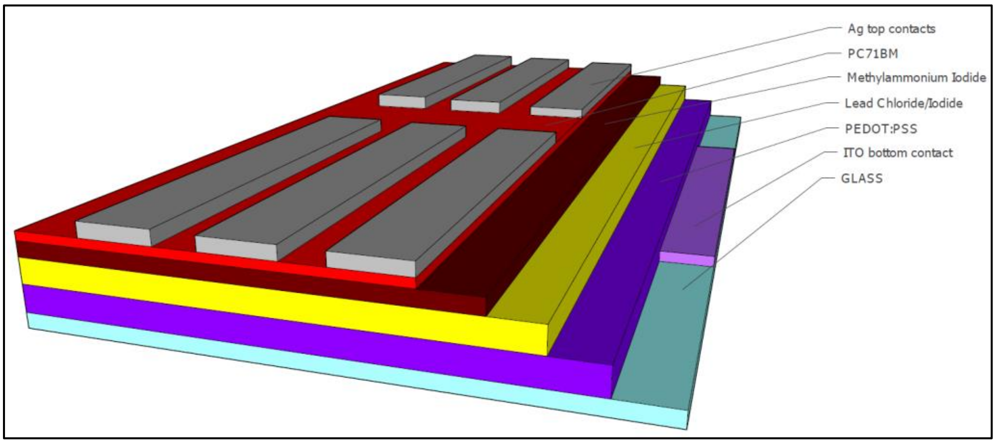

Figure 3.2 a) *- Illustration of final device structure of an inverted device.*

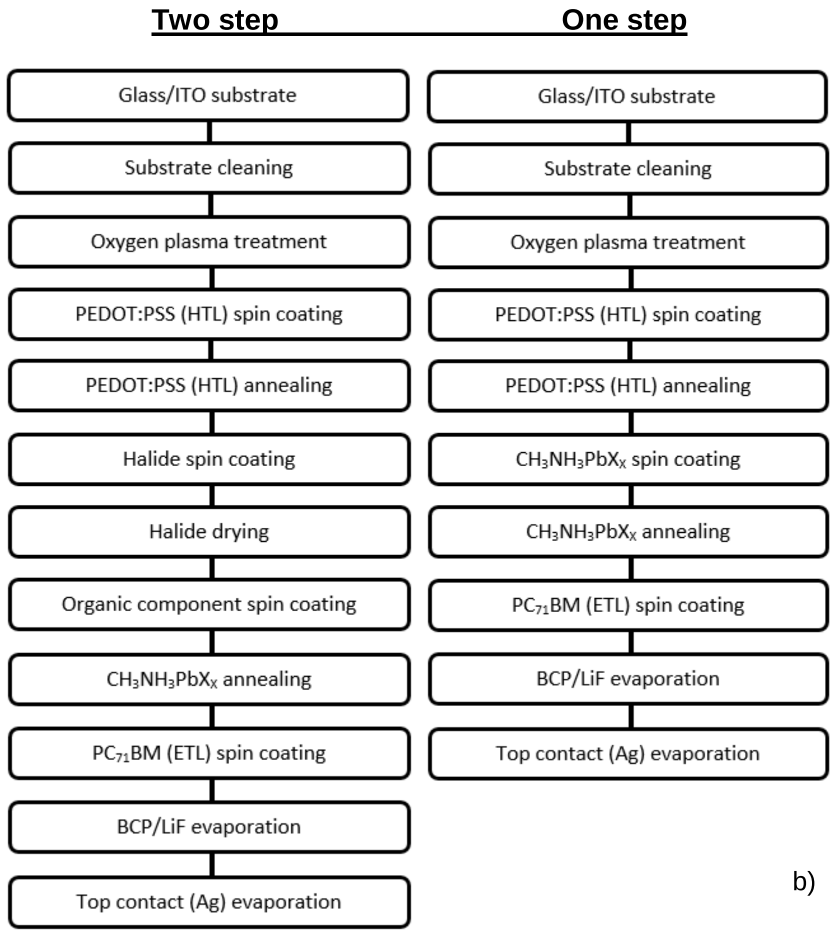

Figure 3.2 b) *- The sequence of steps used for the fabrication of inverted structure PSCs using two step deposition and one step deposition.*

Active Layer Blend Preparation:

$CH_3NH_3PbI_3$ preparation for one step deposition:

PbI_2 (Lumtec, 99.999 %) and CH_3NH_3I (Lumtec, 99.99%) were dissolved at 1:1 molar ratio in DMF in 40 wt. %. The solution was then heated to 70 ^{O}C for 30 minutes while simultaneously stirred. Finally, the material was filtered with a 0.45μm syringe filter.

$CH_3NH_3PbCl_2I$ preparation for one step deposition:

$PbCl_2$ (Lumtec, 99.999 %) and CH_3NH_3I (Lumtec, 99.99%) were dissolved at 1:3 molar ratio in DMF in 40 wt. %. The solution was then heated to 70 ^{O}C for 30 minutes while being stirred and then filtered using a 0.45μm syringe filter.

$CH_3NH_3PbCl_2I_3$ preparation for one step deposition:

PbI_2 (Lumtec, 99.999 %), $PbCl_2$ (Lumtec, 99.999 %) and CH_3NH_3I (Lumtec, 99.99%) were dissolved at 1:1:4 molar ratio in DMF in 40 wt. %. The solution was then heated to 70 ^OC for 30 minutes while being stirred and then filtered using a 0.45µm syringe filter.

$CH_3NH_3PbI_3$ preparation for two step deposition:

PbI_2 (Lumtec, 99.999 %) was dissolved in DMF with concentration 1.0M in 1.0ml solvent. The solution was then heated to 70 ^OC for 30 minutes while being stirred and then filtered using a 0.45µm syringe filter. CH_3NH_3I (Lumtec, 99.99%) was dissolved in IPA with concentration 0.188M in 1.0ml solvent. The solution was then stirred at room temperature until fully dissolved.

$CH_3NH_3PbBr_2I$ preparation for two step deposition:

$PbBr_2$ (Lumtec, 99.999 %) was dissolved in DMF with concentration 1.0M in 1.0ml solvent. The solution was then heated to 70 ^OC for 30 minutes while being stirred and then filtered using a 0.45µm syringe filter. CH_3NH_3I (Lumtec, 99.99%) was dissolved in IPA with concentration 0.188M in 1.0ml solvent. The solution was then stirred at room temperature until fully dissolved.

$CH_3NH_3PbCl_2I$ preparation for two step deposition:

$PbCl_2$ (Lumtec, 99.999 %) (1.078 M) was dissolved in 1.0ml DMSO. The solution was then heated to 70 ^OC for 30 minutes while stirring. CH_3NH_3I (Lumtec, 99.99%) was dissolved in IPA with concentration 0.188M in 1.0ml solvent. The solution was then stirred at room temperature until fully dissolved.

$CH_3NH_3PbCl_2I_3$ preparation for two step deposition:

PbI_2:$PbCl_2$ (Lumtec, 99.999 %) (1.043M:0.521M) were dissolved in 1.0ml DMF. The solution was then heated to 70 ^OC for 30 minutes while stirring. CH_3NH_3I (Lumtec, 99.99%) was dissolved in IPA with concentration 0.188M in 1.0ml solvent. The solution was then stirred at room temperature until fully dissolved.

After preparing the blends in the cleanroom all solutions were backfilled with nitrogen and transferred to the glovebox in a sealed vial.

Electron transporting layer preparation (ETL):

[6,6]-phenyl C71 butyric acid methyl ester ($PC_{71}BM$) preparation:

$PC_{71}BM$ (Nano-C, > 99.95%) was dissolved in chlorobenzene with concentration 0.029M in 1.0ml solvent. The solution was then transferred into the glovebox and stirred at room temperature until fully dissolved. Finally, the solution was filtered using a 0.45μm syringe filter.

Substrate Cleaning:

All samples regardless of type were carefully cleaned before PSC fabrication. The substrates were first washed with DECON 90 and rinsed with warm water. They were then subjected to sonication in solvents including deionized, acetone (99.5%), and isopropanol (IPA) for 5 minutes each. The substrates were then dried under airflow and exposed to oxygen-plasma cleaning for another 5 minutes. The quality of the glass surface cleaning was validated by contact angle measurements, which was found to be 9.3 ± 1^{O} indicating the surface is highly hydrophilic.

Hole transporting layer deposition (HTL):

The substrates were spin coated with PEDOT:PSS (Heraeus Clevios™ Al 4083, Ossila) at 4000rpm for 40 seconds to give a thickness of ~40nm, after which annealed at $150^{O}C$ for 15 minutes before being moved into the glovebox. All subsequent processing was performed in the glovebox.

Active Layer Deposition:

Depending on the prepared blend the deposition was carried out at follows:

$CH_3NH_3PbI_3$ one step deposition:

The active layer was spin coated at 6000rpm for 40 seconds using a pre-heated to $70^{O}C$ solution. The active layer was then annealed at $90^{O}C$ for 60 minutes.

$CH_3NH_3PbI_3$, $CH_3NH_3PbBr_2I$ and $CH_3NH_3PbCl_2I$ two step deposition:

The active layer was grown at 2 stages. The halide solution was spin coated at 6000rpm for 30 seconds and annealed at $90^{O}C$ for 20min. Afterwards the organic CH_3NH_3I 0.188M solution was spin coated on the previously formed halide layer at 6000rpm for 30 seconds and annealed at $90^{O}C$ for 20 minutes.

ETL:

$PC_{71}BM$ deposition:

The ETL was spin coated at 4000rpm for 40 seconds creating a layer thickness of approx. 40nm.

Thermal Evaporation of Top Electrode:

Thermal evaporation of the top electrodes was carried out though a shadow mask to define the electrode pattern and consisted of 0.5nm Lithium fluoride (LiF) (Sigma-Aldrich) and 100nm of silver.

3.3 Degradation setups

All samples were subjected to degradation analysis after fabrication. The main objective of this PhD is the establishment of the lifetime of PSCs and OPVs.

3.3.1 Application of LDS layers on PSCs

Luminescent down-shifting materials were tested as a substitute for commercial UV filters for PSCs. This work was conducted at three stages. The first stage involved the investigation the optical properties of a number of commercially available LDS materials. The second stage involved the performance of perovskite layers with applied LDS material. The third and last phase involved studying both indoor and outdoor stability.

3.3.2 Light aging setup

The light aging setup comprises of a light source Newport Oriel™ Sol1A class ABB and Plasma International GmbH sulphur-plasma standard AM1.5G solar simulators, and SMU unit supplied by Botest Systems GmbH which performs IV curve measurements. The fabricated devices were measured using single sample devices holder supplied by Botest and also a custom made 8-slot x 6-cell device holder used for lifetime testing *figure* 3.3 a). The light aging tests of all devices was conducted using the xenon solar simulator *figure* 3.3 c) or the sulphur-plasma light source *figure* 3.3 b). All lifetime tests were associated with regularly taken IV measurements with frequency of every 15 minutes where the samples were kept at open circuit between scans in agreement to ISOS L1 or L2 [167].

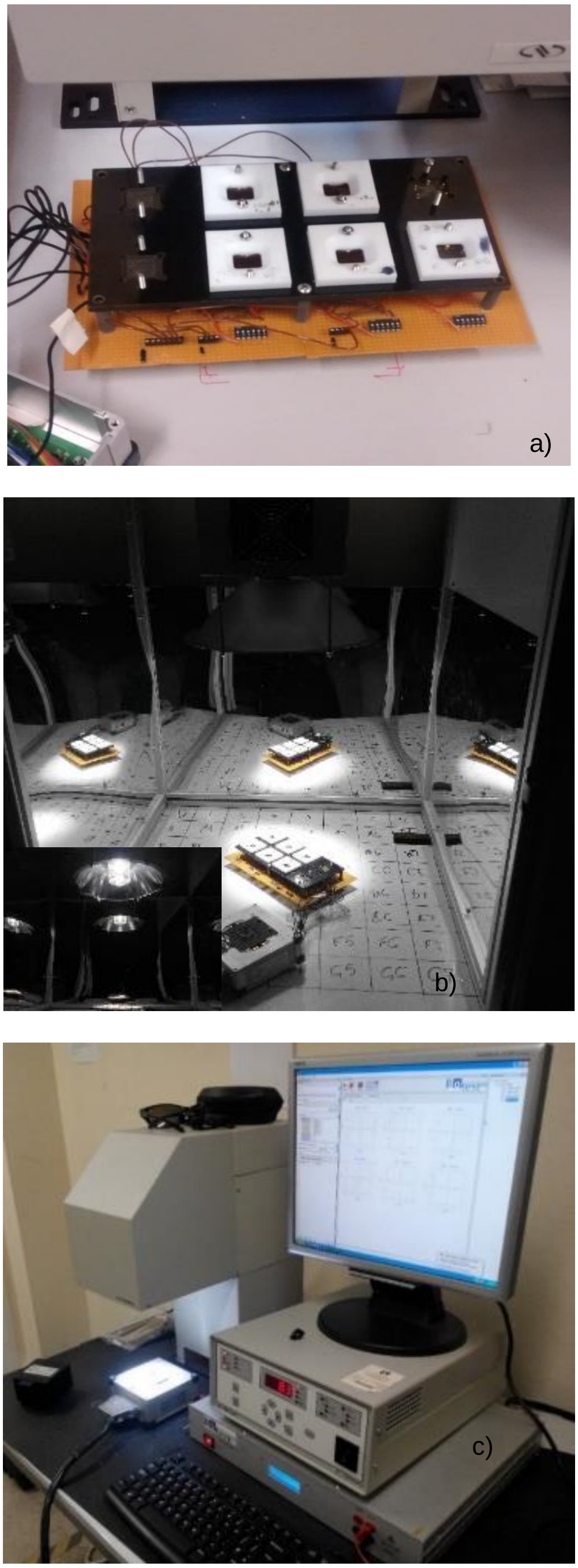

***Figure 3.3** – a) 8-slot test rig with the capability of measuring up to 6-cells on one substrate. b) Plasma International AAA sulphur-plasma AM1.5G solar simulator (inset demonstrating the top of the light source) c) and Newport Oriel™ Sol1A class ABB solar simulator with one Botest SMU unit used for IV characterisation.*

3.3.3 Atmospheric chamber tests

A bespoke environmental chamber, supplied by Scanwel Ltd. was used for controlled atmosphere experiments. The chamber consists of two BNC connectors allowing up to two PSCs to be aged simultaneously. The chamber also has a top window and a base viewport for in-situ absorption measurements under various conditions. It also comprises of a two terminal feedthrough which is used for the controlling of Peltier plates and a gas inlet and outlet. The inlet includes a blow off valve which will stop unintentional over pressuring of the chamber. The system could be operated under vacuum, nitrogen gas or high humidity levels.

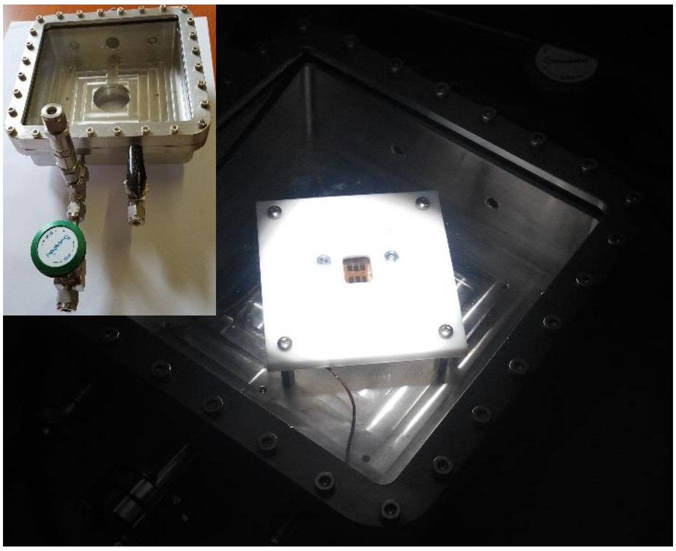

Figure 3.4 *– Bespoke environmental controlled degradation chamber with a 6-cell* $CH_3NH_3PbCl_2I$ *device under test, manufactured by Scanwel ltd (inset showing a photograph of the chamber when not in use)*

3.3.4 Concentrator light testing at Ben Gurion University

All concentrated lifetime tests of PSCs and active layers were conducted using a 20cm diameter Minidish dual-axis tracking solar concentrator located at Jacob Blaustein Institute for Desert Research in the Negev Desert at a Latitude 30.8N, Longitude 34.8E and Altitude 475m. The exposed samples were subjected to concentrated sunlight indoors the intensity of which was checked prior initiation of the light aging experiment. The setup collects the sunlight outdoors and guides it indoors through a fibre optic core [168], [169] and points it over a 2.5cm long kaleidoscope which focuses the light over the sample underneath. All concentrated sunlight experiments were conducted at 12 o’clock during days of clear direct irradiation in order to get as close as possible AM1.5G solar spectrum. Once calibrated pointing directly towards the sun, the solar tracker's pyranometer was capable of following the sun's course with accuracy of no less than 95%.

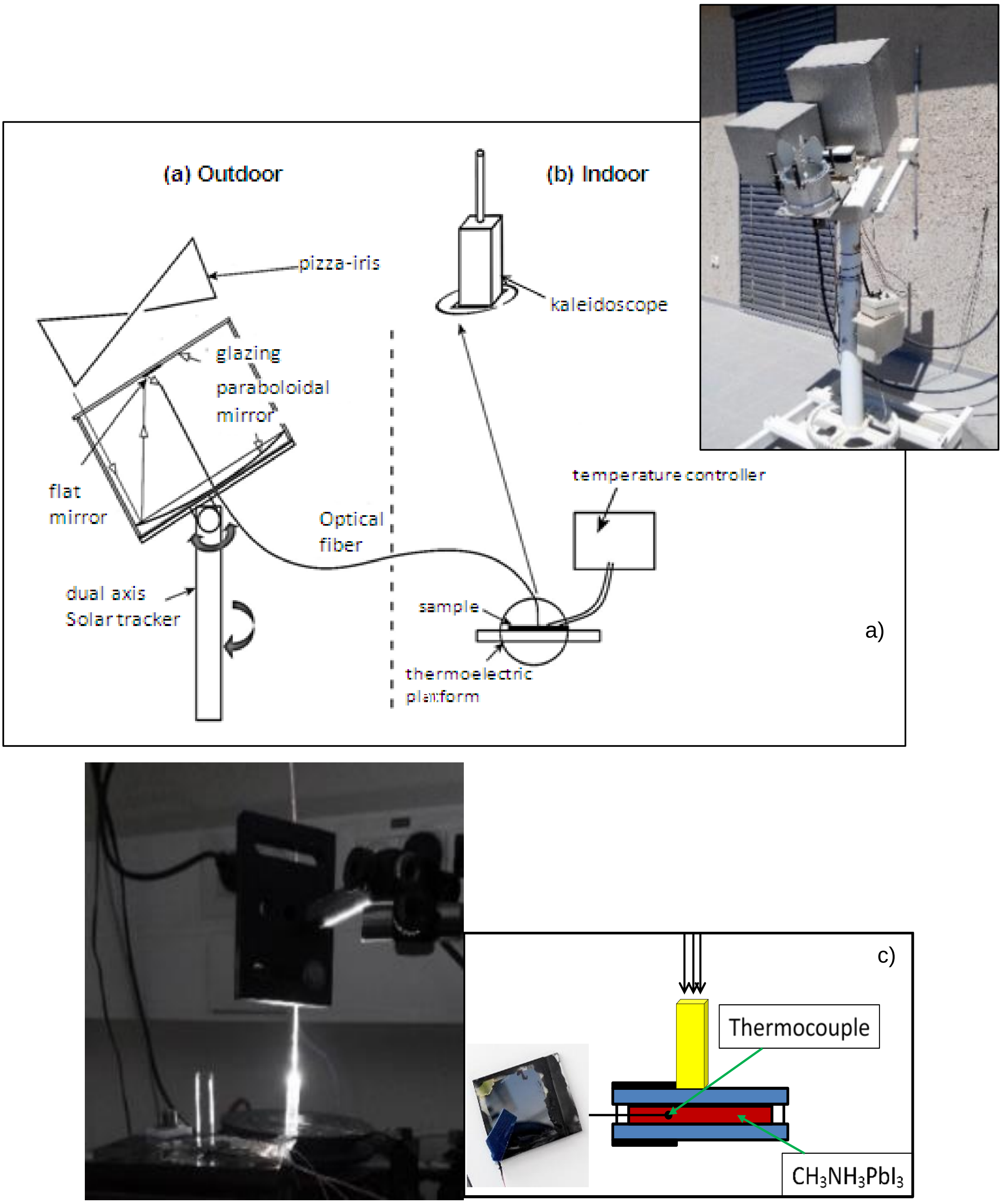

Figure 3.5 *– a) Diagram of the solar concentrator setup. Sunlight is being collected by the mini-dish and guided indoors over a kaleidoscope placed on a tested sample* [98] *(inset shows a photograph of the solar tracker). b) Concentrated sunlight passed into a kaleidoscope placed on a power meter to verify the intensity. c) Illustration and photograph of encapsulated sample for concentrated sunlight temperature measurement*

The multimode solarisation-resistant optical fibre core installed was with length of 2m, measured from the solar tracker to the sample, a diameter of 600μm and transferred light in the wavelength range 180-1200nm, [170].

The samples were bonded to a thermoelectric temperature-controlled platform indoors, with a surface temperature fixed to $25^{O}C$ measured by a T-type thermocouple. The sample temperature was measured by integrating another T-type thermocouple in an encapsulated sample and blocking the area of direct exposure of the thermocouple's tip to the concentrated sunlight, *figure* 3.5 c), in order to eliminate false reading. During light exposure the sample temperature reached $95^{O}C$ unless cooled.

LDS Preparation:

The LDS was applied via a host material Poly(methyl methacrylate) (PMMA) which could be spin coated ontp the surface of PV devices. The solution was prepared by dissolving LDS and PMMA in anisole and chloroform in the ratio 0.25:0.75. The concentration of PMMA was kept constant at $20mg\ ml^{-1}$ solvent while the amount of LDS was varied and optimised during this study. After solution preparation the vials were left stirring on a heated to $60^{O}C$ hotplate for the duration of 12 hours. The application of LDS was done by spin coating the LDS material at 4000rpm for 60 seconds on fused silica substrates after which the samples were annealed at $60^{O}C$ for 15 minutes. The film thickness measured showed a very high consistency of 300nm ±5nm and roughness R_A of ~1nm at an area of $0.0057mm^2$.

Indoor Stability Testing of LDS Materials at BU

The effect of LDS application to perovskite layers was also conducted at BU. All experiments were conducted using a standard AM1.5G light source. The stability tests were carried out for both active layers and also devices. The active layers were kept at constant heating at $60^{O}C$, figure 3.6 a) provided by a custom made heated platform, figure 3.6 b). The devices were exposed for light aging with and without encapsulation (using the encapsulation technique in figure 3.7, using fast drying nitrocellulose epoxy). The stability of the samples was real-time monitored for absorption decay using an Ocean Optics HR4000 spectrometer connected to the in-situ setup where measurements were recorded every 2 minutes.

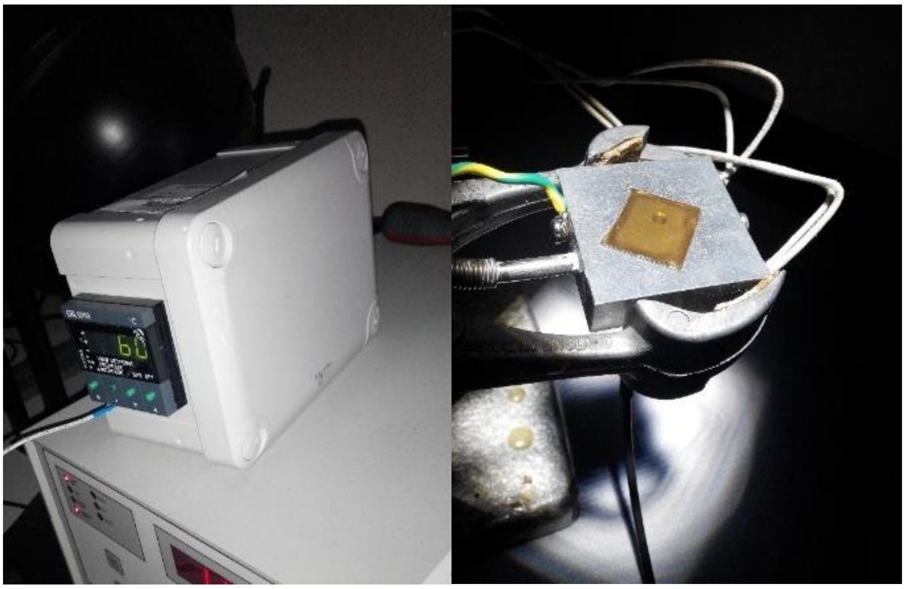

***Figure* 3.6 –** *Indoor test setup at Bangor University. Newport standard AM1.5G light source and heated platform keeping a constant ambient temperature.*

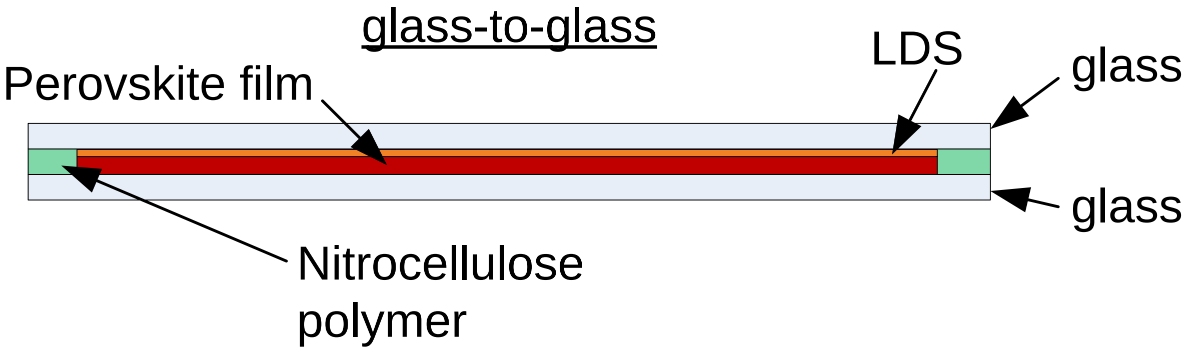

***Figure* 3.7 –** *Cross sections of LDS protected perovskite films tested indoors at BU and outdoors at Ben Gurion University*

Outdoor Stability Testing of LDS Materials at Ben Gurion University of the Negev, Israel

Concentrator testing of LDS on Perovskite active layers was undertaken at Jacob Blaustein Institutes for Desert Research in the Negev Desert. All samples were encapsulated using the glass-to-glass method using nitrocellulose polymer interlayers prior to outdoor exposure, figure 3.6. The LDS film was coated on the inside of the encapsulation top glass slide prior its attachment to the perovskite carrying substrate.

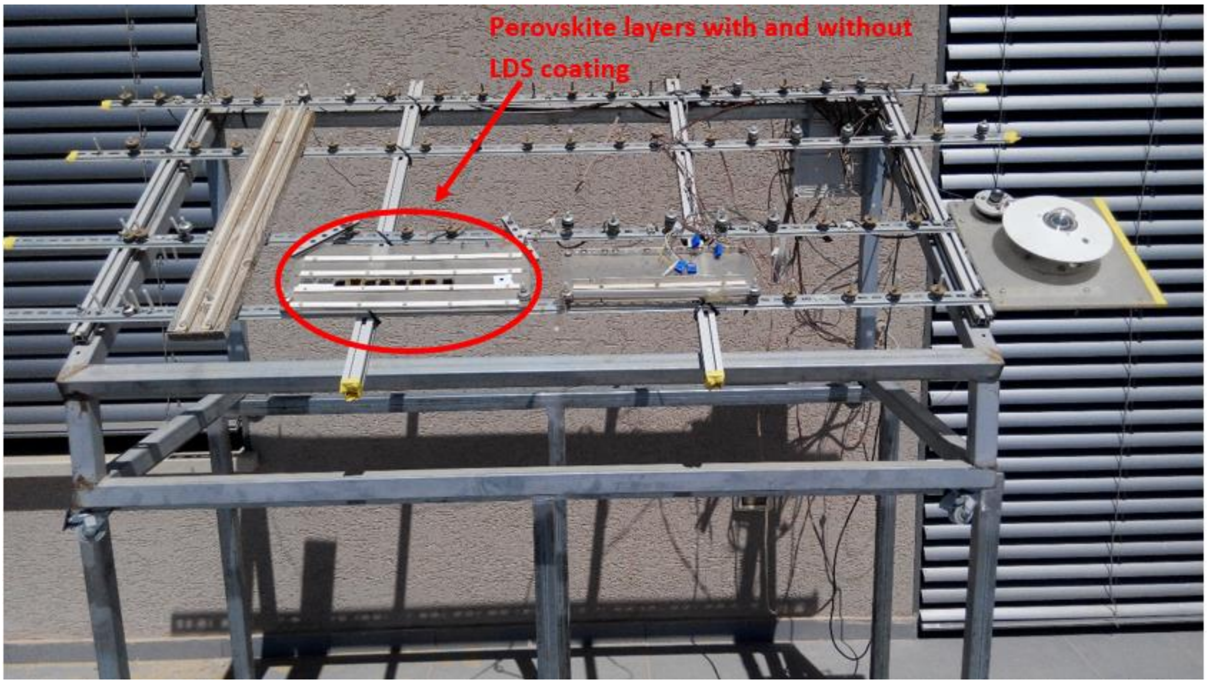

***Figure* 3.8 –** *Outdoor OPV rack at Jacob Blaustein Institutes for Desert Research, in the Negev Desert*

3.4 OPV modules

Over the course of this project, SPECIFIC were developing PSC modules that only became available at the end of this project, it was decided to undertake module testing using OPVs, given they are readily available. Two generations of OPV modules supplied from the Danish Technical University (DTU) and later InfinityPV were used for experimental work. InfinityPV was founded in 2014 by Prof. Frederik Krebs from the group at DTU. The modules used for this work are produced on a R2R plant and subsequently laser cut according to the template [171]–[173].

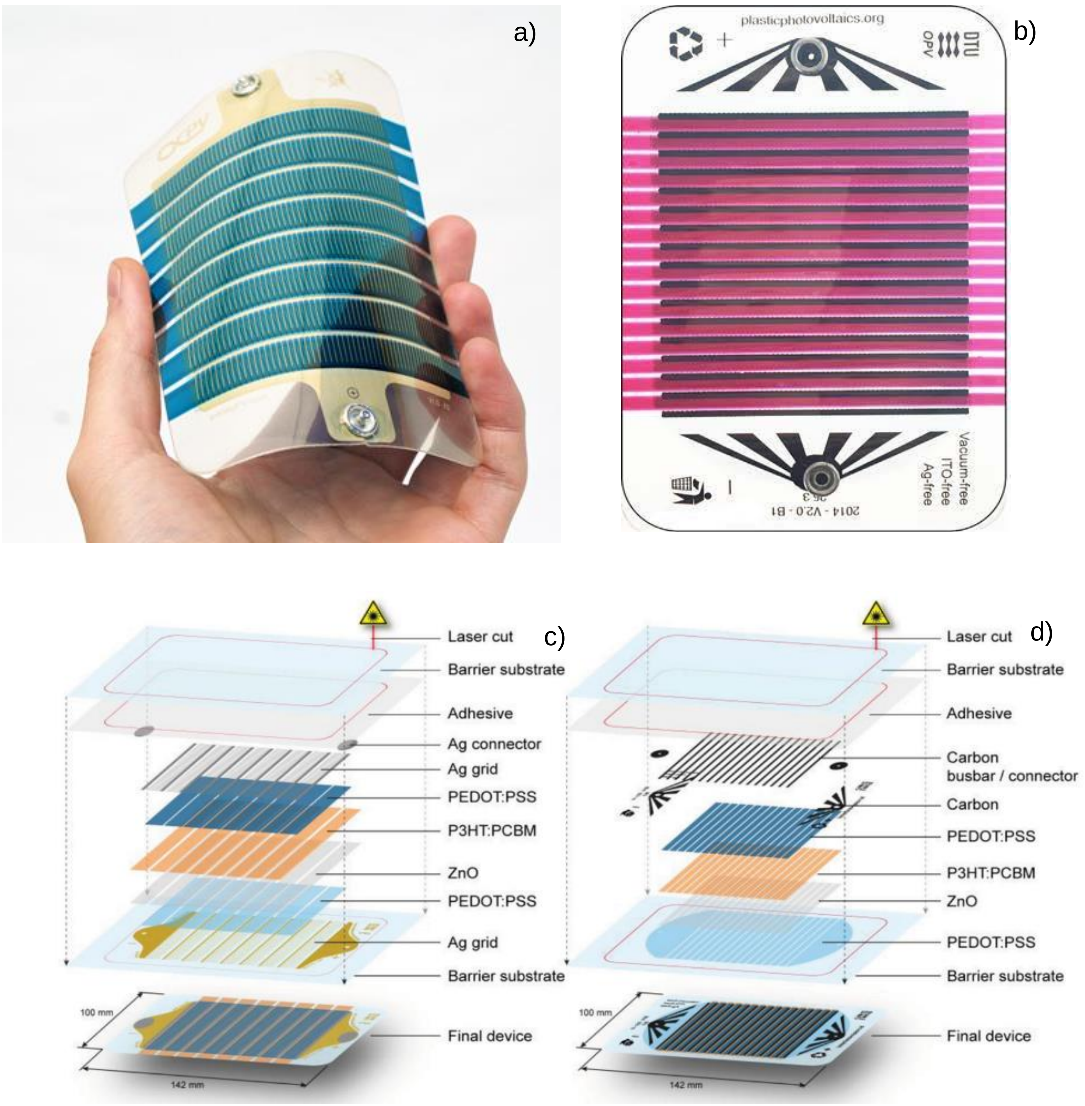

***Figure* 3.9** – *a) InfinityPV module with silver nanowire grid and b) with graphite busbars. Multilayer structure of silver grid modules c) and of Carbon busbar structure d)* [174][175].

Two different active layers were used; in the case of, *figure* 3.9 ('Generation 1'), the active layers is P3HT:PCBM, whilst for the tests in section 5.3, the material is undisclosed, however, based on its appearance it should be a low bandgap polymer [5]–[8]. For these modules, the front electrode consisted of a highly conductive PEDOT:PSS and carbon (graphite) busbars between the cells, and the back PEDOT:PSS and ZnO. The module consists of 16 serially connected cells and an active area of 30 cm^2 [174][177]. These modules were used for an accelerated lifetime testing campaign conforming to ISOS D1, L1, L3 and T3 test protocols conducted at BU.

The 'Generation 2' modules were also supplied by InfinityPV the architecture of which comprises of 8 serially connected cells and an active area of 64.8 cm^2 [177]. They were further encapsulated using a technique developed at Bangor University (BU). After encapsulation the modules were laminated to a cuboid building prototype which was deployed on the roof of the Electronics Engineering department at BU and studied for a period of one year.

3.4.1 Encapsulation of InfinityPV modules

A number of non-encapsulated modules were installed and monitored outdoors and their output was analysed. The results showed a very fast degradation due to contact delamination which occurs where the contacts pierces the foils [131], [179], [174]. A technique to improve their lifetime was developed in this project.

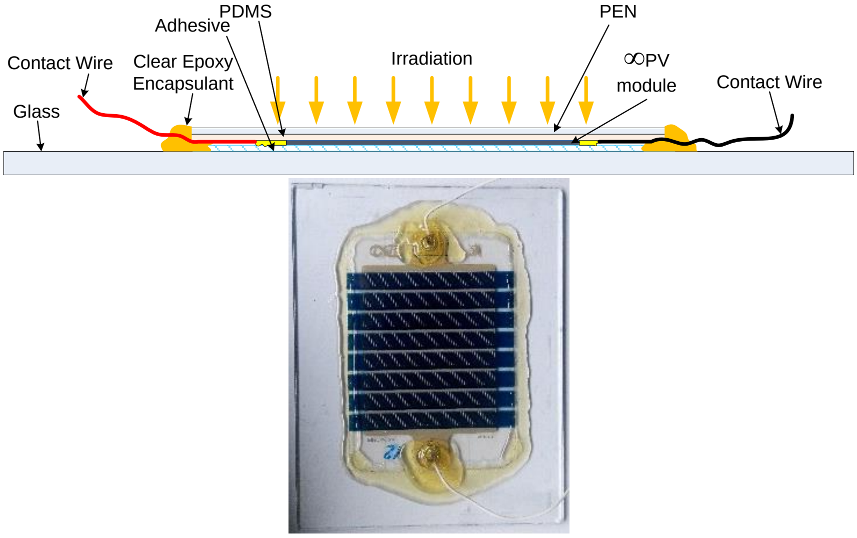

__Figure 3.10__ – a) Cross-section view of the finalised encapsulated OPV purchased from InfinityPV and b) encapsulated OPV module on a glass backing sheet ready for outdoor testing.

The wires were soldered to the contacts and the modules were fixed onto 205mm x 160mm glass backplanes using commercially available adhesive. The next step involved preparation of PolyDiMethylSiloxane (PDMS) (Sylgard 184, Dow Corning). After combining the two part PDMS it was degassed under vacuum before it was applied over the module. The entire module was covered with a thin layer of PDMS providing adhesion on the surface. This allowed for a pre-cut to bespoke shape PolyEthylene Naphthalate (PEN) film (DuPont Teijin) to be fixed over the layer of PDMS isolating the top surface of the module from the extreme outdoor conditions. The PDMS was then allowed to cure in indoor ambient temperature for 24 hours without applying thermal/UV curing. The final stage of the encapsulation was concluded by sealing the edges of the modules with low temperature two part fast curing sealing epoxy (Dyesol UK).

3.5 Accelerated lifetime testing (ALT)

Accelerated Lifetime Testing was conducted using an environmental chamber, shown in figure 3.11, 3.13b. The modules supplied from InfinityPV were subjected to a number of environmental tests conforming to the ISOS test protocols.

***Figure* 3.11** – *a) Climacell 111 - Comfort environmental chamber capable of keeping a constant temperature from 0^{O}C to 100^{O}C and relative humidity up to 100%. b) halogen solar simulator used for the execution of this experiment*

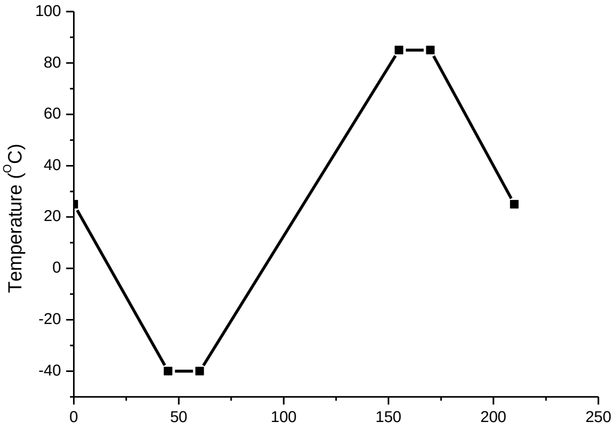

***Figure* 3.12** – *Temperature profile of a single cycle used for thermal cycle testing.*

In order to examine the degradation of OPV modules eliminating light irradiation, two dark aging studies were conducted.

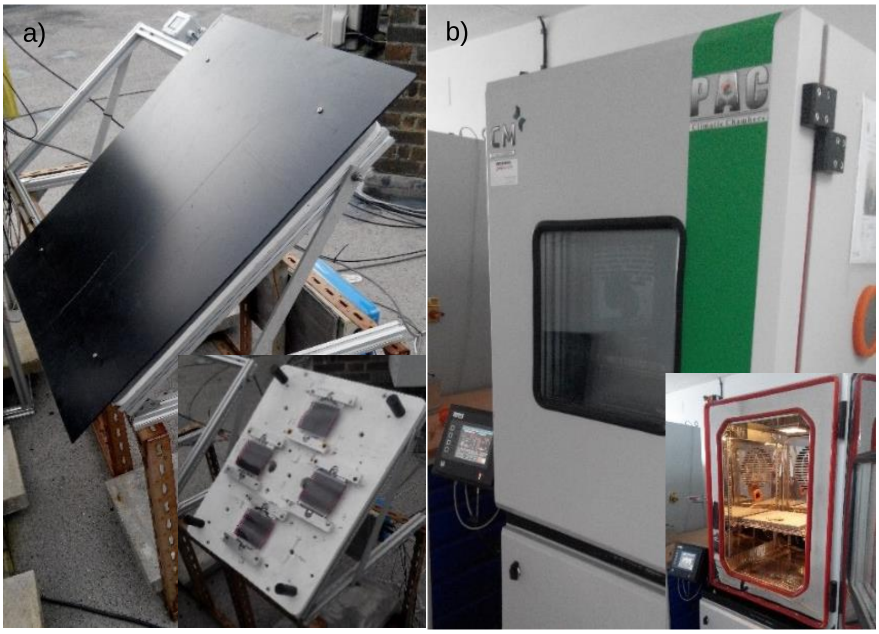

***Figure* 3.13** – *a) outdoor dark ambient aging setup capable of accommodating up to four modules for simultaneous aging. b) PAC climatic chamber used for thermal cycling of OPV modules capable of reaching -40^{O}C to 180^{O}C*

In order to define the degradation of the tested OPV modules most accurately, an in-situ setup was created composed of an environmental chamber and halogen solar simulator. The OPV modules were subjected to varying environmental conditions including all known degradation factors (humidity, thermal and solar).

To test the susceptibility of OPV modules to degradation due to thermal cycling, ISOS-T3 tests were conducted. The profile of this test for thermal cycling is shown in figure 3.12. The test condition involves cycling from -40^{O}C to 85^{O}C with a 10 minute hold time at the ‘hot stage’ and the ‘cold stage’. The thermal range, ΔT, used for this test is 125K, therefore an additional test was done using a lower temperature range of 105K, to relate degradation during test to an ‘operational’ stress level.

The first experiment involved the construction of an outdoor test facility which allows the performance of ambient humidity and thermal cycling while stopping solar degradation figure 3.13 a). The second dark aging experiment was conducted indoors where modules were subjected to a combination of humidity and thermal variables. All modules both the ones tested outdoors and indoors were collectively measured between runs at regular basis under 1 sun AM1.5G standard solar simulator.

3.6 Outdoor Measurement System at Bangor

The outdoor monitoring conducted at BU took place on the roof of the School of Electronic Engineering, Dean St., Bangor, Gwynedd (53.23°N 4.13°W), at an altitude of 40 m above sea level. The climatic averages for Bangor (sourced from the Meteorological Office for RAF Valley on Anglesey) are 14°C during summer and 4.7°C during the winter. The humidity levels are similar all year round, with an average monthly mean of 79%, an average monthly maximum of 90%, and an average monthly minimum of 61% in summer and 65% in winter. The UV indices are highly variable, with an average mean of 1.07 in the summer (average maximum of 5.45) and 0.43 in the winter (average maximum of 2.38). All our metrological and measurement equipment is located next to the monitored samples in a brick building at 2m distance from the module mounting rigs.

3.6.1 Outdoor Monitoring – Hardware

BU is one of a few institutions having a complete outdoor measurement system for 3rd generation PVs. The equipment meets ISOS-O2 [122] module testing protocol. It is built to fit up to 16 modules (with a possibility of expansion) which can be fixed to adjustable mounting racks for optimum inclination or horizontally/vertically to a building prototype structure. The readings are recorded by two 8-channel source measure units (SMU) (supplied by Botest Systems GmbH) with two 8-channel multiplexers. Two silicon irradiance sensors (supplied by IMT Solar) are used to measure irradiance. One is mounted horizontally and the other in-plane with the module mounting racks.

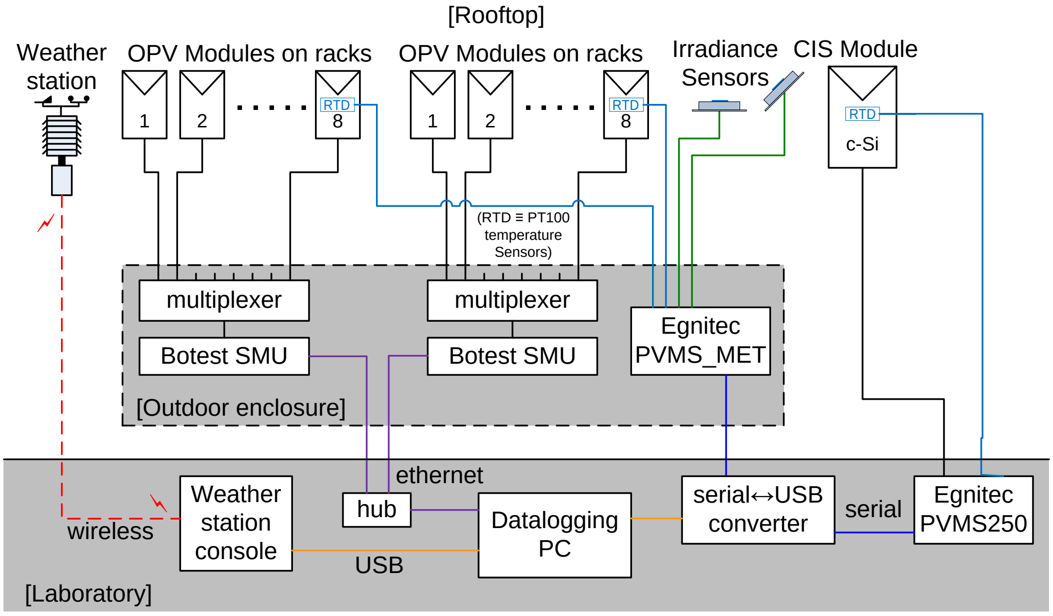

***Figure* 3.14** – *System schematic of the outdoor monitoring system on the roof of the School of Electronic Engineering at Dean Street, Bangor* [180].

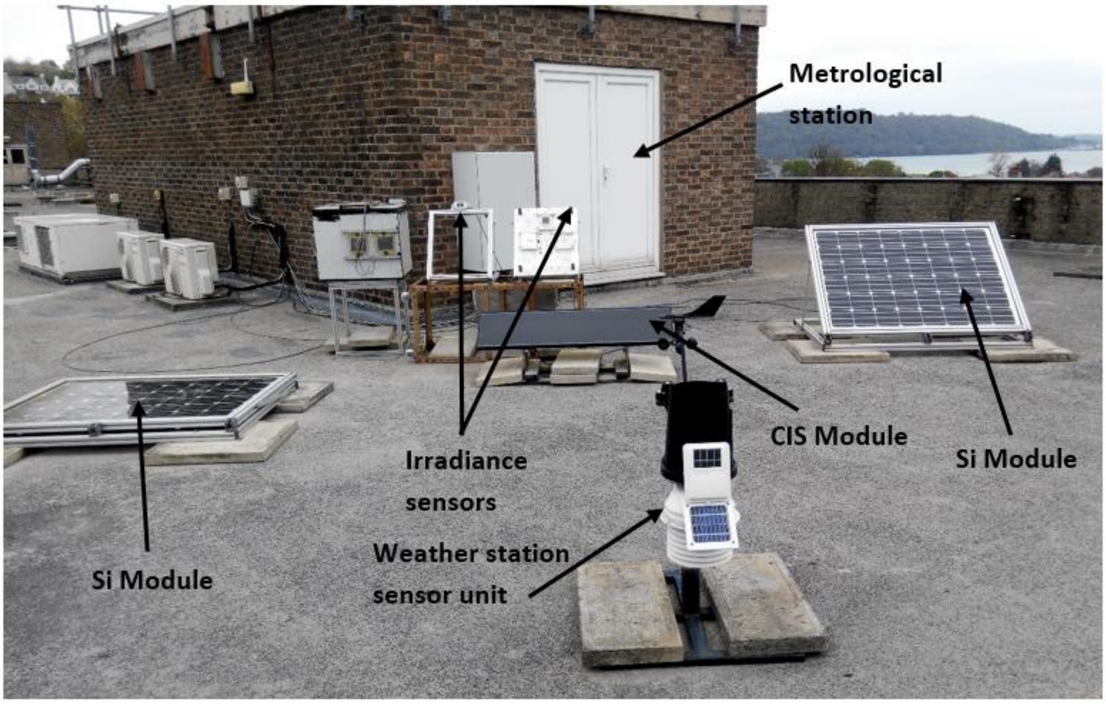

***Figure* 3.15** – *Photograph of the outdoor monitoring system on the roof of the School of Electronic Engineering at Dean Street, Bangor.*

Reference reading from two 185 W_P polycrystalline silicon modules (supplied by Pure Wafer Solar Ltd.) and one more 36 W_P copper indium diselenide (CIS) module (supplied by Shell) next to the test rig are constantly being recorded. One module is mounted horizontally and the other two inclined at 35° and facing due south. They are monitored by three PVMS-250 measurement systems (supplied by Egnitec Ltd.). Each module has a PT100 temperature sensor, attached to its backplane, monitored by the Egnitec PVMS units.

3.6.2 Outdoor Monitoring – Weather Station

The weather data is collected by a Davis Vantage Pro 2 weather station capable of recording temperature, humidity, wind speed and direction, solar radiation, UV, rainfall, and air pressure wirelessly [181]. The solar powered (with backup battery) sensor unit detects and wirelessly sends information to the console located in the metrological station. The receiver is connected to a main computer which downloads the data from the console.

3.6.3 Outdoor Monitoring – Software

There are three main software packages all operated by the main metrological computer.

The Botest SMU unit software manages the IV measurements and the recording frequency set by the user. One computer controlled all available SMU units each with a total of 8 channels. In this PhD a number of experiments were conducted where the frequency of IV measuring was taken every 15 minutes, while depending on the stability of the tested module measurements were taken at a higher frequency down to every 5 minutes. Each IV sweep takes between 5 and 60 seconds to complete depending on the start and end points, step size and pre-set delay. When not swept the OPV modules are left at open circuit.

The second software manages the records from the irradiance sensors and the Si and CIS modules connected to Egnitec PVMS_MET and PVMS250. The datalogger software linking the Egnitec units and the main computer was configured to measure current and voltage (I_{MPP}, V_{MPP}), irradiances (horizontal and in-plane) and PT100 temperature sensors once every 15 seconds. All modules are kept at maximum power point (MPP) between measurements with a 3-5 seconds IV sweep carried out once every 1 minute.

The weather station is the third software operated on the main metrological computer. It gives the user the ability to observe real time weather information updated every 10 seconds. The software stores minute to minute averages decreasing the size of the data files substantially.

3.6.4 Outdoor Monitoring – Data Analysis

The stored files from all three sources are recorded in different formats at a different recording frequency. A data organising platform in Microsoft Access was designed by Dr Noel Bristow. The database management system imports all collected data files and also extracts the performance parameters (I_{SC}, V_{OC}, FF, I_{MPP} and V_{MPP}) from the IV curves. Then the software synchronises the data from all sources end eliminates the timing mismatch to the nearest irradiance and weather record. After collating all the available data the software then calculates the individual module efficiency according to the irradiance at the given point in time.

3.7 Characterisation Techniques

3.7.1 IV Characterisation and Lifetime Testing

The IV measurements assist in the evaluation of the main performance parameters V_{OC}, I_{SC}, FF and PCE. All IV measurements processed during this PhD were recorded by one of the four available on sight SMUs supplied by Botest Systems GmbH. The IV measurements were subject to light intensity controlled by one of the used standard AM1.5G solar simulators.

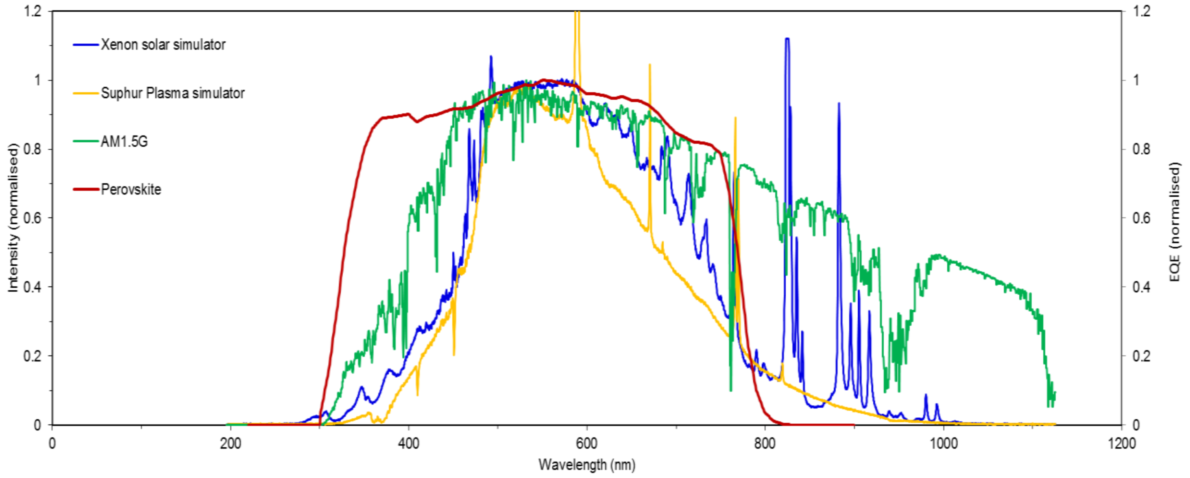

***Figure* 3.16 –** *Spectral measurement of the light sources used for light aging experiments. a) Newport solar simulator (Xenon solar simulator), b) Plasma International simulator (Sulphur-plasma), c) standard light spectra for AM1.5G at Bangor and d) the EQE measurement of $CH_3NH_3PbCl_2I$ device.*

For ISOS-L1 measurements, the Newport Oriel solar simulator was used which contains a filtered xenon bulb with calibrated irradiance at 100mW/cm^2 and a focal area of

10cm x 10cm. For ISOS L2 tests the ‘Plasma International GmbH’ sulphur-plasma source was used. Due to the spectral mismatch between light sources the measured efficiency from the tested devices was slightly different in advantage to the Newport light source which showed a slightly higher spectral response in the visible and near infrared range while the UV mismatch compared to AM1.5G is very high for both cases.

3.7.2 Indoor angular performance characterisation

Prior to outdoor testing, an OPV module was characterised for its indoor angular performance to evaluate the effect of solar angle on OPV performance. The module performance was recorded using a Botest SMU to obtain an IV measurement from which the performance parameters could were calculated.

These measurements were conducted at the School of Engineering at Cardiff University using a Lucas Nuellesolar simulator. The simulator comprises of a tilted platform and halogen light source also adjustable from 0 to 500 W. The tilting feature allows for simulation of solar path at different times of the day and of the year through adjusting the altitude and azimuth angles. The altitude (defined as the angle of the sun in the horizontal plane) is adjustable to 180° in increments of 10° where the azimuth (defined as the angle of the sun away from the normal incidence) reaches a maximum of 120° in 15° increments.

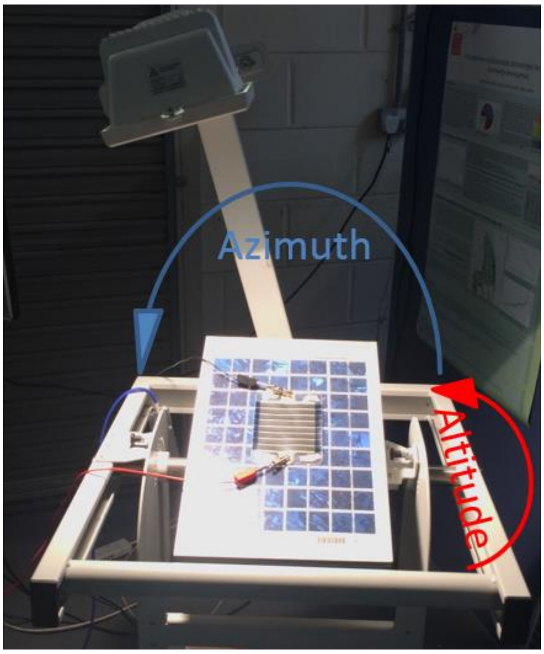

Figure 3.17 *– Lucas Nuelle solar simulator at Cardiff School of Engineering during angular test of InfinityPV OPV module*

3.7.3 Optical measurements

Photoluminescence (PL) and photoluminescence quantum yield (PLQY) measurements

The PL and PLQY for all LDS materials were measured using a Horiba Scientific Fluoromax-4 Spectro fluorometer. To obtain the absorption peak of the material its UV-Vis spectum was obtained using a Shimadzu UV-3600 spectrophotometer. Afterwards the sample was excited at the wavelength corresponding to the measured absorption peak and the PL spectrum was obtained. The PLQY was obtained by the Spectro fluorometer with connected to it integrating sphere [182].

UV-Vis Spectrophotometry

UV-Vis spectrophotometry was used in the absorption peak measurements of LDS materials (Shimadzu UV-3600 spectrophotometer) and also the absorption decay analysis of PSC and absorption layers. The Shimadzu UV-3600 spectrophotometer has three detectors with resolution of 0.1 nm and has a wavelength range of 185-3300nm. It allows for comparing against variation of references due to its dual beam feature.

The spectrometer used for in-situ absorption measurements was an HR4000 UV-Vis-NIR supplied from Ocean Optics Inc. The unit has a wavelength range of 350-1100nm. This device requires the reference to be taken prior the absorption measurement.

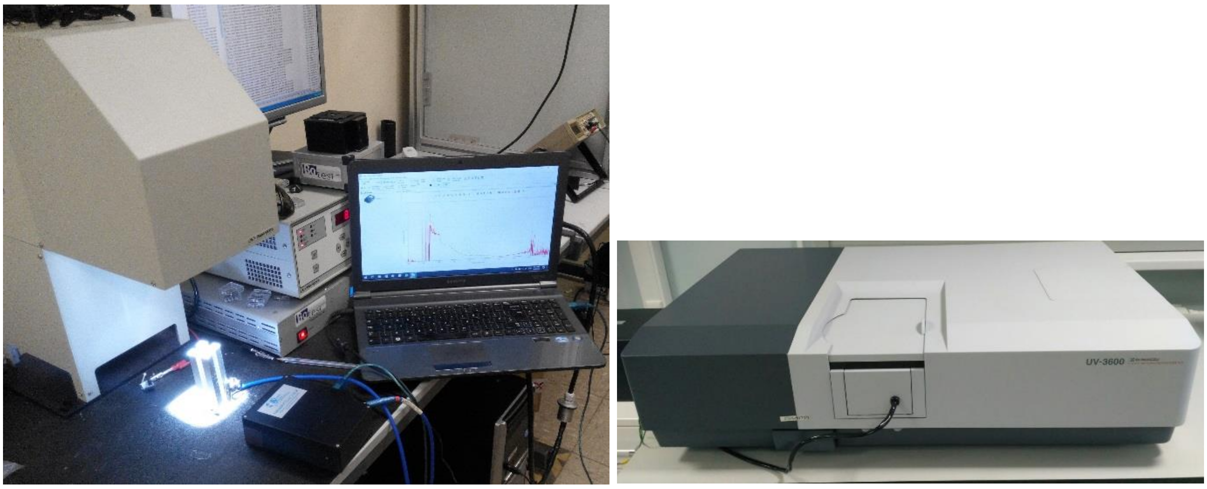

***Figure 3.18** – a) Ocean Optics HR4000 UV-Vis-NIR spectrometer and b) Shimadzu UV-3600 spectrophotometer.*

3.7.4 Atomic Force Microscopy

Atomic force microscopy (AFM) was used to measure film thicknesses by scanning across a scratch made in the layer. AFM was also used to measure average surface roughness (R_A). These measurements were performed using a Digital Instruments Nanoman V running in tapping mode.

3.7.5 Scanning electron microscopy

Scanning electron microscopy (SEM) was used to obtain high resolution surface and cross section imaging of fabricated perovskite layers. SEM was also used for its energy dispersive X-ray analysis mode which provided elemental identification and quantitative compositional information.

Chapter 4. Degradation studies of perovskite solar cells (PSCs)

4.1 Introduction

In order for PSCs to be used in outdoor environment, the indoor stability needs to be proven. This will provide some assurance of device stability prior to outdoor testing. In an outdoor environment, the solar cell needs to be stable against light, humidity and temperature fluctuations and be able to withstand many extreme conditions which are applied simultaneously. One particular stress factor is UV light, which is a known major degradation factor is PSCs [183]. In this thesis, attempts have been made to study this further. The first part of this chapter is divided into two parts; firstly indoor testing at low irradiance conducted at Bangor University, followed by accelerated degradation at high irradiance sunlight testing, conducted at Ben Gurion University of the Negev, Israel. A replacement for traditional UV filtering was then sought by adopting luminescent downshifting (LDS) layers. A number of LDS dyes were analysed and evaluated for their suitability for PSCs.

4.2 Initial performance optimisation

For the lifetime data to be relevant, the initial performance needs to be comparable to state of the art devices. Therefore, between November 2015 and April 2016, extensive material and device architecture optimisation was conducted. This was divided into optimising the absorber film and optimising the device performance. PSCs can manufactured for inverted or non-inverted devices [184]–[187], however, the focus of this PhD is on the inverted configuration. Both single step and 2-step processes were optimised.

For the 2-step process, the halide PbX_2 was dissolved in either Dimethylformamide (DMF) or Dimethyl sulfoxide (DMSO) and the organic precursor CH_3NH_3I (MAI) was dissolved in isopropanol (IPA). Two orthogonal solvents are needed for precursors and a sufficient time lapse for the first solvent to completely evaporate before the second solution is dispersed. The second layer ‘seals’ the first layer resulting in a uniform final film. After annealing for 20min at $90^{O}C$ and cooling to room temperature the sample was spin coated for a second time with (MAI) and annealed at $90^{O}C$ for another 20min. During this time the surface pigments to a dark brown colour, providing visible confirmation of the perovskite formation.

After some optimisation, it was found that the formation of high quality perovskite layers depends largely on the amount of MAI dispersed on the surface of the halide, supporting the results shown by by Lee *et. al.* [187] who show the exponential decay in cuboid crystal size with increasing of MAI concentration and with it drop in performance. It was found that proper balance of content of halide and MAI play a critical role in the performance of manufactured solar cells. In order to obtain a better understanding of the quality of the optimised fabricated perovskite film an X-ray diffraction diffractogram was taken and compared against a perovskite model diffractogram. The data in figure 4.1 shows consistency with the expected XRD diffractogram.

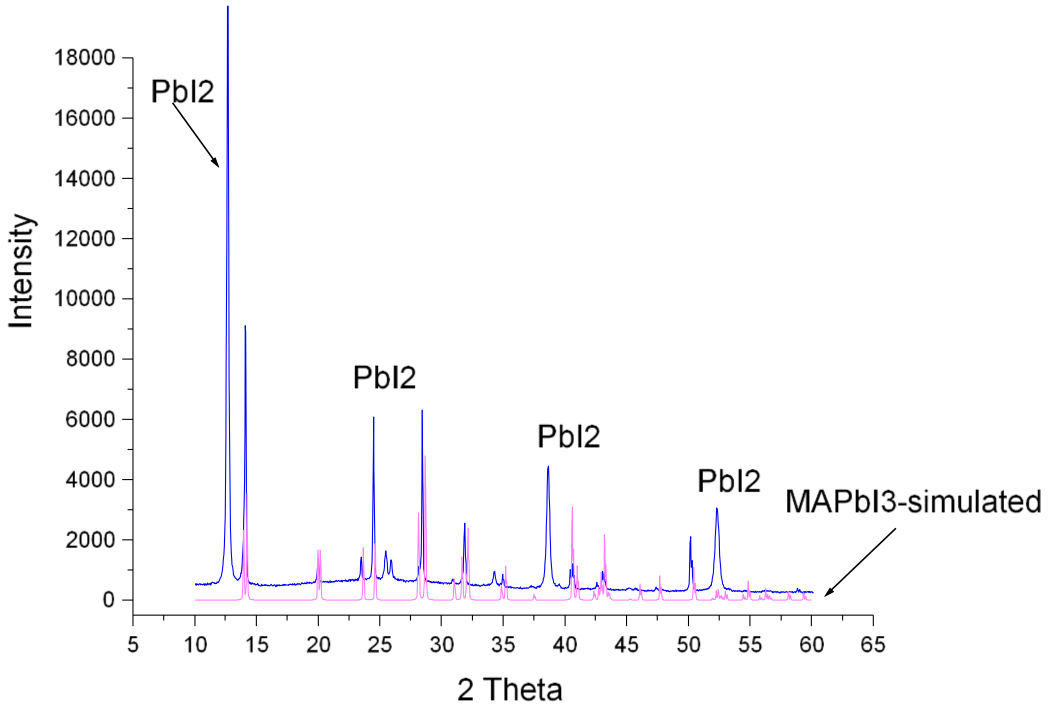

***Figure* 4.1 –** *XRD of fresh $MAPbI_3$ with marked PbI_2 peaks. Simulated XRD pattern of $MAPbI_3$ (Pink) is for comparison.*

In terms of device performance, the maximum power conversion efficiency (PCE) achieved was 10.88%. Shown in figure 4.2 is the best performing device, which show s V_{OC} = 0.88V, Jsc=16.93mA, FF =73.34%. For stability measurements, the highest efficiency is not possible to achieve for every device. Therefore, a limit was set, whereby for all stability experiments used in this thesis, devices had to display a PCE ≥10% with a maximal variation of ±1%.

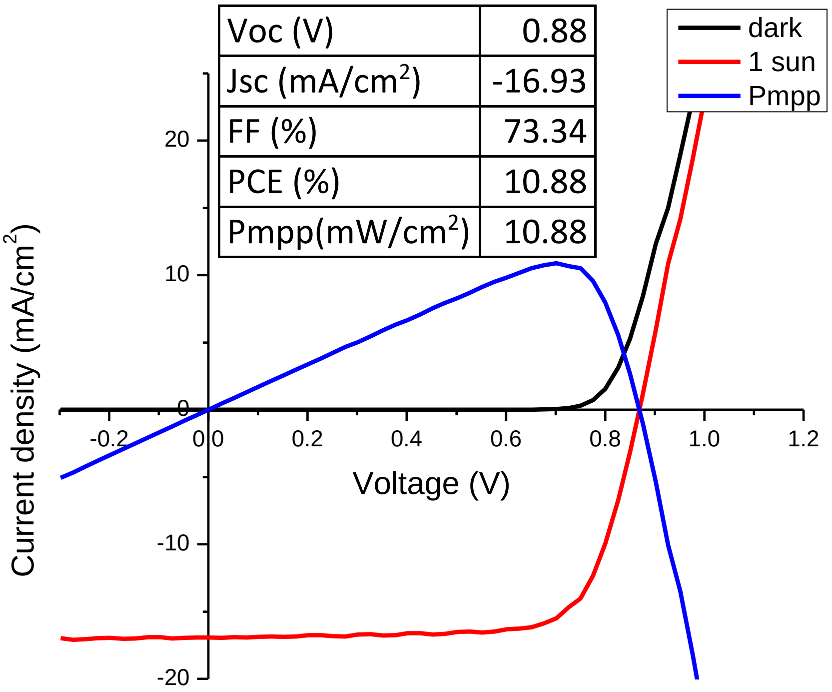

***Figure 4.2** – Dark, 1 sun and maximum power point (Pmpp) characteristics of highest efficiency solar cells manufactured during this PhD measured using a standard ABB AM1.5G solar simulator*

4.3 Effect of filtering on degradation

As the stability of PSCs is known to be low, initial studies focused on the effect of spectral filtering to improve the stability. Due to the poor stability of the devices, it was decided to focus initially on absorption measurements of films rather than device performance. In the early days of OPV development, many studies focused on using just absorption to study the performance decay. A similar approach is adopted here. Furthermore, the properties of PbI_2 are studied as it can be used in PSCs as a material that can filter out harmful portions of the solar spectrum.

Initially, two different optical filters were applied that filtered two distinct regions of the solar light spectrum. The first type of filter was a ultraviolet (UV) filter, as it is believed that most of light induced degradation is a direct result of UV photo oxidation. Further filtering was conducted with an IR filter which is supposed to reduce the temperature increase during the course of the conducted light soaking.

4.3.1 Effect of spectral filtering on the stability of $CH_3NH_3PbI_3$ Perovskite films

Initial studies to identify how spectral filtration affects perovskite film stability was conducted at Ben Gurion University. These were conducted using concentrated to 100 suns natural sunlight collected by Fresnel lens which is then guided to the sample through a fibre optic core and irradiated over the sample via kaleidoscope [95]. Photovoltaics degrade as a result to a number of factors including intensity of light, humidity and temperature[188]–[191]. These processes can be mitigated by a number of preparation techniques including addition of environmental barrier layers and UV filters[192], as well as by optimizing active layer materials to develop more robust absorbers[193] or control of grain size in the films[98], [194]. UV degradation is shown to be very significant in PSCs. Therefore, the initial studies in this work have focused upon this.

Shown in figure 4.3 is the measured transmission spectra of a UV and IR filter used in this examination. These filters were placed in between the light source and samples in order to limit the spectrum being applied to the studied active layers. Tests were conducted to ensure the filters were stable to high irradiance levels so no deterioration can be expected.

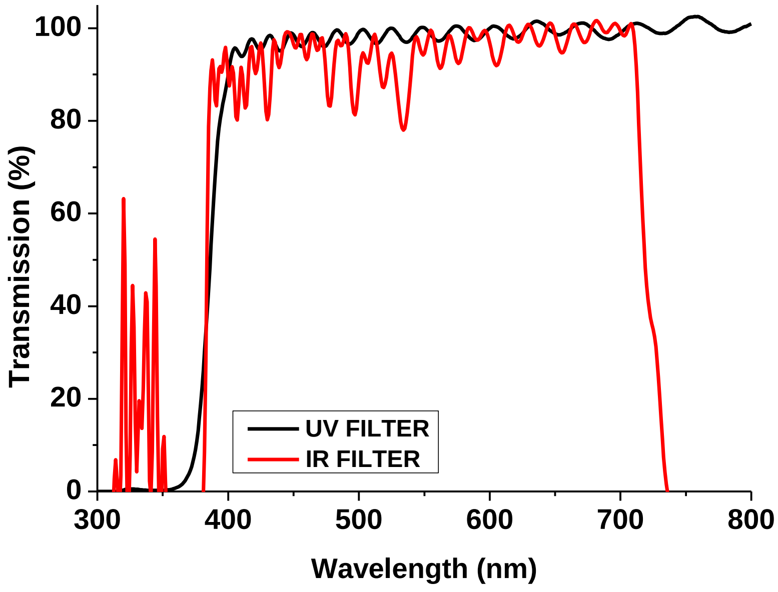

***Figure* 4.3** – *Transmission spectra of IR filter and UV filter used in this study*

Shown in figure 4.4 (a,c and f) are the absorption spectra of 2-step fabricated $MAPbI_3$ active layers as a function of time when exposed to 100 sun irradiance. The control sample indicates no filtration. The control sample saw complete decomposition with light exposure in total of 60 minutes. The stability, however, was significantly improved once an IR filter was applied where in total of 60 min exposure, the sample decayed by only 1.4% of its initial photon absorption in the perovskite region 500nm-780nm. The measured the sample temperature reduced from 100^{O}C to 77^{O}C. During these tests the samples were cooled by an active heat-sink set to 25^{O}C. Almost complete suppression of photo degradation was achieved by the application of a UV filter which retarded the degradation to 0.35% in 60 minutes of light soaking at 100 suns concentrated natural sunlight. The results support the studies of Snaith *et al.* [94], Donghwan Kim *et al.* [195] and Yong Qiu *et al.*[196].

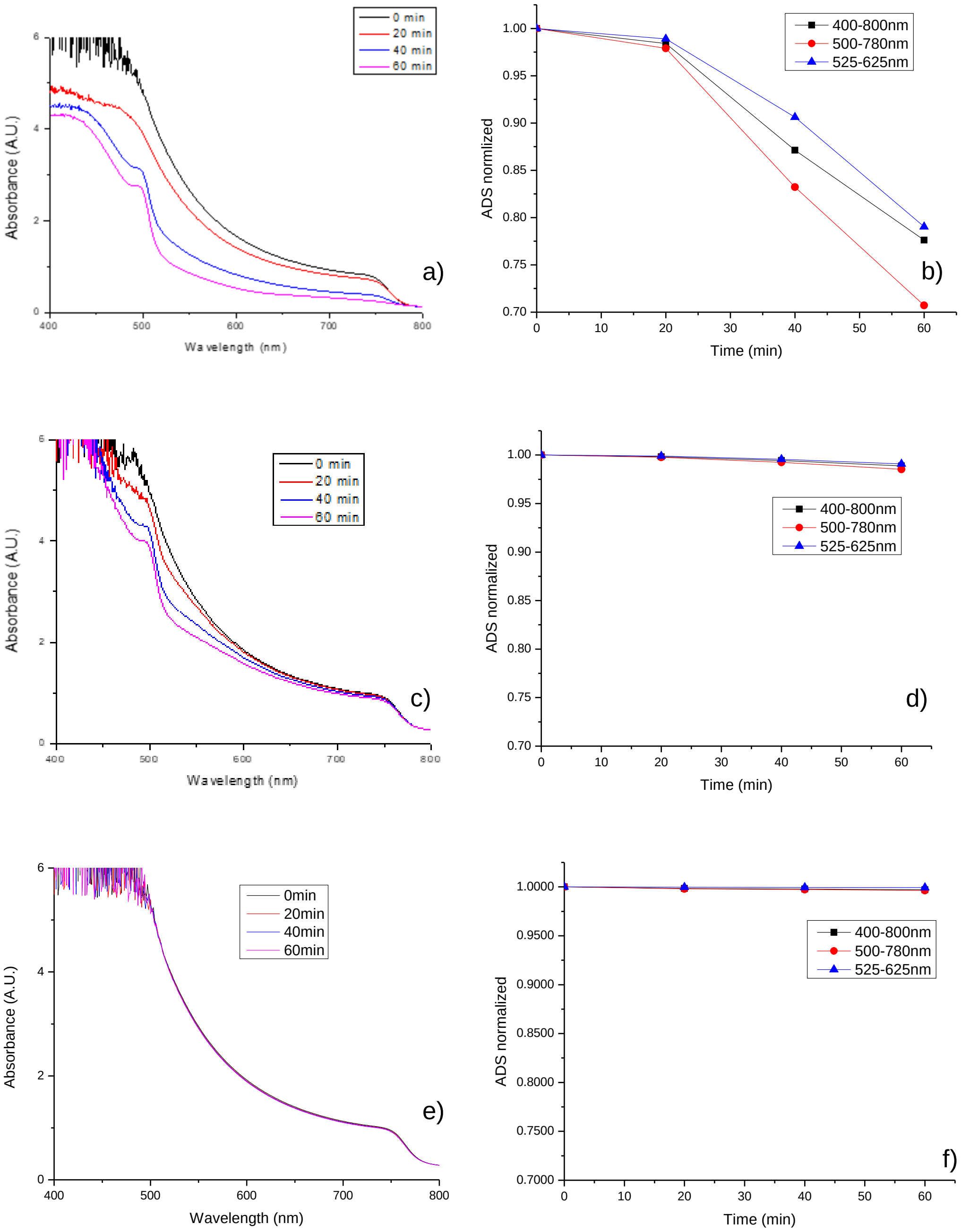

***Figure 4.4** – a) absorption degradation graphs of control sample, b) with IR filtered and e) UV filtered e). (b,d and f) present the calculated ADS decay of the samples in total of 60 minutes.*

The data shown in figure 4.4 d-f) was calculated using the Absorption Degradation State (ADS) method [98]. This method was used to quantify the degradation of the optical absorption spectra of perovskite materials subjected to means of spectral filtration compared to control samples. The ADS calculation is described by Misra et al. [95], [98] and it determines the ratio of absorbed photons by a fresh film to an aged measured under standard AM1.5G solar simulator. The data confirms that most of the absorption lost at higher solar irradiance is due to perovskite decomposition to PbI_2. As shown in figure 4.4 b) the perovskite region 500-780nm decays with the highest magnitude. The PbI_2 region 525-625nm is more stable showing continuous loss in iodide which can be seen from figure 4.4 a) and the pronunciation of the peak at 500nm (Pb).

4.3.2 Effect of spectral filtering on the performance of $CH_3NH_3PbI_3$ Perovskite devices

In section 4.3.1, the positive effects of UV filtering to ensure stable perovskite films was shown. This section demonstrates the effect of spectral filtering on the performance of PSCs under 1 sun AM1.5G irradiation. Figure 4.5 shows the current density-voltage curve of PSCs under AM1.5G simulated sunlight with 100mW/cm^2 of irradiance for devices without filtration and with a commercial UV and infrared (IR) filter. The values for the electrical performance parameters of the cells are shown in Table 4.1.

Parameter	**AM1.5G (no filter)**	**with UV filter**	**with NIR-IR filter**
V_{OC} (V)	1.022	1.021	1.03239
I_{SC} (mA)	0.856	0.723	0.63244
FF	0.745	0.735	0.73274
PCE (%)	9.31	7.76	6.83465

***Table* 4.1** – *Electrical parameters of cells exposed to 1 sun irradiance without spectral filtration, with a commercial UV filter and with NIR-IR filter. The results are an average value from six devices.*

As observed, the use of the UV and IR filter leads to a decrease in the I_{SC} value, which results in lower PCE when compared to the device without filtration. The drop-in performance when compared to the reference device is to be expected as PSCs have a high spectral response between 300 and 800nm. Shown in figure 4.3 is the spectral ranges of the filters and it is clear that both the UV and IR filters cut-off part of the photo-spectrum. Therefore, the application of filters will limit the photo current that is generated in the PSCs spectral response region and this accounts for the drop.

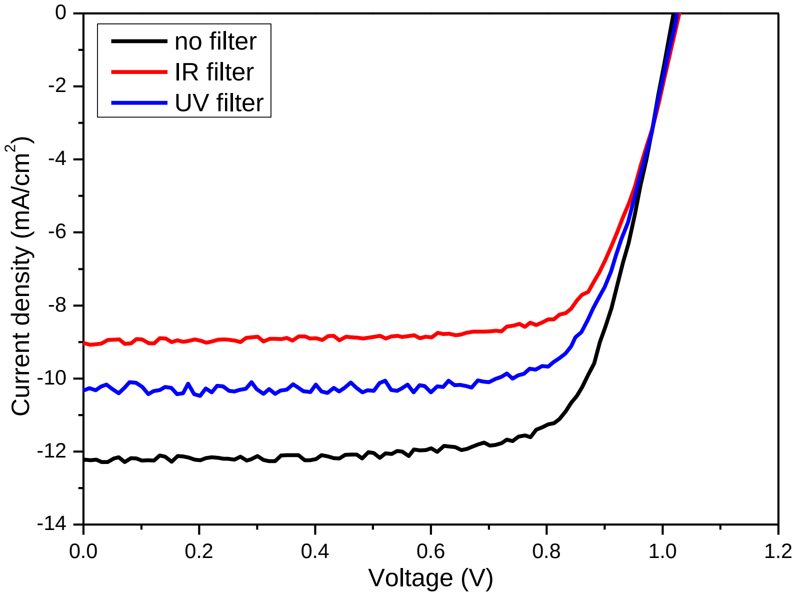

***Figure* 4.5**– *Current density-voltage plots for perovskite-based devices under 100 mW/cm^2 AM1.5G simulated sunlight. The temperature of the devices was maintained at 60 °C during all measurements*

4.3.3 Effect of spectral filtering on the stability of $CH_3NH_3PbI_3$ Perovskite devices

In section 4.3.1, it was clear that by adding a UV filter, the stability is increased, although section 4.3.2. shows the PSC performance decreases. Furthermore, adding an NIR-IR filter, figure 4.6 does not improve the long-term stability significantly. Optical filtering appears to decelerate degradation in the initial 2 hours after exposure, after which the decay returns to the same degradation trend as the non-filtered device. It is believed that the deceleration of the degradation initially is due to the broader light barrier the NIR-IR filter presents, figure 4.3, which filters some of the UV light as well as the longer wavelengths. However, the NIR filter reduces the thermal degradation of the device by limited IR transmission into the sample, which improves the stability of the perovskite devices. Figure 4.6 shows the evolution of the electrical parameters (I_{SC}, V_{OC}, FF and PCE) with exposure time under AM1.5G illumination. It is clear that UV filtering significantly improves the longevity of the devices. For example, after 30 hours of exposure without filtration to the sunlight, the PCE of the unfiltered device decreases to around 10% of the original value, whereas for the devices with a UV filtering layer the PCE value was around 60% of its initial value. The NIR-IR filtration had some initial positive effect after which the device dropped to degradation state. This work supports Reynaa *el al.* [101] who show a total of 72 hours lifetime on PSC devices without UV filtration and also Abdelmageed *et al.* [197] who demonstrate the abrasive effect of elevated surface temperature.

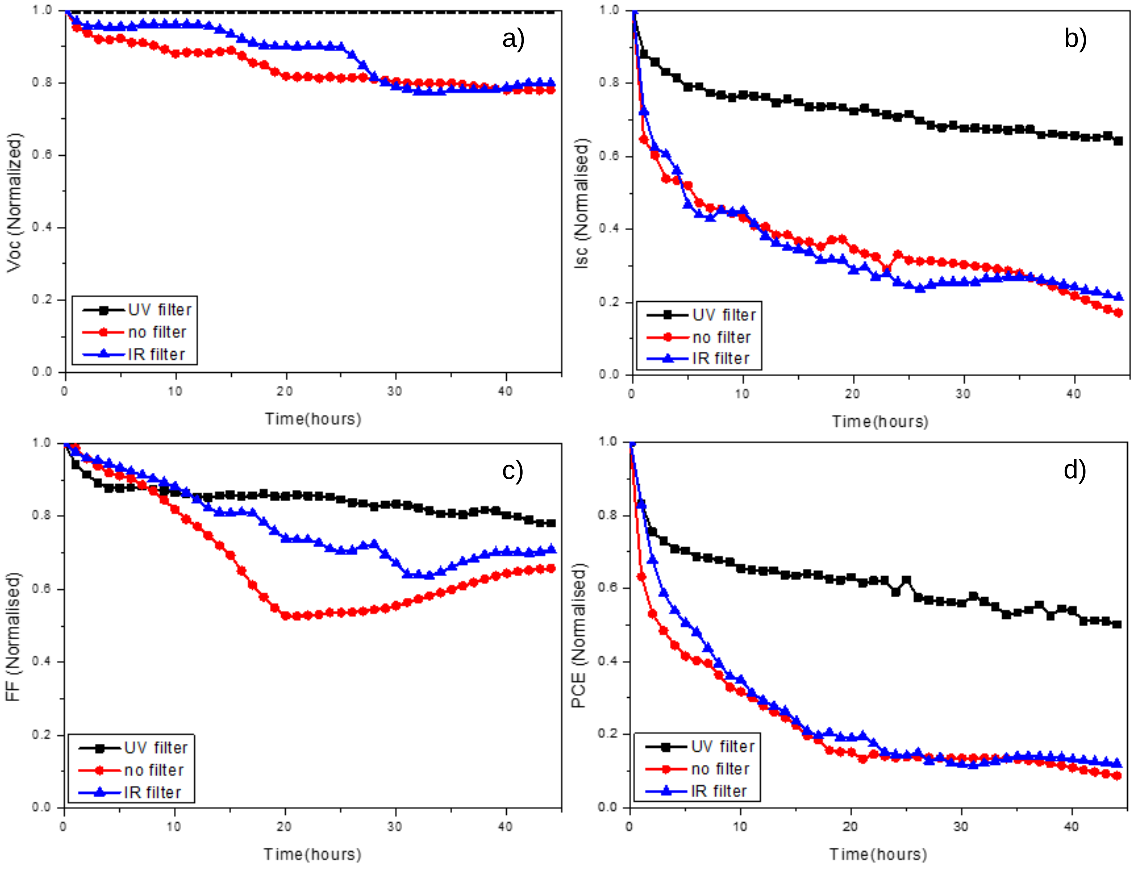

***Figure* 4.6** – *Evolution of electrical parameters with irradiation time (AM1.5G) for devices without filtration and with UV and IR filter: a) open circuit voltage, b) short-circuit current, c) fill factor and d) PCE. The temperature of the devices was maintained at 60 °C during all measurements*

4.4 Effect of 1-step and 2-step process on stability

The initial studies in section 4.33 show some rapid degradation of the absorber film. To improve the stability, initially the impact of one and two step deposition processes was studied. Both one step and two step fabricated perovskite films were prepared and examined for this experiment.

4.4.1 Effect of one step and two step process on stability of $CH_3NH_3PbX_x$ layers with illumination from 'light facing side'

The degradation of encapsulated one step and two step $CH_3NH_3PbI_3$ Perovskite films using concentrated sunlight was studied, figure 4.7. Both films show grain sizes of 400-1000 nm, figure 4.8 a-b), nevertheless, one step deposition produces a final surface abundant in pinholes where in contrast using the two step technique, the surface is very uniform with no visible pores.

The absorption spectra of fresh $CH_3NH_3PbI_3$ films prepared by both methods had an absorption edge close to the $CH_3NH_3PbI_3$ band gap at 780 nm. It has to be noted that the two step fabrication process resulted in films with significant absorption at 500nm with increasing effect approaching the shorter wavelengths which can be speculated is due to the remnant unreacted PbI_2 under the formed perovskite layer which on the other hand cannot be accounted by assessing the absorption spectra of prepared by one step fresh sample.

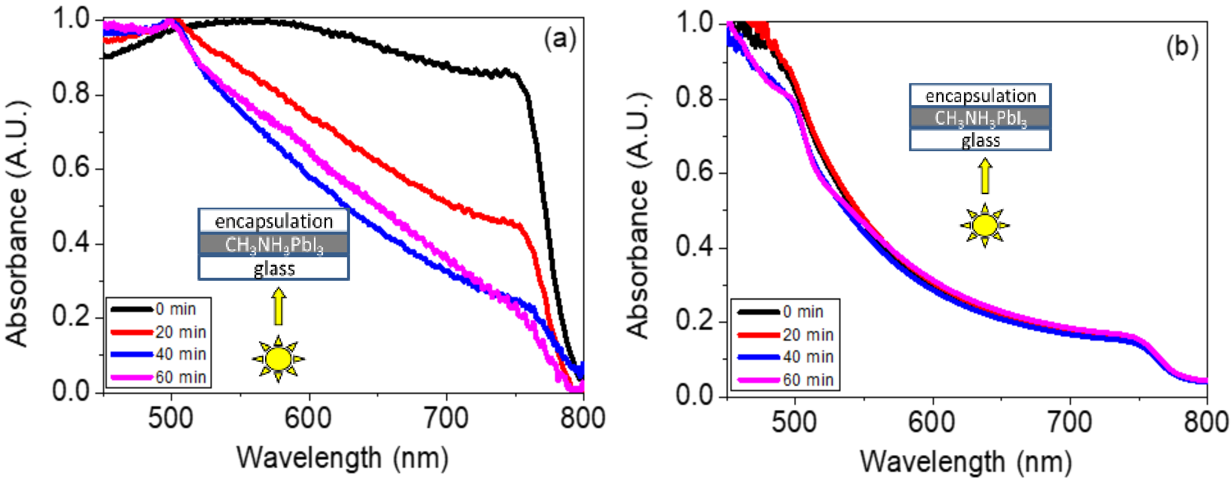

Figure 4.7 *– a) UV-vis absorbance spectra of encapsulated $CH_3NH_3PbI_3$ films fabricated by one step and b) two step-deposition techniques, for different exposure times at 100 suns; Insets illustrate the illumination method applied in this experiment*

The degradation of the produced films using both techniques was analysed using ADS as a function of exposure time to 100 suns concentrated sunlight where the light dose is proportional to the intensity.

After 20 minutes and for a total of one hour of light exposure the one step fabricated film showed a significant drop in absorption in the wavelength range from 500-780nm, figure 4.7 a), which is attributed to $CH_3NH_3PbI_3$ degradation and increase in the absorption from 500-

400nm which on the other hand is attributed to the exposure of PbI_2 which is left remaining on the surface after the decomposition of perovskite.

In comparison the film obtained by two step deposition showed around 10% drop in absorption in the wavelength range from 500-400nm in total of 60 minutes exposure and almost no change in the perovskite absorption region 500-780nm.

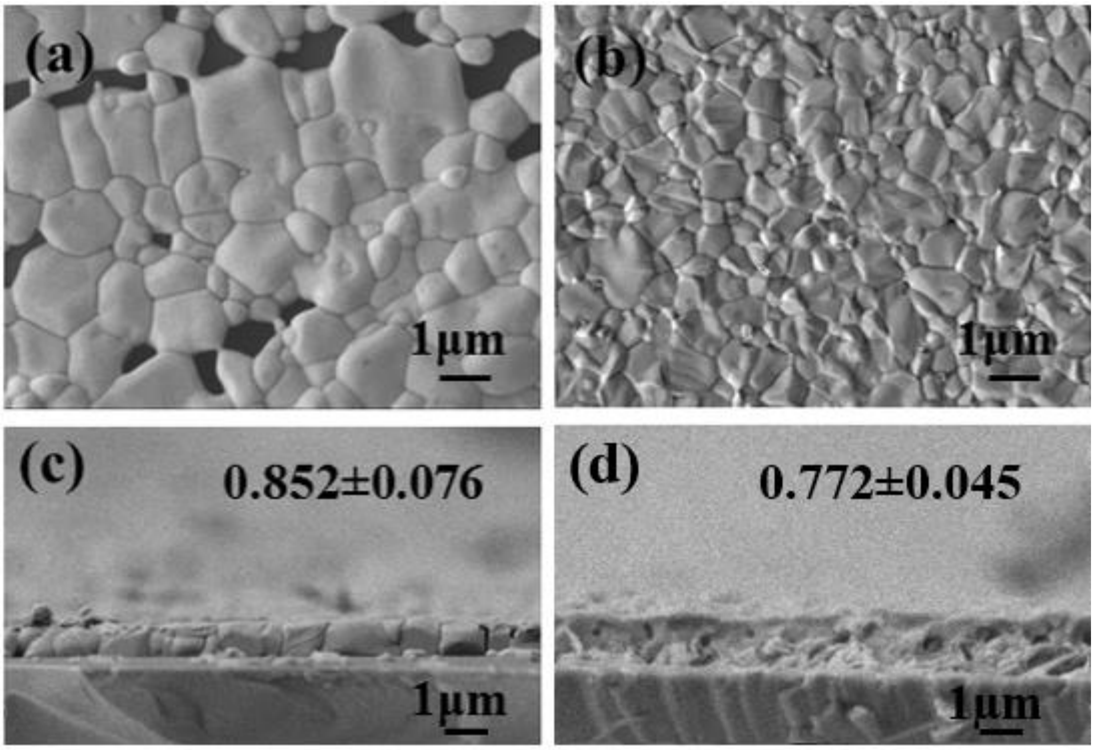

Figure 4.8 – *SEM images of fresh $CH_3NH_3PbI_3$ films obtained through one step (a, c) and two step (b, d) deposition methods in top and cross-section views.*

4.4.2 Effect of 1-step and 2-step process on stability of $CH_3NH_3PbX_x$ layers with illumination from 'non-light facing side'

In order to verify the hypothesis that the residue halide responds as an active UV filter both one step and two step fabricated perovskite films were subjected to 100 suns light exposure through the opposite side of the bulk, figure 4.9. As a result in the first 20 minutes after initiation of the experiment the two step deposited sample reached approximately 50% of its initial absorption value in the wavelength range from 500-780nm which developed to full decomposition and exposure of the underlying PbI_2 layer in the next 20 minutes of continuous light irradiation. At the same time the one step sample remained almost identical, to the previous experiment, degradation pace.

The formation of PbI_2 following exposure to 100 suns was further confirmed by SEM and XRD studies. EDS showed a transition of the I/Pb ratio from 2.5 before exposure to 1.8 after exposure, showing increased presence of Pb at the surface, confirmation by SEM imaging showed sharp smaller crystals typical of PbI_2, figure 4.10 a-b). In agreement with the results by *Misra et at.*[98], [165] the XRD revealed decreased peak intensities of $CH_3NH_3PbI_3$ compared to PbI_2 peak intensities after the exposure, figure 4.10 c-d). Qualitatively similar differences were noted in exposed *vs* non-exposed films of both synthesis methods.

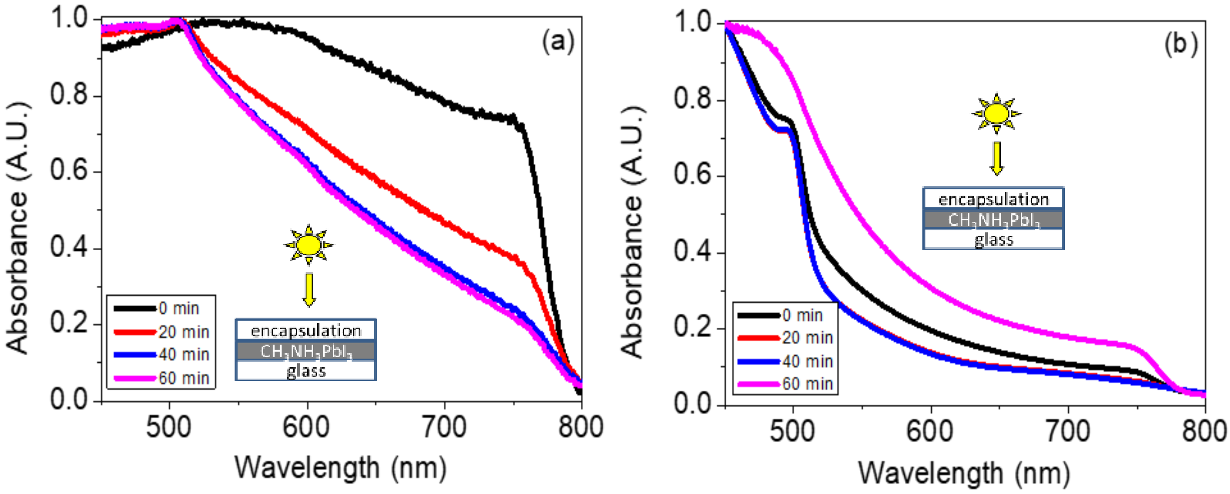

***Figure* 4.9** – *UV-vis absorbance spectra of encapsulated $CH_3NH_3PbI_3$ films synthesized by a) one step and b) two step deposition techniques for different exposure times to 100 suns illuminated through the encapsulation slide. The insets depict the illumination direction in this experiment*

One step deposited perovskite films showed a significant absorption loss when exposed to light where the films obtained through two step deposition showed negligible photo bleaching. The results obtained by the light degradation study conducted on two step fabricated perovskite films show that remnants of unreacted PbI_2 performed as a UV filter and reduce ultraviolet light-induced degradation. The results obtained reveal the significance of preparing perovskite devices using two step fabrication method.

The perovskite film and device lifetimes were found to depend on its composition and morphology [10]–[13] therefore, the deposition method is expected to affect the stability via determining the film morphology. The two step deposition method frequently results in unreacted PbI_2 layer under the formed $CH_3NH_3PbI_3$ due to diffusion limitations imposed by the growing perovskite film at the PbI_2 surface.[198] Remnant PbI_2 can also be found throughout the perovskite film due to initial degradation during inadequate fabrication process or local stoichiometric deviation even at one-step deposition.[201]

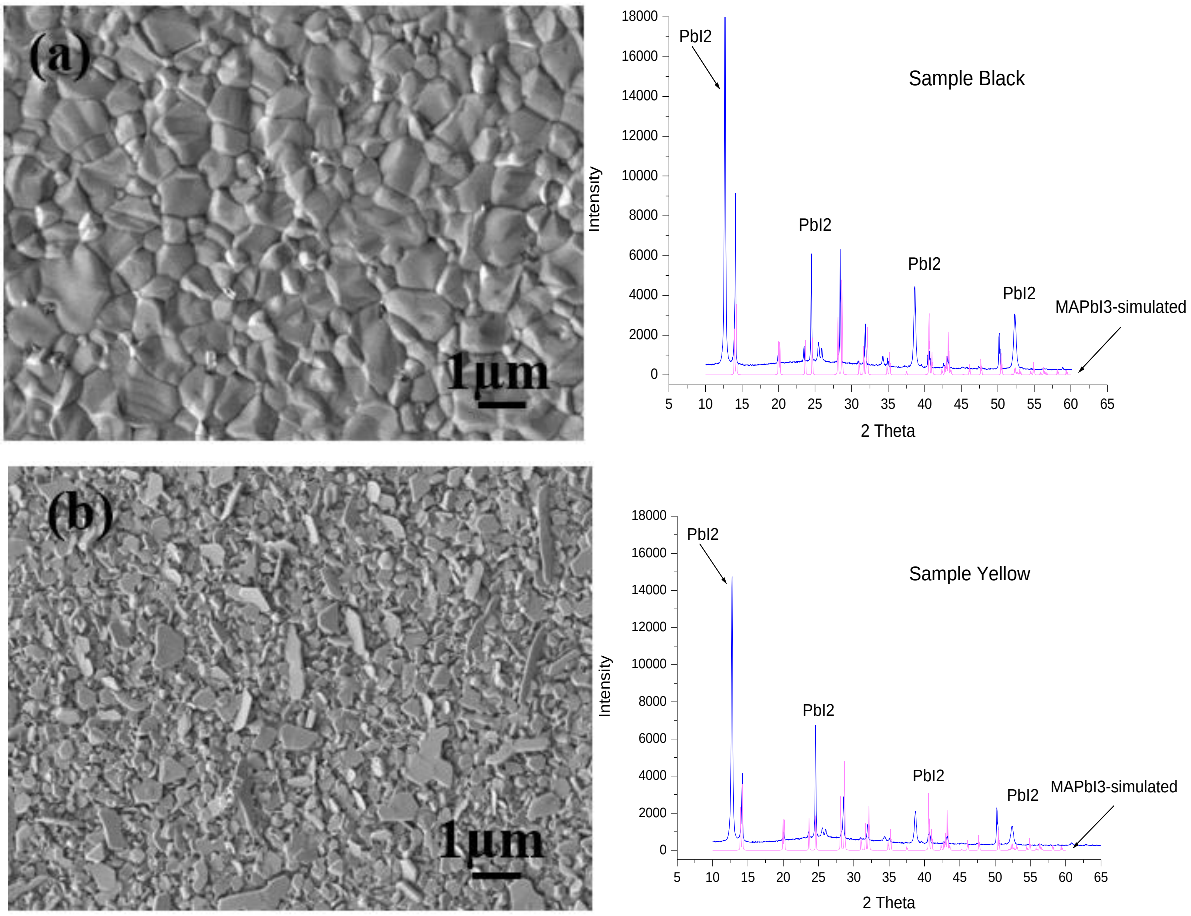

***Figure** 4.10 – SEM images in top view a-b) and XRD diffractograms of $CH_3NH_3PbI_3$ deposited a) by the two step method in areas non-exposed and b) exposed to 100 suns for 60mins. The experimental diffractograms (blue) are compared to simulated $CH_3NH_3PbI_3$ diffractograms (pink) to identify PbI_2-related peaks*

4.5 Examination of the impact of residue PbI_2 on photo-stability of $CH_3NH_3PbX_x$ layers

With two step perovskite deposition there is always a portion of unreacted PbI_2 under the formed $CH_3NH_3PbI_3$ which can be referred to as being diffusion limitations as a result of the growth of the perovskite film at the PbI_2 interface [198]. Unreacted PbI_2 can also be found throughout the perovskite film due to initial degradation during poor fabrication process or local stoichiometric deviation even at one-step deposition [201]. PbI_2 presence was found to have a positive effect on the efficiency of devices due to passivation of grain boundaries and/or the TiO_2 surface [201]. PbI_2 role as a charge selective layer was also suggested [202], [203] while if too thick it may block the desirable charge transfer [204]. However, the effect of unreacted PbI_2 on the material degradation is not well examined.

In this study, the presence of PbI_2 was found to have a positive effect on the photo-stability of $CH_3NH_3PbI_3$ films where the stability of films fabricated by the one step and two step deposition techniques was compared. The effect of illuminating by concentrated sunlight through the unreacted PbI_2 layer compared to direct illumination through the formed $CH_3NH_3PbI_3$ was examined.

4.5.1 Absorption measurements of PbI_2

A UV filter purchased from Solaronix, Switzerland, was applied onto a glass slide and its transmission spectra was taken. The results were then compared to the transmission spectra of only lead iodide spin coated onto glass, shown in figure 4.11. It became evident that the reason for the remarkable degradation difference depending on sample orientation, in the case of two step deposition, is due to the fact that the PbI_2 layer is demonstrating a negligible transmission of wavelengths shorter than approximately 500 nm and no transmission below 400nm which replicate fully the function of a UV filter.

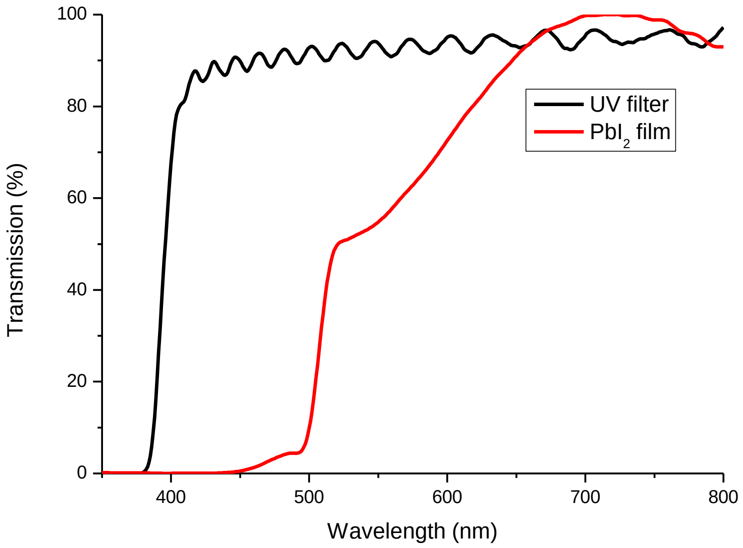

***Figure** 4.11 – Transmission spectra of a) PbI_2 film of ~200 nm thickness and b) the UV filter used in this study*

4.5.2 Comparison of the UV filtering effect of PbI_2 on one step and two step deposited perovskite with illumination from both sides of the samples

To test this hypothesis, exposure to concentrated sunlight was carried out in the presence of the used for the transmission analysis UV filter. As expected, the presence of the UV filter eliminated almost entirely the absorption degradation of $CH_3NH_3PbI_3$ fabricated in both deposition methods when illuminated from either the side of the sample, figure 4.12. There was no evident photo-bleaching taking place in all cases which leads to the conclusion that primarily the degradation of perovskite active layers is due to the presence of UV light during light exposure.

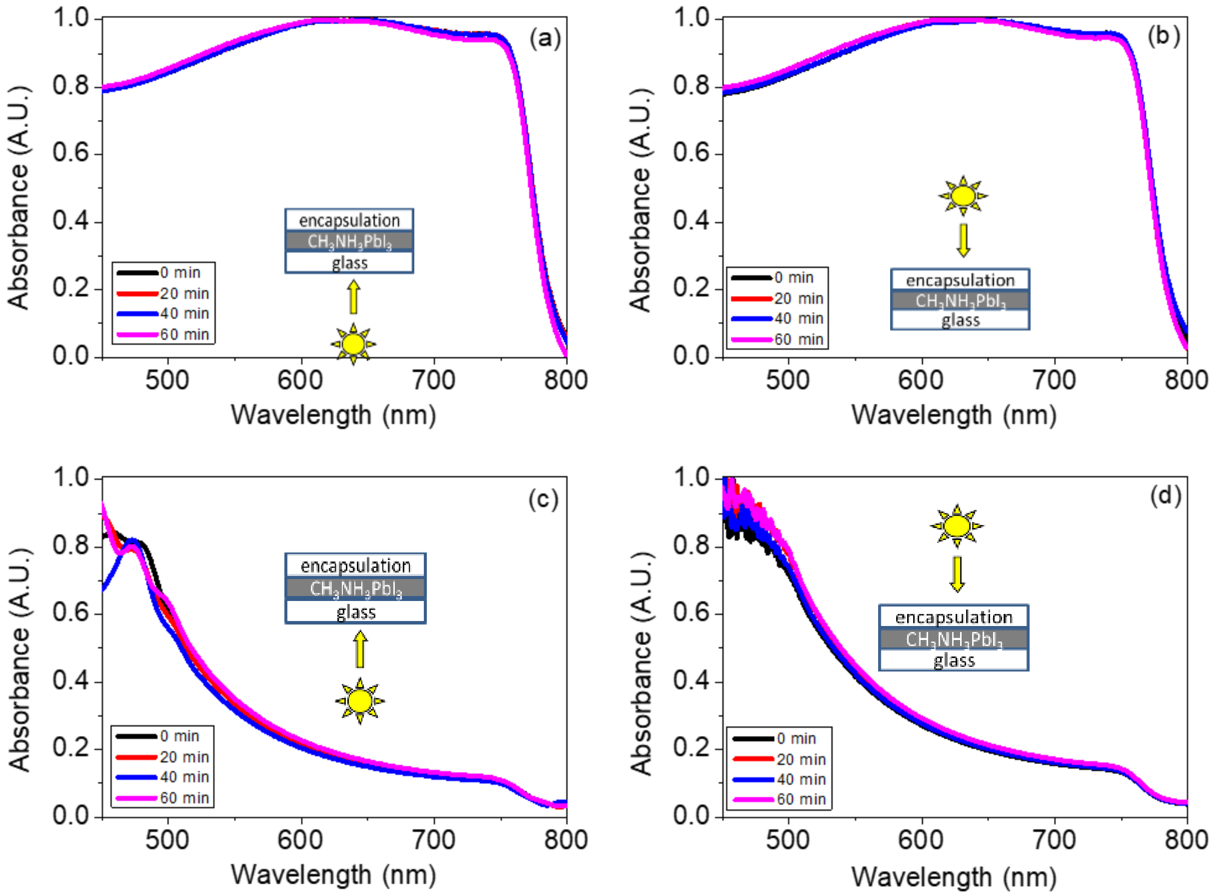

***Figure* 4.12** – *UV-VIS absorption spectra of encapsulated $CH_3NH_3PbI_3$ films synthesized by a-b) one step and c-d) two step-deposition techniques after illumination by 100 suns in the presence of a UV filter placed in front of samples as a barrier to UV rays. The samples were illuminated through the substrate a-c) and through the encapsulation slide b-d)*

In order to obtain a better knowledge and verify the presence of unreacted PbI_2 at the bottom of the formed perovskite, serving as a UV filter, a grazing and rotating angle XRD measurements were applied. Grazing angle diffractions are expected to be more surface sensitive than the rotating angle measurements and less sensitive to species buried far from the surface, such as the suspected PbI_2 layer in two step deposited $CH_3NH_3PbI_3$. The result from the diffractograms obtained by the $CH_3NH_3PbI_3$ films prepared by two step deposition showed intense PbI_2 peaks where those obtained from the perovskite films prepared using one step method show very weak readings figure 4.13.

For the case of two step $CH_3NH_3PbI_3$ perovskite films, the grazing angle diffractogram showed the PbI_2 (001) peak at $2\theta=12.6^o$ at almost equal intensity to the $CH_3NH_3PbI_3$ (110) peak at 14.1^o, while the rotating angle diffractogram showed smaller $CH_3NH_3PbI_3$ (110) peak than the PbI_2 (001) peak, figure 5.16 c-d). This difference points to larger content of PbI_2 buried away from the surface, proving the presence of PbI_2 layer below the formed perovskite.

The data obtained by the one step deposition showed negligible differences between the grazing angle and the rotating angle diffractograms, figure 4.13 a-b) indicating low PbI_2 content, which is homogeneously distributed as a function of distance from the film surface.

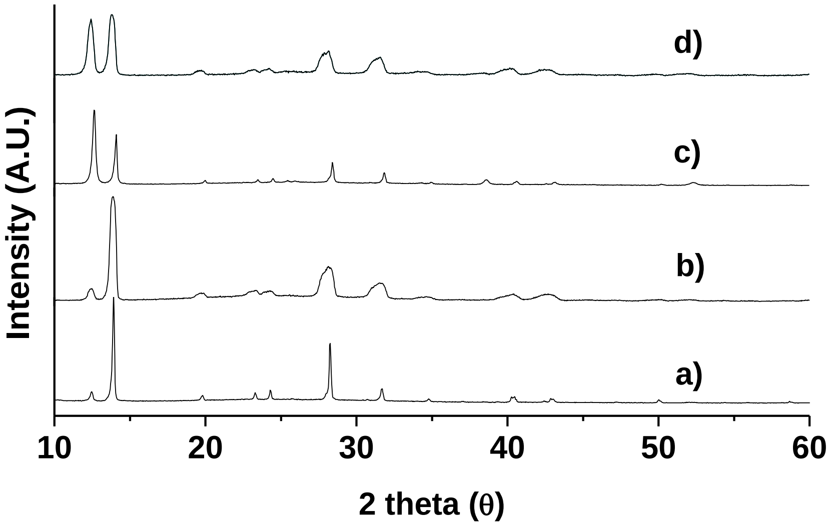

***Figure* 4.13** – *(a,c) Rotating and (b,d) grazing angle XRD diffractograms of $CH_3NH_3PbI_3$ films obtained by (a, b) one step and (c, d) two step deposition*

4.5.3 Decoupling light intensity and temperature with concentrated sunlight

The temperature measurement of $CH_3NH_3PbI_3$ films under exposure to various sunlight intensities [205] was measured to study the impact of light degradation by remnant PbI_2 layer and to rule out temperature differences as the main degradation factor. Since heating of the absorbing layer under sunlight exposure is induced mostly by thermalisation of photons with energies larger than the absorber's band gap [205], significantly larger dose of the absorbed photons is expected to increase the sample temperature.

The results showed no significant difference between the temperatures of the illuminated $CH_3NH_3PbI_3$ films prepared by the one step and two step deposition methods, figure 4.14

indicating that the unreacted PbI_2 film is so thin that it cannot stop the sample from heating up by the propagated light of the solar concentrator.

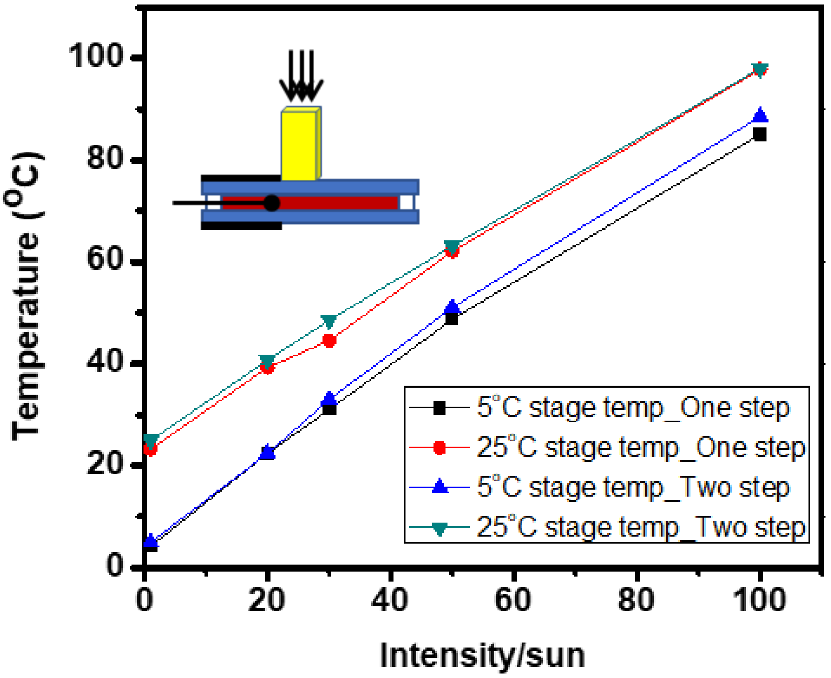

***Figure** 4.14 – $CH_3NH_3PbI_3$ temperature vs light intensity of films prepared by one step and two step deposition when the sample stage was set to 5^{O}C or 25^{O}C. Inset illustrates the schematic description of the experimental setup for temperature measurements.*

4.5.4 Analysis of degradation studies

The stability of perovskite has been addressed in a number of reviews [191], [206], [207]. The relevant factors that are already established as main in the decomposition of perovskite are moisture, oxygen, UV radiation, and temperature. In this thesis, there was only time for one factor to be studied, in this case UV light. However, by eliminating this, it is clear that degradation is significantly reduced. After 240 min of irradiation at 100 sun, the ADS of the film under with UV filter drops to only around 90% of the original value, thus, providing evidence that the use of UV filters can be an effective strategy to increasing the lifespan perovskite absorber layers.

The effectiveness of UV filtering may affect the degradation pathways. Firstly, it can reduce the formation of oxygen atom radical and/or ozone which attack the perovskite layer by limiting the UV inside the films [94]. In this case, the light and oxygen induce the formation of halide anions through donation of electrons to the surrounding oxygen. The anions generate free radicals that deprotonate the methylammonium cation and form the highly volatile

CH_3NH_2 molecules that escape and leave pure PbI_2 behind [196]. This degradation pathway is supported by the data in figure 4.9 b) where the formation of PbI_2 is seen with the absorption peak. Secondly, UV excitation is known to lead to photolysis which creates organic breakages.

4.6 Application of luminescent down shifting layers to PSCs

This section examines an alternative strategy to optically enhance the performance of PSCs by the application of LDS layers. This can have two impacts: improving the performance of the devices under solar irradiation and extending the lifetime by cutting UV light. The first situation is improved by increasing the performance over the range of wavelengths where light can be harvested. Extending the lifetime is usually achieved by filtering the ultraviolet spectra which prevents UV propagation and extrinsic degradation caused by photo-oxidation, as demonstrated in the previous section. As discussed in section 4.5, UV filtering has a very positive effect on the stability of PSC absorber films. UV filtering can also be achieved by the use of LDS layer which does not only filter a section of the light spectrum but also down-shifts the light, in this particular case UV to visible region, where it is being reabsorbed by the underlying layer as a result improving the photo conversion performance of the devices.

This work (and the remainder of the thesis) was conducted in Bangor University and compliment the studies undertaken in BGU, Israel.

4.6.1 Selection of LDS

A series of luminescent materials were evaluated from a previous study according to an optimization process reported by Fernandes/Stoichkov *et al.* [144]. In this thesis, a range of 10 LDS materials were studied, from metal complexes to organic dyes. The relevant aspects to considering the LDS application of the materials were their optical properties, processability, commercial availability and cost effectiveness. Table 4.2 shows a range of performance parameters used to assess the optimum LDS layer. The detailed definitions of the performance parameters are listed below [144]. The performance parameters used for this systematic study are as follows.

***Radiative Overlap (RO)**: A measure of the overlap between the absorption and Photoluminescence. The calculated figure (RO) is the proportion of emitted light which will be reabsorbed by the dye itself and for an ideal material will be 0%.*

***UV Coverage (UV)**: This is defined as the fraction of incident light, within the UV region (300-400nm), which is absorbed by the LDS layer and prevented from reaching the solar cell. Ideally this figure will be high providing the cell with good UV filtering.*

***Photoluminescent Quantum Yield (PLQY)**: This is a measure of the efficiency of the luminescent material and is the proportion of absorbed photons which will be emitted.*

***Absorption Spectral Matching (ASM)**: This is a measure of how well the LDS layer absorbs photons which are not utilised by the solar cell. Ideally this will be 100%.*

***Parasitic absorption (PA)**: This is a measure of the absorption in the region where the solar cell performs well. Ideally this will be 0%.*

***Emission Spectral Matching (ESM)**: This is a measure of how well the photoluminescence of the LDS material matches with the solar cell. Ideally this will be 100%.*

***MATCH**=PLQY’ + UV’ + (1-RO’) + ASM’ + ESM’ + (1-PA’)*

The calculations of the FOMs were based on absorbance and photoluminescence (PL) spectra of the PMMA:KB layer, and on the External Quantum Efficiency (EQE) curve of the perovskite-based device, as shown in figure 4.16. PL was measured with a Horiba Scientific Fluoromax 4 spectrofluorometer, with excitation at 375 nm (at the maximum of optical absorption of the layer). EQE spectra were recorded using a Bentham TMC300 monochromator, with measurements taken every 1 nm using a Stanford Research System SR830 lock-in amplifier.

The LDS material was dissolved with PMMA into anisole at a concentration of 8% by weight. The layers were deposited by spin coating onto the top facing side of a fused silica substrates and annealed for 15 minutes at 60 °C. The average film thickness was measured to be 300 nm.

The material selected for this work was Kremer fluorescent blue (KB), which is based upon a Triazine-toluene sulfonamide-paraformaldehyde-based resin [208]. This material was selected because the intention of this study is mimicking the absorption of commercial UV filters. Figure 4.15 demonstrates the section of LDS dies which were analysed for this study. As seen in figure 4.16, the optical absorption of the PMMA:KB layer is between 350-420 nm, so this should prevent any UV light in this region entering the absorber layer. For this work, a control UV filter was also used, which was supplied from Solaronix (Switzerland), This cuts off light with wavelengths less than 390nm. Table 5.2 shows the values for the figures of merit (FOM) calculated for PMMA:KB films.

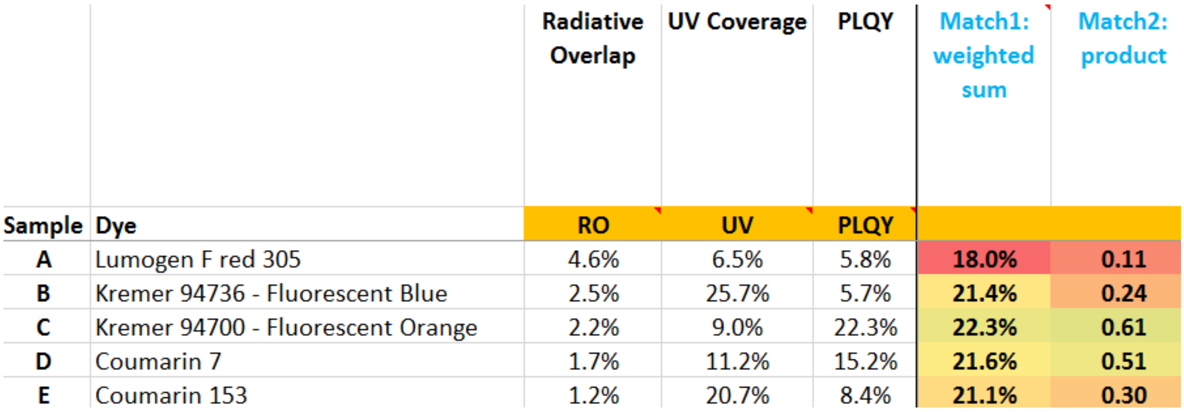

		Radiative Overlap	UV Coverage	PLQY	Match1: weighted sum	Match2: product
Sample	Dye	RO	UV	PLQY		
A	Lumogen F red 305	4.6%	6.5%	5.8%	18.0%	0.11
B	Kremer 94736 - Fluorescent Blue	2.5%	25.7%	5.7%	21.4%	0.24
C	Kremer 94700 - Fluorescent Orange	2.2%	9.0%	22.3%	22.3%	0.61
D	Coumarin 7	1.7%	11.2%	15.2%	21.6%	0.51
E	Coumarin 153	1.2%	20.7%	8.4%	21.1%	0.30

***Figure* 4.15** *– selection of LDS materials assessed against perovskite EQE overlap*

Figure of Merit (FOM)	**RO**	**ASM**	**ESM**	**PA**	**PLQY**	**UV**
Value (%)	2.5	40	78.2	8.7	5.7	25.7

***Table* 4.2** *– Figures of merit for PMMA:KB luminescent layer.*

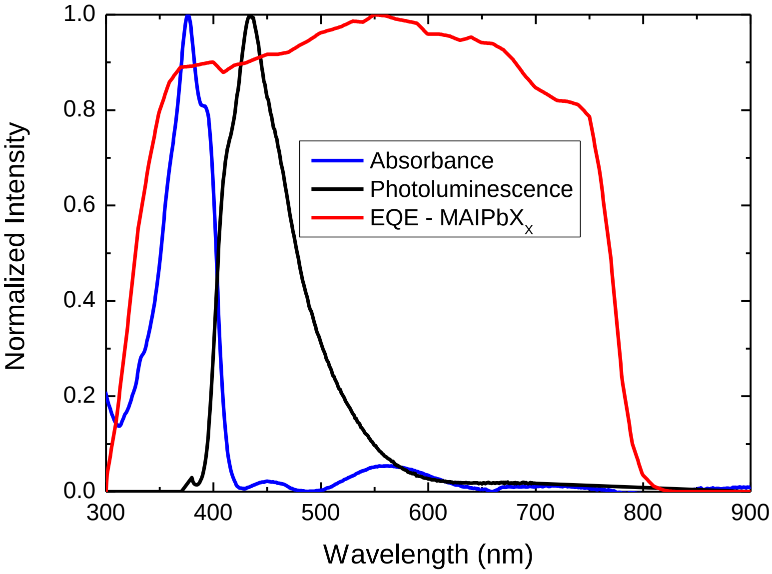

***Figure* 4.16** *– Normalized absorbance (blue line) and photoluminescence (black line) of PMMA:KB layer, and EQE curve of a* $CH_3NH_3PbX_X$ *-based photovoltaic device (red line)*

4.6.2 Effect of LDS layer on film stability

For this work, samples were fabricated using two step deposition. The devices used here were mixed halide $CH_3NH_3PbCl_2I$ which show the highest sensitivity to light exposure.

In this section, the ADS values were calculated over the 400-800 nm range of the absorbance spectra. Figure 4.17 demonstrates the ADS results obtained from light soaked samples. The results show that if no spectral filtration is applied the perovskite degrades rapidly with absorption values decreasing to 10% of the original value recorded after four hours of exposure, confirming the finding in section 4.3 where single halide PbI_2 was used. By contrast, samples prepared with a PMMA:KB filter showed a comparable level of stability as a film prepared with a commercial UV filter. The work shows that the LDS filter can perform as well as a commercial UV filter.

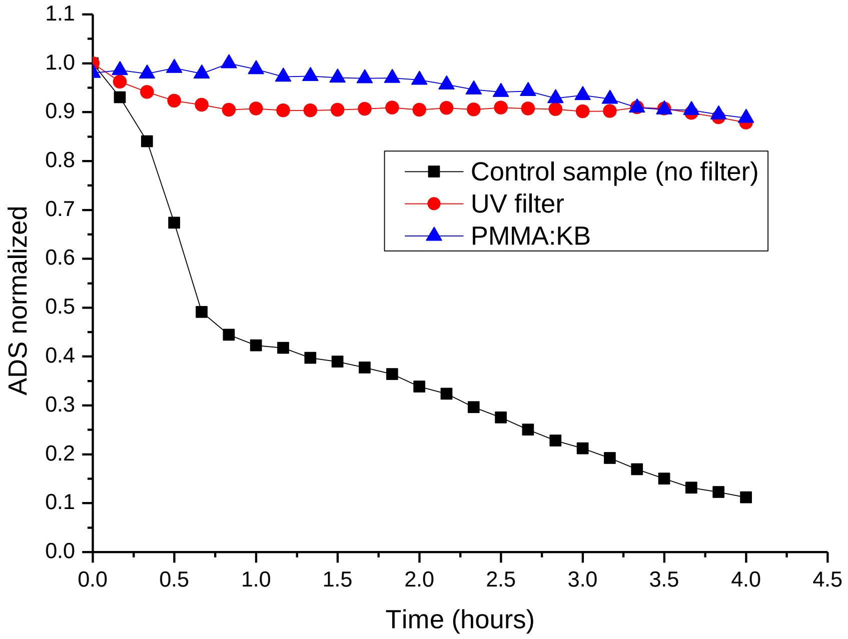

***Figure 4.17** – Evaluation of the Absorption Degradation State (ADS) parameter in the range of 400-800nm of perovskite films with no light filtration, UV filter and LDS layer. The temperature of the samples was maintained at 60 °C during all measurements*

4.6.3 Effect of LDS layer on device performance

In order to assess the photo-degradation effects on spectrum filtered devices, with commercial UV filters and LDS material samples were manufactured, and light soaked in accordance with

ISOS-L-2 standards. The JV curve of the manufactured PSCs is in figure 4.18. The results obtained are shown in Table 4.3. It was seen that, compared to the control devices, the use of filters or LDS layers leads to a slight decrease in the Jsc which resulted in lower efficiency.

The drop in performance is to be expected as perovskite has a high spectral response between 300 and 800 nm and therefore, the application of a UV filter will significantly decrease the photo-current generated in the UV region. The absorption of the LDS layer is mainly in the UV which will in turn reduce the photon generation in the 300-400 nm region of the light spectrum. Nevertheless, the luminescence of the LDS layers occurs randomly and some of the re-emitted light will also be lost before it reaches the device's active layer. As a result, due to these losses, the light absorbed by the active layer will not be as high of a dose as to the amount absorbed by the control devices. The results demonstrate that the devices with an LDS layer resulted in better I_{SC} compared to the devices with commercial UV filter, nonetheless worse compared to the control devices.

Despite the reduction in PCE, by placing an LDS protection increased the stability of the devices as shown in figure 4.19. Both the LDS material and the UV filter significantly improve the longevity of the devices. In the timeframe of this test, there appears no difference between the stability of the cells with covered by a commercial UV filter and LDS layer.

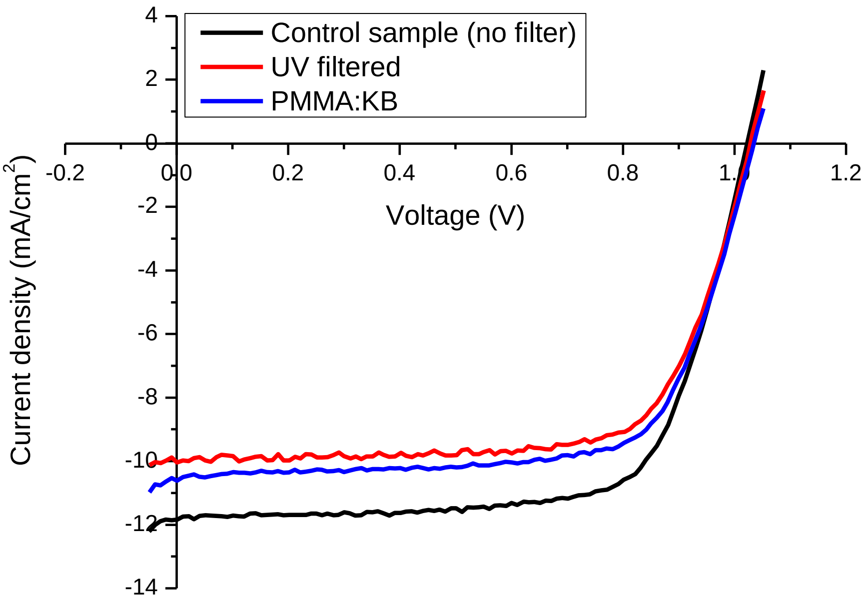

***Figure 4.18** – Current density-voltage plot of perovskite devices exposed to 1sun AM1.5G irradiance. The temperature of the devices was maintained at 60 °C during all measurements*

Parameters	AM1.5G	With PMMA:KB	With UV filter
V_{OC}	1.02 ± 0.01	1.02 ± 0.01	1.01 ± 0.01
I_{SC}	0.83 ± 0.01	0.74 ± 0.01	0.70 ± 0.01
FF	0.72 ± 0.02	0.70 ± 0.02	0.72 ± 0.01
PCE	9.1 ± 0.4	7.9 ± 0.4	7.6 ± 0.4

Table 4.3 *– Electrical parameters of cells exposed to 1 sun irradiance without spectral filtration, with PMMA:KB and with a commercial UV filter. The results above are the average value across three devices examined for every instance.*

4.6.4 Effect of LDS layer on device stability

After applying LDS onto a PSC, the stability of the device was compared against the parameters recorded by using a UV filter and a control sample, as shown in figure 4.19. The results of using LDS layer show close overlap to stability of a device fabricated with a commercial filter UV filter. In fact the current generation by the use of LDS layer delivers a higher value throughout the experiment which supports the concept of light re-emission. Nonetheless, the fill factor appears to decrease slightly quicker in comparison with the UV filtered data which dictates a possibility of small portion of UV propagating through the layers causing a decrease in shunt resistance. This may be improved by increasing the LDS concentration in PMMA. In the timeframe of this test, there appears to be no significant difference between the PCE of the cells with UV filter and LDS layer. By comparison, the stability is greatly enhanced when compared to a PSC without UV filtration. The PSC made and without a UV filter using the same processing conditions decreased by 50% in 45 hours. This result shows an improvement on the data reported recently by Cui et al., who used a magnesium based luminescent compound [209]. Thus, by using FOM to better identify suitable LDS layers, improved stability can be found. Organic dyes such as KB are cheaper and commercially available, which makes them a very promising option for use both as LDS layer and as UV protective layer in PSCs.

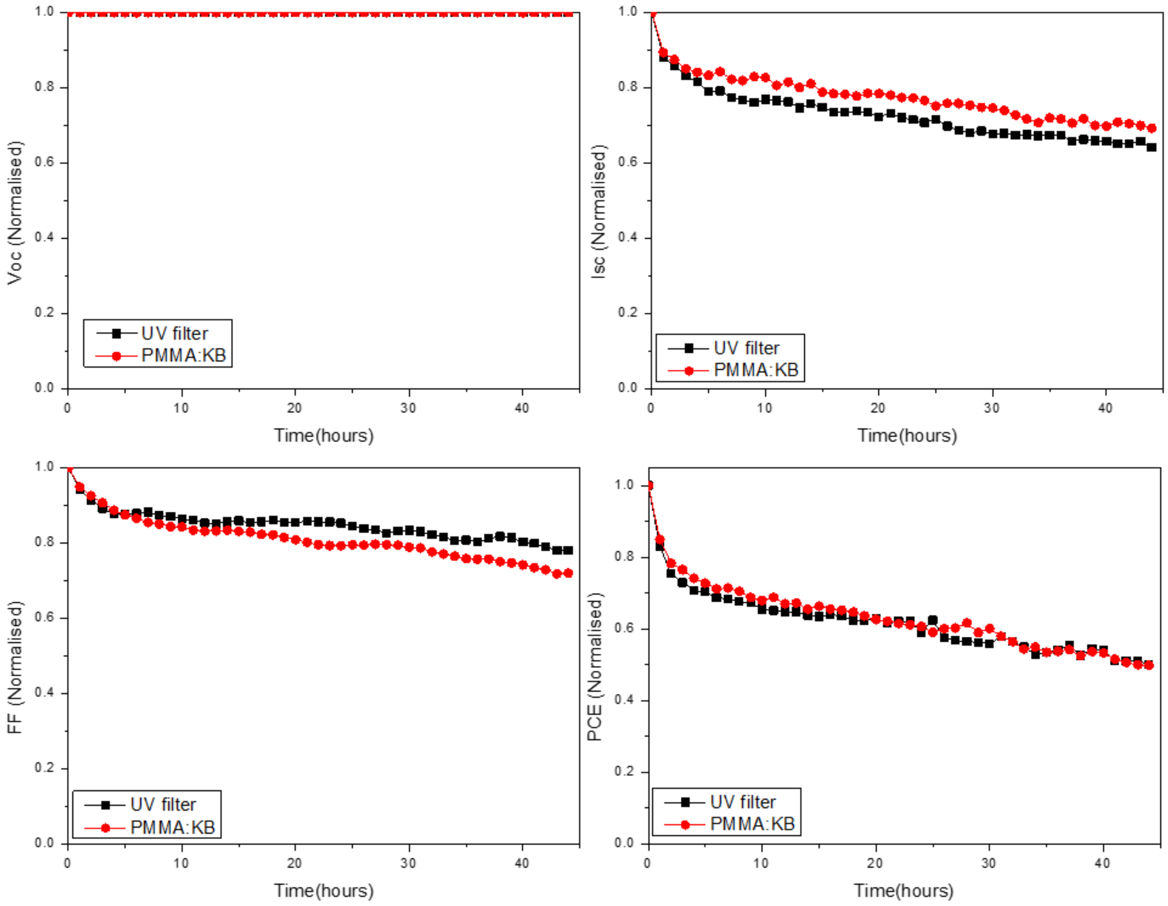

Figure 4.19 *– Evolution of electrical parameters with irradiation time (AM1.5G) for devices with UV filter and LDS: a) open circuit voltage, b) short-circuit current, c) fill factor and d) PCE. The temperature of the devices was maintained at 60 °C during all measurements*

4.7 Conclusion

This chapter demonstrates some of the most significant optimisation steps undertaken in order for sufficiently high device performance to be obtained. Once sufficiently high performance devices were achieved a gradual study of the degradation factors and their elimination was conducted. First the effect of light degradation was investigated where the effect of light filtering on perovskite films was the initial step of this study. In the second step the effect of light filtering against the performance change using PSC devices was analysed. Finally, the stability of PSC devices with spectral filtering was analysed.

The third section of this chapter concentrates on the stability of PSC fabricated using one and two step manufacturing process and the effect of orientation against the source of light was observed.

In the fourth section the effect of unreacted PbI_2 was on the stability of perovskite layers was investigated. It was seen that PbI_2 introduces the same filtering properties as using a commercial UV filter.

In the final section of this chapter a substitution of UV filtering with LDS coating was examined. The results of this study show a promising ground for LDS application as UV filtration, demonstrating over 40 hours of continuous light soaking coated on PSC devices. The devices coated with LDS show lower degradation under light in comparison to devices filtered using a commercially supplied UV filter.

Chapter 5. Outdoor Monitoring of next generation solar cells for BIPV applications

5.1 Introduction

In order for emerging PV technologies to become commercially viable it is important that it is understood how they perform under real world conditions. This chapter focuses upon studying the performance and stability of PSCs and OPVs with the view to integration into Building Integrated Photovoltaics (BIPVs). Over the course of several outdoor monitoring campaigns, PSCs and OPVs, were examined for their performance parameters (V_{OC}, I_{SC}, FF and PCE) which were related to their orientation against the sun and also the performance decay as a function of time. The initial focus of this work was to study the performance of PSCs; however, there were some delays in receiving modules and the stability was a concern. Towards the end of the project, PSC modules were received from SPECIFIC at Swansea University. Outdoor monitoring was conducted whereby diurnal performance and performance in different climates characterised. However, the stability of the modules was very poor and therefore longer-term studies focused on using OPV modules supplied by the Danish Technical university (DTU) for further studies. In particular, the effect of orientation on OPV performance was studied. This is particularly pertinent for one potential 3rd generation PV application, BIPVs.

5.2 Outdoor measurements of PSCs from SPECIFIC

The outdoor monitoring of PSCs was conducted over two campaigns between April 2017 until July 2017. All outdoor monitoring in this thesis was conducted using a setup installed on the roof of our institute in Bangor, Gwynedd at coordinates latitude 53.2280N, longitude -4.1290W and altitude approximately 20m above sea level.

The modules manufactured by SPECIFIC, with dimensions 50mm x 50mm x 2mm and a total active area of 13.5cm^2 consisted of 5 cells monolithically connected in series and were mounted on a 35^O inclined rack facing due south. All modules were initially prepared for outdoor exposure by encapsulation, described in chapter 3. In the initial experiment the modules tested were encapsulated and exposed to the ambient conditions without UV filtration, but showed poor stability. In the second campaign, due to the observed rapid photo-oxidation in the first campaign, all modules included a UV filter purchased from Solaronix SA, Switzerland [210]. The initial efficiency of the modules in the first campaign was 7.0% PCE with ±0.6% standard deviation which demonstrated variation in film qualities from the production process. In both campaigns the modules were supplied with a PT100 temperature sensor attached to the back of the bulk which constantly monitored the change in module temperature according to the ambient weather conditions.

5.2.1 Diurnal performance

Initially diurnal device performance was sought from the PSC modules delivered from SPECIFIC. Two different types of modules were received; The first batch consisted of single cation $CH_3NH_3PbI_3$ (MAPI) modules of the structure Glass/FTO/NiO_X/MAPI/PCBM/Ag similar to [211]. The second batch consisted of triple cation (FMC) perovskite modules, with identical architecture. During this period of operation, a mixture of overcast and sunny days were observed so a comparison of diffuse and direct light performance could be made.

Shown in figure 5.1 is the performance over the course of the first week of operation. On a sunny day, the MAPI modules experience a decrease in PCE which is related to the negative temperature coefficient (NTC) of these devices [212]–[214]. While the single cation decreases in efficiency during sunny days, the triple cation modules demonstrate greater stability as well as higher initial PCE at 1 sun of up to 6%, as shown in figure 5.1. On a cloudy day, the module temperature is lower and the single cation MAPI performs better than the FMC modules as the module temperature does not increase quite so significantly and stays below $25^{O}C$.

Shown in figure 5.2 is the measured irradiance, module temperature, relative humidity and outdoor temperature over the same measurement period as the data in figure 5.1. As can be expected for a summer period in Wales, the irradiance reaches as much as 1000 W/m^2 on sunny days. As to be expected, the temperature tracks irradiance over the course of a day. The RH mostly has an inverse relationship with the temperature, except on overcast days or days with precipitation. The average module temperature fluctuates from near $15^{O}C$ to $42^{O}C$, which occurred on June 18th and is likely to have been exaggerated due to the effect of cloud lensing. The outdoor temperature during sunny days (defined as when the highest irradiance was measured at $987W/m^2$, at the peak sun-hour 12:45 to 13:45), is $24.6^{O}C$.

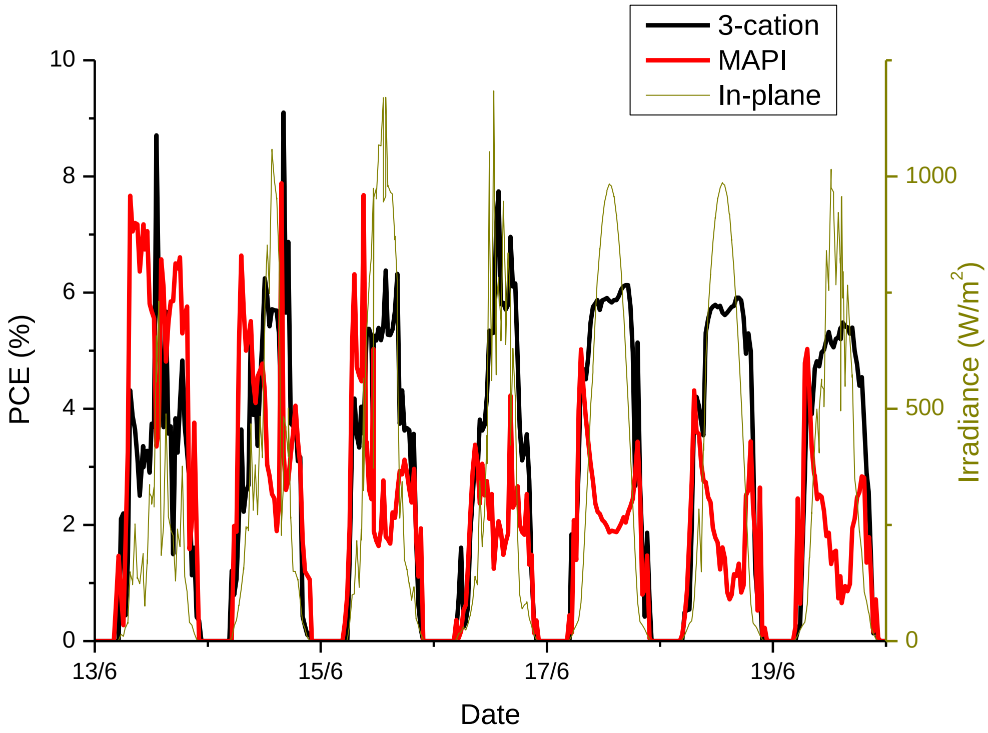

***Figure 5.1** – PCE of perovskite modules in the first week of the second campaign of outdoor testing. The curve highlighted in dark yellow represents the irradiance levels during the monitoring period*

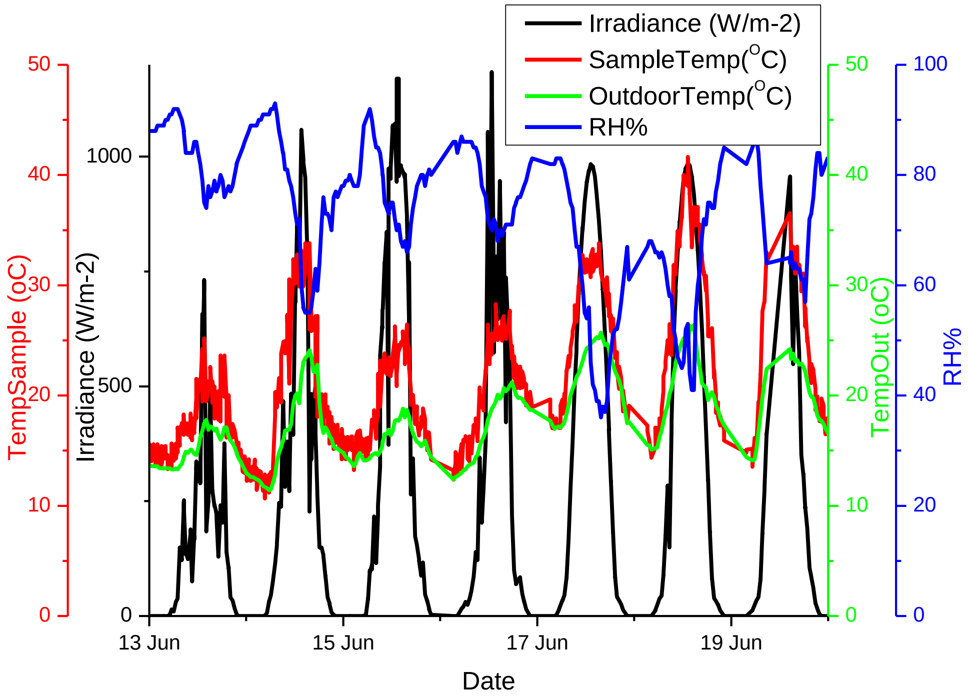

***Figure 5.2** – Outdoor solar irradiance measurement, relative humidity (RH%), average module temperature and outdoor temperature for the first week of the experiment*

Shown in figure 5.3 is the diurnal PCE of two modules of both compositions on sunny and on cloudy day. As it can be seen in figure 5.3 a) the FMC modules demonstrate an increase in PCE linear to the solar dose with a saturation at near 6% PCE. The MAPI modules on the other hand present an inverse response to solar dose with a distinctive drop in power conversion after 7:15am and a partial recovery at 7:45pm. If figure 5.4 is considered it will be seen that the performance drop on the MAPI modules in mainly dictated by the loss in fill factor (FF) and short circuit current (I_{SC}) which is it driven by. The open circuit voltage remains relatively constant. The reduction in FF and I_{SC} is due to the increasing series resistance which in turn demonstrates a flaw in the interfaces, most likely, between the transport layers and the electrode contacts which is stimulated by the increase in module temperature.

Figure 5.3 b) nevertheless, shows that the MAPI module demonstrates a slightly better performance in cloudy conditions in comparison to the FMC module which appears in agreement with the NTC observed experienced by the MAPI modules.

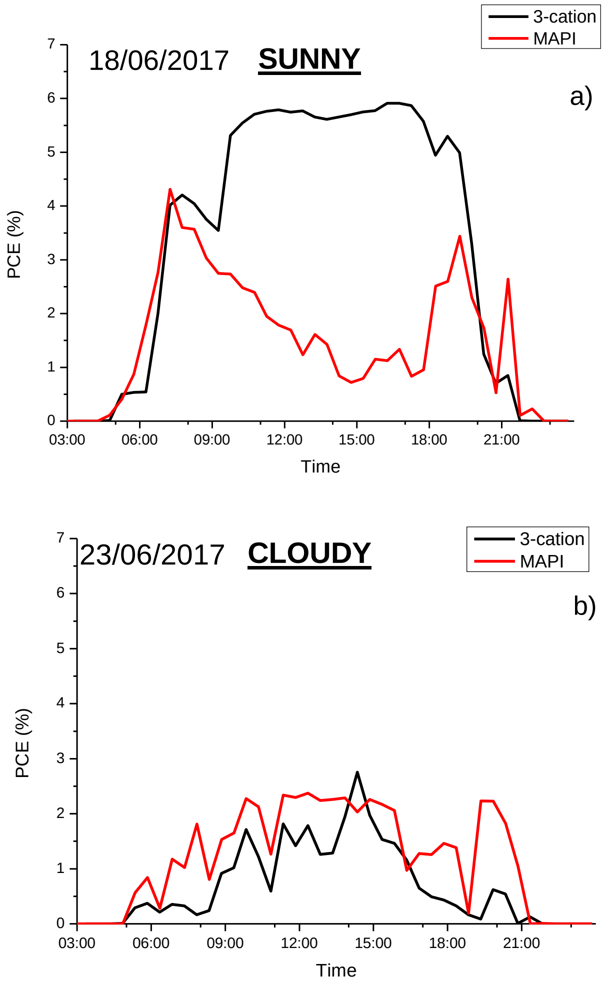

***Figure 5.3** – Diurnal PCE of a) sunny against b) cloudy day recorded from MAPI and FMC modules in Bangor*

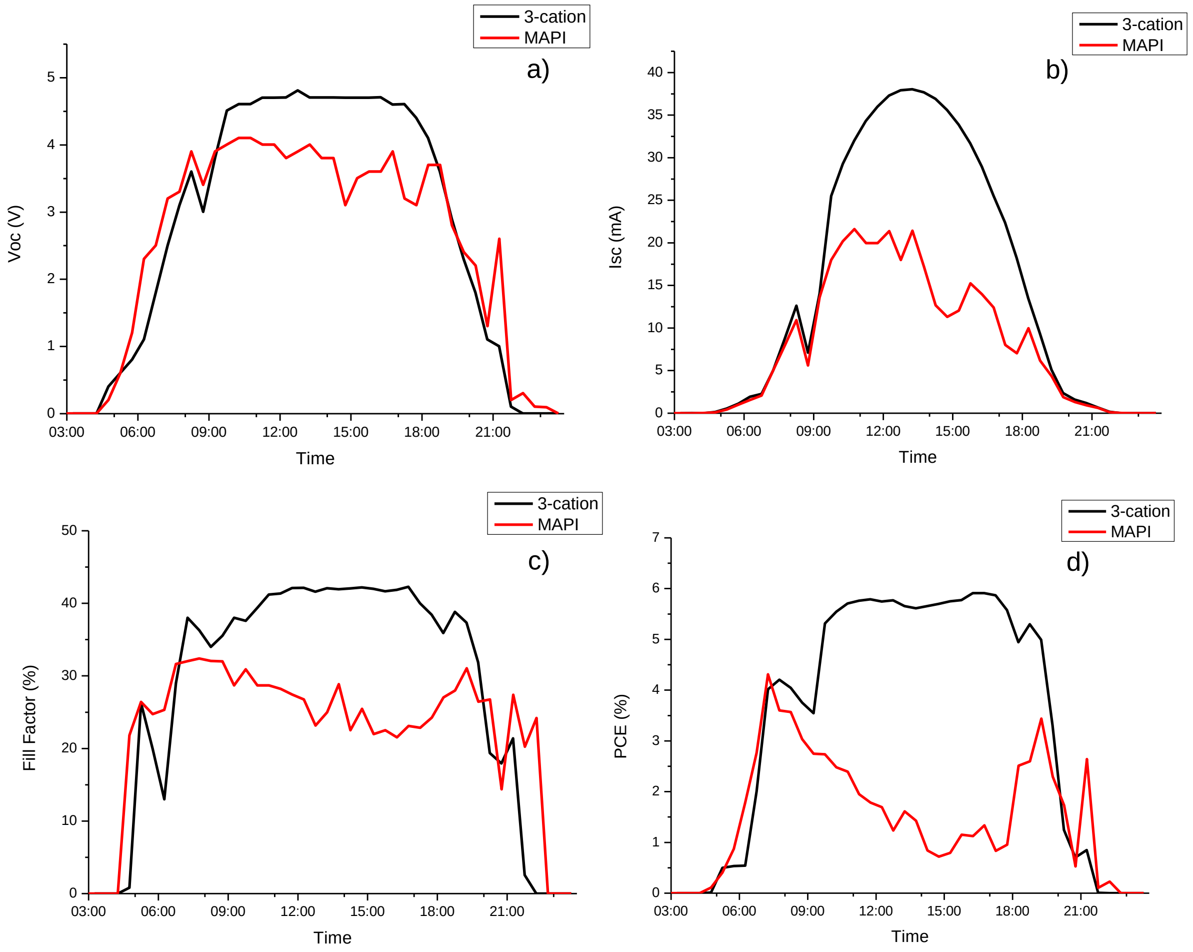

Figure 5.4 *– Diurnal performance parameters of MAPI and FMC perovskite modules recorded on June 18th 2017, the day with highest direct solar insolation measured*

5.2.2 Module Degradation

In addition to diurnal studies, the modules were studied for degradation. The graphs in figure 5.5 and 5.6 show the change in performance against irradiance on weekly basis for MAPI and FMC modules. In both cases, despite the glass-on-glass encapsulation, all PSC modules (with and without UV filtration) were seen to degrade relatively quickly. In figure 5.5 a), the V_{OC} dependence upon irradiance is shown for the MAPI module. As to be expected, it demonstrates a logarithmic dependence on irradiance [215]. The I_{SC} shows a linear dependence upon irradiance level [216], [217] see figure 5.5 b). Shown in 5.5 a-b) is averaged data for V_{OC} and I_{SC} of 3 weeks continuous outdoor exposure. V_{OC} demonstrates a gradual degradation between weeks one and two followed by a catastrophic failure in the third week due to encapsulation fail and complete water damage causing complete active layer decomposition [218],[219], [220]. The drop in I_{SC} in week two can be speculated to be due to the structure of the device, using PCBM as an ETL was found to increase susceptibility to oxygen/water, and also due to its fine thickness Al/Ag can diffuse trough the ETL and react with the perovskite [199].

The absence of photocurrent observed in week three, is a clear sign of the decomposition of the photoactive layer, supported by visual inspection of the modules, figure 5.8 c-d). If figure 5.5 b) is considered, it can be seen that the results for FF in week one match the response of V_{OC} quite closely. When the irradiance level reaches 250W/m^2 the FF of the MAPI module starts to decay exponentially and by the time the irradiance level reaches 1 sun (1000W/m^2) the FF has dropped by 28% in comparison to its level at quarter of full sun irradiance. This decay can be directly associated to the temperature sensitivity of the MAPI devices [221].

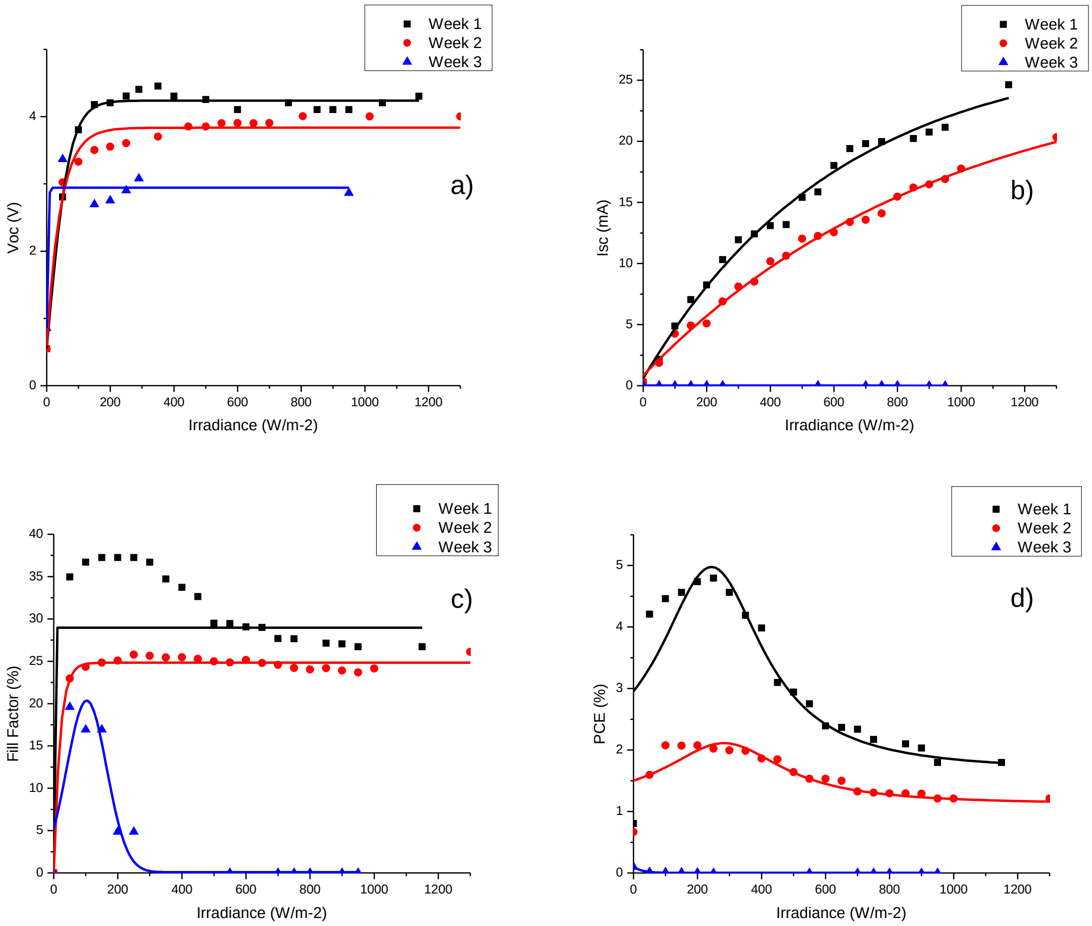

Figure 5.5 – *Degradation of performance parameters for MAPI modules over the period of three weeks. a)* V_{OC}*, b)* I_{SC}*, c) Fill Factor and d) PCE*

Shown in figure 5.6 are the performance parameters as a function of irradiance for the FMC modules over the same measurement period. This result demonstrates a much more stable behaviour presented by short circuit current response in weeks 1 and 2. Nevertheless, even here the FF decays driven by the drop in V_{OC}, which is most likely to be due to the Schottky contact which formed between the selective layer and the electrodes [222]. In week 3 after sustaining a catastrophic water damage, the sample performance drops by nearly 60%, however, in the beginning of the forth week due to the massive water ingress the sample completely malfunctioned.

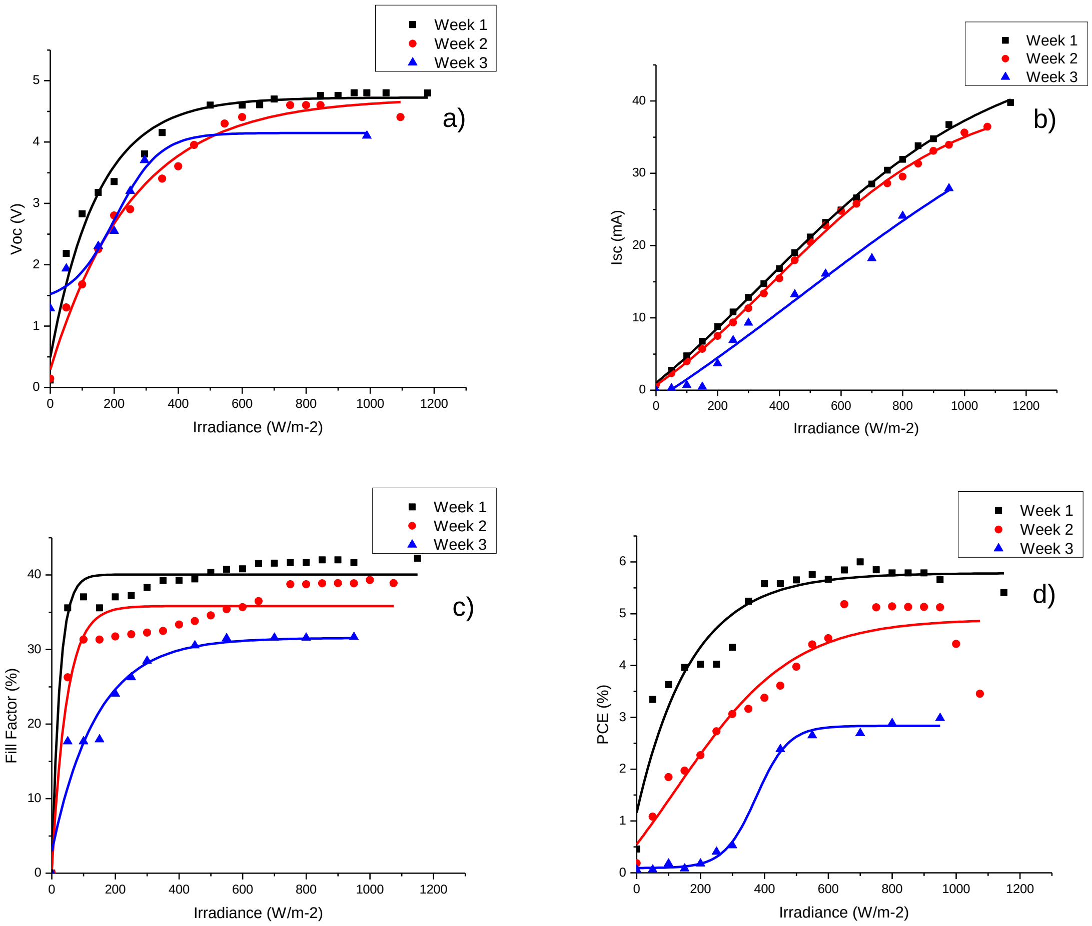

Figure 5.6 *– Degradation of performance parameters for FMC modules over the period of three weeks. a)* V_{OC}*, b)* I_{SC}*, c) Fill Factor and d) PCE.*

For the stability measurements, it is clear that the PSC modules are degrading rapidly as shown in figure 5.7. This is despite rigorous encapsulation using glass-on-glass. Edge sealant was provided from Dyesol and the properties of this are well-studied as a stable sealant. However, it is still likely that degradation is still occurring at the edges where water ingress occurs between the glass substrates, leading to rapid decomposition of the active layer, as seen in the photos in figure 5.8. The photographs show how water and oxygen can penetrate through the edges leading to chemical decomposition of all layers. PSC are shown to be unstable to oxygen and water in reference [222], [223]. Although the modules were with glass-to-glass encapsulation and an edge sealant with known stability, degradation was still observed. Water and oxygen molecules will not migrate through the glass in this time period. This was the same strategy used for the OPV modules described later in this thesis, which were still working after 1 year of outdoor operation. This indicates a number of potential issues; Firstly, the PSC module is much less stable than the OPV modules used in this work. Secondly, it is possible that the best edge sealant for OPVs/DSCs needs to be redesigned for PSCs. Thirdly, a better strategy for encapsulating modules needs to be considered. Possibly encapsulation on site at SPECIFIC is needed in the future.

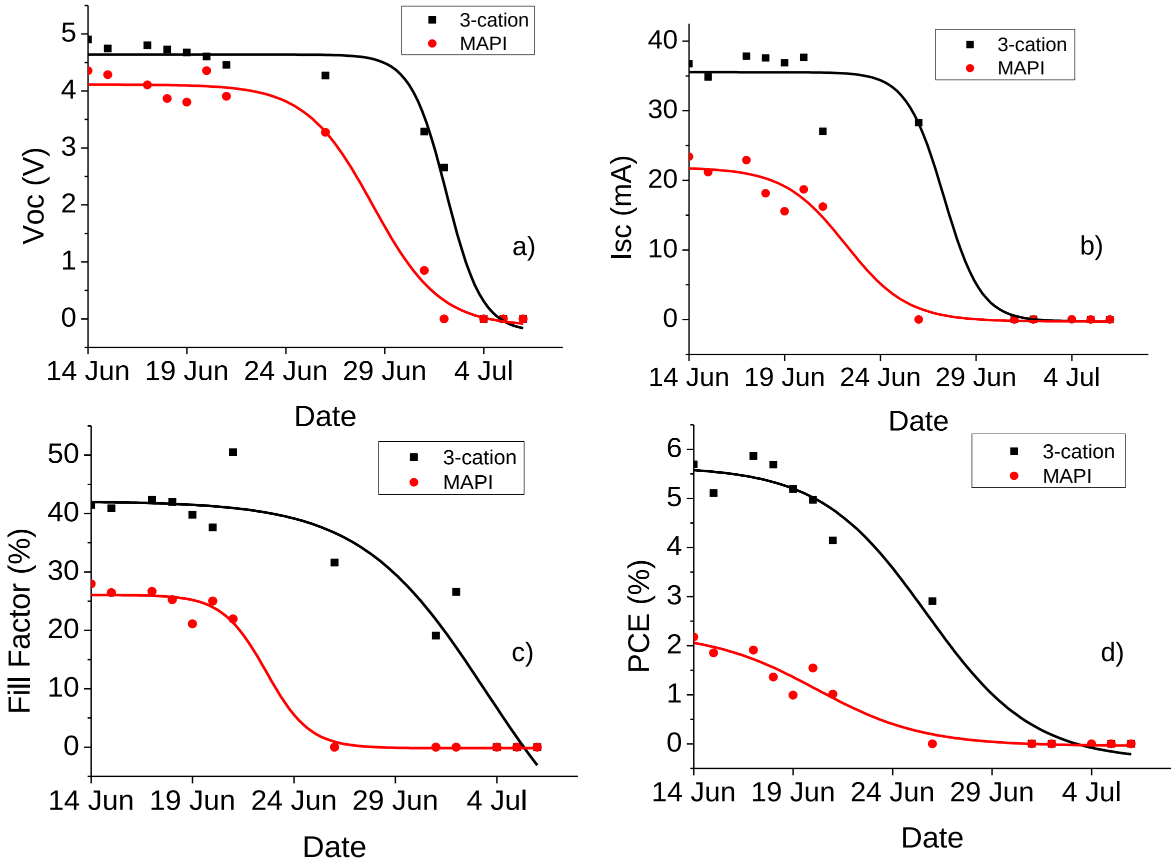

Figure 5.7 *Performance parameters of three cation versus MAPI modules. Change in a)* V_{OC}, *b)* I_{SC}, *c) Fill factor and d) PCE over time demonstrating sharp degradation in* I_{SC} *for MAPI and sudden* V_{OC} drop for the three cation which is most likely to be due to the Schottky contact which formed between the selective layer and the electrodes [222].

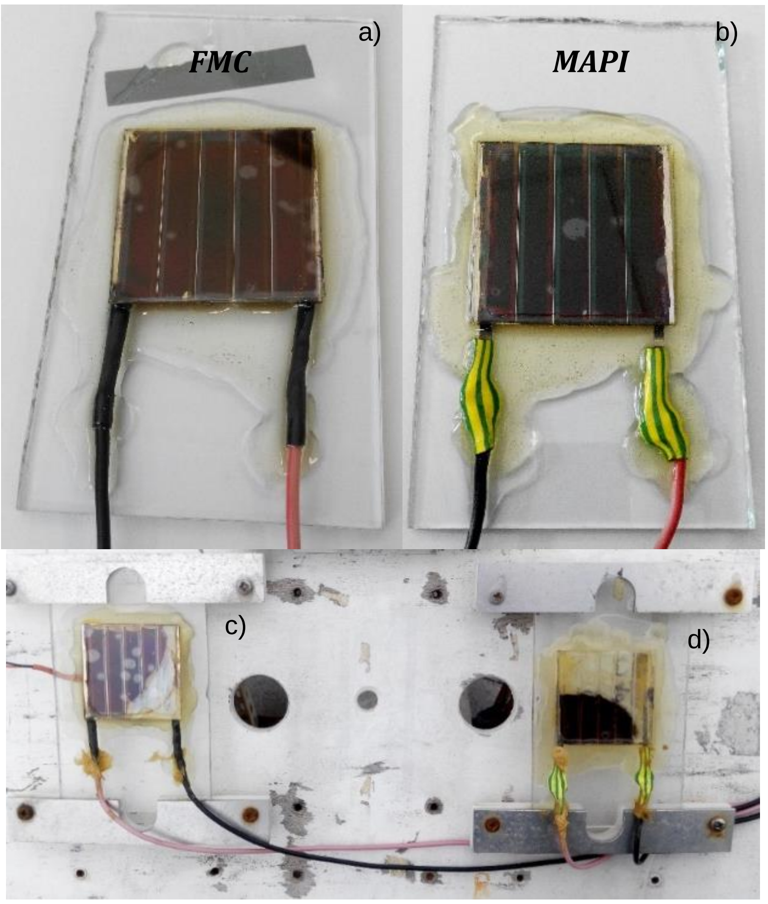

***Figure 5.8** – Two of the monitored modules before installing outdoors a-b) and after three weeks ambient outdoor exposure c-d). Catastrophic failure on the encapsulation led to water ingress and the complete decomposition of the modules.*

5.3 Effect of PV orientation on BIPV performance

One of the aims of this thesis was to study the performance of PVs on different sides of a building and understand how orientation impacted on PV performance. To undertake such a study, module performance needs to be studied across a minimum of two seasons to see the impact of azimuth and altitude on PV performance. The current PSC modules showed no capability to undertake such a long duration tests, therefore it was decided to use OPV modules which are known to be stable (T_{50} >6 months). Whilst this is not ideal for the thesis, it did enable results to be captured in a timely manner.

Gen. 2 OPV modules were acquired from DTU and encapsulated using the procedure described in chapter 3 section 3.4.2. The modules used for this work are produced on a R2R plant and subsequently laser cut according to the template, figure 3.9. The module architecture comprises of 8 serially connected cells and an active area of 64.8cm^2.

In order to study the effect of module orientation without having to install a large BIPV setup on an existing building, a miniature building prototype was built and installed on the rooftop of the school of Electronics Engineering at BU, figure 5.9.

Figure 5.9 *– Outdoor Organic BIPV test rigs after their installation. East, South, West and Horizontal/Flat modules mounted on cuboid shape industrial building prototype (left), North facing modules mounted on a separate panel (right).*

The OPV modules were installed on two separate test rigs due to the allocation of the metrological station on the roof of the Electronics Engineering building. In order to eliminate shading over the modules positioned due North, a second test rig was procured.

The OPV data was processed prior to data analysis. To calculate the Maximum power point, equation 5.3.1 was used, where P_{max} is maximum generated power, I_{mpp} is the current at maximum power point and V_{mpp} is the voltage at maximum power point. Subsequently, the efficiency (η_{STC}) was calculated under Standard Test Conditions (STC) of 25°C and 1000W/m^2 AM 1.5G spectrum, as shown in equation 5.3.2, where A is module active area and P_{in} is the solar irradiance. Finally, energy yield (Y) and energy Yield per unit area (Y/A) was calculated based upon the measurement time interval (ti) in equation 5.3.3 and 5.3.4.

$$P_{max} = I_{mpp} * V_{mpp} \qquad \text{equation 5.3.1}$$

$$\eta_{STC} = \frac{Pmax}{A*Pin} \qquad \text{equation 5.3.2}$$

$$Y = \int Pdt \cong \sum iPi\Delta ti \qquad \text{equation 5.3.3}$$

$$\frac{Y}{A} = \int Pdt/A \cong \sum iPi\Delta ti\,/A \qquad \text{equation 5.3.4}$$

5.3.1 Diurnal performance

The outdoor monitoring experiment was carried out for a period of eight months, December 2015 – July 2016. Throughout the entire period of this investigation the incident irradiance and weather conditions were monitored alongside the OBIPV modules. The incident irradiance was monitored by two calibrated reference cells positioned in-plane at 35^{O} inclination and a horizontal positioned at 0^{O} inclination.

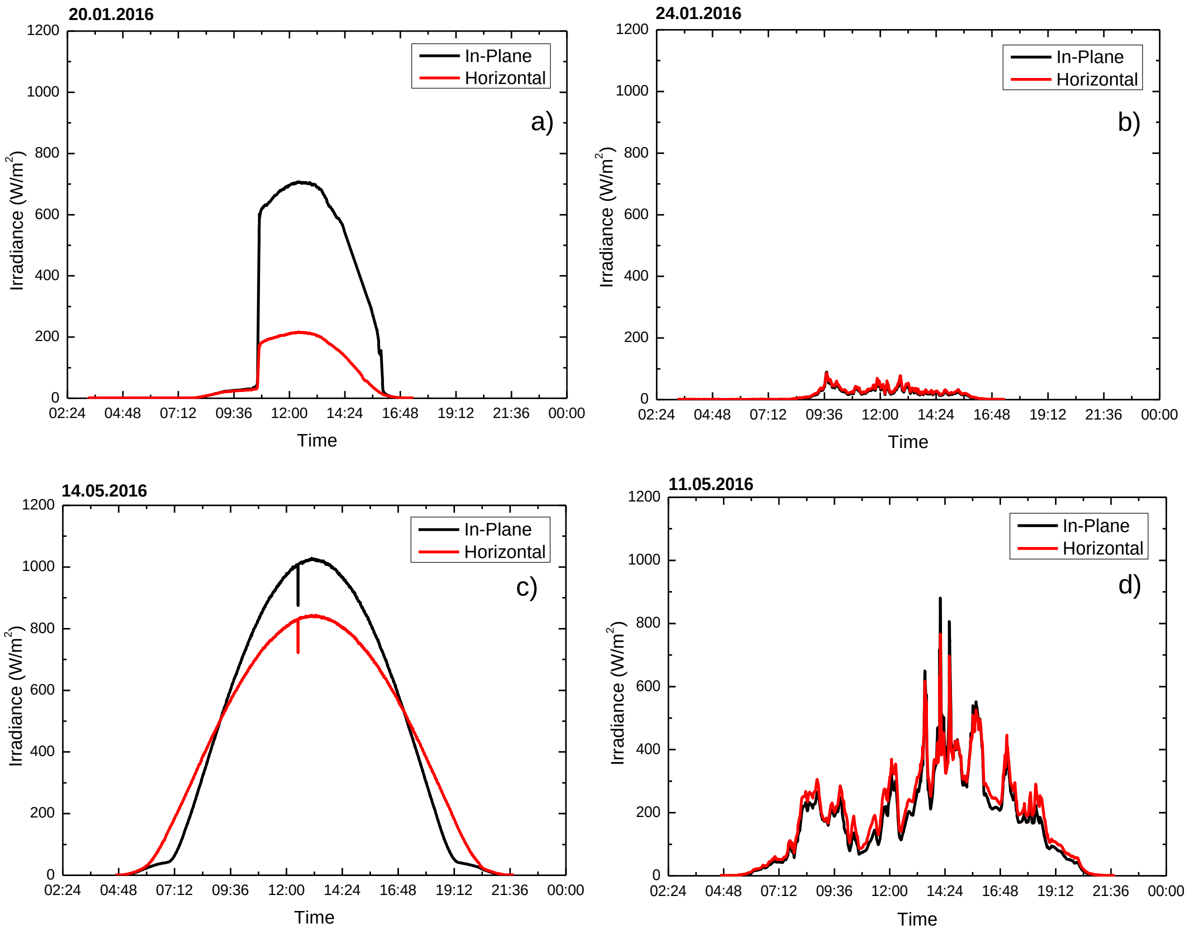

Figure 5.10 –*Irradiance measurements recorded during a) sunny and b) cloudy day in winter, and c) sunny and d) cloudy day in summer.*

In order to evaluate the diurnal performance, four contrasting days were selected and divided into two categories. A sunny day in the summer versus the winter and a cloudy day in the summer versus the winter.

With the intention of defining sunny and cloudy metrological conditions more accurately, the data obtained in the summer time as well as in the winter was organised in portions depending on the season and the recorded solar insolation, figure 5.10. A clear day in the summer was defined to deliver energy between 600-1000W/m^2 while on a cloudy day the expected energy yield would be between 200-500W/m^2. The winter period, as expected, demonstrated very few sunny days, however, enough to distinguish between one another. The set energy yield requirement for a sunny winter day was between 100-400W/m^2, while cloudy day was set to deliver between 25-100W/m^2 of solar energy.

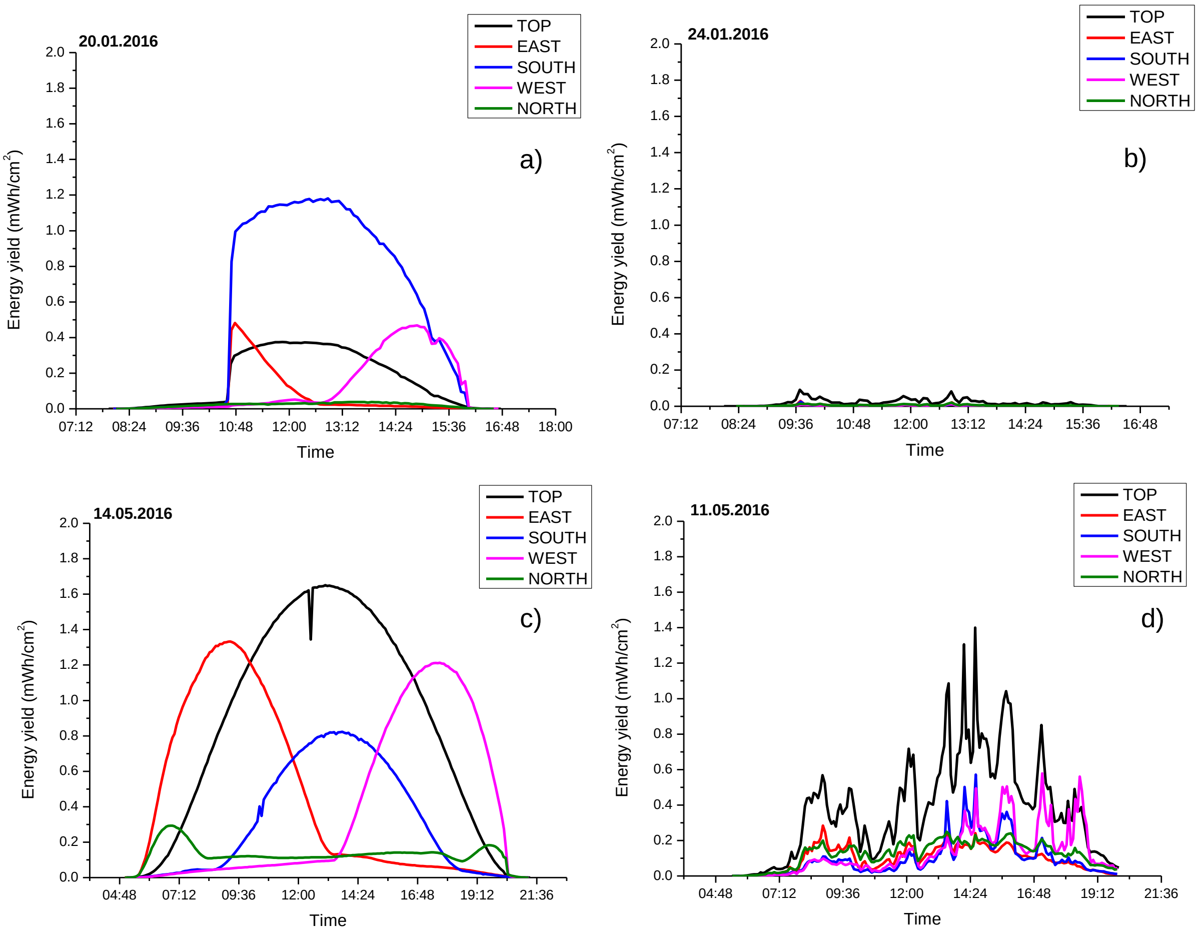

Figure 5.11 *– Diurnal performance of the OPV modules for a) sunny and b) cloudy day in winter, and c) sunny and d) cloudy day in summer.*

When considering sunny days in figure 5.11 (a,c) it is clear that orientation has an impact on the module performance and also which module performs best at different periods of the day. During the winter time when the sun's maximum elevation only reaches 16.35^{O} the south facing modules outperform all others. This trend continues until the end of February when the maximum solar elevation reaches 28.8^{O}. The zenith angle between sunrise and sunset increases leading to the top-facing module having the greatest diurnal power output in May, see figure 5.11 c).

The performance of East and West facing modules, which are rarely reported for PV performance show a different impact on power generation depending on the season. In summer months, they can significantly impact on power generation in the early morning and late evening, respectively, and these modules could contribute to the balancing of PV power generation during peak hours. It was just recently when the photovoltaic community decided to break off from the routine and in September 2013 the deployment of a first of its kind solar farm, with east-west facing modules, was commenced [224] a novel idea which was then upscaled from 6.4MWp to 300MWp in November 2015 [225]. However, in winter time, the modules do not have such a signfiicant impact, owing to the tilt of the Earth allowing much lower irradiance to be absorbed and the shorter hours of daylight. Therefore, the power generation is only marginally better in mornings and evenings. As to be expected, the north facing module exhibits the worst performance on sunny days, as only diffuse irradiation is incident on the module.

When considering the days of high cloudiness, figures 5.11 (b,d), the top facing modules appear to always outperform modules positioned side-facing. This has been previously reported in c-Si [226] and is explained by the distribution of scattered radiation in the sky. When there is no overcasting the sun rays reach the surface of the earth at an optimum of 90^{O} angle, still, when sky is covered with clouds the diffuse radiation is considered to be equally distributed which allows the horizontally positioned PV installations to generate most of the power available during those periods. It is noticeable that during days of considerable cloud cover, all other modules have almost identical level of performances, including the north facing modules, indicating that if OPVs could be manufactured cheaply enough, power generation would still be feasible on a north-facing wall.

5.3.2 Monthly yield

Monthly energy yield was calculated from equation 5.3.4 and plotted in figure 5.12, where it is evident that the best performing modules are the ones oriented due south or horizontal/flat, however, this changes as a function of a calendar month.

During the winter period (December – February), the south facing modules contribute the greatest portion to the electricity generation. This is due to the lower solar elevation of between 16.35^{O} and 28.8^{O} and thus is better positioned for sunlight absorption. In fact, south facing modules generate a factor of two more energy during these months than the next best performing module (the top-facing module). North, West and East facing modules generate similar levels of power, although the east facing modules are affected by shading losses due to nearby undulations.

From March onwards, the top-facing module has the greatest monthly energy yield due to the higher solar elevation. By June, this is approximately a factor of two greater than the south facing module. From May, the east and west facing modules generate greater output power than the south facing module. This trend can be explained by the longer days and lower proportion of diffused light. The latter also explains the significant relative drop in yield from the north-facing module. When considering east and west facing modules and their greater output over the south-facing ones, the attributed cause is the critical angle of incidence of 45^{O} which by midday (1:15pm), south facing module's peak time, the solar elevation has already reached 58.8^{O}. East and west facing modules, however, experience their peak times and solar elevation respectively at 9:15am for east with 35.30^{O} and 5:30pm for west with 32.90^{O}. Interestingly, the east facing module is always moderately better performing than the west facing one possibly due to morning sun glare (albedo) from the reflected light from the Menai Strait located 500m from School of Electronic Engineering where the test rig is positioned.

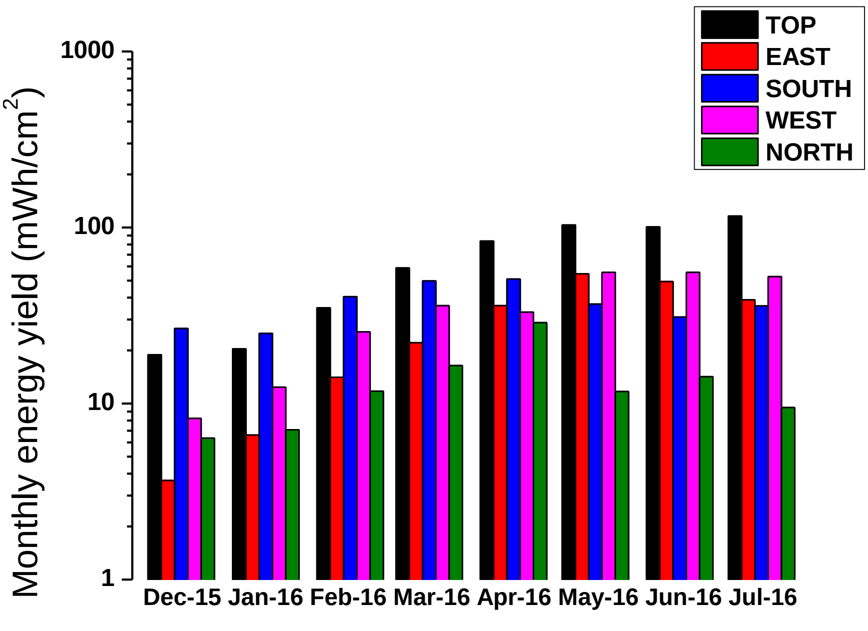

Figure 5.12 *– Graph of the monthly energy yield as a function of module position from December 2015 through to July 2016.*

5.3.3 Performance during peak hours

The importance of balancing energy generation is of growing importance for renewable energy generators. Techniques such as battery storage are being heavily researched to balance against energy needs. Peak demand in the UK occurs from 16:30–19:30pm and during this time retail electricity prices are elevated for many consumers[227]. The peak hour power generation by buildings with multi-sided PV installations could act as a strategy to balance peak demands.

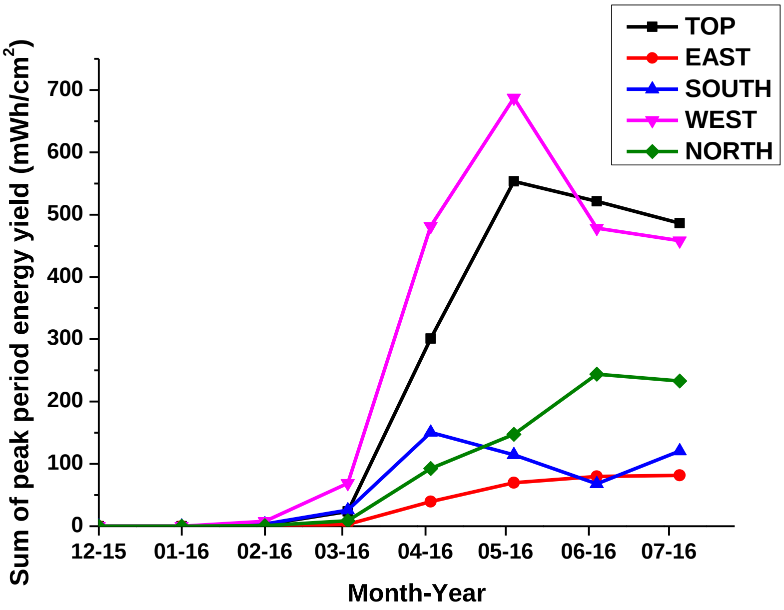

Figure 5.13 *– Plot of peak energy generated as a function of month and position of module. No peak-period power generation during winter months with gradual increase in mid-February to March followed by a sharp rise thereafter.*

	TOP	EAST	SOUTH	WEST	NORTH
Dec-15	0.00	0.00	0.00	0.00	0.00
Jan-16	0.01	0.00	0.00	0.01	0.00
Feb-16	2.67	0.37	3.60	8.10	1.09
Mar-16	23.61	3.27	25.88	68.69	8.61
Apr-16	301.21	39.70	150.66	481.56	92.68
May-16	553.33	69.70	114.46	687.41	147.47
Jun-16	521.27	79.80	68.12	478.38	244.03
Jul-16	486.26	81.62	120.84	457.95	233.21

Table 5.1 *- The sum of monthly and peak-period yield from outdoor performance monitoring*

Considering figure 5.13 and table 5.1, west-facing modules have the greatest capacity to contribute to power generation during peak hours. The west-facing module outperforms all other modules during peak times, except in July (when there was an abnormally large number of diffuse days). The top-facing modules are considered being the second best for peak-hour power generation position. However, it is important to note that in winter months (Dec-Feb), small amounts of power are generated by a module, so this strategy is only effective during summer months.

5.3.4 Performance under different climates

Based upon the data in section 5.2, it is clear that the relative module performance is affected by climatic conditions. Figure 5.14 shows the monthly yield accumulated by all the available modules under specific weather conditions for January and May.

To view the climatic effect, the power generation was divided into sunny, intermittent and cloudy/diffuse conditions according to the solar insolation levels relative to the nominal maximum daily irradiation [228]. Sunny conditions were defined with a daily insolation ≥80% nominal maximum value, intermittent ≥40% & <80% and cloudy <40%. In the winter, the south facing modules are best performing except in cloudy conditions where the top-facing mounted are superior. West appears to be the third best followed by east and north. In May, the top-facing module performs best in all conditions. In sunny days, the east facing modules appears second best, which can be equated to the summer trend in the UK of higher direct radiation in morning and greater cloudiness in the afternoon [110]. In cloudy conditions, all modules except top-facing, including the North appear to perform similarly. This study is particularly important for countries with temperate climatic conditions, where the average annual insolation levels can be factored to be within the “intermittent” category where the positive influence of multiple module positions can be recognised.

Daily Energy yield (mWh/cm^2)	**Power %**	**Winter**	**TOP**	**EAST**	**SOUTH**	**WEST**	**NORTH**	**TOTAL**
Jan-16	>=80%	Sunny	18.39	6.06	57.79	14.71	3.04	100
Jan-16	>=40%&<80%	Intermittent	28.55	8.91	46.49	9.39	6.66	100
Jan-16	<40%	Cloudy	44.85	8.63	21.00	13.10	12.41	100
Daily Energy yield (mWh/cm^2)		**Summer**	**TOP**	**EAST**	**SOUTH**	**WEST**	**NORTH**	**TOTAL**
May-16	>=80%	Sunny	42.49	20.27	15.97	13.95	7.33	100
May-16	>=40%&<80%	Intermittent	36.64	15.32	22.89	16.25	8.90	100
May-16	<40%	Cloudy	38.54	13.88	16.27	16.74	14.57	100

Daily Energy yield (mWh/cm-2)		**Winter**	**TOP**	**EAST**	**SOUTH**	**WEST**	**NORTH**	**TOTAL**
Jan-16	>=80%	Sunny	36.76	12.12	115.54	29.41	6.08	199.92
Jan-16	>=40%&<80%	Intermittent	21.42	6.68	34.87	7.04	5.00	75.02
Jan-16	<40%	Cloudy	9.66	1.86	4.52	2.82	2.67	21.54
Daily Energy yield (mWh/cm-2)		**Summer**	**TOP**	**EAST**	**SOUTH**	**WEST**	**NORTH**	**TOTAL**
May-16	>=80%	Sunny	446.33	212.99	167.72	146.50	76.98	1050.52
May-16	>=40%&<80%	Intermittent	294.64	123.18	184.12	130.66	71.60	804.20
May-16	<40%	Cloudy	173.18	62.38	73.12	75.24	65.49	449.40

***Table 5.2** – (Top) Percentage of energy yield generated in summer and winter in sunny, intermittent and cloudy days. (Bottom) Energy yield generation (mWh/cm^2) in summer and winter defining the accumulated power under three distinctive categories (sunny, intermittent and cloudy).*

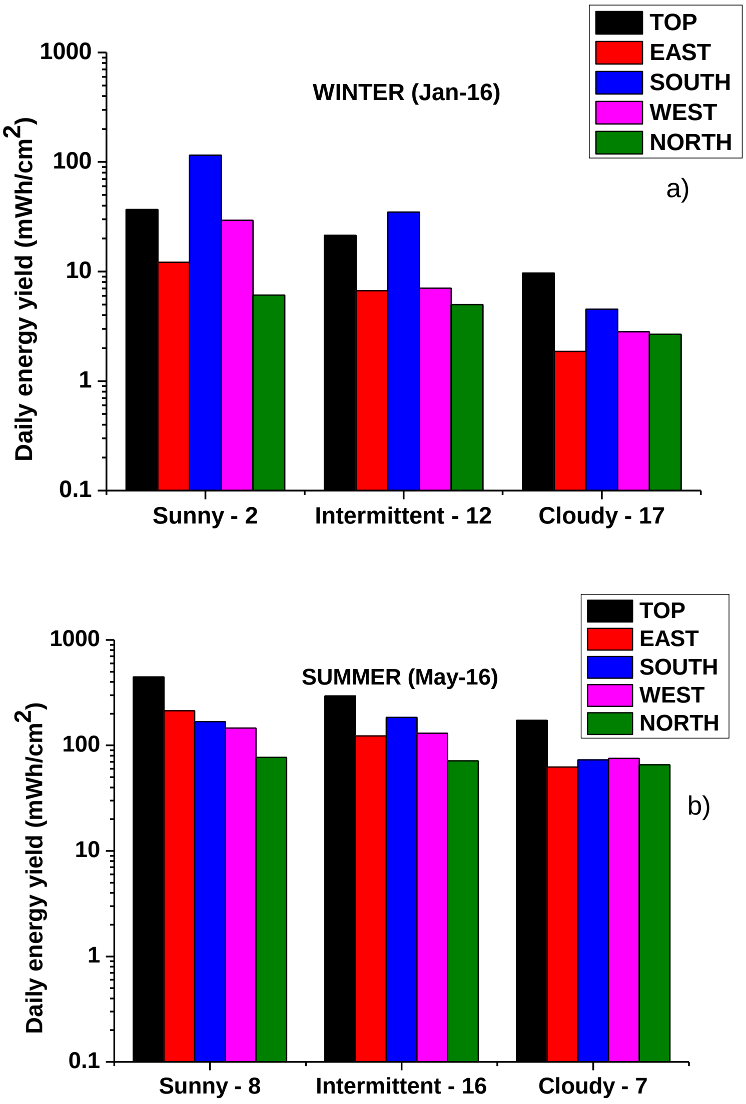

Figure 5.14 *– a) and b) bar charts illustrate the energy yield (mWh/cm^2) defining the accumulated power under three distinctive categories (sunny, intermittent, and cloudy).*

If table 5.2 a) is considered it will be seen that in the winter only the top and south fixed modules contribute to most of the power generation where in summer the top facing modules outperform the other orientations in all categories. It must be noted that in summer east, west and south have very similar yield.

5.3.5 Module degradation

All modules were monitored on weekly basis, using a calibrated indoor AM1.5G solar simulator in accordance with ISOS-O1 protocol. Shown in figure 5.15 is the mean drop in the performance of the modules over the course of 8 months constant outdoor exposure. The south facing modules experienced the worst degradation overall compared to all other modules.

The modules with the next worst stability appear to be west and north-facing ones. The likely cause for this is the accumulation of condensed water vapour in early morning. Whilst other modules are likely to experience direct sunlight in the morning, these modules do not. Therefore, these module temperatures remain low in the early morning, and often at temperatures around the dew point.

It is only possible to speculate the causes of the drop-in performance of the south-facing module as the module shows similar degradation characteristics to all other modules, just in a shorter period of time. During the initial 3 months of the test, the south facing module experienced the greatest irradiance, reflected in highest yield during these periods. However, in doing so, the failure mechanisms related to light induced degradation are triggered first and this cascades the continued degradation of the module. It is also possible that this is related to condensation. Based upon wind direction data, the south facing module experiences the least exposure to wind (it is approximately similar in all other directions). Therefore, condensation present in the air to less likely to be circulated by the viscous flow of air around this module.

Over the first three months of the monitoring campaign some defects related to the rigidity of the encapsulation, against the abrasive winter outdoor conditions, were observed. The south positioned modules as shown also in figure 5.15 suffered the most degradation during the winter period. The top PEN barrier protection layer began to fracture as a result of the substantial temperature fluctuation it experienced between night and day times, with negative temperatures in the night-time and sudden high solar irradiation of 476W/m^2 at 10:40, figure 5.10 and figure 5.11.

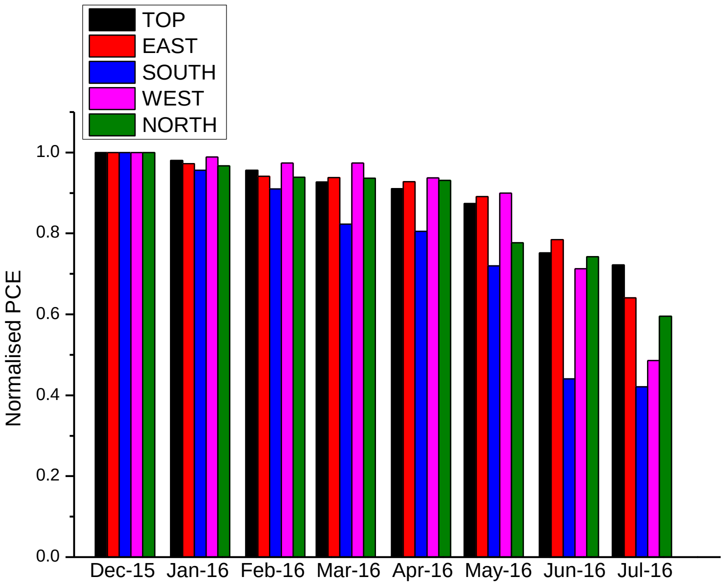

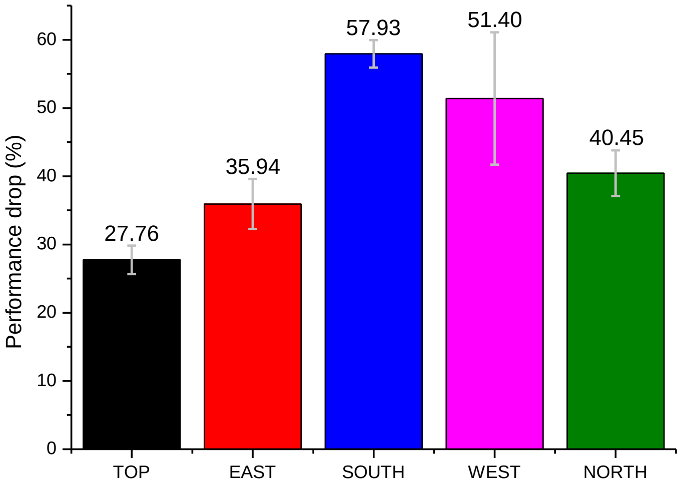

***Figure 5.15** – (Top) Module degradation as a function of month and position, (Bottom) averaged performance decrease with deviation. South suffers the worst degradation followed west and north facing modules due to the higher morning condensation which is not evaporated by the sun during the morning periods.*

Figure 5.16 shows the damage of the contraction and expansion experienced by the PEN material observed three months after the beginning on the experiment. The modules were disconnected and the top surface was analysed using optical microscopy, figure 6.16 d). It clearly shows the amount of fracturing along the plane.

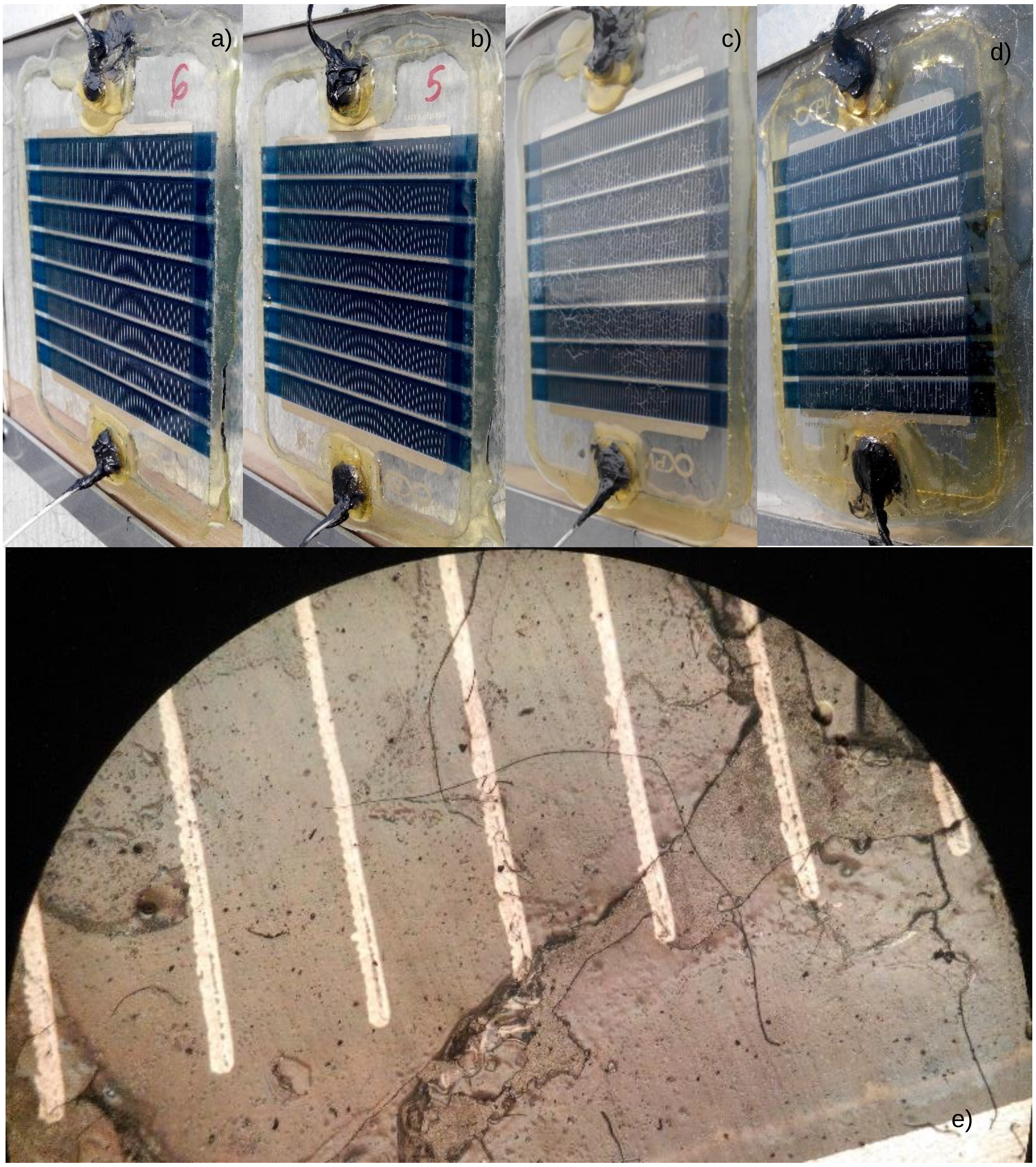

***Figure 5.16** – a,b) South positioned modules at the beginning of the monitoring campaign and and c,d) three months later. A top surface microscopic image of the fractured PEN layer of one of the modules with a fracture over a portion of the top Ag contacts busbar*

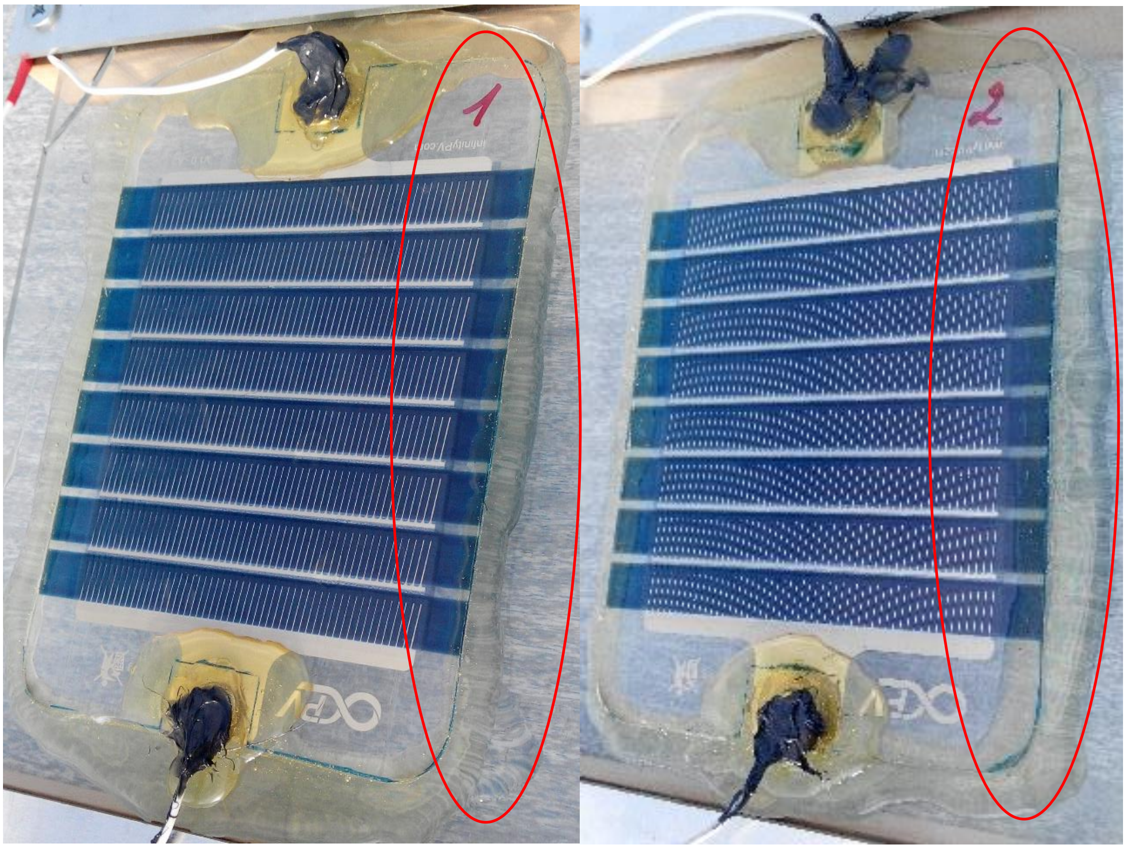

***Figure 5.17** – Horizontal/flat modules with visible encapsulation damages three months after installation*

Despite the rigid encapsulation suitable for the adverse outdoor weather conditions of North Wales, the great amount of rainfall during the winter days followed by low to negative temperatures at night caused regular expansion and contraction to the edge sealant over the PEN barrier, figure 5.17. This process resulted in it's separation from the underlying layer allowing small amounts of water to get trapped between the PEN barrier layer and the OPV module. In the following months the water trapped between the layers ingressed in the modules triggering a long term decay which by the summer time completely delaminated the modules from the glass backplane.

5.4 Fingerprint method for yield calculation

When studying the effect of orientation on OPV modules yield, the energy yield was monitored by collecting the day-to-day IV sweep and calculating the average sum of power conversion efficiencies across all modules positioned at the same direction. This method of assessing the performance of modules is relatively slow and requires daily performance monitoring. An alternative technique was sought that is fast and simple technique to undertake such calculations.

With the intention of devising a way for faster calculation a of the energy yield over longer periods of time and also establishing a way of predicting annual power production, a data analysis technique was developed at Bangor University.

The data collected thus far was investigated in further depth. The daily energy yield gathered was summed to month periods and collated against the measured irradiance at the time of OPV measurement. Figure 5.18 a) and c) show the resulting data for the (a) top and (c) south facing modules. For the consideration of the reader, not all module performance data is shown. Based upon the data in 5.18(a) and (c), line of best fits were applied to model the energy yield as a function of irradiance, which is shown in 5.18 (b) and (d).

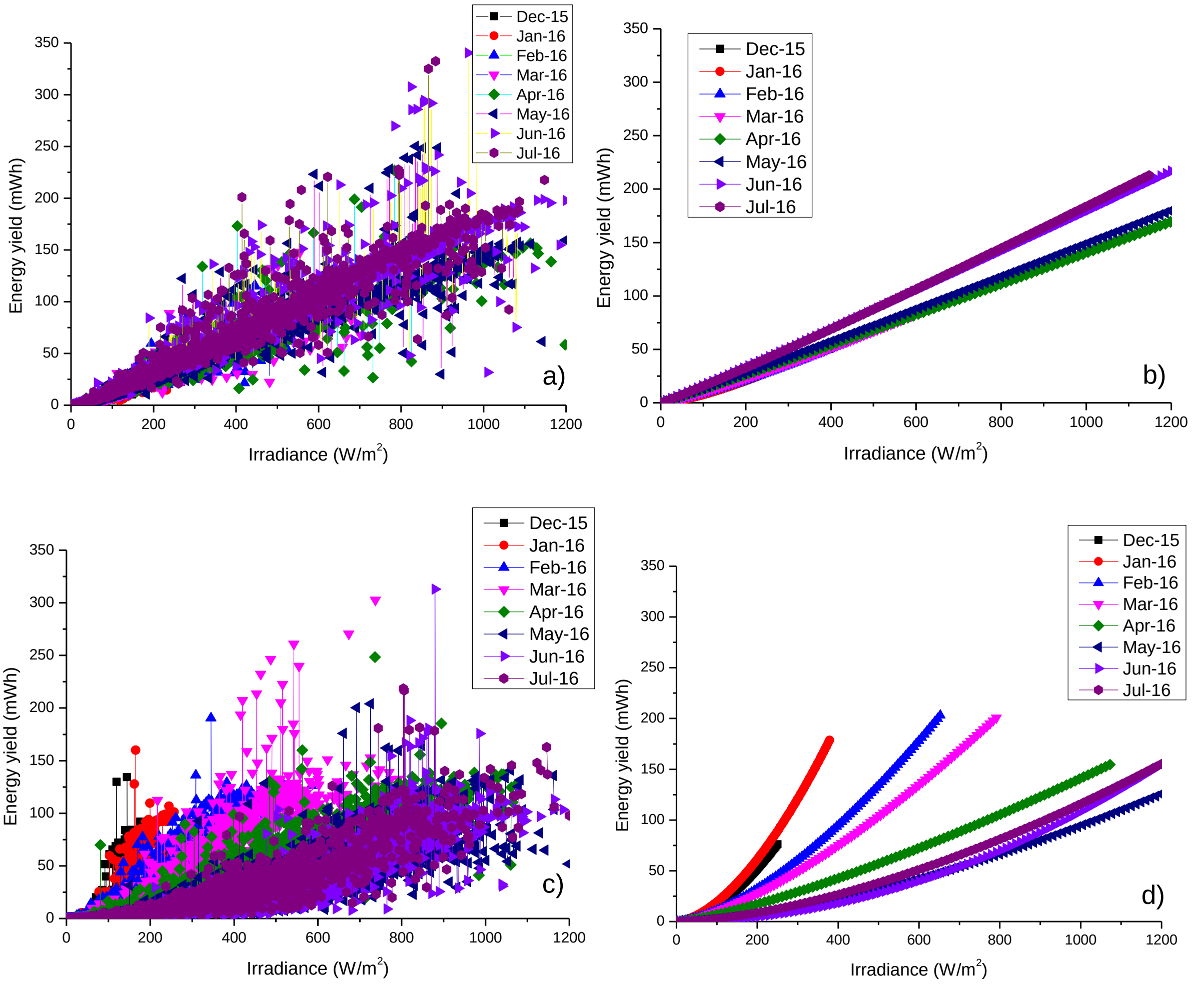

***Figure 5.18** – a) Raw average sum of the energy yield generated by the horizontal/flat modules and c) the south facing ones. b,d) Results after lensing and noise filtration.*

As it can be noted the top facing modules show almost perfectly linear energy conversion response to dose of irradiation where the south positioned modules follow a growing exponential curve. The relationship between energy yield and irradiance can be used to estimate performance at any geographic location if irradiance data is available This process is discussed in the remainder of the chapter.

Firstly, in order for the most accurate assessment to be conducted, the energy yield at standard test conditions (STC) needs to be re-calculated. Shown in figure 5.19 a) is the relationship between ambient and module temperature obtained from one month of data for the top-facing module. Naturally, it was found that the difference between ambient temperature and module temperature depends on irradiance level.

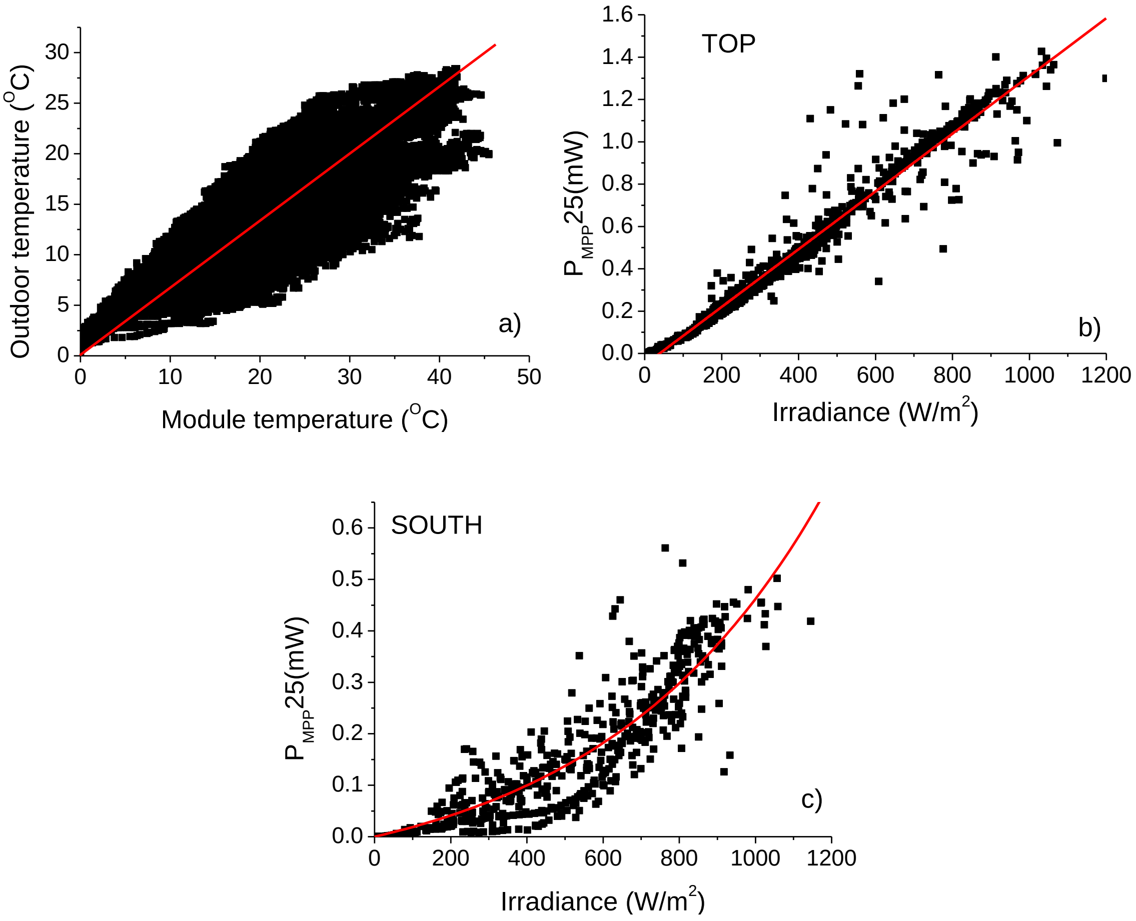

***Figure 5.19** – a) Ambient vs. module temperature relationship during a sunny day in the summer. Average maximum power point Pmpp measured by b) horizontal and c) south facing modules during a sunny day in the summer.*

After removing the white noise created by cloud lensing and fitting a regression line to the energy generation at STC conditions, the average maximum power point (M_{PP}) for each direction was found, figure 5.19 (b-c) representing the results for horizontal and south orientations. This shows the P_{MPP}, as a function of irradiance at the STC conditions. The P_{MPP} was then defined against exposure time at STC, figure 5.20.

Finally, the power generated over the monitoring period had to be divided by the active area of the OPV modules, in order to calcualte the energy yield per unit area and is shown table 5.3. With slight over-estimation of 8mW/cm^2 for the east oriented modules, the other four estimations resulted to be almost identical to the manually calculated results over the entire monitoring period.

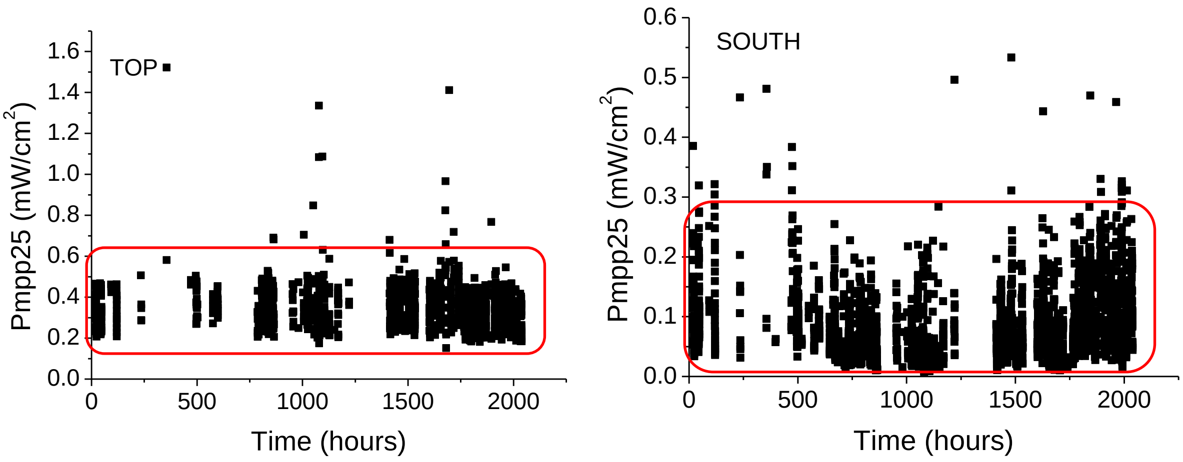

Figure 5.20 *– P_{MPP} at 25^{O}C. The horizontal mounted modules (left) have a very uniform response with an average maximum of 0.5mW/cm^2. The South facing modules (right) experience a slight Pmpp fluctuation during the monitoring period and have an average maximum of 0.275mW/cm^2*

Energy yield generation (mW/cm^2)	***TOP***	***EAST***	***WEST***	***NORTH***	***SOUTH***
8 month study	*453.40*	*189.76*	*226. 70*	*91.80*	*224.56*
Fingerprint method	*456.12*	*197.86*	*227.10*	*92.24*	*227.13*

Table 5.3 *– Comparison between power generation data collected over the period of eight continiuos months and the fingerprint method which requires data from only one sunny summer day in order to predict the power to be generated over a desired period*

5.5 Conclusion

This chapter demonstrates some of the first outdoor lifetime studies of PSC modules and the comparison between conventional MAPI and FMC devices is discussed. Over the course of nearly a month the degradation of PSCs was monitored and analysed. It was seen that if well encapsulated the FMC modules have a better chance of survival exposed to the harsh outdoor conditions.

The second part of this chapter focuses on the studying of OPVs with the intention of their application into Building Integrated Photovoltaics (BIPVs). The performance parameters demonstrated a possible benefit in applying photovoltaics onto all possible sides of a building façade mainly due to power generation attained by east, west and horizontal in the summer time and east, west and south in the winter period. The degradation depending on orientation was also discussed and it was seen that south sustains the worst degradation mainly due to the solar insolation in the winter time.

In the third part of the chapter a novel method for predicting BIPV performance based on OPV anywhere around the world was demonstrated, the results of which showed a very accurate estimation of the annual energy yield production based only on metrological data, sample temperature and the energy yield of a module taken on a sunny day.

Chapter 6. Accelerated Lifetime Testing (ALT) of Organic Photovoltaics and Perovskite solar cells

6.1 Introduction

Over the past 5-10 years OPVs and PSCs attracted the attention of scientists due to the potential of these technologies for energy harvesting, generation and BIPV. Nevertheless, most R2R manufacturers focus their R&D efforts on upscaling and commercialisation [229]–[231]. Still, the stability and lifetime of these products remains a critical issue for both researchers and industrialists.

In order to commercialise a PV product for outdoor deployment, manufacturers must have predictive aging models which help them to estimate warranty periods. The most common approach for the latter is indoor ALT using meta data analysis [113] and round-robin experiments [129], [152]. ALT assesses the strength and flaws of materials and devices demonstrating the suitability of the subject under investigation to the environment it will be exposed to [232], [233].

This chapter aims to further previous knowledge in the area by developing quantitative accelerated life testing (QALT) models to predict the lifetime of OPV modules under normal operating conditions by relating degradation at an elevated level to expected degradation in a 'normal operating' condition. This chapter reports the use of analytical methods to analyse collected experimental data during several outdoor and indoor monitoring campaigns. We estimated that at least 50 reproducible modules are needed for such work. Therefore, no PSCs were used for this work as there are insufficient samples for conducting a life testing campaign as this technology is at an early stage. Therefore, work was conducted using the 'freeOPV' module supplied by DTU. Furthermore, data was received from Prof Krebs, who had already conducted some testing at DTU prior to the start of the PhD. The combination of data from his group and the data from work conducted during this PhD is used for analysis in this chapter.

6.2 Data acquisition

All data was acquired in the manner described in the experiment. However, to further improve the life test fitting models, additional data was sought from Frederick Krebs group at DTU. As a result of the analysis conducted, a number of different 'datasets' was produced. All of the experiments conducted by DTU have been undertaken in accordance with ISOS testing standards. Shown in table 6.1 are number of modules used each dataset. Furthermore, in table 6.2, the performance of each of these modules is summarised. To summarise each dataset; dataset 1 was all different types of module (spin coated, mini-roll coated and roll-to-roll coated, and were all made and measured at DTU. Dataset 2 selected only roll to roll module types from DTU. Dataset 3 used a combination of DTU and BU data. Finally, dataset 4 only used BU data.

	Dataset 1-D (all DTU data)	**Dataset 2-D (just R2R DTU data)**	**Dataset 3-D (DTU R2R +45/85 data)**	**Dataset 4 (BU)**
No. of modules	54	6	9	12

	Dataset 1-L (all DTU data)	**Dataset 2-L (just R2R DTU data)**	**Dataset 3-L (DTU R2R + BU data)**	**Dataset 4-L (BU data) - using sulphur**	**Dataset 5-L (BU data) - using halogen light soaker - T_{80}**	**Dataset 5-L (BU data) - using halogen light soaker - T_{50}**
No. of modules	36	4	7	15	15	15

***Table 6.1** – Data compiled from multiple sources from modules aged without light in the presence of temperature and humidity (top) and modules subjected to light soaking only (bottom)*

	PCE %	**J_{SC} (mA/cm^2)**	**V_{OC} (V)**	**FF (%)**	**Area (cm^2)**	**Sample quantity**
Spin coated normal geometry (DTU)	2.31 ± 0.38	8.57 ± 0.82	0.53 ± 0.04	51.25 ± 7.36	0.25	15
Spin coated inverted geometry (DTU)	1.76 ± 0.44	6.90 ± 0.95	0.55 ± 0.07	46.25 ± 7.76	0.25	20
Mini roll coated (DTU)	1.48 ± 0.16	6.07 ± 0.73	0.48 ± 0.04	49.58 ± 2.83	1	43
OPV module (DTU & BU)	1.86 ± 0.06	5.79 ± 0.20	0.53 ± 0.04 (per cell)	60.6 ± 3.20	57	9

***Table 6.2** – Summary of the averaged performance of the module data used for this study*

6.3 Data analysis

After concluding a number of indoor and outdoor OPV campaigns, the gathered data was processed using commercially available reliability and statistical software purchased from Reliasoft. After processing, a suitable life test model was chosen which accurately modelled the life degradation characteristics from literature [110], [129], [231]. The model was then optimised using maximum likelihood estimation (MLE). Using an MLE allowed for the best fit for a particular lifetime model to be obtained. Using the lifetime model's parameters, the lifetime at standard test conditions (STC) of the examined products can be extracted.

The STC were taken from the weather data generated by our weather station, Davis Inc. 'Vantage pro' and synchronised with our calibrated silicon reference cells from IMT-solar GmbH [157]. In order to compare the processed life estimation with the gathered outdoor data, the lifetime model was used to calculate the time to failure of 63% of the modules to T_{80} and T_{50}, which often is defined as B63% [234].

Location	**Mean temperature (K)**	**Mean RH (%)**	**Mean Irradiance (W/m^2)**
Bangor, Gwynedd (summer)	289K	76	185
Bangor, Gwynedd (winter)	280K	83	81

Table 6.3 *– Mean weather conditions in Bangor, Wales in the summer and winter period*

6.4 Developing life test models from ISOS standard testing

Life-test models are used for relating the degradation measured at a high stress level to that measured under normal operating condition or lower level. ALT can be separated into two branches, quantitative and qualitative ALT. Quantitative ALT is used for predicting the lifetime of products at STC where qualitative studies the failure mechanisms regardless of the lifetime of the tested samples.

Currently, there is lots of data produced by groups such as as those led by Prof Fred Krebs at DTU. This gives a large database of degradation values to analyse and then to form lifetest models that could predict ageing in certain environments. Most testing has been conducted relative to ISOS-D (darkness) or ISOS-L (light) testing. The data collated for ISOS-

D testing could be used to predict degradation due to thermal-humidity effects and data from the ISOS-L testing could be used to estimate the degradation due to light-induced effects. By using such a life test model, performance under normal operation conditions can be used to quantify the lifetime of the OPV [235], [236]. In addition to a lifetest model being selected, a probability density function (pdf) needed to be selected to define the failure rate at a particular stress level. For this we used a 2-point Weibull pdf, as shown in equation 6.1, where β is defined as the shape parameter, η is the scale parameter, t is the time and is the f(t) is the probability of failure.

$$\boldsymbol{f(t) = \frac{\beta}{\eta}\left(\frac{t}{\eta}\right)^{\beta-1} e^{-\left(\frac{t}{\eta}\right)^{\beta}}}$$

equation 6.1

6.4.1 Temperature – Humidity (T-H)

Most ISOS testing has been conducted at standard test conditions such as 65%^{O}C-85%RH and 65^{O}C (with no humidity). This makes fitting life-test models difficult as there is a wide test range between the testing standards. Therefore, additional tests were conducted by BU at an intermediate temperature level, 45%^{O}C-85%RH and an intermediate relative humidity level, 65^{O}C-65%RH. This data was used in dataset 3 and 4. For life-test model fitting a combined life-stress with temperature and humidity components along with fitting parameters was used which is shown in equation 6.2. The mean life is shown as a function of temperature (T) and humidity (H). A and Φ are fitting parameters. b is another fitting parameter which is also known as the activation energy for humidity. Shown in equation 6.3 is the AF, which shows how much the degradation is accelerated by increasing the stress level, as compared to normal operating conditions.

Using equation 6.2, the lifetime of the OPV can be plotted against stress level (i.e. temperature or humidity), when the other stress level is kept constant. This is shown in figure 6.1 which shows the mean life versus temperature (top) and relative humidity (bottom). This is only showing the dataset 3. The methodology in analysing the results in figure 6.1 can be found in section 2.6.1. As to be expected, by increasing the stress level, the expected life of the module decreases.

$$\boldsymbol{L(V,H) = Ae^{\frac{\emptyset}{T}+\frac{b}{H}}}$$

equation 6.2

$$AF = \frac{L_{USE}}{L_{Accelerated}} = \frac{Ae^{-\left(\frac{\emptyset}{T_u}+\frac{b}{H_u}\right)}}{Ae^{-\left(\frac{\emptyset}{T_A}+\frac{b}{H_A}\right)}} = e^{\emptyset\left(\frac{1}{T_u}-\frac{1}{T_A}\right)+b\left(\frac{1}{H_u}-\frac{1}{H_A}\right)} \qquad \text{equation 6.3}$$

Outdoor test number	Date	Median irradiance (kW/m^2)	Median Relative Humidity (%)	Median Temperature (K)	B(63)(hours)
1 (dark)	Jan 2017	N/A	79%	282K	480
2	July 2013	0.277 (0.281)	74%	291K	352 (428)
3	July 2014	0.260 (0.260)	76%	288K	368 (703)
4	June 2016	0.217 (0.243)	75%	289K	228 (732)

***Table 6.4** – Experimental data obtained from outdoor testing at Bangor University (BU). Median irradiance, relative humidity and temperature over the testing period are shown and time taken for 63% of modules to reach the point of failure time are shown B(63). For the latter, failure time is defined as T_{80} or (in brackets) T_{50}. Note: The B(63) times for test 2-4 were calculated excluding non-daylight hours, so assumes only light-induced degradation of modules.*

	Dataset 1 (all DTU data)	Dataset 2 (just R2R DTU data)	Data set 3 (DTU R2R +45/85 data)	Dataset 4 (BU)
β	1.68	1.37	1.38	3.81
η	15	196	176	915
b	375	46	166	140
Φ	29	915	2785	3748
Φ/T	0.10	3.24	9.87	13.29
b/H	4.75	0.58	2.10	1.77

***Table 6.5** – Fitted parameters obtained using mean likelihood estimation (MLE) for Dataset 1-4 for temperature-humidity analysis. β is defined as the shape parameter, η the scale parameter from the Weibull 2-point probability distribution. The values of b and Φ are also fitting parameters from the temperature-humidity model in equation 6.2.*

The fitting parameters for these figures is shown in table 6.6. The shape parameter of the pdf **β** is in all cases is greater than 1, which, according to literature [237], indicates that the tested OPVs are degrading gradually in time, 'wear-out', and not suffering from an early-life failure. If for example β<1 the failure rate would decrease in time so the functioning samples. If β=1 the failure will have a constant rate. The scale parameter η enables direct comparison between experimental data in table 6.4 and predicted life from table 6.5. The fitted parameters for Dataset 2, 3 and 4 provide the closest simulated lifetime to experimentally obtained outdoor data, by comparing the value of simulated to experimental values of η.

B/H and Ø/T show that temperature or RH do not have a considerable impact to the degradation of the modules. According to the literature [237] **Φ** and **b** represent the slope of the lines in the T-H graphs above in figure 6.1. **Φ** represents the slope line for the life plot versus temperature and **b** represents the slope line for life versus humidity when the factors are individually tested by keeping the second factor constant. The higher the resulting values for both **Φ** and **b** the higher the dependency of life on the respective factors.

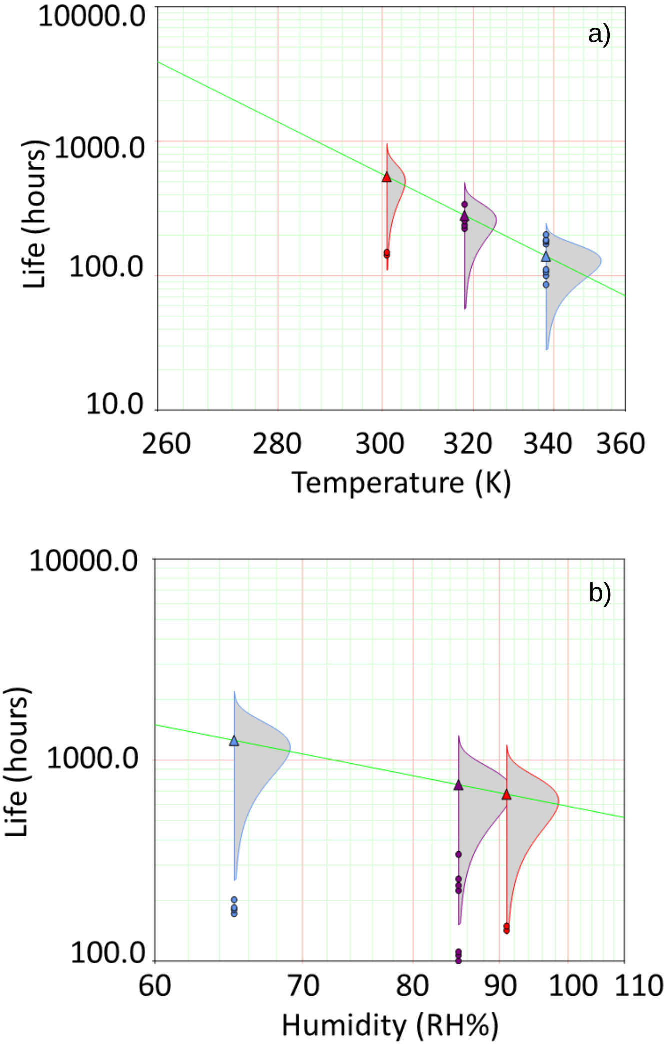

***Figure 6.1** – Lifetime prediction to 80% of initial value (T_{80}) as a result of a) temperature and b) relative humidity.*

Dataset 4 in table 6.5 shows an overestimation for η which is due to the limitation of factors considered in this experiment which is not taking into account factors such as thermal cycling stress and also condensation. The presented predicted lifetime is only accurate when the computed factors is equal to real life situation.

The AF for a T-H relationship is shown in equation 6.3. In the AF equation the fitting parameters are **b** and $\mathbf{\Phi}$. $\mathbf{T_u}$ and $\mathbf{T_A}$ is the temperature at normal stress and accelerated temperature level, respectively. $\mathbf{H_u}$ and $\mathbf{H_A}$ are the RH at normal stress and accelerated stress, respectively.

The AF can be used with a range of stress factors, however, when one factor is being analysed the other is kept constant. The data in figure 6.2 shows how AF changes as a function of humidity and temperature as the other factor is kept constant. The data in this figure can provide a straightforward and rapid technique for predicting the ageing for a range of different stress conditions. It is apparent that both the temperature and humidity have an excellent relationship with AF.

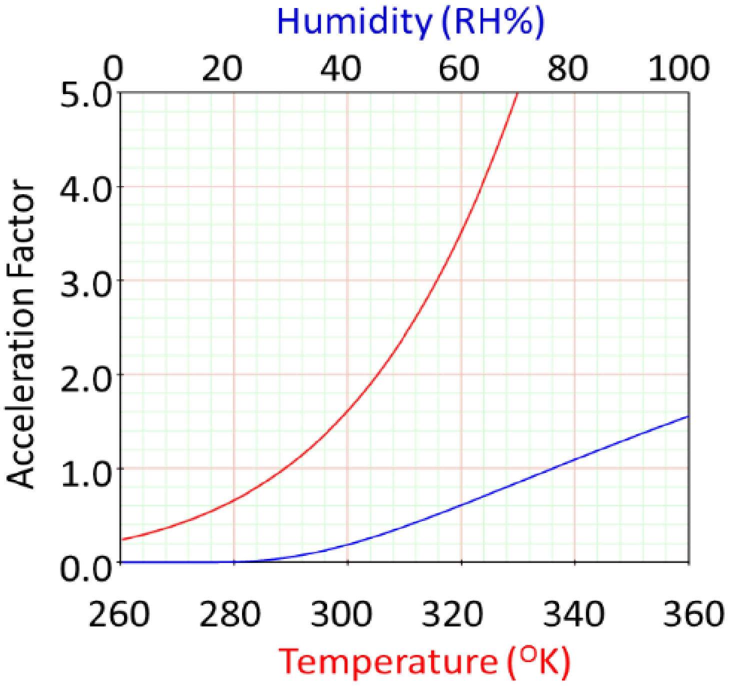

Figure 6.2 *– Acceleration Factor as a function of temperature and RH humidity.*

6.4.2 Light degradation analysis using the Inverse Power law (IPL)

For nonthermal stress factors such as voltage or pressure, an Inverse Power law (IPL) is model most commonly used to relate stress levels to the mean life. Shown in equation 6.4 is the IPL, where $\boldsymbol{K}$ and $\boldsymbol{n}$ are fitting parameters and I is the irradiance level in mW/cm^2. The parameter, $\boldsymbol{n}$, is used to determine the effect of stress on life, such that when $\boldsymbol{n}$ is high, then a tested device would experience a much shorter lifetime of the module.

$$\boldsymbol{L(I) = \frac{1}{KI^n}} \qquad \text{equation 6.4}$$

$$\boldsymbol{AF = \frac{L_{USE}}{L_{Accelerated}} = \frac{\frac{1}{KI_O^n}}{\frac{1}{KI_A^n}} = \left(\frac{I_A}{I_O}\right)^n} \qquad \text{equation 6.5}$$

K – fitting parameter, $\mathrm{I_O}$ is the use stress, $\mathrm{I_A}$ is the accelerated stress

	Dataset 1 (all DTU data)	**Dataset 2 (just R2R DTU data)**	**Data set 3 (DTU R2R + BU data)**	**Dataset 4 (BU data) –using sulphur plasma**	**Dataset 5 (BU data) –using halogen light soaker- T_{80}**	**Dataset 5 (BU data) –using halogen light soaker – T_{50}**
$\boldsymbol{n}$	0.65	0.81	0.91	0.71	0.80	0.68
β	1.1	1.3	1.55	2.1	2.37	3.15
η	261	282	96	37	444	555

***Table 6.6** – Fitted parameters obtained using mean likelihood estimation (MLE) for Dataset 1-5 for light degradation analysis. β is defined as the shape parameter, η the scale parameter from the Weibull 2-point probability distribution in equation 6.1. The values of A, B and Ø are also fitting parameters from the temperature-humidity model in equation 6.2.*

Table 6.6 demonstrates five sets of data which were for analysis with the IPL model in equation 6.4. In the table of specific light sources was testing is noted, as you do get spectral variations from the different light sources used during the test. The data in set 1 and 2 were irradiated in an indoor UV irradiation chamber (in DTU) where sets 3 and 4 were light soaked under a sulphur-plasma lamp. Dataset 5 was aged in a halogen lights soaker. As the case of the temperature-humidity tests, the values show **β>1**. This supports the previous few that early life failures are not significant in OPVs and the degradation is driven by wear out. A further important point from table 6.6 is that the value of $\boldsymbol{n}$ is always less than one. This is a very significant result and hasn't been noted before. This shows that as a tester keeps increasing light degradation, the rate in degradation drops. This is particularly significant result for those who use concentrated sunlight for testing, as it shows that increasing irradiance follows a 'law of diminishing returns'.

In Figure 6.3 a), the mean life as a function of irradiance is shown using the results from dataset 5. As to be expected, as the irradiance level is increased the degradation is shown to increase significantly as well. This is to be expected as light as a significant factor in the degradation of OPV's. In figure 6.3 b) the AF calculated using equation 6.5 as a function of irradiance is also shown. As discussed previously, due to the fact that $n < 1$, this shows a sublinear relationship and that effectively increasing the light level results in a reduction in light induced degradation. When comparing the values of $\boldsymbol{n}$, it is evident that for dataset 3 and 4, the values are far-off what we expect. However, datasets 1-2 and 5 actually provide relatively close match.

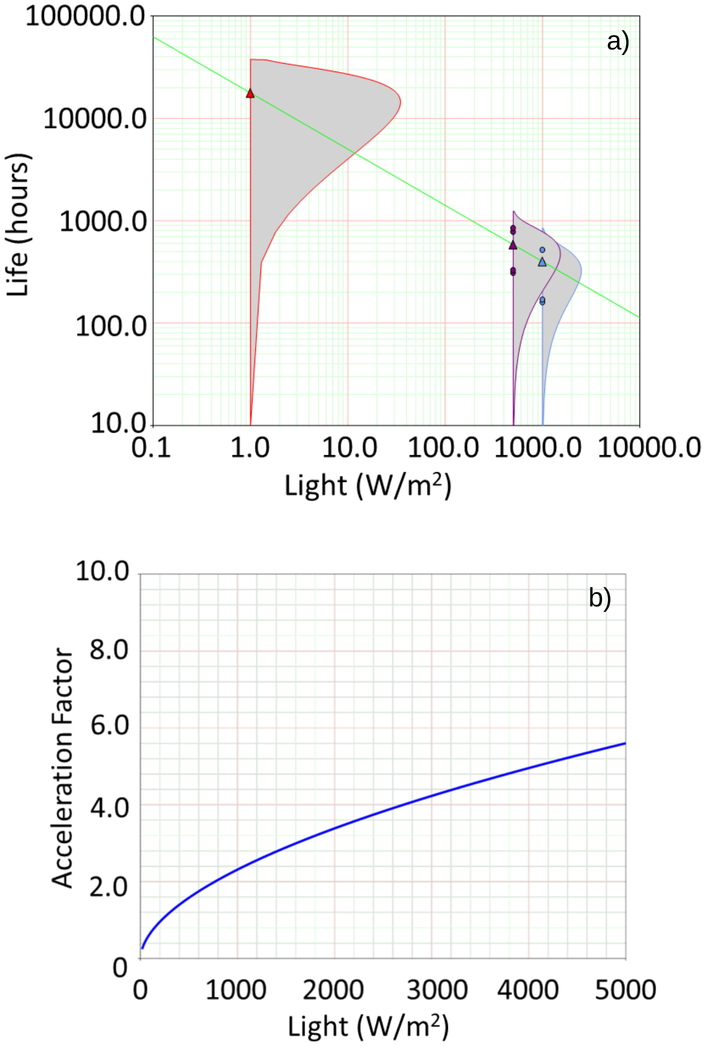

Figure 6.3 *– a) Life versus light dose and the expected life to 80% of the initial performance. b) The AF on the modules depending on irradiance level.*

6.4.3 Temperature-light (T-L) degradation

One of the limitations of the IPL law is that it doesn't include thermal stresses. When studying the degradation under light soaking, the temperature of the modules increases during testing.

Therefore, degradation during light soaking is both light induced and temperature induced. When a thermal and non-thermal stress factors are combined, the Arrhenius-IPL relationship [238], equation 6.6, must be used.

$$\boldsymbol{L(I,\, T) = \frac{C}{I^{n} e^{-\frac{D}{T}}}} \qquad \text{equation 6.6}$$

$\mathbf{I}$ – non-thermal stress, $\mathbf{T}$ is the thermal stress, $\mathbf{D, C}$ and $\mathbf{n}$ are fitting parameters

$$\boldsymbol{AF = \frac{L_{USE}}{L_{Accelerated}} = \frac{I_A}{I_O}^{n} e^{D\left(\frac{1}{V_O} - \frac{1}{V_A}\right)}} \qquad \text{equation 6.7}$$

For this work we used a 2^2 full-factorial design to design the experiment prior to initiation [239]. Therefore, the modules are tested at two different irradiance levels to different temperatures; in this case we used 0.25 Sun/45^{O}C, 0.25 Sun/65^{O}C, 0.5 Sun/45^{O}C and 0.5 Sun/65^{O}C. The results for the fitting parameters shown in table 6.7 The same pattern is shown with the value of β>1, indicating the failures are due to wear-out and not an early life failure. The other values including, n, C and D are fitting parameters.

Table 6.8 shows a comparison of the results from the simulated data with both the IPL and T-L models. While the T-L results seem worse compared to the IPL model the T-L model provides a much more reasoned approach to light induced degradation analysis. The T-L modelling can be used as an alternative for predicting degradation in different climatic conditions [157].

	T_{80}	**T_{50}**
D	4463	2923
c	3.6e-5	0.013
$\boldsymbol{n}$	0.66	0.59
β	5.8	4.98
η	498	733

Table 6.7: *Fitting parameters for the Temperature-Light (TL) relationship using the Weibull 2-point PDF. Fitting parameters obtained for module degradation to T_{80} and T_{50}.*

Test run	**Median irradiance to T_{80}**	**Experimental η – T_{80}**	**Simulated η – T_{80}**	**Median irradiance to T_{50}**	**Experimental η – T_{50}**	**Simulated η – T_{50}**
Inverse Power law (IPL)						
July 2014	0.277 Sun	352	397 (+12%)	0.281 Sun	428	500 (+16%)
May 2015	0.260 Sun	368	418 (+13%)	0.260 Sun	501	527 (+5%)
June 2016	0.217 Sun	228	483 (+115%)	0.243 Sun	838	552 (-35%)
Temperature-Light (TL) model						
July 2014	0.277 Sun	352	424 (+20%)	0.281 Sun	428	652 (+52%)
May 2015	0.260 Sun	368	442 (+20%)	0.260 Sun	501	703 (+40%)
June 2016	0.217 Sun	228	498 (+118%)	0.243 Sun	838	733 (-13%)

***Table 6.8** – A comparison of experimental values of versus simulated values of η can be calculated for the three outdoor measurement campaign at T_{80} and T_{50} for the Inverse Power law (IPL) and Temperature Light (TL) model. For the IPL, dataset 5 and 6 was used for the fitting parameters (see table 6.6). With exception to June 2016, T_{80} simulation, or values of η are predicted to within 35%. For the TL, whilst the relative prediction is slightly worse than the IPL model, the model provides a more robust technique for predicting light induced degradation at normal operational temperatures.*

6.5 Analysis using life test models

Life models provide some interesting data for analysis; however, these can be used for better understanding of how the OPV modules can exist in real life conditions and provides data that can be of use to the community.

6.5.1 Assessing the severity of ISOS tests

One of the first uses of the life test models is that they can be used to assess the relative severity of existing standard tests. Currently there is no work being undertaken to calculate the acceleration factor of the different ISOS test standards. In order to assess the severity of the ISOS test protocols, I calculated the number of hours required indoors to replicate the same stress levels as an for an outdoor degradation test to be conducted based on median weather data taken from June 2014 in Bangor, Gwynedd. Therefore, the AF was calculated for each standard test condition and are summarised in table 6.9.

The shelf life test ISOS-D1 shows a AF of less than 1 which indicates a reduction of degradation when compared to outdoor degradation. This is not surprising as it is a shelf life test. With increasing the ambient temperature in ISOS-D2, the AF approaches 2 indicating that the degradation indoors becomes faster compared to outdoor exposure. ISOS-D3 with elevated humidity and temperature produces an AF of over 12 which compares to 1 month accelerated degradation which outdoors will take one full year.

Further calculations were obtained of the ISOS-L standards using the TL model. Due to the reason of comparing ALT to ambient exposure (L1) only ISOS-L2 and ISOS-L3 were tested. Both ISOS-L2 and ISOS-L3 result show high AFs; ISOS-L2 shows an AF of 15 which translates into just over 23 days of testing to fulfil 1 year of outdoor testing. And ISOS-L3 results in an AF of 25 which means that one year of outdoor ageing can be conducted in around 15 days of indoor test.

Test name	**Temperature (C)**	**Relative Humidity (%)**	**Irradiance (kW/m^2)**	**AF**	**Test hours needed for 1 year outdoor simulation**
ISOS-D-1	25	50	n/a	0.45	19393
ISOS-D-2	65	50	n/a	2.00	4377
ISOS-D-3	65	85	n/a	12.11	717
ISOS-L-2	65	n/a	1	15.70	558
ISOS-L-3	85	50	1	24.70	355

Table 6.9 *– Acceleration factors for ISOS-D and ISOS-L tests based upon the temperature-humidity model and temperature-light model, respectively. Included are the test hours required to simulate 1-year outdoor performance in Bangor, Wales using each ISOS test.*

6.5.2 Variability of degradation in different climates

A further use of the life test models can be to predict the ageing in different environmental conditions around world. To achieve this, the AF has to be specifically calculated using the fitting parameters obtained for the IPL and temperature humidity models, the resulting expression being equation 6.8. One of the dangers of using this equation is that we have to assume that the light induced degradation mechanisms are independent of the thermal humidity ones. This might not necessarily be true, however, it does provide a relatively simple mechanism for comparing module degradation using different climatic data using defined fitting parameters from tables 6.5 dataset 4 and table 6.6 dataset 5.

$$\boldsymbol{AF = e^{\emptyset\left(\frac{1}{V_O}-\frac{1}{V_A}\right)+B\left(\frac{1}{H_O}-\frac{1}{U_A}\right)}.\left(\frac{I_A}{I_O}\right)^{n}} \qquad \text{equation 6.8}$$

In table 6.10, the calculated values tor the value for **η** (i.e. 63% of the modules to have reached T_{80}) in a range of climates is shown. These are relative calculations based upon a measured experimental result in Bangor, Wales. Two different climates were considered; firstly a sunny and dry climate (Madrid), secondly sunny and humid climate (Rio de Janeiro). It can be seen the OPV module is predicted to be actually more stable in Madrid than in Bangor, due to the dryness of the climate. However, the stability in a climate such as Rio de Janeiro is much lower due to high humidity, highlight high-temperature. The technique for predicted lifetime provides some confidence in being able to predict the stability in different climates based only on meteorological information.

Location	**Mean temperature (K)**	**Mean RH (%)**	**Mean Irradiance (kW/m^2)**	**AF**	**T_{80} (measured or simulated)**
Bangor, Gwynedd (June, 2014)	289K	76	0.185	n/a	41 days (measured)
Madrid (June)	294K	50	0.302	0.77	53 days (simulated)
Rio de Janiero (June)	294.5K	77	0.242	2.11	19 days(simulated)
Bangor, Gwynedd (Jan, 2015)	280K	83	0.081	0.57	52 days (measured) 71 days (simulated)

***Table 6.10** – Simulated ageing of modules in different environmental conditions, relative the degradation measured in Bangor (June 2014). Module lifetime is simulated to be greater in wintertime due to lower irradiance, which is supported by experimental data*

6.5.3 Variation of degradation in different seasons

Predictive modelling can also be applied for examining the effects of seasonal shift to the stability of outdoor exposed modules. Figure 6.4 a) shows the temperature, RH and irradiance shift across 12 months for Bangor, Gwynedd. As it can be seen the RH throughout the year is relatively constant. The temperature fluctuates between 5^{O} and 18^{O} in the winter and summer respectively. The irradiance levels are low in winter time due to the short days and a factor 4-5 times greater in summer time. When the resulting model in figure 6.4 b) is considered it can be seen that the changes in degradation due to T-H is relatively low which can be considered being related to the relatively low range of temperature and RH fluctuation over the course of 12 months. Nevertheless, the T-L model result illustrates a considerable light degradation depending on seasonal change with worst degradation in the summer period driven by irradiation dose which is also supported by the literature [180].

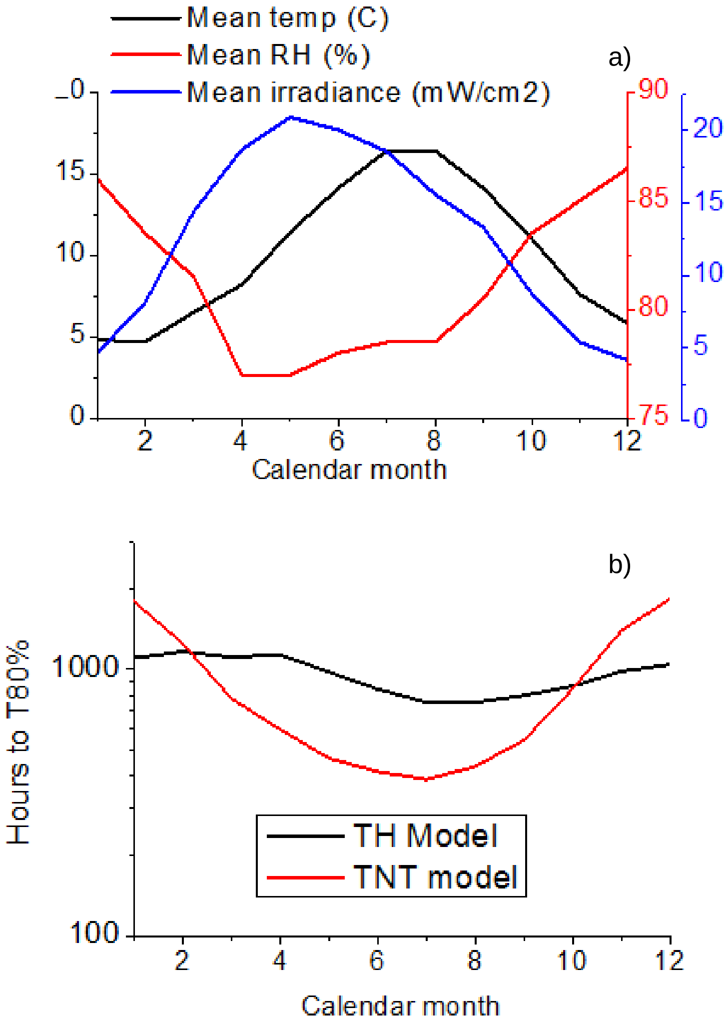

***Figure 6.4** – a) Mean temperature, RH% and In-plane irradiance for Bangor, Gwynedd, UK over a full calendar year. b) Impact on expected life to T_{80} as a function of calendar month as predicted by the T-H and T-L models.*

6.6 Multi-stress testing of OPV modules

With experiencing multiple failure factors, the summed activation energy equates the activation energy required for the triggering of the weakest failure factor. The combination of life distributions can be examined for the definition of only combined effect of multiple failure factors.

So far, the ALT conducted studied a maximum of two stress factors which in essence can be thought of as a flaw in the experimental procedure as light induced, thermal and humidity related induced defects are unlikely to be independent of one another and should be considered simultaneously [157]. There is a dramatic difference between testing modules in controlled environments indoors and installing them outdoors where the devices undergo all available environmental stresses that continuously vary with time including light, temperature and humidity [110], [128].

Having all factors factored in the degradation study allows the examination to investigate the presence of all possible factors interacting with each other [240], [241]. Interaction can be interpreted as the combined effect of multiple factors on a device. When two or more factors are in an interaction it is expected the combination to have the worst effect on the samples. This is particularly important in OPVs as very often interactions increase degradation significantly; for example, when temperature and humidity are simultaneously applied, much greater degradation is observed when compared to a scenario whereby temperature or humidity is increased on their own [156].

In order to fully understand the degradation of a device all individual stress factors and the combination of associated stress factors must be considered. The result should more likely replicate a realistic outdoor environment which will allow the full range of flaws and weakness of a device to be resolved.

6.6.1 Design of Experiments (DOE)/ Analysis of Variance (ANOVA) analysis of degradation

DOE is a useful tool for examining the stress factors which can deteriorate device's integrity and identifies the significant degradation factors which have to be eliminated [239].

ANOVA is a technique which allows the comparison of the degradation of devices under multiple stress levels and defines the significant and non-significant effects of ALT experiments [242].

Furthermore, the understanding of the effects of different variables upon one another can be studied and a 'cause-and-effect' relationship between the independent variables and dependent variables of interest can be developed. To undertake this analysis, both the degradation observed between modules stressed at the same level ('within run variation') and variation caused by changing the stress level ('between run variation') must be calculated. As OPVs have been shown to exhibit large module to module variation, even at the same stress level, one can see the benefit of considering the changes 'in-between run variation', in the context of differences observed in the 'within run variation'.

The experimental data in table A2 (appendix) has been used to examine whether the between-run variation caused by changing the level of the stress factor, is larger than the within-run variation, caused by module-to-module variance. To do this this, the total variation can be defined by calculating the total sum of squares (SS_T). The total sum of squares can be obtained by adding the random variance (SS_E) and the between run variation (SS_R), thus can be defined as $SS_T = SS_R + SS_E$, equation 6.9. SS_E and SS_R are calculated using equations 6.10 and 6.11 respectively.

$$\boldsymbol{\sum_{i=1}^{n}(y_i - \bar{y})^2 = \sum_{i=1}^{n}(\widehat{y_\imath} - \bar{y})^2 + \sum_{i=1}^{n}(y_i - \widehat{y_\imath})^2} \qquad \text{equation 6.9}$$

$$\boldsymbol{SS_E = \sum_{i=1}^{n} e_i^2 = \sum_{i=1}^{n}(y_i - \widehat{y_\imath})^2} \qquad \text{equation 6.10}$$

$$\boldsymbol{SS_R = \sum_{i=1}^{n}(\widehat{y_\imath} - \bar{y})^2} \qquad \text{equation 6.11}$$

By calculating SS_E and SS_R, the mean square of regression (MS_R) and mean square of error (MS_E) can be calculated. The value for MS_R is used to measure the between-run variance that is caused by each stress factor. Additionally, the value for MS_E represents the within-run variance caused by module-to-module variation (or ‘noise’). If these are calculated for each stress factor, then the effect of the significance of that stress factor compared to the effect of variance can be evaluated, which is achieved using ANOVA.

To obtain the MS_E the between run variation SS_E must be divided by its associated degrees of freedom (DoF), equation 6.12. The degrees of freedom are the total samples used for these tests minus the groups.

$$\boldsymbol{MS_R = \frac{\sum_{i=1}^{n}(y_i - \widehat{y_\imath})^2}{1} = \frac{SS_R}{1}} \qquad \text{equation 6.12}$$

The MS_Ron the other hand is obtained by dividing the $SS_R$by its degrees of freedom. The degrees of freedom are the total number of groups (‘test runs’) minus one.

To conduct an ANOVA analysis, F-ratio, equation 6.13, is used to test whether there is no difference between the variance caused by stress factor (e.g. light, humidity, temperature) and the variance caused by noise, the null hypothesis (H_0).

$$\boldsymbol{F_O = \frac{MS_R}{MS_E}} \qquad \text{equation 6.13}$$

The other option or also called the alternative hypothesis (H_1) states that the variance caused by stress factor (e.g. light, humidity, temperature) is larger than the variance caused by noise, in which case the testing is valid [243].

Under the null hypothesis, the ratio follows the *F* distribution. Finally, the P-value is computed from the F-ratio, and this can be used to calculate the difference between the variance caused by the corresponding stress level change and the variance caused by noise.

By applying ANOVA to the data for T_{80} and T_{50} degradation, the following ANOVA table 6.11 was sourced. The sixth column shows the *F*-ratio of each factor. All the values are bigger than 1. The last column is the *P*-value which for all cases is relatively small. A small P-value (typically ≤ 0.05) indicates strong evidence against the null hypothesis, which tells that the null hypothesis is rejected.

Based upon the data obtained, it is possible to conclude that different factors impact the degradation with varying levels of severity as the modules degrade.

The significant effects can be better represented by the use of a Pareto chart [244] as shown in figure 6.5, which lists in order how each environmental degradation factor affects the degradation, over the range selected in table 6.11. It is important to note that this regression analysis was conducted over a finite temperature range and should the temperature ranges alter then the value and type of significant effect might also alter.

		T_{80} values				**T_{50} values**			
Factor	DoF	Sum of Squares [Partial]	Mean Squares [Partial]	P Value	F Ratio	Sum of Squares [Partial]	Mean Squares [Partial]	P Value	F Ratio
A:Temp.	1	939.24	939.24	0.0235	6.2660	0.0026	0.0026	0.0039	11.3805
B:Humidity	1	1303.01	1303.01	0.0094	8.6928	0.0000	0.0000	0.8636	0.0305
C:Light	1	2871.96	2871.96	0.0005	19.1598	0.0025	0.0025	0.0049	10.6362
A • B	1	825.86	825.86	0.0321	5.5096	0.0004	0.0004	0.2171	1.6509
A • C	1	537.17	537.17	0.0766	3.5836	0.0003	0.0003	0.2706	1.3025
B • C	1	1037.43	1037.43	0.0182	6.9211	0.0016	0.0016	0.0191	6.7905
A • B • C	1	582.41	582.41	0.0663	3.8855	0.0000	0.0000	0.7314	0.1221
Residual	16	2398.31	149.89			0.0037	0.0002		
Model	7	8097.10	1156.72	0.0004	7.7169	0.0074	0.0011	0.0057	4.5590
Total	23	10495.39				0.0111			

***Table 6.12** – ANOVA summary of impacting factors and interactions*

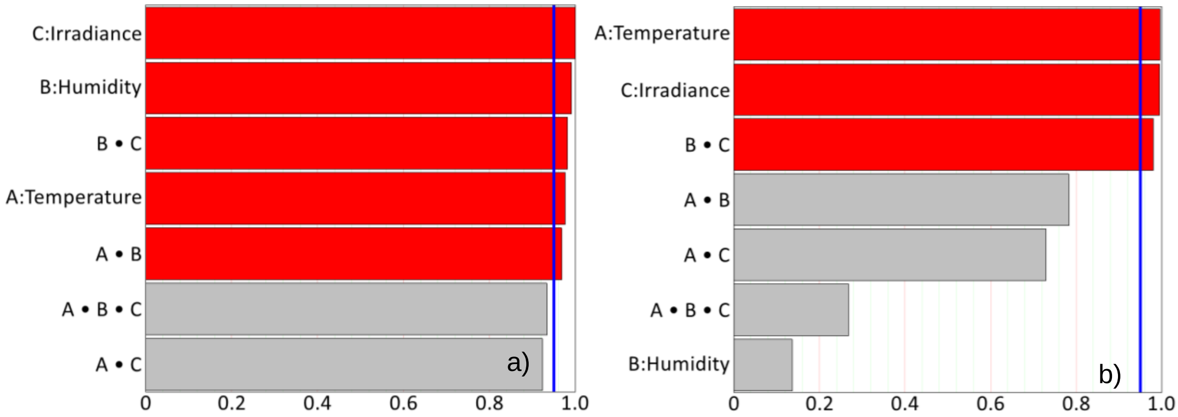

Figure 6.5 *– Pareto chart analysing the a)* T_{80} *and b)* T_{50} *mark of processed data. Results showing individual and combination of the most significant factors deteriorating the OPV modules*

It is worth considering the impact of the factor temperature. Previous studies indicate that temperature does not play a significant impact upon OPV module degradation [156], [161], [245]. Previous reports indicate this conclusion is valid when temperature is the only stress factor. However, it is clear from the data in this experiment is that is possesses a much more complex interaction with other stress factors. In particular, it appears to increase degradation significantly when applied in the presence of either humidity or light. This provides confirmation indicating that to fully resolve all defects that are likely to occur during normal operation, multi-factorial or multi-stress testing is imperative.

6.6.2 Life test models using Generalized Log–Linear (GLL) model

Using multi-stress test data can also be used for predictive ageing. Most lifetime test models only allow for two stress factors to be considered. As a result, a bespoke life-test model was created. The GLL life-stress relationship to evaluate and predict the life of modules in an outdoor environment is proposed. GLL has previously been used for predictive lifetimes of optical components in an outdoor test condition, where a number of environmental factors impact upon stability [246], [247].

The formulation of the general log-linear model begins with the assumption of a log-linear relation for the characteristic life as shown in equation 6.14.

$$\boldsymbol{L(X) = e^{a_0 + a_1 X_1 + a_2 X_2 + a_3 X_3 + \cdots a_n X_n}} \qquad \text{equation 6.14}$$

The coefficients of this equation are the parameters of the life-stress relationship. The variables $X = (X1, X2 \dots, Xn)$ are the covariates. The advantage of representing the characteristic life with the GLL relationship is that relationships such as the Arrhenius and IPL models can be assumed for the covariates by performing a simple transformation. According to previous study [160], the ‘inverse power’ model can be used for light induced degradation and Arrhenius relationships are suited for temperature and RH stresses. In the course of this work, a number of relationships were trialled, however the best fitting was obtained from the data in Table 6.13. The table was obtained by assuming a Weibull distribution, an Arrhenius life-stress relationship for temperature and RH and an inverse power life-stress relationship for light.

	T_{80}	T_{50}
α_0	-2.36	-1.43
α_1	2578.43	2532.87
α_2	-0.03	-0.015
α_3	-0.89	-0.39
η	224.71	835.81
β	1.88	2.80
LK-value	-111.39	-155.23

Table 6.13 – Summary of analysis parameters obtained from the GLL model

Using MLE, the fitting parameters were sought. In table 6.13, the coefficients of each variable are listed along with the fitted parameters from the Weibull pdf.

Here a_0 and a_n are model parameters. As discussed previously the value for η corresponds to the time taken for 63% of the modules to have reached a degradation time (in this case T_{80} and T_{50}). This can provide a direct comparison of experimentally obtained data to compare how the fitted model compares to two outdoor experimental datasets.

Based on the fitting parameters in table 6.13, a set of life versus stress graphs were obtained and shown in figure 6.6 below.

The results were obtained using indoor in-situ accelerated testing data and outdoor test data to improve the regression line fitting of the life test model.

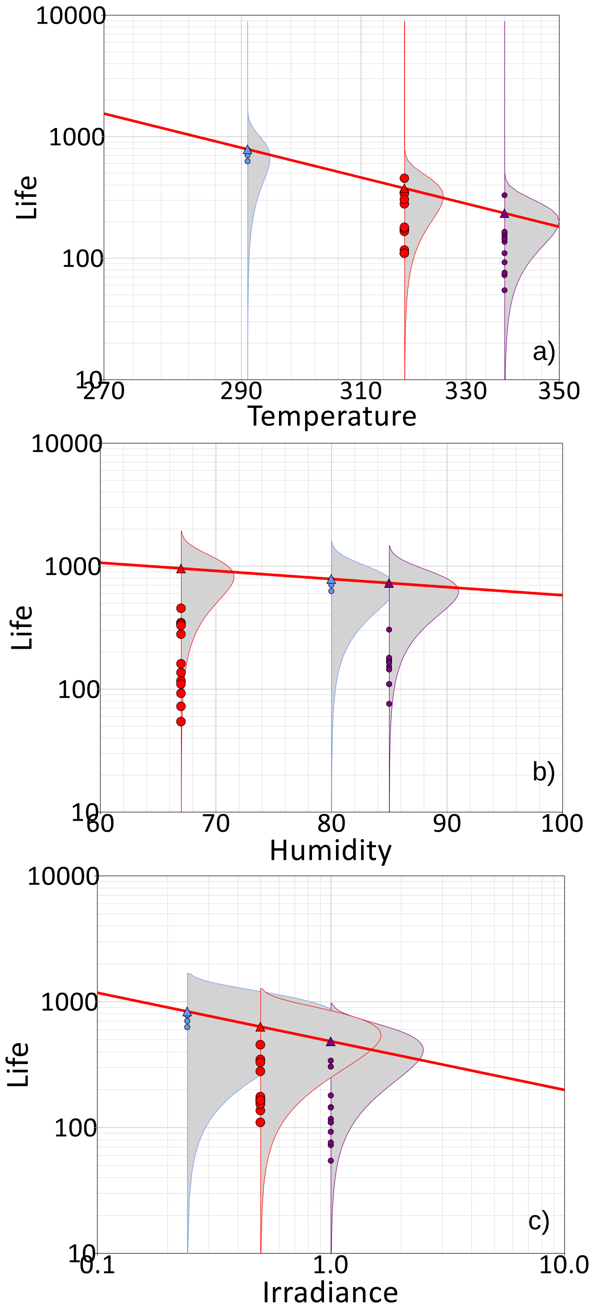

***Figure 6.6** – Live versus stress data generated by the module data up to* T_{50}*. a) representing temperature as a stress factor, b) representing RH affected degradation and c) light dose increase.*

6.6.3 Comparison to field data

AF demonstrating the operational versus accelerated stress levels

The AF is an important characteristic to lifetime analysis as it defines the operational stress level to the accelerated stress level of devices. AF is defined in equation 6.15.

$$\boldsymbol{AF} = \frac{\boldsymbol{L_{USE}}}{\boldsymbol{L_{Accelerated}}} = \boldsymbol{e}^{\emptyset\left(\frac{1}{V_O}-\frac{1}{V_A}\right)+b\left(\frac{1}{H_O}-\frac{1}{H_A}\right)} + \left(\frac{I_A}{I_O}\right)^{n}$$ equation 6.15

Figure 6.7 shows the AF versus temperature, RH and Light individually while the other two stresses are kept constant.

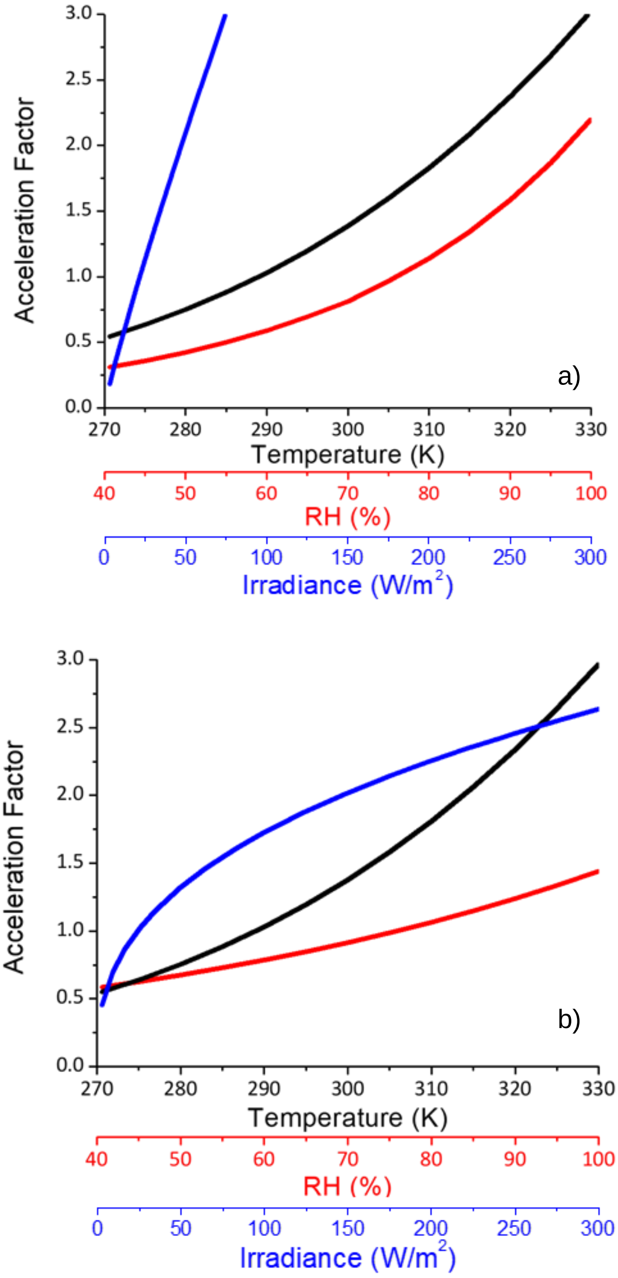

Figure 6.7 *– Acceleration factor as a function of Temperature, RH and Light for a) T$_{80}$ and b)* T$_{50}$ *mark.*

Interestingly it can be noted from the T$_{80}$ data is the exponential increase in the AF with increasing temperature and RH which are almost with the same magnitude. Where the light level increase has a distinct linear relationship. After burn-in elevating temperature has the most prominent effect in stability, contrary to [156], [161], [245] where 100% RH reaches an AF of only 1.25.

Overall module reliability in normal operational conditions

In order to predict the reliability against time of the modules under normal operational conditions, the failure rate can be used to calculate the cumulative failure rate and subsequently the Reliability (between 1.0 and 0.0), as shown in figure 6.8.

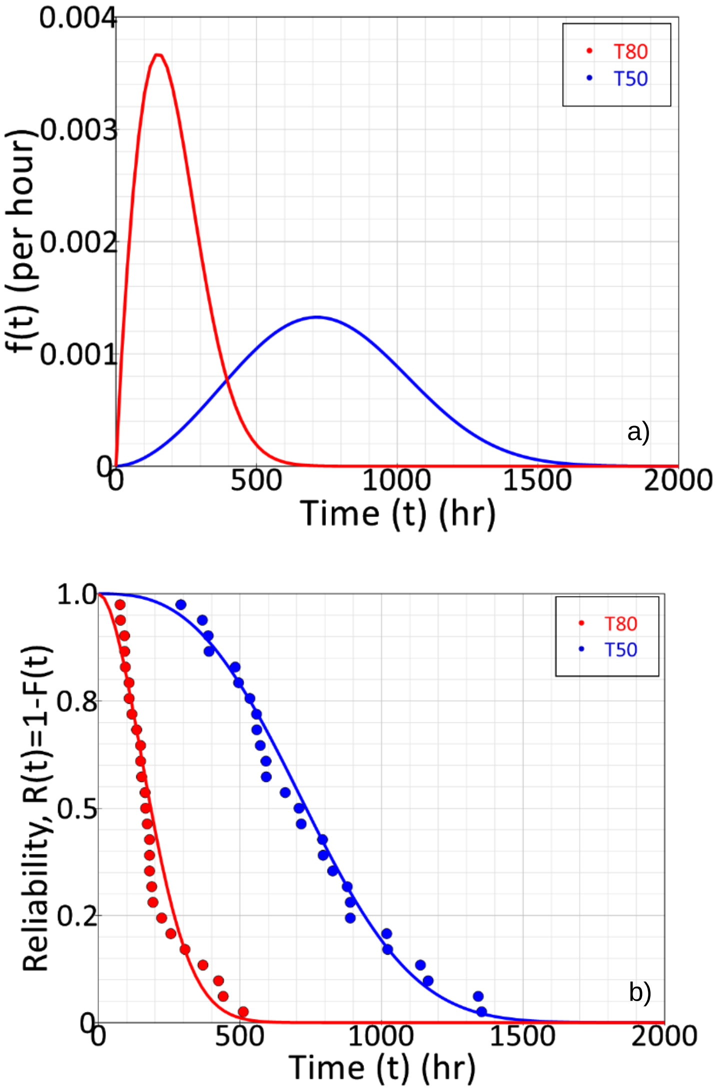

***Figure 6.8** – a) pdf for T_{80} and T_{50}. b) Reliability versus time for T_{80} and T_{50}.*

With using average mean stress levels based on collected weather data with temperature T=289^{O}K, RH=76% and Light dose of 243W/m^2 the following results in figure 6.8

were obtained. It can be seen that by 1500 hours, all OPV modules would have reduced to 50% of their original value.

6.7 Conclusion

This chapter demonstrates the utilisation of commercially available analytical software to predict the lifetime of solar cell modules both exposed outdoors and subjected to ALT conditions indoors. The initial experiments demonstrate the influence of temperature and humidity to the lifetime of devices keeping the test modules in dark conditions. The second experiment then shows the impact of only solar dose. When comparing the acceleration factor results from experiment one and two it can be seen that thermal degradation has the highest impact showing an AF of 5 at only 330^{O}K which level is reached by elevated solar dose to approximately 4.5 Sun. As a result of the finding the impact of temperature and light to the stability is then analysed which demonstrates slightly higher stability compared to the using IPL for light degradation analysis, all due to the balanced conditions the devices are exposed to. The next step of the analysis assessed the ISOS testing protocols, the degradation in different climates and different seasons. The final analysis looks at multi-stress testing demonstrating the importance of combining and using all stress factors when predicting the lifetime of a device, approach which shows the most accurate lifetime estimation figure.

Chapter 7. Conclusions and future work

The work presented in this thesis was focused on the performance monitoring of PSCs and OPVs indoors and outdoors aiming towards lifetime and efficiency assessment and improvement. Both technologies underwent similar degradation paths when exposed outdoors, the main degradation being ingress of oxygen and water leading to photo-oxidation. Regardless, of the encapsulation methods and the materials used, the main failure places occurred at the contacts and sample edges. PSC is a technology which has potential to be inexpensive and simple to manufacture. Upscaled PSCs are currently not as efficient as commercial silicon modules, however, it is anticipated that they will soon reach comparable level of efficiency and stability to become viable for mass production. Nevertheless, the long-term stability of this still relatively young technology is yet not certain. In an outdoor environment, a solar cell needs to be stable against light, humidity, temperature fluctuations and bias, and be able to withstand many extreme conditions which are applied simultaneously. UV light, is a well-known major degradation factor in PSCs.

Before any research on the stability of PSCs could be initiated the most optimal fabrication technique had to be obtained. Following some optimisations, it was found that a proper balance of the content of halide and MAI play a critical role in the performance of manufactured solar cells. After having developed the most optimum fabrication technique, the focus was divided into two parts, initially the fabricated devices were tested indoors at low irradiance and then a set was made and examined in extreme conditions at high irradiance levels, conducted at Ben Gurion University of the Negev, Israel. As part of the initial work the use of LDS coating to replace traditional UV filtering and improve the stability of PSCs was looked at. A number of studies with LDS materials also demonstrate device performance increase, an effect which was not observed in this thesis. The indoor experiments conducted at Bangor University show that LDS coating substantially improves the lifetime of PSCs and show that LDS coated devices have higher PCE compared to using conventional UV filters. The dyes used were selected based on their compatibility with the EQE of $CH_3NH_3PbI_3$ perovskite. The compatibility was analysed based on the figure of merit for every LDS material which was derived using a weighted sum equation.

In the second part of this thesis the outdoor monitoring of PSCs and also OPVs with the intention of building-integrated photovoltaic application is described. BIPV is an ideal market for flexible solution-processed semi-transparent devices which can be fabricated in multiple colours and shapes. The OPV modules used throughout this thesis, over the course of several campaigns were purchased from InfinityPV, Denmark. All outdoor monitoring in this thesis was conducted using a setup installed on the roof of our institute in Bangor, Gwynedd. Two types of PSC modules were monitored (MAPI and FMC). The PSC modules were received as a part of a collaboration between Bangor University and SPECIFIC, Swansea University. The modules manufactured by SPECIFIC, with dimensions 50mm x 50mm x 2mm and a total active area of 13.5cm^2 produced by 5 cells monolithically connected in series and were mounted on a 35^O inclined rack facing due south. The outdoor monitoring of PSCs was conducted over two campaigns between April 2017 until July 2017. In the initial campaign the modules were encapsulated and exposed to the ambient conditions without UV filtration, but showed poor stability. In the second campaign, due to the observed rapid photo-oxidation, all modules included a UV filter purchased from Solaronix SA, Switzerland. The initial efficiency of the modules in the first campaign was 7.0% PCE with ±0.6% standard deviation which demonstrated variation in film qualities from the production process. Detailed device performances including V_{OC}, I_{SC}, FF, PCE and module temperature were recorded and analysed for OPVs, PSCs and p-Si. It was seen that all have a linear relationship when analysing irradiance and module temperature above ambient. It was discovered that PSCs have a negative temperature coefficient which is a typical signature of silicon modules.

Despite robust encapsulation the stability of the modules was very poor and therefore longer-term studies focused on using OPV modules. The OPV modules used for this work comprise of 8 serially connected cells with an active area of 64.8cm^2 and are produced on a R2R plant subsequently laser cut to shape which also provides a degree of edge encapsulation. The main aim of the outdoor monitoring study using OPVs was to define the performance and degradation of modules positioned at multiple sides of a building. The outdoor monitoring experiment was carried out for a period of eight months, December 2015 – July 2016. Throughout the entire period the incident irradiance and weather conditions were monitored alongside the OPV performance which helped us understand the impact of azimuth and altitude onto the efficiency of this type of modules. A total of ten OPV modules were encapsulated and installed on a miniature building prototype which was built and installed on the rooftop of the school of Electronics Engineering at Bangor University. The performance parameters extracted showed a possible benefit in applying photovoltaics onto all possible sides of a building façade mainly due to power generation by east, west and horizontal in the summer time and east, west and south in the winter period. The degradation depending on orientation was also discussed and it was seen that south sustains the worst degradation mainly due to the solar insolation in the winter time.

Finally, a novel method for predicting OPV performance anywhere around the world was demonstrated, the results of which showed a very accurate estimation of the annual energy yield production based only on metrological data, sample temperature and the energy yield of a module taken on a sunny day. In the final experimental chapter of this thesis an accelerated lifetime study on PSCs and OPVs was conducted. ALT is a common technique applied by manufacturers which provides predictive aging models assessing the strength and flaws of materials and devices demonstrating their suitability to the environment it will be exposed to. Using a commercially available analytical software we were able to predict the lifetime of solar cell modules both exposed outdoors and subjected to ALT conditions indoors. The results of this work were a combination of data collected during this PhD and data received from Prof. Krebs from DTU who had already conducted some testing on OPV modules in the past. Initially, two sets of experiments were conducted. In the first set the model created used the ISOS protocols to generate a degradation profile by studying the influence of temperature and humidity to the lifetime of devices keeping the test modules in dark conditions. The second set determined the impact of solar irradiation only. This study showed that thermal degradation has the highest impact on the lifetime of photovoltaic devices. In order to avail of simulating variation of outdoor conditions within the convenience of a laboratory environment a multi-stress test was developed. Using this technique allowed us to most accurately estimate the lifetime of the monitored at Bangor University solar devices.

7.1 Future work

Both PSCs and OPVs are emerging technologies which are a few steps away from becoming commercially available. Yet, both have hurdles related to the long-term stability and efficiency which need resolving. Development of effective encapsulation is of utmost importance in preventing water and oxygen ingress. The use of stable LDS layers or UV filters is essential in order the photo-oxidation to be suppressed. Perovskite is a relatively simple material inexpensive to synthesise which does not require high annealing temperatures. If fabricated in well-controlled environment it is capable of reaching sufficiently high efficiencies which will soon help it take its place on the market alongside silicon PV. During this PhD the positive effects of LDS were seen, however, due to this work being in such an immature state not all LDS materials suitable for perovskite could be applied. Blended dyes could result in much better device protection and could also be able to increase the efficiency of PSCs by increased PLQY. Varying LDS concentration and also the thickness of the coating should be studied in order the most optimal recipe to be obtained.

The next challenge to be addressed will be the use of anti-solvent treatment in manufacturing of single step PSC. Due to time constraints in the beginning of this PhD 2-step fabrication of inverted PSCs was found to be easier than single step. Given more time, further work on single step PSCs utilising anti-solvent treatment would have been conducted. PEDOT:PSS is proven to be the main reason for the low stability of fabricated devices using it as a HTL which lead to poor long-term performance of inverted architecture PSCs. The next step of the research would have been the optimisation of non-inverted devices using metal oxide transporting layers which are anticipated to substantially improve the long-term stability of PSCs. The next step which would have been taken is the replacement of the organic cation methylammonium iodide with caesium iodide which will help eliminate the hysteresis and promote for a higher environment stability. In order for this exciting technology to become commercially available sooner PSCs require upscaling of the laboratory scale devices to modules which must have decent surface uniformity to sustain the laboratory scale record breaking efficiencies. The next challenge in this project would have been tackling the difficulty of upscaling with spin coating using spray-coating and slot-dye deposition.

As a final phase of the research the effects of multiple orientations of PSCs would have been investigated. It is certain that perovskite will outperform OPVs due to the very high EQE absorption which will help harvest solar power even by north facing modules.

Appendix

Table A1 showing the entire list of ISOS test protocols and table A2 showing the stress conditions for the designed indoor ALT experiment and also an estimated AF for each of the runs.

Dark	**ISOS D1**	**ISOS D2**	**ISOS D3**
Light Source	None	None	None
Temperature	Ambient	65/85 °C	65/85 °C
Relative Humidity	Ambient	Ambient (low)	85%
Environment	Ambient	Oven	Environmental chamber
Characterisation Light Source	Solar sim/Sunlight	Solar sim	Solar sim
Load	Open circuit	Open circuit	Open circuit
Outdoor	**ISOS O1**	**ISOS O2**	**ISOS O3**
Light Source	Sunlight	Sunlight	Sunlight
Temperature	Ambient	Ambient	Ambient
Relative Humidity	Ambient	Ambient	Ambient
Environment	Outdoor	Outdoor	Outdoor
Characterisation Light Source	Solar sim	Sunlight	Solar sim/Sunlight
Load	MPP/Open circuit	MPP/Open circuit	MPP
Laboratory weathering	**ISOS L1**	**ISOS L2**	**ISOS L3**
Light Source	Simulator	Simulator	Simulator
Temperature	Ambient	65/85 °C	65/85 °C
Relative Humidity	Ambient	Ambient	Near 50%
Environment	Light only	Light and temp	Light, temp and RH
Characterisation Light Source	Solar sim	Solar sim	Solar sim
Load	MPP/Open circuit	MPP/Open circuit	MPP
Thermal cycling	**ISOS T1**	**ISOS T2**	**ISOS T3**

Light Source	None	None	None
Temperature	RT to 65/85 °C	RT to 65/85 °C	-40°C to +85°C
Relative Humidity	Ambient	Ambient	Near 55%
Environment	Oven/Hotplate	Oven/Env chamber	Environmental chamber
Characterisation Light Source	Solar sim/Sunlight	Solar sim	Solar sim
Load	Open circuit	Open circuit	Open circuit
Solar-thermal-humidity	**ISOS LT1**	**ISOS LT2**	**ISOS LT3**
Light Source	Simulator	Simulator	
Temperature	linear/step ramp RT to 65 °C	linear ramp 5°C to 65 °C	linear ramp -25°C to 65°C
Relative Humidity	Uncontrolled/Monitored	Monitored/50% at +40° C	Monitored/50% at +40° C
Environment	Environmental chamber	Environmental chamber+solar sim	Environmental chamber+solar sim+chiller
Characterisation Light Source	Solar simulator	Solar sim	Solar sim
Load	MPP/Open circuit	MPP/Open circuit	MPP/Open circuit

Table A1 – ISOS testing protocols

Test ID	Test run order	Temperature (K)	Relative Humidity (%)	Light (Sun)	AF based on previous calculations	Estimate time to T_{80} based on previous calculations
1		318 (-1)	67 (-1)	0.5 (-1)	2.89	148
2		318 (-1)	67 (-1)	1 (1)	4.63	92
3		318 (-1)	85 (1)	0.25 (-1)	4.64	92
4		318 (-1)	85 (1)	0.5 (1)	7.43	57
5		338 (1)	67 (-1)	0.25 (-1)	4.78	89
6		338 (1)	67 (-1)	0.5 (1)	7.66	55
7		338 (1)	85 (1)	0.25 (-1)	7.68	55
8		338 (1)	85 (1)	0.5 (1)	12.31	34

Table A2 *– 2^3 matrix showing in detail the stress conditions for the designed experiment and also an estimated AF for each of the runs.*

References

[1] British Petroleum, “BP Statistical Review of World Energy 2017,” *Br. Pet.*, no. 66, pp. 1–52, 2017.

[2] IEA, *KEY WORLD ENERGY STATISTICS*. 2017, p. 95.

[3] EIA, “International Energy Outlook 2017 Overview,” *U.S. Energy Inf. Adm.*, vol. IEO2017, no. 2017, p. 143, 2017.

[4] Intergovernmental Panel on Climate Change, “Future Global and Regional Climate Change - AR5 WG1 Summary for Policymakers,” *IPCC books online*, 2013.

[5] BBC, “Greenhouse effect.” [Online]. Available: http://www.bbc.co.uk/schools/gcsebitesize/geography/climate_change/greenhouse_effect_rev1.shtml. [Accessed: 14-Dec-2017].

[6] IEA, “World Energy Outlook 2017,” 2017. [Online]. Available: https://www.iea.org/weo2017/. [Accessed: 26-Nov-2017].

[7] Renewable Energy Policy Network for the 21st Century, *Renewables 2017: global status report*, vol. 72, no. October 2016. 2017.

[8] R. Perez *et al.*, “A Fundamental Look At Supply Side Energy Reserves For The Planet,” *Int. Energy Agency SHC Program. Sol. Updat.*, vol. 62, no. April 2009, pp. 4–6, 2015.

[9] Enerdata, “Global Energy Statistical Yearbook 2017.” [Online]. Available: https://yearbook.enerdata.net/electricity/electricity-domestic-consumption-data.html. [Accessed: 14-Dec-2017].

[10] S. Ingrams, “Solar PV Prices and Savings,” *Which?* [Online]. Available: https://www.which.co.uk/reviews/solar-panels/article/solar-panels/solar-pv-prices-and-savings. [Accessed: 22-Oct-2017].

[11] IEA, “Next Generation Wind and Solar Power - From cost to value,” p. 40, 2016.

[12] International Energy Agency Photovoltaic Power Systems Programme, “Snapshot of global photovoltaic markets 2016,” pp. 1–16, 2017.

[13] W. Shockley and H. J. Queisser, “Detailed balance limit of efficiency of p-n junction solar cells,” *J. Appl. Phys.*, vol. 32, no. 3, pp. 510–519, 1961.

[14] National Renewable Energy Laboratory (NREL), “Best Research Cell Efficiencies Chart.” [Online]. Available: https://www.nrel.gov/pv/assets/images/efficiency-chart.png. [Accessed: 10-Dec-2017].

[15] “Perovskite Photovoltaics 2018-2028,” *Idtechex*. [Online]. Available: http://www.idtechex.com/research/reports/the-rise-of-perovskite-solar-cells-2015-2025-

000442.asp. [Accessed: 09-Mar-2018].

[16] Fraunhofer, “Photovoltaics Report - 2017,” 2017.

[17] M. A. Green, “Third generation photovoltaics: Assessment of progress over the last decade,” *Conf. Rec. IEEE Photovolt. Spec. Conf.*, pp. 000146–000149, 2009.

[18] G. F. Brown *et al.*, “Third generation photovoltaics,” *Laser Photonics Rev.*, vol. 3, no. 4, pp. 394–405, 2009.

[19] B. O’Regan *et al.*, “A Low-Cost, High-Efficiency Solar-Cell Based on Dye-Sensitized Colloidal TiO_2 Films,” *Nature*, vol. 353, no. 6346, pp. 737–740, 1991.

[20] E. M. Sanehira *et al.*, “Enhanced mobility $CsPbI_3$ quantum dot arrays for record-efficiency, high-voltage photovoltaic cells,” *Sci. Adv.*, vol. 3, no. 10, p. eaao4204, 2017.

[21] J. You *et al.*, “A polymer tandem solar cell with 10.6% power conversion efficiency,” *Nat. Commun.*, vol. 4, p. 1446, 2013.

[22] J. Zhao *et al.*, “Efficient organic solar cells processed from hydrocarbon solvents,” *Nat. Energy*, vol. 1, no. 2, p. 15027, 2016.

[23] Heliatek, “Heliatek sets new Organic Photovoltaic world record efficiency of 13.2%.” [Online]. Available: http://www.heliatek.com/en/press/press-releases/details/heliatek-sets-new-organic-photovoltaic-world-record-efficiency-of-13-2. [Accessed: 28-Oct-2017].

[24] T. Leijtens *et al.*, “Overcoming ultraviolet light instability of sensitized TiO_2 with meso-superstructured organometal tri-halide perovskite solar cells.,” *Nat. Commun.*, vol. 4, no. DECEMBER, p. 2885, 2013.

[25] B. Saparov *et al.*, “Thin-film preparation and characterization of $Cs3Sb_2I_9$: A lead-free layered perovskite semiconductor,” *Chem. Mater.*, p. 150709082114007, 2015.

[26] A. Marchioro *et al.*, “Unravelling the mechanism of photoinduced charge transfer processes in lead iodide perovskite solar cells,” *Nat. Photonics*, vol. 8, no. 3, pp. 250–255, 2014.

[27] K. A. Bush *et al.*, “Tandem Solar Cells With Improved Stability,” *Nat. Energy*, vol. 2, no. February, pp. 1–7, 2017.

[28] P. Heinstein *et al.*, “Building integrated photovoltaics (BIPV): Review, potentials, barriers and myths,” *Green*, vol. 3, no. 2, pp. 125–156, 2013.

[29] A. K. Shukla *et al.*, “A comprehensive review on design of building integrated photovoltaic system,” *Energy Build.*, vol. 128, pp. 99–110, 2016.

[30] W. S. Yang *et al.*, “Iodide management in formamidinium-lead-halide–based perovskite layers for efficient solar cells,” *Science (80-.).*, vol. 356, no. 6345, pp. 1376–1379, 2017.

[31] G. Peng *et al.*, “Hybrid Organic-Inorganic Perovskites Open a New Era for Low-Cost , High Efficiency Solar Cells,” vol. 2, no. d, 2014.

[32] J. Troughton *et al.*, “Humidity resistant fabrication of $CH_3NH_3PbI_3$ perovskite solar cells and modules,” *Nano Energy*, vol. 39, no. February, pp. 60–68, 2017.

[33] Z. Xiao *et al.*, “Efficient, high yield perovskite photovoltaic devices grown by interdiffusion of solution-processed precursor stacking layers,” *Energy Environ. Sci.*, vol. 7, pp. 2619–2623, 2014.

[34] A. Marchioro *et al.*, “Unravelling the mechanism of photoinduced charge transfer processes in lead iodide perovskite solar cells,” *Nat Phot.*, vol. 8, no. 3, pp. 250–255, 2014.

[35] D. Chapin *et al.*, “Perovskite Solar Cell - A Source of Renewable Green,” vol. 5, no. 7, pp. 1–5, 2015.

[36] N.-G. Park, “Perovskite solar cells: an emerging photovoltaic technology,” Mater. Today (Oxford, U. K.), vol. 18, no. 2, pp. 65–72, 2014.

[37] Y.-J. Jeon *et al.*, “Planar heterojunction perovskite solar cells with superior reproducibility,” *Sci. Rep.*, vol. 4, no. 1, p. 6953, 2015.

[38] M. Grätzel *et al.*, “Organometal Halide Perovskite Photovoltaics: a Diamond in the Rough,” *Nano*, vol. 9, no. 5, p. 1440002, 2014.

[39] J. H. Noh *et al.*, “Chemical management for colorful, efficient, and stable inorganic-organic hybrid nanostructured solar cells,” *Nano Lett.*, vol. 13, no. 4, pp. 1764–1769, 2013.

[40] A. S. Verma *et al.*, “Lattice constant of cubic perovskites,” *J. Alloys Compd.*, vol. 485, no. 1–2, pp. 514–518, 2009.

[41] F. Wei *et al.*, “The synthesis, structure and electronic properties of a lead-free hybrid inorganic–organic double perovskite $(MA)_2KBiCl_6$(MA = methylammonium),” *Mater. Horiz.*, vol. 3, no. 4, pp. 328–332, 2016.

[42] W.-J. Yin *et al.*, “Halide perovskite materials for solar cells: a theoretical review,” *J. Mater. Chem. A*, vol. 3, pp. 8926–8942, 2014.

[43] S. D. Stranks *et al.*, “Electron-Hole Diffusion Lengths Exceeding,” *Science*, vol. 342, no. 2013, pp. 341–344, 2014.

[44] G. E. Eperon, “Active Layer Control for High Efficiency Perovskite Solar Cells,” 2015.

[45] N. G. Park, “Perovskite solar cells: An emerging photovoltaic technology,” *Mater. Today*, vol. 18, no. 2, pp. 65–72, 2015.

[46] Y. Chen *et al.*, “Extended carrier lifetimes and diffusion in hybrid perovskites revealed by Hall effect and photoconductivity measurements,” *Nat. Commun.*, vol. 7, 2016.

[47] “Perovskite solar cells: Why are electron/hole-transporting layers required?” [Online]. Available: https://physics.stackexchange.com/questions/363966/perovskite-solar-cells-why-are-electron-hole-transporting-layers-required. [Accessed: 02-Nov-2017].

[48] K. Yan *et al.*, “Memristive property’s effects on the I–V characteristics of perovskite solar cells,” *Sci. Rep.*, vol. 7, no. 1, p. 6025, 2017.

[49] L. S. Ze Yu, “Recent Progress on Hole-Transporting Materials for Emerging Organometal Halide Perovskite Solar Cells,” *Adv. Energy Mater.*, vol. 5, no. 12, 2015.

[50] S. S. Mali *et al.*, “p-i-n/n-i-p type planar hybrid structure of highly efficient perovskite solar cells towards improved air stability: synthetic strategies and the role of p-type hole transport layer (HTL) and n-type electron transport layer (ETL) metal oxides,” *Nanoscale*, vol. 8, no. 20, pp. 10528–10540, 2016.

[51] L. Dongxue *et al.*, “Recent progress of dopant-free organic hole-transporting materials in perovskite solar cells,” *J. Semicond.*, vol. 38, no. 1, p. 11005, 2017.

[52] P. Vivo *et al.*, “Hole-transporting materials for printable perovskite solar cells,” *Materials (Basel).*, vol. 10, no. 9, pp. 1–45, 2017.

[53] V. Gonzalez-pedro *et al.*, “General Working Principles of $CH_3NH_3Pb_{X3}$ Perovskite Solar Cells,” *Nano Lett.*, vol. 14, pp. 888–893, 2014.

[54] T. Salim *et al.*, “Perovskite-based solar cells: impact of morphology and device architecture on device performance,” *J. Mater. Chem. A Mater. energy Sustain.*, vol. 3, pp. 8943–8969, 2015.

[55] G. Hodes, “Perovskite-Based Solar Cells,” *sciencemag*, vol. 342, no. October, pp. 317–319, 2013.

[56] M. Kaltenbrunner *et al.*, “Flexible high power-per-weight perovskite solar cells with chromium oxide–metal contacts for improved stability in air,” *Nat. Mater.*, vol. 14, no. 10, pp. 1032–1039, 2015.

[57] M. Park *et al.*, “High-performance flexible and air-stable perovskite solar cells with a large active area based on poly(3-hexylthiophene) nanofibrils,” *J. Mater. Chem. A*, vol. 4, no. 29, pp. 11307–11316, 2016.

[58] B. Conings *et al.*, “An easy-to-fabricate low-temperature TiO_2 electron collection layer for high efficiency planar heterojunction perovskite solar cells An easy-to-fabricate low-temperature TiO 2 electron collection layer for high efficiency planar heterojunction perovskite ,” vol. 81505, no. 2014, 2015.

[59] A. Yella *et al.*, “Nanocrystalline rutile electron extraction layer enables low-temperature solution processed perovskite photovoltaics with 13.7% efficiency,” *Nano Lett.*, vol. 14, no. 5, pp. 2591–2596, 2014.

[60] D. Liu *et al.*, “Perovskite solar cells with a planar heterojunction structure prepared using room-temperature solution processing techniques,” *Nat. Photonics*, vol. 8, no. 2, pp. 133–138, 2013.

[61] J. Kim *et al.*, “Efficient planar-heterojunction perovskite solar cells achieved via interfacial modification of a sol–gel ZnO electron collection layer,” *J. Mater. Chem. A*, vol. 2, no. 41, pp.

17291–17296, 2014.

[62] J. Y. Jeng *et al.*, “$CH_3NH_3PbI_3$ perovskite/fullerene planar-heterojunction hybrid solar cells,” *Adv. Mater.*, vol. 25, no. 27, pp. 3727–3732, 2013.

[63] S. Sun *et al.*, “The origin of high efficiency in low-temperature solution-processable bilayer organometal halide hybrid solar cells,” *Energy Environ. Sci.*, vol. 7, no. 1, pp. 399–407, 2014.

[64] W. J. Yin *et al.*, “Unique properties of halide perovskites as possible origins of the superior solar cell performance,” *Adv. Mater.*, vol. 26, no. 27, pp. 4653–4658, 2014.

[65] B.-X. Chen *et al.*, “Achieving high-performance planar perovskite solar cell with Nb-doped TiO_2 compact layer by enhanced electron injection and efficient charge extraction,” *J. Mater. Chem. A*, vol. 4, no. 15, pp. 5647–5653, 2016.

[66] A. Guerrero *et al.*, “Interfacial degradation of planar lead halide perovskite solar cells,” *ACS Nano*, vol. 10, no. 1, pp. 218–224, 2016.

[67] K.-W. Tsai *et al.*, “High-performance hole-transporting layer-free conventional perovskite/fullerene heterojunction thin-film solar cells,” *J. Mater. Chem. A*, vol. 3, no. 17, pp. 9128–9132, 2015.

[68] F. Hou *et al.*, “Efficient and stable planar heterojunction perovskite solar cells with an MoO_3 /PEDOT:PSS hole transporting layer,” *Nanoscale*, vol. 7, no. 21, pp. 9427–9432, 2015.

[69] Y.-Y. Yu *et al.*, “Perovskite photovoltaics featuring solution-processable TiO_2 as an interfacial electron-transporting layer display to improve performance and stability,” *Nanoscale*, vol. 6, no. 19, pp. 11403–11410, 2014.

[70] K. G. Lim *et al.*, “Boosting the power conversion efficiency of perovskite solar cells using self-organized polymeric hole extraction layers with high work function,” *Adv. Mater.*, vol. 26, no. 37, pp. 6461–6466, 2014.

[71] J. Y. Jeng *et al.*, “Nickel oxide electrode interlayer in $CH_3NH_3PbI_3$ perovskite/PCBM planar-heterojunction hybrid solar cells,” *Adv. Mater.*, vol. 26, no. 24, pp. 4107–4113, 2014.

[72] S. Y. Park *et al.*, “Organic solar cells employing magnetron sputtered p-type nickel oxide thin film as the anode buffer layer,” *Sol. Energy Mater. Sol. Cells*, vol. 94, no. 12, pp. 2332–2336, 2010.

[73] M. B. Islam *et al.*, “NiOx Hole Transport Layer for Perovskite Solar Cells with Improved Stability and Reproducibility,” *ACS Omega*, vol. 2, no. 5, pp. 2291–2299, 2017.

[74] H.-S. Kim *et al.*, “Lead Iodide Perovskite Sensitized All-Solid-State Submicron Thin Film Mesoscopic Solar Cell with Efficiency Exceeding 9%,” *Sci. Rep.*, vol. 2, pp. 1–7, 2012.

[75] Michael M. Lee, *et al.*, “Efficient Hybrid Solar Cells Based on Meso-Superstructured Organometal Halide Perovskites,” vol. 313, no. September, pp. 1942–1945, 2006.

[76] R. S. Sanchez *et al.*, “Light-induced effects on Spiro-OMeTAD films and hybrid lead halide

perovskite solar cells," *Sol. Energy Mater. Sol. Cells*, vol. 158, pp. 189–194, 2016.

[77] J. You *et al.*, "Improved air stability of perovskite solar cells via solution-processed metal oxide transport layers," *Nat. Nanotechnol.*, vol. 11, no. 1, pp. 75–81, 2015.

[78] F. Fu *et al.*, "Low-temperature-processed efficient semi-transparent planar perovskite solar cells for bifacial and tandem applications," *Nat. Commun.*, vol. 6, p. 8932, 2015.

[79] James M Ball, *et al.*, "Low-temperature processed meso-superstructured to thin-film perovskite solar cells," *Energy Environ. Sci.*, no. 6, pp. 1739–1743, 2013.

[80] D. Koushik *et al.*, "High-efficiency humidity-stable planar perovskite solar cells based on atomic layer architecture," *Energy Environ. Sci.*, vol. 10, no. 1, pp. 91–100, 2017.

[81] Z. Yang *et al.*, "Organolead halide perovskite: A rising player in high-efficiency solar cells," *Chinese J. Catal.*, vol. 35, no. 7, pp. 983–988, 2014.

[82] A. Kojima *et al.*, "Organo Metal Halide Perovskites as Visible-Light Sensitizer for Photovoltaic Cells," *Priv. Commun.*, vol. 1, p. 1, 2009.

[83] M. Liu *et al.*, "Efficient planar heterojunction perovskite solar cells by vapour deposition.," *Nature*, vol. 501, no. 7467, pp. 395–8, 2013.

[84] J. Burschka *et al.*, "Sequential deposition as a route to high-performance perovskite-sensitized solar cells.," *Nature*, vol. 499, pp. 316–9, 2013.

[85] B. Nicholson *et al.*, "Interface engineering of highly efficient perovskite solar cells," *sciencemag*, vol. 27, no. 2004, pp. 238–242, 2013.

[86] W. S. Yang *et al.*, "High-performance photovoltaic perovskite layers fabricated through intramolecular exchange," *Science.*, vol. 348, no. 6240, pp. 1234–1237, 2015.

[87] G. Niu *et al.*, "Review of recent progress in chemical stability of perovskite solar cells," *J. Mater. Chem. A*, vol. 3, no. 17, pp. 8970–8980, 2015.

[88] G. Niu *et al.*, "Study on the stability of $CH_3NH_3PbI_3$ films and the effect of post-modification by aluminum oxide in all-solid-state hybrid solar cells," *J. Mater. Chem. A*, vol. 2, no. 3, p. 705, 2014.

[89] J. a. Christians *et al.*, "Transformation of the Excited State and Photovoltaic Efficiency of $CH_3NH_3PbI_3$ Perovskite upon Controlled Exposure to Humidified Air," *J. Am. Chem. Soc.*, vol. 137, no. 4, pp. 1530–1538, 2015.

[90] S. N. Habisreutinger *et al.*, "Carbon Nanotube/Polymer Composites as a Highly Stable Hole Collection Layer in Perovskite Solar Cells," 2014.

[91] D. Bryant *et al.*, "Light and oxygen induced degradation limits the operational stability of methylammonium lead triiodide perovskite solar cells," *Energy Environ. Sci.*, vol. 9, no. 5, pp. 1655–1660, 2016.

[92] F. T. F. O’Mahony *et al.*, “Improved environmental stability of organic lead trihalide perovskite-based photoactive-layers in the presence of mesoporous TiO_2,” *J. Mater. Chem. A*, vol. 3, no. 14, pp. 7219–7223, 2015.

[93] A. J. Pearson *et al.*, “Oxygen Degradation in Mesoporous $Al_2O_3/CH_3NH_3PbI_{3-x}Cl_x$ Perovskite Solar Cells: Kinetics and Mechanisms,” *Adv. Energy Mater.*, vol. 6, no. 13, pp. 1–10, 2016.

[94] T. Leijtens *et al.*, “Overcoming ultraviolet light instability of sensitized TiO_2 with meso-superstructured organometal tri-halide perovskite solar cells,” *Nat. Commun.*, vol. 4, p. 28885.1-8, 2013.

[95] E. A. Katz *et al.*, “Temperature- and Component-Dependent Degradation of Perovskite Photovoltaic Materials under Concentrated Sunlight,” *J. Phys. Chem. Lett.*, vol. 6, pp. 326–330, 2015.

[96] W. L. Leong *et al.*, “Identifying Fundamental Limitations in Halide Perovskite Solar Cells,” *Adv. Mater.*, vol. 28, no. 12, pp. 2439–2445, 2016.

[97] B. Conings *et al.*, “Intrinsic Thermal Instability of Methylammonium Lead Trihalide Perovskite,” *Adv. Energy Mater.*, vol. 5, no. 15, pp. 1–8, 2015.

[98] R. K. Misra *et al.*, “Effect of Halide Composition on the Photochemical Stability of Perovskite Photovoltaic Materials,” *ChemSusChem*, vol. 9, no. 18, pp. 2572–2577, 2016.

[99] R. K. Misra *et al.*, “Temperature- and component-dependent degradation of perovskite photovoltaic materials under concentrated sunlight,” *J. Phys. Chem. Lett.*, vol. 6, no. 3, pp. 326–330, 2015.

[100] X. Li *et al.*, “Outdoor Performance and Stability under Elevated Temperatures and Long-Term Light Soaking of Triple-Layer Mesoporous Perovskite Photovoltaics,” *Energy Technol.*, vol. 3, no. 6, pp. 551–555, 2015.

[101] Y. Reyna *et al.*, “Performance and stability of mixed $FAPbI_{3(0.85)}MAPbBr_{3(0.15)}$ halide perovskite solar cells under outdoor conditions and the effect of low light irradiation,” *Nano Energy*, vol. 30, no. August, pp. 570–579, 2016.

[102] C. S. Peskin *et al.*, “Efficient Hybrid Solar Cells Based on Meso-Superstructured Organometal Halide Perovskites,” vol. 323, no. July, pp. 736–740, 2009.

[103] M. Yang *et al.*, “Facile fabrication of large-grain $CH_3NH_3PbI_3{-}_xBr_x$ films for high-efficiency solar cells via CH_3NH_3Br-selective Ostwald ripening,” *Nat. Commun.*, vol. 7, no. May, p. 12305, 2016.

[104] W. Zhang *et al.*, “Enhanced optoelectronic quality of perovskite thin films with hypophosphorous acid for planar heterojunction solar cells,” *Nat. Commun.*, vol. 6, no. May, pp. 1–9, 2015.

[105] K. Li *et al.*, “An efficient, flexible perovskite solar module exceeding 8% prepared with an ultrafast PbI2deposition rate,” *Sci. Rep.*, vol. 8, no. 1, pp. 1–8, 2018.

[106] M. Xiao *et al.*, “A fast deposition-crystallization procedure for highly efficient lead iodide

perovskite thin-film solar cells," *Angew. Chemie - Int. Ed.*, vol. 53, no. 37, pp. 9898–9903, 2014.

[107] N. J. Jeon *et al.*, "Solvent engineering for high-performance inorganic-organic hybrid perovskite solar cells," *Nat. Mater.*, vol. 13, no. 9, pp. 897–903, 2014.

[108] H. Zhou *et al.*, "Polymer homo-tandem solar cells with best efficiency of 11.3%," *Adv. Mater.*, vol. 27, no. 10, pp. 1767–1773, 2015.

[109] L. Dou *et al.*, "25th anniversary article: A decade of organic/polymeric photovoltaic research," *Adv. Mater.*, vol. 25, no. 46, pp. 6642–6671, 2013.

[110] N. Bristow *et al.*, "Outdoor performance of organic photovoltaics: Diurnal analysis, dependence on temperature, irradiance, and degradation," *J. Renew. Sustain. Energy*, vol. 7, no. 1, 2015.

[111] J. Kettle *et al.*, "Three dimensional corrugated organic photovoltaics for building integration; improving the efficiency, oblique angle and diffuse performance of solar cells," *Energy Environ. Sci.*, vol. 8, no. 11, pp. 3266–3273, 2015.

[112] S. Lizin *et al.*, "The future of organic photovoltaic solar cells as a direct power source for consumer electronics," *Sol. Energy Mater. Sol. Cells*, vol. 103, pp. 1–10, 2012.

[113] M. Jørgensen *et al.*, "The state of organic solar cells - A meta analysis," *Sol. Energy Mater. Sol. Cells*, vol. 119, pp. 84–93, 2013.

[114] Y. Y. G. Li, R. Zhu, "Polymer solar cells," *Nat. Photonics*, vol. 11, no. 6, p. 153.161, 2012.

[115] L. Biniek *et al.*, "Organic photovoltaics: More than ever, an Interdisciplinary field," *Polymers (Basel).*, vol. 8, no. 3, pp. 6–7, 2016.

[116] R. Po, A. Bernardi *et al.*, "From lab to fab: how must the polymer solar cell materials design change? – an industrial perspective," *Energy Environ. Sci.*, vol. 7, no. 3, p. 925, 2014.

[117] D. Gao *et al.*, "Size-dependent behavior of polymer solar cells measured under partial illumination," *Sol. Energy Mater. Sol. Cells*, vol. 95, no. 12, pp. 3516–3519, 2011.

[118] D. Gupta *et al.*, "Area dependent efficiency of organic solar cells," *Appl. Phys. Lett.*, vol. 93, no. 16, 2008.

[119] A. K. Pandey *et al.*, "Size effect on organic optoelectronics devices: Example of photovoltaic cell efficiency," *Phys. Lett. Sect. A Gen. At. Solid State Phys.*, vol. 372, no. 8, pp. 1333–1336, 2008.

[120] InfinityPV, "Demonstrator, infinityPV." [Online]. Available: https://infinitypv.com/products/opv/demonstrator. [Accessed: 10-Nov-2017].

[121] Heliatek, "Heliafilm, Heliatek." [Online]. Available: http://www.heliatek.com/en/heliafilm/technical-data. [Accessed: 10-Nov-2017].

[122] M. O. Reese *et al.*, "Consensus stability testing protocols for organic photovoltaic materials and devices," *Sol. Energy Mater. Sol. Cells*, vol. 95, no. 5, pp. 1253–1267, 2011.

[123] S. A. Gevorgyan *et al.*, "Lifetime of organic photovoltaics: Status and predictions," *Adv. Energy*

Mater., vol. 6, no. 2, 2016.

[124] F. C. Krebs *et al.*, “Roll-to-roll fabrication of monolithic large-area polymer solar cells free from indium-tin-oxide,” *Sol. Energy Mater. Sol. Cells*, vol. 93, no. 9, pp. 1636–1641, 2009.

[125] F. C. Krebs *et al.*, “Printed metal back electrodes for R2R fabricated polymer solar cells studied using the LBIC technique,” *Sol. Energy Mater. Sol. Cells*, vol. 95, no. 5, pp. 1348–1353, 2011.

[126] M. Hösel *et al.*, “Development of Lab-to-Fab Production Equipment Across Several Length Scales for Printed Energy Technologies, Including Solar Cells,” *Energy Technol.*, vol. 3, no. 4, pp. 293–304, 2015.

[127] R. R. Sondergaard *et al.*, “Roll-to-Roll fabrication of large area functional organic materials,” *J. Polym. Sci. Part B Polym. Phys.*, vol. 51, no. 1, pp. 16–34, 2013.

[128] J. A. Hauch *et al.*, “Flexible organic P3HT:PCBM bulk-heterojunction modules with more than 1 year outdoor lifetime,” *Sol. Energy Mater. Sol. Cells*, vol. 92, no. 7, pp. 727–731, 2008.

[129] S. A. Gevorgyan *et al.*, “Interlaboratory outdoor stability studies of flexible roll-to-roll coated organic photovoltaic modules: Stability over 10,000 h,” *Sol. Energy Mater. Sol. Cells*, vol. 116, pp. 187–196, 2013.

[130] R. R. Søndergaard *et al.*, “The use of polyurethane as encapsulating method for polymer solar cells - An inter laboratory study on outdoor stability in 8 countries,” *Sol. Energy Mater. Sol. Cells*, vol. 99, pp. 292–300, 2012.

[131] D. M. Tanenbaum *et al.*, “Edge sealing for low cost stability enhancement of roll-to-roll processed flexible polymer solar cell modules,” *Sol. Energy Mater. Sol. Cells*, vol. 97, pp. 157–163, 2012.

[132] J. a. Duffie, W. a. Beckman, and W. M. Worek, *Solar Engineering of Thermal Processes, 4nd ed.*, vol. 116. 2003.

[133] P. Blanc *et al.*, “Direct normal irradiance related definitions and applications: The circumsolar issue,” *Sol. Energy*, vol. 110, pp. 561–577, 2014.

[134] S. Ransome, “Modelling inaccuracies of PV energy yield simulations,” *Conf. Rec. IEEE Photovolt. Spec. Conf.*, vol. 44, no. 0, pp. 7–11, 2008.

[135] L. Dunn *et al.*, “Comparison of Pyranometers vs . PV Reference Cells for Evaluation of PV Array Performance,” in *Photovoltaic Specialists Conference (PVSC), 2012 38th IEEE*, 2011, pp. 2899–2904.

[136] C. J. Mulligan, C. Bilen, X. Zhou, W. J. Belcher, and P. C. Dastoor, “Levelised cost of electricity for organic photovoltaics,” *Sol. Energy Mater. Sol. Cells*, vol. 133, pp. 26–31, 2015.

[137] M. Manceau *et al.*, “Effects of long-term UV visible light irradiation in the absence of oxygen on P3HT and P3HT: PCBM blend,” *Sol. Energy Mater. Sol. Cells*, vol. 94, no. 10, pp. 1572–1577, 2010.

[138] M. Lira-Cantu *et al.*, "Detrimental Effect of Inert Atmospheres on Hybrid Solar Cells Based on Semiconductor Oxides," *J. Electrochem. Soc.*, vol. 154, no. 6, p. B508, 2007.

[139] G. G. Stokes, "On the change of refrangibility of light," Philos. Trans. R. Soc. London, vol. 142, no. January, pp. 463–562, 1852.

[140] R. Rothemund, "Optical modelling of the external quantum efficiency of solar cells with luminescent down-shifting layers," *Sol. Energy Mater. Sol. Cells*, vol. 120, no. PART B, pp. 616–621, 2014.

[141] H. Ahmed *et al.*, "Characterization of Luminescent Down-Shifting Materials and Applications for PV Devices," *Proc. 8th Photovolt. Sci. Appl. Technol. Conf. Exhib.*, pp. 1–4, 2012.

[142] Z. Hosseini *et al.*, "Enhanced light harvesting with a reflective luminescent down-shifting layer for dye-sensitized solar cells," *ACS Appl. Mater. Interfaces*, vol. 5, no. 12, pp. 5397–5402, 2013.

[143] O. Moudam *et al.*, "Application of UV-absorbing silver(I) luminescent down shifter for PTB7 organic solar cells for enhanced efficiency and stability," *RSC Adv.*, vol. 5, no. 16, pp. 12397–12402, 2015.

[144] R. V. Fernandes *et al.*, "Development of multidye UV filters for OPVs using luminescent materials," *J. Phys. D. Appl. Phys.*, vol. 50, no. 2, p. 25103, 2017.

[145] J. Kettle *et al.*, "Printable luminescent down shifter for enhancing efficiency and stability of organic photovoltaics," *Sol. Energy Mater. Sol. Cells*, vol. 144, pp. 481–487, 2016.

[146] H. Anizelli *et al.*, "Application of luminescence downshifting materials for enhanced stability of $CH_3NH_3PbI_{3(1-x)}Cl_{3x}$ perovskite photovoltaic devices," *Org. Electron.*, vol. 49, pp. 129–134, 2017.

[147] D. Angmo *et al.*, "Over 2 Years of Outdoor Operational and Storage Stability of ITO-Free, Fully Roll-to-Roll Fabricated Polymer Solar Cell Modules," *Energy Technol.*, vol. 3, no. 7, pp. 774–783, 2015.

[148] H. C. Weerasinghe *et al.*, "New barrier encapsulation and lifetime assessment of printed organic photovoltaic modules," *Sol. Energy Mater. Sol. Cells*, vol. 155, pp. 108–116, 2016.

[149] S. B. Darling and F. You, "The case for organic photovoltaics," *RSC Adv.*, vol. 3, pp. 17633–17648, 2013.

[150] "belectric showcases future solar tech for german pavilion at expo 2015." [Online]. Available: https://www.designboom.com/architecture/belectric-reveals-future-solar-tech-for-german-pavilion-at-expo-2015-07-06-2015/. [Accessed: 15-Nov-2017].

[151] J. Robertson, "High density plasma enhanced chemical vapor deposition of optical thin films," *Eur. Phys. J. Appl. Phys.*, vol. 28, pp. 265–291, 2004.

[152] S. A. Gevorgyan *et al.*, "An inter-laboratory stability study of roll-to-roll coated flexible polymer solar modules," *Sol. Energy Mater. Sol. Cells*, vol. 95, no. 5, pp. 1398–1416, 2011.

[153] M. T. Lloyd *et al.*, "Influence of the hole-transport layer on the initial behavior and lifetime of

inverted organic photovoltaics," *Sol. Energy Mater. Sol. Cells*, vol. 95, no. 5, pp. 1382–1388, 2011.

[154] D. M. Tanenbaum *et al.*, "The ISOS-3 inter-laboratory collaboration focused on the stability of a variety of organic photovoltaic devices," *RSC Adv.*, vol. 2, no. 3, pp. 882–893, 2012.

[155] M. H. C.F. Jeff. Wu, *Experiments: Planning, Analysis, and Optimization*, no. 2nd edition. 1988.

[156] S. A. Gevorgyan *et al.*, "Improving, characterizing and predicting the lifetime of organic photovoltaics," *J. Phys. D. Appl. Phys.*, vol. 50, no. 10, p. 103001, 2017.

[157] J. Kettle *et al.*, "Using ISOS consensus test protocols for development of quantitative life test models in ageing of organic solar cells," *Sol. Energy Mater. Sol. Cells*, vol. 167, no. March, pp. 53–59, 2017.

[158] Reliasoft, "Modeling Interactions Between Variables in Accelerated Life Testing or Life-Stress Analysis," *Hotwire*, 2005. [Online]. Available: http://www.weibull.com/hotwire/issue53/hottopics53.htm. [Accessed: 09-Mar-2018].

[159] O. Haillant *et al.*, "An Arrhenius approach to estimating organic photovoltaic module weathering acceleration factors," *Sol. Energy Mater. Sol. Cells*, vol. 95, no. 7, pp. 1889–1895, 2011.

[160] O. Haillant, "Accelerated weathering testing principles to estimate the service life of organic PV modules," *Sol. Energy Mater. Sol. Cells*, vol. 95, no. 5, pp. 1284–1292, 2011.

[161] M. Corazza *et al.*, "Predicting, categorizing and intercomparing the lifetime of OPVs for different ageing tests," *Sol. Energy Mater. Sol. Cells*, vol. 130, pp. 99–106, 2014.

[162] S. Glasstone, THE THEORY OF RATE PROCESS. McGraw-Hill Book Company, Incorporated, 1941

[163] Reliasoft, "Statistical Background." [Online]. Available: http://reliawiki.com/index.php/Statistical_Background. [Accessed: 09-Mar-2018].

[164] Reliasoft, "ALTA Plots." [Online]. Available: http://help.synthesisplatform.net/weibull_alta9/alta_plot_types.htm. [Accessed: 09-Mar-2018].

[165] R. K. Misra *et al.*, "Temperature- and Component-Dependent Degradation of Perovskite Photovoltaic Materials under Concentrated Sunlight," *J. Phys. Chem. Lett.*, vol. 6, no. 3, pp. 326–330, 2015.

[166] National Renewable Energy Laboratory (NREL), "Reference Solar Spectral Irradiance: ASTM G-17." [Online]. Available: http://rredc.nrel.gov/solar/spectra/am1.5/astmg173/astmg173.html. [Accessed: 10-Mar-2018].

[167] D. Energy, "ISOS standards." [Online]. Available: http://plasticphotovoltaics.org/lc/characterization/lc-isos.html. [Accessed: 20-Oct-2017].

[168] J. M. Gordon *et al.*, "Toward ultrahigh-flux photovoltaic concentration," *Appl. Phys. Lett.*, vol. 84, no. 18, pp. 3642–3644, 2004.

[169] E. A. Katz *et al.*, “Photovoltaic characterization of concentrator solar cells by localized irradiation,” *J. Appl. Phys.*, vol. 100, no. 4, pp. 1–8, 2006.

[170] Thorlabs, “UV Solarization-Resistant, Step-Index Multimode Fiber,” 2015. [Online]. Available: https://www.thorlabs.com/thorproduct.cfm?partnumber=FG600AEA. [Accessed: 12-Mar-2018].

[171] D. Angmo *et al.*, “Roll-to-Roll Printed Silver Nanowire Semitransparent Electrodes for Fully Ambient Solution-Processed Tandem Polymer Solar Cells,” *Adv. Funct. Mater.*, vol. 25, no. 28, pp. 4539–4547, 2015.

[172] G. A. Dos Reis Benatto *et al.*, “Roll-to-roll printed silver nanowires for increased stability of flexible ITO-free organic solar cell modules.,” *Nanoscale*, vol. 8, no. 1, pp. 318–26, 2015.

[173] M. Hösel *et al.*, “Development of Lab-to-Fab Production Equipment Across Several Length Scales for Printed Energy Technologies, Including Solar Cells,” *Energy Technol.*, vol. 3, no. 4, pp. 293–304, 2015.

[174] B. Roth *et al.*, “The critical choice of PEDOT:PSS additives for long term stability of roll-to-roll processed OPVs,” *Adv. Energy Mater.*, vol. 5, no. 9, pp. 1–10, 2015.

[175] C. Hoth *et al.*, “Organic solar cells,” *Org. Print. Electron. Fundam. Appl.*, p. 36420367, 2016.

[176] E. Bundgaard *et al.*, “Low band gap polymers for organic photovoltaics,” *Sol. Energy Mater. Sol. Cells*, vol. 91, no. 11, pp. 954–985, 2007.

[177] B. Roth *et al.*, “Improving the Operational Stability of PBDTTTz-4 Polymer Solar Cells Modules by Electrode Modification,” *Adv. Eng. Mater.*, vol. 18, no. 4, pp. 511–517, 2016.

[178] G. A. Dos Reis Benatto *et al.*, “Carbon: The Ultimate Electrode Choice for Widely Distributed Polymer Solar Cells,” *Adv. Energy Mater.*, vol. 4, no. 15, pp. 1–6, 2014.

[179] R. Rösch *et al.*, “Investigation of the degradation mechanisms of a variety of organic photovoltaic devices by combination of imaging techniques—the ISOS-3 inter-laboratory collaboration,” *Energy Environ. Sci.*, vol. 5, no. 4, p. 6521, 2012.

[180] N. Bristow, “OUTDOOR STABILITY STUDIES IN ORGANIC PHOTOVOLTAICS,” Bangor University, 2017.

[181] Davis, “Vantage Pro 2.” [Online]. Available: https://www.davisnet.com/solution/vantage-pro2/. [Accessed: 20-Oct-2017].

[182] J. C. de Mello *et al.*, “An Improved Experimental Determination of External Photoluminescence Quantum Efficiency,” *Adv. Mater.*, vol. 9, no. 3, p. 230, 1997.

[183] W. Li *et al.*, “Enhanced UV-light Stability of Planar Heterojunction Perovskite Solar Cells with Caesium Bromide Interface Modification,” *Energy Environ. Sci.*, vol. 9, pp. 490–498, 2016.

[184] M. R. Ahmadian-Yazdi *et al.*, “Effects of Process Parameters on the Characteristics of Mixed-Halide Perovskite Solar Cells Fabricated by One-Step and Two-Step Sequential Coating,” *Nanoscale Res. Lett.*, vol. 11, no. 1, p. 408, 2016.

[185] N.-G. Park, “Methodologies for high efficiency perovskite solar cells,” *Nano Converg.*, vol. 3, no. 1, p. 15, 2016.

[186] A. Ummadisingu *et al.*, “The effect of illumination on the formation of metal halide perovskite films,” *Nature*, vol. 545, no. 7653, pp. 208–212, 2017.

[187] J.-W. Lee *et al.*, “Two-step deposition method for high-efficiency perovskite solar cells,” *MRS Bull.*, vol. 40, no. 8, pp. 654–659, 2015.

[188] L. Hu *et al.*, “Investigation of the Interaction between Perovskite Films with Moisture via in Situ Electrical Resistance Measurement,” *ACS Appl. Mater. Interfaces*, vol. 7, no. 45, pp. 25113–25120, 2015.

[189] M. Shahbazi *et al.*, “Progress in research on the stability of organometal perovskite solar cells,” *Sol. Energy*, vol. 123, pp. 74–87, 2016.

[190] Z. M. Beiley *et al.*, “Modeling low cost hybrid tandem photovoltaics with the potential for efficiencies exceeding 20%,” *Energy Environ. Sci.*, vol. 5, no. 11, p. 9173, 2012.

[191] J. Yang *et al.*, “Decomposition and Cell Failure Mechanisms in Lead Halide Perovskite Solar Cells,” *Inorg. Chem.*, vol. 56, no. 1, pp. 92–101, 2017.

[192] X. Lin *et al.*, “Efficient and ultraviolet durable inverted polymer solar cells using thermal stable GZO-AgTi-GZO multilayers as a transparent electrode,” *Org. Electron. physics, Mater. Appl.*, vol. 39, pp. 177–183, 2016.

[193] S. N. Habisreutinger *et al.*, “Research Update: Strategies for improving the stability of perovskite solar cells,” *APL Mater.*, vol. 4, no. 9, 2016.

[194] H. J. Yen *et al.*, “Large Grained Perovskite Solar Cells Derived from Single-Crystal Perovskite Powders with Enhanced Ambient Stability,” *ACS Appl. Mater. Interfaces*, vol. 8, no. 23, pp. 14513–14520, 2016.

[195] S.-W. Lee *et al.*, “UV Degradation and Recovery of Perovskite Solar Cells,” *Sci. Rep.*, vol. 6, no. 1, p. 38150, 2016.

[196] G. Niu *et al.*, “Study on the stability of $CH_3NH_3PbI_3$ films and the effect of post-modification by aluminum oxide in all-solid-state hybrid solar cells,” *J. Mater. Chem. A*, vol. 2, no. 3, pp. 705–710, 2014.

[197] G. Abdelmageed *et al.*, “Effect of temperature on light induced degradation in methylammonium lead iodide perovskite thin films and solar cells,” *Sol. Energy Mater. Sol. Cells*, vol. 174, no. August 2017, pp. 566–571, 2018.

[198] J. Cao *et al.*, “Porous PbI_2 films for the fabrication of efficient, stable perovskite solar cells via sequential deposition,” *J. Mater. Chem. A*, vol. 4, no. 26, pp. 10223–10230, 2016.

[199] B. Li *et al.*, “Advancements in the stability of perovskite solar cells: degradation mechanisms and improvement approaches,” *RSC Adv.*, vol. 6, no. 44, pp. 38079–38091, 2016.

[200] A. Merdasa *et al.*, “Super-resolution luminescence microspectroscopy reveals the mechanism of photoinduced degradation in $CH_3NH_3PbI_3$ perovskite nanocrystals,” *J. Phys. Chem. C*, vol. 120, no. 19, pp. 10711–10719, 2016.

[201] T. J. Jacobsson *et al.*, “Unreacted PbI_2 as a Double-Edged Sword for Enhancing the Performance of Perovskite Solar Cells,” *J. Am. Chem. Soc.*, vol. 138, no. 32, pp. 10331–10343, 2016.

[202] Q. Chen *et al.*, “Controllable self-induced passivation of hybrid lead iodide perovskites toward high performance solar cells Controllable self-induced passivation of hybrid lead iodide perovskites toward high performance solar cells,” *Nano Lett.*, vol. 14, no. 7, pp. 4158–4163, 2014.

[203] A. Calloni *et al.*, “Stability of Organic Cations in Solution-Processed $CH_3NH_3PbI_3$ Perovskites: The Formation of Modified Surface Layers,” *J. Phys. Chem. C*, p. 150819161217008, 2015.

[204] Y. yang Du *et al.*, “Undesirable Role of Remnant PbI_2 Layer On Low Temperature Processed Planar Perovskite Solar Cells,” *RSC Adv.*, vol. 6, pp. 101250–101258, 2016.

[205] I. Visoly-Fisher *et al.*, “Concentrated sunlight for accelerated stability testing of organic photovoltaic materials: Towards decoupling light intensity and temperature,” *Sol. Energy Mater. Sol. Cells*, vol. 134, pp. 99–107, 2015.

[206] D. Wang *et al.*, “Stability of perovskite solar cells,” *Sol. Energy Mater. Sol. Cells*, vol. 147, pp. 255–275, 2016.

[207] X. Zhao and N.-G. Park, “Stability Issues on Perovskite Solar Cells,” *Photonics*, vol. 2, no. 4, pp. 1139–1151, 2015.

[208] Kremer, “Fluorescent Blue.” [Online]. Available: http://www.kremer-pigmente.com/media/pdf/94736e.pdf. [Accessed: 04-Nov-2017].

[209] J. Cui *et al.*, “Phosphor coated NiO-based planar inverted organometallic halide perovskite solar cells with enhanced efficiency and stability,” *Appl. Phys. Lett.*, vol. 109, no. 17, pp. 1–6, 2016.

[210] Solaronix, “UV Filter Adhesive Film.” [Online]. Available: http://shop.solaronix.com/uv-filter-adhesive-film.html. [Accessed: 10-Jan-2018].

[211] X. Yin *et al.*, “Highly Efficient Flexible Perovskite Solar Cells Using Solution-Derived NiOx Hole Contacts,” *ACS Nano*, vol. 10, no. 3, pp. 3630–3636, 2016.

[212] S. P. Senanayak *et al.*, “Understanding charge transport in lead iodide perovskite thin-film field-effect transistors,” *Sci. Adv.*, vol. 3, no. 1, p. e1601935, 2017.

[213] H. Zhang *et al.*, “Photovoltaic behaviour of lead methylammonium triiodide perovskite solar cells down to 80 K,” *J. Mater. Chem. A*, vol. 3, no. 22, pp. 11762–11767, 2015.

[214] R. Martínez *et al.*, “High-temperature phase transitions in a quaternary lead based perovskite structured materials with negative temperature coefficient of resistance (NTCR) behavior,” *J.*

Mater. Sci. Mater. Electron., vol. 24, no. 8, pp. 2790–2795, 2013.

[215] N. K. Elumalai *et al.*, “Open circuit voltage of organic solar cells: an in-depth review,” *Energy Environ. Sci.*, vol. 9, no. 2, pp. 391–410, 2016.

[216] G. V. Maria Carmela Di Piazza, “Photovoltaic Sources: Modelling and Emulation.”

[217] R. Steim, “The Impact of Interfaces on the Performance of Organic Photovoltaic Cells.”

[218] M. S. Buday, “Measuring irradiance , temperature and angle of incidence effects on photovoltaic modules in Auburn Hills , Michigan,” 2011.

[219] J. Lee *et al.*, “Degradation and stability of polymer-based solar cells,” pp. 24265–24283, 2012.

[220] N. Grossiord *et al.*, “Degradation mechanisms in organic photovoltaic devices,” *Org. Electron.*, vol. 13, no. 3, pp. 432–456, 2012.

[221] O. Dupré, R. Vaillon, and M. A. Green, *Thermal Behavior of Photovoltaic Devices*. 2017.

[222] Z. Jiang *et al.*, “Amazing stable open-circuit voltage in perovskite solar cells using AgAl alloy electrode,” *Sol. Energy Mater. Sol. Cells*, vol. 146, pp. 35–43, 2016.

[223] A. K. Chauhan *et al.*, “Degradation in perovskite solar cells stored under different environmental conditions,” *J. Phys. D. Appl. Phys.*, vol. 50, no. 32, p. 325105, 2017.

[224] P. Release, “IBC SOLAR Commissions Megawatt Scale PV Power Plant for Commercial Self-consumption,” 2013.

[225] “Inside Cestas Record project , in record time,” *pv magazine*. [Online]. Available: http://www.qosenergy.com/wp-content/uploads/2015/12/20151222_QOS_Energy@PV-Magazine.pdf. [Accessed: 26-Nov-2017].

[226] M. Mehrtash *et al.*, “Performance Evaluation of Sun Tracking Photovoltaic Systems in Canada,” *20th Annu. Int. Confernece Mech. Eng.*, pp. 18–21, 2012.

[227] A. J. Roscoe *et al.*, “Supporting high penetrations of renewable generation via implementation of real-time electricity pricing and demand response,” *IET Renew. Power Gener.*, no. August 2009, pp. 369–382, 2010.

[228] J. Kettle *et al.*, “Three dimensional corrugated organic photovoltaics for building integration; improving the efficiency, oblique angle and diffuse performance of solar cells,” *Energy Environ. Sci.*, vol. 8, pp. 3266–3273, 2015.

[229] Solaronix, “Solaronix Achieves Major Breakthrough Toward Perovskite Solar Cell Industrialization.” [Online]. Available: https://www.solaronix.com/news/solaronix-achieves-major-breakthrough-toward-perovskite-solar-cell-industrialization/. [Accessed: 20-Oct-2017].

[230] InfinityPV, “HeLi-on - The World’s Most Compact Solar Charger.” [Online]. Available: https://infinitypv.com/products/heli-on. [Accessed: 22-Nov-2017].

[231] F. C. Krebs *et al.*, “The OE-A OPV demonstrator anno domini 2011,” *Energy Environ. Sci.*, vol.

4, no. 10, p. 4116, 2011.

[232] K. Rajkumar *et al.*, “Accelerated wear testing for evaluating the life characteristics of copper-graphite tribological composite,” *Mater. Des.*, vol. 32, no. 5, pp. 3029–3035, 2011.

[233] “Accelerated Testing Terms.” [Online]. Available: http://www.weibull.com/knowledge/rel_glossary_at.htm. [Accessed: 14-Mar-2018].

[234] “An Overview of Weibull Analysis.” [Online]. Available: www.barringer1.com/pdf/Chpt1-5th-edition.pdf. [Accessed: 10-Oct-2017].

[235] S. Oman *et al.*, “Estimation of air-spring life based on accelerated experiments,” *Mater. Des.*, vol. 31, no. 8, pp. 3859–3868, 2010.

[236] D. J. Groebel *et al.*, “Determination and interpretation of activation energy using accelerated-test data,” *Annu. Reliab. Maintainab. Symp. 2001 Proceedings.*, pp. 58–63, 2001.

[237] “The Weibull Distribution.” [Online]. Available: http://reliawiki.org/index.php/The_Weibull_Distribution. [Accessed: 11-Dec-2017] [238] “Reliability Design of Mechanical Systems,” *Springer*.

[239] X. Sheng, “Optimizing and improving the growth quality of ZnO nanowire arrays guided by statistical design of experiments,” *ACS Nano*, vol. 3, no. 7, pp. 1803–1812, 2009.

[240] M. H. C.F. Jeff. Wu, “Experiments: Planning, Analysis, and Optimization,” *Wiley sons*, 1988.

[241] H. Guo *et al.*, “Design of Experiments and Data Analysis,” *Ieee*, 2012.

[242] M. G. Larson, “Analysis of variance,” *Circulation*, vol. 117, no. 1, pp. 115–121, 2008.

[243] D. C. Montgomery, *Design and Analysis of Experiments*, 5th edition. Arizona: John Wiley and Sons, 2000.

[244] Reliasoft, “Example 11 - Two Level Fractional Factorial Reliability Design.” [Online]. Available: http://www.reliasoft.com/doe/examples/rc11/index.htm. [Accessed: 05-Sep-2017].

[245] C. M. et al., “Lifetime of organic photovoltaics: Linking outdoor and indoor tests,” *Sol. Energy Mater. Sol. Cells*, vol. 143, pp. 467–472, 2015.

[246] A. Mettas, “Modeling and analysis for multiple stress-type accelerated life\ndata,” *Annu. Reliab. Maintainab. Symp. 2000 Proceedings. Int. Symp. Prod. Qual. Integr. (Cat. No.00CH37055)*, 2000.

[247] C. F. Lam *et al.*, “Time-varying multi-stress ALT for modeling life of outdoor optical products,” *2007 Proc. - Annu. Reliab. Maintainab. Symp. RAMS*, pp. 265–270, 2007.